

Ref: NHESS-2017-41

Dear Editor,

We provided to enter/address the annotation provided by the reviewers and followed their suggestions we revised the manuscript.

Sincerely,

Alessandro Valentini

(Corresponding author)

1 **Integrating faults and past earthquakes into a probabilistic seismic hazard**
2 **model for peninsular Italy**

3

4 Alessandro Valentini¹, Francesco Visini² and Bruno Pace¹

5 ¹ DiSPUTer, Università degli Studi “Gabriele d’Annunzio”, Chieti, Italy

6 ² Istituto Nazionale di Geofisica e Vulcanologia, L’Aquila, Italy

7

8 **Abstract**

9

10 *Italy is one of the most seismically active countries in Europe. Moderate to strong earthquakes, with*
11 *magnitudes of up to ~7, have been historically recorded for many active faults. Currently,*
12 *probabilistic seismic hazard assessments in Italy are mainly based on area source models, in which*
13 *seismicity is modelled using a number of seismotectonic zones and the occurrence of earthquakes is*
14 *assumed uniform. However, in the past decade, efforts have increasingly been directed towards using*
15 *fault sources in seismic hazard models to obtain more detailed and potentially more realistic patterns*
16 *of ground motion. In our model, we used two categories of earthquake sources. The first involves*
17 *active faults, and **geological** slip rates were used to quantify the seismic activity rate. We produced an*
18 *inventory of all fault sources with details of their geometric, kinematic and energetic properties. The*
19 *associated parameters were used to compute the total seismic moment rate of each fault. We*
20 *evaluated the magnitude-frequency distribution (MFD) of each fault source using two models: a*
21 *characteristic Gaussian model centred **at** the maximum magnitude and a Truncated Gutenberg-*
22 *Richter model. The second earthquake source category involves **grid-point** seismicity, **with** a fixed-*
23 *radius smoothed approach and a historical catalogue were used to evaluate seismic activity. Under*
24 *the assumption that deformation is concentrated along faults, we combined the MFD derived from the*
25 *geometry and slip rates of active faults with the MFD from the spatially smoothed earthquake sources*
26 *and assumed that the smoothed seismic activity in the vicinity of an active fault gradually decreases*
27 *by a fault size-driven factor. Additionally, we computed horizontal peak ground acceleration maps for*
28 *return periods of 475 and 2,475 yrs. Although the ranges and gross spatial distributions of the*
29 *expected accelerations obtained here are comparable to those obtained through methods involving*
30 *seismic catalogues and classical zonation models, the spatial pattern of the hazard maps obtained*
31 *with our model is far more detailed. Our model is characterized by areas that are more hazardous*
32 *and that correspond to mapped active faults, while previous models yield expected accelerations that*
33 *are almost uniformly distributed across large regions. In addition, we conducted sensitivity tests to*

Alessandro 6/10/y 15:57

Eliminato: fault

Alessandro 6/10/y 15:57

Eliminato: on

Alessandro 6/10/y 15:57

Eliminato: distributed

Alessandro 6/10/y 15:57

Eliminato: and

38 determine the impact on the hazard results of the earthquake rates derived from two MFD models for
39 faults and to determine the relative contributions of faults versus distributed seismic activity. We
40 believe that our model represents advancements in terms of the input data (quantity and quality) and
41 methodology used in the field of fault-based regional seismic hazard modelling in Italy.

42

43 1. Introduction

44 In this paper, we present the results of an alternative seismogenic source model for
45 use in a probabilistic seismic hazard assessment (PSHA) for Italy that integrates
46 active fault and seismological data. The use of active faults as an input for seismic
47 hazard analysis is a consolidated approach in many countries characterized by high
48 strain rates and seismic releases, as shown, for example, by Field et al. (2015) in
49 California and Stirling et al. (2012) in New Zealand. Moreover, in recent years, active
50 fault data have also been successfully integrated into seismic hazard studies or
51 models, in regions with moderate-to-low strain rates, such as SE Spain (e.g., Garcia-
52 Mayordomo et al., 2007), France (e.g., Scotti et al., 2014), and central Italy (e.g.,
53 Peruzza et al., 2011).

54 In Europe, a working group of the European Seismological Commission, named
55 *Fault2SHA*, is discussing fault-based seismic hazard modelling
56 (<https://sites.google.com/site/linkingfaultpsha/home>). The working group, born to
57 motivate exchanges between field geologists, fault modellers and seismic hazard
58 practitioners, and it is a community initiative with long term vision on studying the
59 active faults. The work we are presenting here stems from the activities of the
60 *Fault2SHA* working group.

61 Combining active faults and background sources is one of the key aspects in this
62 type of approach. Although the methodology remains far from identifying a standard
63 procedure, common approaches combine active faults and background sources by
64 applying a threshold magnitude, generally between 5.5 and 7, above which
65 seismicity is modelled as occurring on faults and below which seismicity is modelled
66 via a smoothed approach (e.g., Akinci et al., 2009; Danciu et al., 2017), area sources
67 (e.g., the so-called FSBG model in the 2013 European Seismic Hazard Model,
68 ESHM13; Woessner et al., 2015) or a combination of the two (Field et al., 2015;
69 Pace et al., 2006).

Alessandro 6/10/y 15:57

Eliminato: a new

Alessandro 6/10/y 15:57

Eliminato: (PSH) model

Alessandro 6/10/y 15:57

Eliminato: includes significant advances in the use of integrated

Alessandro 6/10/y 15:57

Eliminato: PSH

Alessandro 6/10/y 15:57

Eliminato: However

Alessandro 6/10/y 15:57

Eliminato: PSH assessments

Alessandro 6/10/y 15:57

Eliminato: organizes workshops, conference sessions, and special issues and stimulates collaborations between researchers.

Alessandro 6/10/y 15:57

Eliminato: main issues

Alessandro 6/10/y 15:57

Eliminato: SHARE

82 Another important aspect in the use of active faults to build a seismogenic source
83 model is the use of an appropriate MFD to characterize the temporal model
84 describing the seismic activity of faults. Gutenberg-Richter (GR) and characteristic
85 earthquake models are commonly used, and the choice sometimes depends on the
86 knowledge of the fault and data availability. Often, the choice of the “appropriate”
87 MFD for each fault source is a difficult task because palaeoseismological studies are
88 scarce, and it is often difficult to establish clear relationships between mapped faults
89 and historical seismicity. Recently, Field et al. (2017) discussed the effects and
90 complexity of the choice, highlighting how often the GR model results are not
91 consistent with data; however, in other cases, uncharacteristic behaviour, with rates
92 smaller than the maximum, are possible. The discussion is open (see for example
93 the discussion by Kagan et al., 2012) and far from being solved with the available
94 observations, including both seismological and/or geological/paleoseismological
95 observations. In this work, we explore the calculations of these two MFD, a
96 characteristic Gaussian model and a Truncated Gutenberg-Richter model, to
97 explore the epistemic uncertainties and to consider a *Mixed model* as a so-called
98 “expert judgment” model. This *Mixed model* approach, in which we assigned one of
99 the two MFDs to each fault source, is useful for comparison analysis. The rationale
100 of the choice of the MFD of each fault source is explained in detail later in this paper.
101 However, this approach obviously does not solve this issue, that can be treated as
102 epistemic uncertainties using logic tree or random sampling but, in any case, the
103 choice of MFD remains an open question in fault-based PSHA.

104 In Italy, the current national PSH model for building code (Stucchi et al., 2011) is
105 based on area sources and the classical Cornell approach (Cornell, 1968), in which
106 the occurrence of earthquakes is assumed uniform in the defined seismotectonic
107 zones. However, we believe that more efforts must be directed towards using
108 geological data (e.g., fault sources and paleoseismological information) in PSHA to
109 use slip-rates that describe longer seismic cycles to match the larger magnitudes,
110 extend the observational time required to capture the recurrence of large-magnitude
111 events and therefore improve the reliability of seismic hazard assessments. In fact,
112 as highlighted by the 2016-2017 seismic sequences in central Italy, a zone-based
113 source model is not able to model local spatial variations in ground motion (Meletti et
114 al., 2016), whereas a fault-based model can provide insights for aftershock time-

Alessandro 6/10/y 15:57

Eliminato: issue

Alessandro 6/10/y 15:57

Eliminato: in PSHA

Alessandro 6/10/y 15:57

Eliminato: assigning

Alessandro 6/10/y 15:57

Eliminato: “correct” magnitude-frequency distribution (

Alessandro 6/10/y 15:57

Eliminato:)

Alessandro 6/10/y 15:57

Formattato: Inglese (Stati Uniti)

Alessandro 6/10/y 15:57

Formattato: Inglese (Stati Uniti)

Alessandro 6/10/y 15:57

Eliminato: fault sources

Alessandro 6/10/y 15:57

Formattato: Inglese (Stati Uniti)

Alessandro 6/10/y 15:57

Formattato: Inglese (Stati Uniti)

Alessandro 6/10/y 15:57

Formattato: Inglese (Stati Uniti)

Alessandro 6/10/y 15:57

Formattato: Inglese (Stati Uniti)

Alessandro 6/10/y 15:57

Eliminato: MFDs

Alessandro 6/10/y 15:57

Eliminato: judgement

Alessandro 6/10/y 15:57

Eliminato: is useful for comparative analysis, and

Alessandro 6/10/y 15:57

Eliminato: the issue, and

Alessandro 6/10/y 15:57

Eliminato: PSH models

Alessandro 6/10/y 15:57

Eliminato: obtain detailed patterns of ground motion

Alessandro 6/10/y 15:57

Formattato: Inglese (Stati Uniti)

Alessandro 6/10/y 15:57

Eliminato: PSH

131 | dependent hazard analysis (Peruzza et al., 2016). In conclusion, even if the main
132 | purpose of this work is to integrate active faults into hazard calculations for the Italian
133 | territory, this study does not represent an official update of the seismic hazard model
134 | of Italy.

Alessandro 6/10/y 15:57

Eliminato: PSH

135

136 | 2. Source Inputs

137 | Two earthquake-source inputs are considered in this work. The first is a fault source
138 | input that is based on active faults and uses the geometries and slip rates of known
139 | active faults to compute activity rates over a certain range of magnitudes. The
140 | second is a classical smoothed approach that accounts for the rates of expected
141 | earthquakes with a minimum moment magnitude (Mw) of 4.5 but excludes
142 | earthquakes associated with known faults based on a modified earthquake
143 | catalogue. Note that our seismogenic source requires the combination of the two
144 | source inputs related to the locations of expected seismicity rates into a single
145 | source model. Therefore, these two earthquake-source inputs are not independent
146 | but complementary, in both the magnitude and frequency distribution, and together
147 | account for spatial and temporal distribution of the seismicity in Italy.

Alessandro 6/10/y 15:57

Eliminato: magnitude

Alessandro 6/10/y 15:57

Eliminato: PSH model

148 | In the following subsections, we describe the two source inputs and how they are
149 | combined in the seismogenic source model.

Alessandro 6/10/y 15:57

Eliminato: all

150 | 2.1 Fault Source Input

Alessandro 6/10/y 15:57

Eliminato: PSH

151 | In seismic hazard assessment, an active fault is a structure that exhibits evidence of
152 | activity in the late Quaternary, has a demonstrable or potential capability of
153 | generating major earthquakes and is capable of future reactivation (e.g. Machette,
154 | 2000, Danciu et al., 2017). The evidence of Quaternary activity can be
155 | geomorphological and/or paleoseismological when activation information from
156 | instrumental seismic sequences and/or association to historical earthquakes is not
157 | available. Fault source data and location are useful for seismic hazard studies, and
158 | we compiled a database for Italy via the analysis and synthesis of neotectonic and
159 | seismotectonic data from approximately 90 published studies of 110 faults across
160 | Italy. Our database included, but was not limited to, the Database of Individual
161 | Seismogenic Sources (DISS vers. 3.2.0, <http://diss.rm.ingv.it/diss/>), which is already

Alessandro 6/10/y 15:57

Eliminato: (i.e., in the past 125 kyr),

Alessandro 6/10/y 15:57

Eliminato: see

Alessandro 6/10/y 15:57

Eliminato: for a discussion on terminology

Alessandro 6/10/y 15:57

Eliminato: inputs

171 available for Italy. It is important to highlight that the DISS is currently composed of
172 two main categories of seismogenic sources: individual and composite sources. The
173 latter are defined by the DISS' authors as "*simplified and three-dimensional*
174 *representation of a crustal fault containing an unspecified number of seismogenic*
175 *sources that cannot be singled out. Composite seismogenic sources are not*
176 *associated with a specific set of earthquakes or earthquake distribution", and*
177 *therefore are not useful for our PSHA approach; the former is "a simplified and three-*
178 *dimensional representation of a rectangular fault plane. Individual seismogenic*
179 *sources are assumed to exhibit characteristic behaviour with respect to rupture*
180 *length/width and expected magnitude"* ([http://diss.rm.ingv.it/diss/index.php/about/13-](http://diss.rm.ingv.it/diss/index.php/about/13-introduction)
181 [introduction](http://diss.rm.ingv.it/diss/index.php/about/13-introduction)). Even if in agreement with our approach, we note that some of the
182 individual seismogenic sources in the DISS are based on geological and
183 paleoseismological information, and many others used the *Boxer* code (Gasperini et
184 al., 1999) to calculate the epicentre, moment magnitude, size and orientation of a
185 seismic source from observed macroseismic intensities. We carefully analysed the
186 individual sources and some related issues: (i) the lack of updating of the geological
187 information of some individual sources and (ii) the nonconformity between the input
188 data used by DISS in *Boxer* and the latest historical seismicity (CPTI15) and
189 macroseismic intensity (DBMI15) publications. Thus, we performed a full review of
190 the fault database. We then compiled a fault source database as a synthesis of
191 works published over the past twenty years, including DISS, using all updated and
192 available geological, paleoseismological and seismological data (see the
193 supplemental files for a complete list of references). We consider our database as
194 complete as possible in terms of individual seismogenic sources, and it contains all
195 the parameters necessary to construct an input dataset for fault-based PSHA.

196 The resulting database of normal and strike-slip active and seismogenic faults in
197 peninsular Italy (Fig. 1, Tables 1 and 2; see the supplemental files) includes all the
198 available geometric, kinematic, slip rate and earthquake source-related information.
199 In the case of missing data regarding the geometric parameters of dip and rake, we
200 assumed typical dip and rake values of 60° and -90°, respectively, for normal faults
201 and 90° and 0° or 180°, respectively, for strike-slip faults. In this paper, only normal
202 and strike-slip faults are used as fault source inputs. We decided not to include thrust
203 faults in the present study because, with the methodology proposed in this study (as

204 discussed later in the text), the maximum size of a single-rupture segment must be
205 defined, and segmentation criteria have not been established for large thrust zones.
206 Moreover, our method uses long-term geological slip rates to derive active seismicity
207 rates, and sufficient knowledge of these values is not available for thrust faults in
208 Italy. Because some areas of Italy, such as the NW sector of the Alps, Po Valley, the
209 offshore sector of the central Adriatic Sea, and SW Sicily, may be excluded by this
210 limitation, we are considering an update to our approach to include thrust faults and
211 volcanic sources in a future study. The upper and lower boundaries of the
212 seismogenic layer are mainly derived from the analysis of Stucchi et al. (2011) of the
213 Italian national seismic hazard model and locally refined by more detailed studies
214 (Boncio et al., 2011; Peruzza et al., 2011; Ferranti et al., 2014).

215 Based on the compiled database, we explored three main aspects associated with
216 defining a fault source input: the slip rate evaluation, the segmentation model and
217 the expected seismicity rate calculation.

218 2.1.1 Slip rates

219 Slip rates control fault-based seismic hazards (Main, 1996, Roberts et al., 2004; Bull
220 et al., 2006; Visini and Pace, 2014) and reflect the velocities of the mechanisms that
221 operate during continental deformation (e.g., Cowie et al., 2005). Moreover, long-
222 term observations of faults in various tectonic contexts have shown that slip rates
223 vary in space and time (e.g., Bull et al., 2006; Nicol et al., 2006, 2010, McClymont et
224 al., 2009a-b; Gunderson et al., 2013; Benedetti et al., 2013, D'Amato et al., 2016),
225 and numerical simulations (e.g., Robinson et al., 2009; Cowie et al., 2012; Visini and
226 Pace, 2014) suggest that variability mainly occurs in response to interactions
227 between adjacent faults. Therefore, understanding the temporal variability in fault slip
228 rates is a key point in understanding the earthquake recurrence rates and their
229 variability.

230 To evaluate the minimum and maximum slip rates, that we assumed representatives
231 of the long-term slip rate, variability over time, we used slip rates determined in
232 different ways and at different time scales (e.g., at the decadal scale based on
233 geodetic data or at longer scales based on the displacement of Holocene or Plio-
234 Pleistocene horizons). These values were derived from approximately 65 available

Alessandro 6/10/y 15:57

Eliminato: issues

Alessandro 6/10/y 15:57

Eliminato: 2009

Alessandro 6/10/y 15:57

Eliminato: In this work, we used the mean of the minimum and maximum slip rate values listed in Table 1 and assumed that it is representative of the long-term behaviour (over the past 15 ky in the Apennines).

Alessandro 6/10/y 15:57

Spostato in giù [1]: These values were derived from approximately 65 available neotectonics, palaeoseismology and seismotectonics papers (see the supplemental files).

Alessandro 6/10/y 15:57

Eliminato: To evaluate the long-term slip rate, which is representative of the average slip behaviour, and its

Alessandro 6/10/y 15:57

Spostato (inserimento) [1]

250 neotectonics, palaeoseismology and seismotectonics papers (see the supplemental
251 files). In this work, we used the mean of the minimum and maximum slip rate values
252 listed in Table 1 and assumed that they are representative of the long-term
253 behaviour (over the past 15 ky in the Apennines). Because a direct comparison of
254 slip rates over different time intervals obtained by different methods may be
255 misleading (Nicol et al., 2009), we cannot exclude the possibility that uncertainties
256 and errors compilation could affect the original data in some cases. The discussion
257 of these possible biases and their evaluation via statistically derived approaches
258 (e.g., Gardner et al., 1987; Finnegan et al., 2014; Gallen et al., 2015) is beyond the
259 scope of this paper and will be explored in future work. Moreover, we are assuming
260 that slip rate values used are representative of seismic movements, and aseismic
261 factors are not taken into account. Therefore, we believe that investigating the effect
262 of this assumption could be another issue explored in future work; for example, by
263 differentiating between aseismic slip factors in different tectonic contexts.

264 Because 28 faults had no measured slip (or throw) rate (Fig. 1a), we proposed a
265 statistically derived approach to assign a slip rate to these faults. Based on the slip
266 rate spatial distribution shown in Figure 1b, we subdivided the fault database into
267 three large regions—the Northern Apennines, Central-Southern Apennines and
268 Calabria-Sicilian coast—and analysed the slip rate distribution in these three areas.
269 Figure 1b, indicates that the slip rates tend to increase from north to south. The fault
270 slip rates in the Northern Apennines range from 0.3 to 0.8 mm/yr, with the most
271 common values ranging from approximately 0.5-0.6 mm/yr; the slip rates in the
272 Central-Southern Apennines range from 0.3 to 1.0, and the most common rate is
273 approximately 0.3 mm/yr; and the slip rates in the southern area (Calabria and Sicily)
274 range from 0.9 to 1.8, with the most common being approximately 0.9 mm/yr.

275 Keeping in mind that average and minimum-maximum range of slip rate represents
276 two different aspects of the slip rate behaviour of a fault (average long-term and its
277 variability), we analysed them independently to assign values to active faults without
278 measures.

279 The first step in assigning an average slip rate and a range of variability to the faults
280 with unknown values is to identify the most representative distribution among known
281 probability density functions using the slip rate data from each of the three areas. We
282 test five well-known probability density functions (*Weibull, normal, exponential,*

Alessandro 6/10/y 15:57

Eliminato: epistemic

Alessandro 6/10/y 15:57

Eliminato: In

Alessandro 6/10/y 15:57

Eliminato: ,

286 *Inverse Gaussian* and *gamma*) against mean slip rate observations. The resulting
287 function with the highest log-likelihood is the *normal* function in all three areas. Thus,
288 the mean value of the *normal* distribution is assigned to the faults with unknown
289 values. We assign a value of 0.58 mm/yr to faults in the northern area, 0.64 mm/yr to
290 faults in the Central-Southern area, and 1.10 mm/yr to faults in the Calabria-Sicilian
291 area. To assign a range of slip rate variability to each of the three areas, we test the
292 same probability density functions against slip rate variability observations. Similar to
293 the mean slip rate, the probability density function with the highest log-likelihood is
294 the *normal* function in all three areas. We assign a variability of 0.25 mm/yr to the
295 faults in the northern area, 0.29 mm/yr to the faults in the Central-Southern area, and
296 0.35 mm/yr to the faults in the Calabria-Sicilian area.

Alessandro 6/10/y 15:57

Eliminato: value

297

298 2.1.2 Segmentation rules for delineating fault sources

299 An important issue in the definition of a fault source input is the formulation of
300 segmentation rules. In fact, the question of whether structural segment boundaries
301 along multisegment active faults act as persistent barriers to a single rupture is
302 critical to defining the maximum seismogenic potential of fault sources. In our case,
303 the rationale behind the definition of a fault source is based on the assumption that
304 the geometric and kinematic features of a fault source are expressions of its
305 seismogenic potential and that its dimensions are compatible for hosting major (M_w
306 ≥ 5.5) earthquakes. Therefore, a fault source may consist of a fault or an ensemble
307 of faults that slip together during an individual major earthquake. A fault source is
308 defined by a *seismogenic master fault* and its surface projection (Fig. 2a).
309 *Seismogenic master faults* are separated from each other by first-order structural or
310 geometrical complexities. Following the suggestions by Boncio et al. (2004) and
311 Field et al. (2015), we imposed the following segmentation rules in our case study: (i)
312 4-km fault gaps among aligned structures; (ii) intersections with cross structures
313 (often transfer faults) extending 4 km along strike and oriented at nearly right angles
314 to the intersecting faults; (iii) overlapping or underlapping en echelon arrangements
315 with separations between faults of 4 km; (iv) bending $\geq 60^\circ$ for more than 4 km; (v)
316 average slip rate variability along a strike greater than or equal to 50%; and (vi)

Alessandro 6/10/y 15:57

Eliminato: is considered

319 changes in seismogenic thickness greater than 5 km among aligned structures.
320 Example applications of the above rules are illustrated in Figure 2a.

321 By applying the above rules to our fault database, the 110 faults yielded 86 fault
322 sources: 9 strike-slip sources and 77 normal-slip sources. The longest fault source is
323 *Castelluccio dei Sauri* (fault number (*id in Table 1*) 42, L = 93.2 km), and the shortest
324 is *Castrovillari* (*id* 63, L = 10.3 km). The mean length is 30 km. The dip angle varies
325 from 30° to 90°, and 70% of the fault sources have dip angles between 50° and 60°.
326 The mean value of seismogenic thickness (ST) is approximately 12 km. The source
327 with the largest ST is *Mattinata* (*id* 41, ST = 25 km), and the source with the thinnest
328 ST is *Monte Santa Maria Tiberina* (*id* 9, ST = 2.5 km). This low value is due to the
329 presence of an east-dipping low angle normal fault, the Alto-Tiberina Fault (Boncio et
330 al., 2000), located a few kilometres west of the Monte Santa Maria Tiberina fault.
331 Maximum observed moment magnitude values (MObs) have been assigned to 35
332 fault sources (based on Table 2), and the values vary from 5.90 to 7.32. The fault
333 source inputs are shown in Figure 3.

334 2.1.3 Expected seismicity rates

336 Each fault source is characterized by data, such as kinematic, geometry and slip rate
337 information, that we use as inputs for the FiSH code (Pace et al., 2016) to calculate
338 the global budget of the seismic moment rate allowed by the structure. This
339 calculation is based on predefined size-magnitude relationships in terms of the
340 maximum magnitude (Mmax) and the associated mean recurrence time (Tmean).
341 Table 1 summarizes the geometric parameters used as FiSH input parameters for
342 each fault source (seismogenic box) shown in Figure 3. To evaluate Mmax of each
343 source, according to Pace et al., (2016) we first computed and then combined up to
344 five Mmax estimates (see the example of the Paganica fault source in Fig. 2b, details
345 in Pace et al., 2016). Specifically, these five Mmax estimates are as follows: MM0
346 based on the calculated scalar seismic moment (M0) and the application of the
347 standard formula $M_w = 2/3 (\log M_0 - 9.1)$ (Hanks and Kanamori, 1979; IASPEI,
348 2005); two magnitude estimates using the Wells and Coppersmith (1994) empirical
349 relationships for the maximum subsurface rupture length (MRLD) and maximum
350 rupture area (MRA); a estimate that corresponds to the MObs, if available; and a

Alessandro 6/10/y 15:57
Eliminato:)

Alessandro 6/10/y 15:57
Eliminato: Observed values of maximum

Alessandro 6/10/y 15:57
Eliminato: (M_w

Alessandro 6/10/y 15:57
Formattato: Rientro: Sinistro: -1.27 cm, Sporgente: 1.27 cm, Puntato + Livello: 1 + Allinea a: 0.63 cm + Rientra di: 1.27 cm, Tabulazioni: 0 cm, Left + 0.39 cm,

Alessandro 6/10/y 15:57
Formattato: Tipo di carattere:Non Corsivo

Alessandro 6/10/y 15:57
Formattato: Tipo di carattere:Non Corsivo

Alessandro 6/10/y 15:57
Formattato: Tipo di carattere:Non Corsivo

Alessandro 6/10/y 15:57
Formattato: Tipo di carattere:Non Corsivo

Alessandro 6/10/y 15:57
Eliminato: values

Alessandro 6/10/y 15:57
Formattato: Tipo di carattere:Non Corsivo

Alessandro 6/10/y 15:57
Eliminato: values

Alessandro 6/10/y 15:57
Formattato: Tipo di carattere:Non Corsivo

Alessandro 6/10/y 15:57
Formattato: Tipo di carattere:Non Corsivo

Alessandro 6/10/y 15:57
Formattato: Tipo di carattere:Non Corsivo

Alessandro 6/10/y 15:57
Eliminato: values

Alessandro 6/10/y 15:57
Eliminato: value

Alessandro 6/10/y 15:57
Eliminato: maximum observed magnitude (

Alessandro 6/10/y 15:57
Eliminato:),

360 | estimate (MASP, ASP for aspect ratio) computed by reducing the fault length input if
361 | the aspect ratio (W/L) is smaller than the value evaluated by the relation between the
362 | aspect ratio and rupture length of observed earthquake ruptures, as derived by
363 | Peruzza and Pace (2002) (not in the case of Paganica in Fig. 2b). In some cases,
364 | the use of MObs it was useful to better constrain the seismogenic potential of
365 | individual seismogenic sources. For this reason and to take into account MObs in the
366 | estimation of Mmax, for each source we (i) calculated the maximum expected
367 | magnitude (M_{max1}) and the relative uncertainties using only the scaling
368 | relationships and (ii) compared the maximum of observed magnitudes of the
369 | earthquakes potentially associated with the fault. If MObs was within the range of
370 | $M_{max} \pm 1$ standard deviation, we considered the value and recalculated a new
371 | M_{max} (M_{max2}) with a new uncertainty. If MObs was larger than $M_{max1} + 1$
372 | standard deviation, we reviewed the fault geometry and/or the earthquake-source
373 | association. Conversely, if MObs was lower than $M_{max1} - 1$ standard deviation we
374 | considered a GR behaviour for that source, without using the MObs in the M_{max2}
375 | calculation As an example, for the Irpinia Fault (id 51 in Tables 1 and 2), the
376 | characteristics of the 1980 earthquake ($M_w \sim 6.9$) can be used to evaluate M_{max} via
377 | comparison with the M_{max} derived from scaling relationships.

378 | Because all the empirical relationships, as well as observed historical and recent
379 | magnitudes of earthquakes, are affected by uncertainties, the *MomentBalance* (MB)
380 | function of the FiSH code (Pace et al., 2016) was used to account for these
381 | uncertainties. MB computes a probability density function (PDF) for each magnitude
382 | derived from empirical relationships or observations and summarizes the results as a
383 | maximum magnitude value with a standard deviation. The uncertainties in the
384 | empirical scaling relationship, in FiSH, are taken from the studies of Wells and
385 | Coppersmith (1994), Peruzza and Pace (2002) and Leonard (2010). Currently, the
386 | uncertainty in magnitude associated with the seismic moment is fixed and set to 0.3,
387 | whereas the catalogue defines the uncertainty in MObs. Moreover, to combine the
388 | evaluated maximum magnitudes, MB creates a probability curve for each magnitude
389 | by assuming a normal distribution (Fig. 2). We assumed a two-sides untruncated
390 | normal distribution of magnitudes. MB subsequently sums the probability density
391 | curves and fits the summed curve to a normal distribution to obtain the mean of the
392 | maximum magnitude M_{max} and its standard deviation.

Alessandro 6/10/y 15:57

Eliminato: value

Alessandro 6/10/y 15:57

Eliminato: Although incorrect to consider MObs a possible M_{max} value and treat it the same as other estimations, in

Alessandro 6/10/y 15:57

Eliminato: potentials

Alessandro 6/10/y 15:57

Eliminato: As an example

Alessandro 6/10/y 15:57

Eliminato: the Irpinia Fault (id 51 in Tables 1 and 2), the characteristics of the 1980 earthquake ($M_w \sim 6.9$) can be used to evaluate M_{max} via comparison with the M_{max} derived from scaling relationships. In such cases,

Alessandro 6/10/y 15:57

Formattato: Tipo di carattere:Non Corsivo

Alessandro 6/10/y 15:57

Formattato: Tipo di carattere:Non Corsivo

Alessandro 6/10/y 15:57

Formattato: Tipo di carattere:Non Corsivo, Non Apice/ Pedice

Alessandro 6/10/y 15:57

Formattato: Tipo di carattere:Non Corsivo

Alessandro 6/10/y 15:57

Formattato: Tipo di carattere:Non Corsivo

Alessandro 6/10/y 15:57

Formattato: Tipo di carattere:Non Corsivo, Non Apice/ Pedice

Alessandro 6/10/y 15:57

Eliminato: portion

Alessandro 6/10/y 15:57

Eliminato: an

Alessandro 6/10/y 15:57

Eliminato: at both sides.

Alessandro 6/10/y 15:57

Eliminato: successively

408 Thus, a unique M_{max} with a standard deviation is computed for each source, and this
 409 value represents the maximum rupture that is allowed by the fault geometry and the
 410 rheological properties.

411 Finally, to obtain the mean recurrence time of M_{max} (i.e., T_{mean}), we use the criterion
 412 of “segment seismic moment conservation” proposed by Field et al. (1999). This
 413 criterion divides the seismic moment that corresponds to M_{max} by the moment rate
 414 for given a slip rate:

$$415 \quad T_{mean} = \frac{1}{Char_Rate} = \frac{10^{(1.5 M_{max} + 9.1)}}{\mu VLW} \quad (1)$$

416 where T_{mean} is the mean recurrence time in years, $Char_Rate$ is the annual mean
 417 rate of occurrence, M_{max} is the computed mean maximum magnitude, μ is the shear
 418 modulus, V is the average long-term slip rate, and L and W are along-strike rupture
 419 length and downdip width, respectively. Finally, we calculated the seismic moment
 420 rate corresponding to M_{max} and the MFDs of expected seismicity. For each fault
 421 source, we use two “end-member” MFD models: (i) a *Characteristic Gaussian (CHG)*
 422 model, a symmetric Gaussian curve (applied to the incremental MFD values) centred
 423 on the M_{max} value of each fault with a range of magnitudes equal to 1-sigma, and (ii)
 424 a *Truncated Gutenberg-Richter (TGR)* (Ordaz, 1999; Kagan, 2002) model, with M_{max}
 425 as the upper threshold and $M_w = 5.5$ as the minimum threshold for all sources. We
 426 consider a constant b -value equal to 1.0 for all faults, as single-source events are
 427 insufficient for calculating the required statistics; this value corresponds to the mean
 428 b -value determined from the CPTI15 catalogue. The a -values were computed with
 429 the ActivityRate tool of the FiSH code. ActivityRate calculated activity rates at
 430 magnitudes given by each MFD, balancing the total MFD expected seismic moment
 431 rate with the seismic moment rate that was obtained based on M_{max} and T_{mean}
 432 (details in Field et al., 1999; Field et al., 2015; Pace et al., 2016; Woessner et al.,
 433 2015). In Figure 2c, we show an example of the expected seismicity rates in terms of
 434 the annual cumulative rates for the Paganica source using the two above-described
 435 MFD models.

436 Finally, we create a so-called “expert judgement” model, called the *Mixed* model, to
 437 determine the MFD for each fault source based on the earthquake-source
 438 associations. In this case, we decided that if an earthquake assigned to a fault

Alessandro 6/10/y 15:57

Eliminato: $\frac{10^{1.5 M_{max} + 9.1}}{\mu VLW}$

Alessandro 6/10/y 15:57

Formattato: Tipo di carattere:Corsivo

Alessandro 6/10/y 15:57

Eliminato: geometrical parameters of the fault

Alessandro 6/10/y 15:57

Eliminato: This approach was used for both MFDs in this study, and, in particular, we evaluated M_{max} and T_{mean} based on the fault geometry and the slip rate of each individual source. Additionally

Alessandro 6/10/y 15:57

Eliminato: total expected

Alessandro 6/10/y 15:57

Eliminato: using equation 1. Then, we partitioned the total expected seismic moment rate based on a range given by $M_{max} \pm 1$ standard deviation following a Gaussian distribution. ... [1]

Alessandro 6/10/y 15:57

Formattato: Tipo di carattere:Non Corsivo

Alessandro 6/10/y 15:57

Eliminato: The b-values are

Alessandro 6/10/y 15:57

Formattato: Inglese (Stati Uniti)

Alessandro 6/10/y 15:57

Eliminato: and

Alessandro 6/10/y 15:57

Formattato: Inglese (Stati Uniti)

Alessandro 6/10/y 15:57

Eliminato: and they are obtained by the interpolation of earthquake data from the CPTI15 catalogue,

Alessandro 6/10/y 15:57

Eliminato: .

Alessandro 6/10/y 15:57

Formattato: Inglese (Stati Uniti)

Alessandro 6/10/y 15:57

Eliminato: balances

Alessandro 6/10/y 15:57

Eliminato: MFDs

461 source (see Table 2 for earthquake-source associations) has a magnitude lower than
462 the magnitude range in the curve of the *CHG* model distribution, the *TGR* model is
463 applied to that fault source. Otherwise, the *CHG* model, which peaks at the
464 calculated M_{max} , is applied. We decided to not use a logic tree for every fault to
465 capture the model options because one of the aims of this work is to compare the
466 different MFD choices in terms of results and impact in the hazard curves. Of course,
467 errors in this approach can originate from the misallocation of historical earthquakes,
468 and we cannot exclude the possibility that potentially active faults responsible for
469 historical earthquakes have not yet been mapped. The MFD model assigned to each
470 fault source in our *Mixed* model is shown in Figure 3.

471

472 2.2 Distributed Source Inputs

473 Introducing distributed earthquakes into the seismogenic source model is necessary
474 because researchers have not been able to identify a causative source (i.e., a
475 mapped fault) for important earthquakes in the historical catalogue. This lack of
476 correlation between earthquakes and faults may be related to (i) interseismic strain
477 accumulation in areas between major faults, (ii) earthquakes occurring on unknown
478 or blind faults, (iii) earthquakes occurring on unmapped faults characterized by slip
479 rates lower than the rates of erosional processes, and/or (iv) the general lack of
480 surface ruptures associated with faults generating $M_w < 5.5$ earthquakes.

481 We used the historical catalogue of earthquakes (CPTI15; Rovida et al., 2016; Fig.
482 4) to model the occurrence of moderate-to-large ($M_w \geq 4.5$) earthquakes. The
483 catalogue consists of 4,427 events and covers approximately the last one thousand
484 years from 01/01/1005 to 28/12/2014. Before using the catalogue, we removed all
485 events not considered mainshocks via a declustering filter (Gardner and Knopoff,
486 1974). This process resulted in a catalogue composed of 1,839 independent events,
487 which we denote as the “complete” catalogue. Moreover, to avoid double counting
488 due to the use of two seismicity sources, i.e., the fault sources and the distributed
489 seismicity sources, we removed events associated with known active faults from the
490 CPTI15 earthquake catalogue. If the causative fault of an earthquake is known, that
491 earthquake does not need to be included in the seismicity smoothing procedure. The
492 earthquake-source association is based on neotectonics, palaeoseismology and

Alessandro 6/10/y 15:57

Eliminato: PSH

Alessandro 6/10/y 15:57

Eliminato: 1977

Alessandro 6/10/y 15:57

Eliminato: complete

Alessandro 6/10/y 15:57

Eliminato: .

Alessandro 6/10/y 15:57

Eliminato: any artificial effects related to

498 seismotectonics papers (see the supplemental files) and, in a few cases,
 499 macroseismic intensity maps. In Table 2, we listed the earthquakes with known
 500 causative fault sources. The differences in the smoothed rates given by eq. (2) using
 501 the complete and modified catalogues are shown in Figure 5.

502 We applied the standard methodology developed by Frankel (1995) to estimate the
 503 density of seismicity in a grid with latitudinal and longitudinal spacing of 0.05°. The
 504 smoothed rate of events in each cell i is determined as follows:

$$505 \quad n_i = \frac{\sum_j n_j e^{-\frac{\Delta_{ij}^2}{c^2}}}{\sum_j e^{-\frac{\Delta_{ij}^2}{c^2}}} \quad (2)$$

506 where n_i is the cumulative rate of earthquakes with magnitudes greater than the
 507 completeness magnitude M_c in each cell i of the grid and Δ_{ij} is the distance between
 508 the centres of grid cells i and j . The parameter c is the correlation distance. The sum
 509 is calculated in cells j within a distance of $3c$ of cell i .

510 To compute earthquake rates, we adopted the completeness magnitude thresholds
 511 over different periods given by Stucchi et al. (2011) for five large zones (Fig. 4).

512 To optimize the smoothing distance Δ in eq. (2), we divided the earthquake
 513 catalogue into four 10-yr disjoint learning and target periods from the 1960s to the
 514 1990s. For each pair of learning and target catalogues, we used the probability gain
 515 per earthquake to find the optimal smoothing distance (Kagan and Knopoff, 1977;
 516 Helmstetter et al., 2007). After assuming a spatially uniform earthquake density
 517 model as a reference model, the probability gain per earthquake G of a candidate
 518 model relative to a reference model is given by the following equation:

$$519 \quad G = \exp\left(\frac{L-L_0}{N}\right) \quad (3)$$

520 where N is the number of events in the target catalogue and L and L_0 are the joint
 521 log-likelihoods of the candidate model and reference model, respectively. Under the
 522 assumption of a Poisson earthquake distribution, the joint log-likelihood of a model is
 523 given as follows:

524

$$L = \sum_{i_x=1}^{N_x} \sum_{j_y=1}^{N_y} \log p [\lambda(i_x, i_y), \omega] \quad (4)$$

525 where p is the Poisson probability, λ is the spatial density, ω is the number of
 526 observed events during the target period, and the parameters i_x and i_y denote each
 527 corresponding longitude-latitude cell.

528 Figure 6 shows that for the four different pairs of learning-target catalogues, the
 529 optimal smoothing distance c (the mean curve) ranges from 25-40 km. Finally, the
 530 mean of all the probability gains per earthquake yields a maximum smoothing
 531 distance of 30 km (Fig. 6), which is then used in eq. (2).

Alessandro 6/10/y 15:57
 Eliminato: 30

532 The b-value of the GR distribution is calculated on a regional basis using the
 533 maximum-likelihood method of Weichert (1980), which allows multiple periods with
 534 varying completeness levels to be combined. Following the approach recently
 535 proposed by Kamer and Hiemer (2015), we used a penalized likelihood-based
 536 method for the spatial estimation of the GR b-values based on the Voronoi
 537 tessellation of space without tectonic dependency. The whole Italian territory has
 538 been divided into a grid with a longitude/latitude spacing of 0.05° , and the centres of
 539 the grid cells represent the possible centres of Voronoi polygons. We vary the
 540 number of Voronoi polygons, N_v , from 3 to 50, generating 1000 tessellations for
 541 each N_v . The summed log-likelihood of each obtained tessellation is compared with
 542 the log-likelihood given by the simplest model (prior model) obtained using the entire
 543 earthquake dataset. We find that 673 random realizations led to better performance
 544 than the prior model. Thus, we calculate an ensemble model using these 673
 545 solutions, and the mean b-value of each grid node is shown in Figure 4.

546 The maximum magnitude M_{max} assigned to each node of the grid, the nodal planes
 547 and the depths have been taken from ESHM13 (Woessner et al., 2015). The
 548 ESHM13 project evaluated the maximum magnitudes of large areas of Europe
 549 based on a joint procedure involving historical observations and tectonic
 550 regionalization. We adopted the lowest value of the maximum magnitude
 551 distributions proposed by ESHM13, but evaluating the impact of different maximum
 552 magnitudes is beyond the scope of this work.

Alessandro 6/10/y 15:57
 Eliminato: the SHARE European project

Alessandro 6/10/y 15:57
 Eliminato: SHARE

Alessandro 6/10/y 15:57
 Eliminato: magnitudes

Alessandro 6/10/y 15:57
 Eliminato: SHARE

558 Finally, the rates of expected seismicity for each node of the grid are assumed to
559 follow the TGR model (Kagan 2002):

560
$$\lambda(M) = \lambda_0 \frac{\exp(-\beta M) - \exp(-\beta M_u)}{\exp(-\beta M_0) - \exp(-\beta M_u)} \quad (5)$$

561 where the magnitude (M) is in the range of M_0 (minimum magnitude) to M_u (upper or
562 maximum magnitude); otherwise $\lambda(M)$ is 0. Additionally, λ_0 is the smoothed rate of
563 earthquakes at $M_w = 4.5$ and $\beta = b \ln(10)$.

564 2.3 Combining Fault and Distributed Sources

565 To combine the two source inputs, we introduced a distance-dependent linear
566 weighting function, such that the contribution from the distributed sources linearly
567 decreases from 1 to 0 with decreasing distance from the fault. The expected
568 seismicity rates of the distributed sources start at $M_w = 4.5$, which is lower than the
569 minimum magnitude of the fault sources, and the weighting function is only
570 applicable in the magnitude range overlapping the MFD of each fault. This weighting
571 function is based on the assumption that faults tend to modify the surrounding
572 deformation field (Fig. 7), and this assumption is explained in detail later in this
573 paper.

574 During fault system evolution, the increase in the size of a fault through linking with
575 other faults results in an increase in displacement that is proportional to the quantity
576 of strain accommodated by the fault (Kostrov, 1974). Under a constant regional
577 strain rate, the activity of **fault sections** arranged across strike must eventually
578 decrease (Nicol et al., 1997; Cowie, 1998; Roberts et al., 2004). Using an analogue
579 modelling, Mansfield and Cartwright (2001) showed that faults grow via cycles of
580 overlap, relay formation, breaching and linkage between neighbouring segments
581 across a wide range of scales. During the evolution of a system, the merging of
582 neighbour faults, mostly along **strike**, results in the formation of major faults, which
583 **accommodate** the majority of displacement. These major faults are surrounded by
584 minor faults, which **accommodate** lower **amounts** of displacement. To highlight the
585 spatial patterns of major and minor faults, Figures 7a and 7b present diagrams from
586 the Mansfield and Cartwright (2001) experiment in two different stages: the
587 approximate midpoint of the sequence and the end of the sequence. Numerical
588 modelling performed by Cowie et al. (1993) yielded similar evolutionary features for

Alessandro 6/10/y 15:57

Eliminato: the

Alessandro 6/10/y 15:57

Eliminato: are associated with

Alessandro 6/10/y 15:57

Eliminato: are associated with

Alessandro 6/10/y 15:57

Eliminato: degrees

593 major and minor faults. The numerical fault simulation of Cowie et al. (1993) was
594 able to reproduce the development of a normal fault system from the early nucleation
595 stage, including interactions with adjacent faults, to full linkage and the formation of a
596 large thoroughgoing fault. The model also captures the increase in the displacement
597 rate of a large linked fault. In Figures 7c and 7d, we focus on two stages of the
598 simulation (from Cowie et al., 1993): the stage in which the fault segments have
599 formed and some have become linked and the final stage of the simulation.

600 Notably, the spatial distributions of major and minor faults are very similar in the
601 experiments of both Mansfield and Cartwright (2001) and Cowie et al. (1993), as
602 shown in Figures 7a-d. Developments during the early stage of major fault formation
603 appear to control the location and evolution of future faults, with some areas where
604 no major faults develop. The long-term evolution of a fault system is the
605 consequence of the progressive cumulative effects of the slip history, i.e.,
606 earthquake occurrence, of each fault. Large earthquakes are generally thought to
607 produce static and dynamic stress changes in the surrounding areas (King et al.,
608 1994; Stein, 1999; Pace et al., 2014; Verdecchia and Carena, 2016). Static stress
609 changes produce areas of negative stress, also known as shadow zones, and
610 positive stress zones. The spatial distributions of decreases (unloading) and
611 increases (loading) in stress during the long-term slip history of faults likely influence
612 the distance across strike between major faults. Thus, given a known major active
613 fault geometrically capable of hosting a $M_w \geq 5.5$ earthquake, the possibility that a
614 future $M_w \geq 5.5$ earthquake will occur in the vicinity of the fault, but is not caused by
615 that fault, should decrease as the distance from the fault decreases. Conversely,
616 earthquakes with magnitudes lower than 5.5 and those due to slip along minor faults
617 are likely to occur everywhere within a fault system, including in proximity to a major
618 fault.

619 In Figure 7e, we illustrate the results of the analogue and numerical modelling of
620 fault system evolution and indicate the areas around major faults where it is unlikely
621 that other major faults develop. In Figure 7f, we show the next step in moving from
622 geologic and structural considerations. In this step, we combine fault sources and
623 distributed seismicity source inputs, which serve as inputs of the seismogenic model.

624 Fault sources are used to model major faults and are represented by a master fault
625 (i.e., one or more major faults) and its projection at the surface. Distributed seismicity
626 is used to model seismicity associated with minor, unknown or unmapped faults.

Alessandro 6/10/y 15:57

Eliminato: through

Alessandro 6/10/y 15:57

Eliminato: for

Alessandro 6/10/y 15:57

Eliminato: PSH

630 Depending on the positions of distributed seismicity points with respect to the buffer
631 zones around major faults, the rates of expected distributed seismicity remain
632 unmodified or decrease and can even reach zero.

633 Specifically, we introduced a slip rate and a distance-weighted linear function based
634 on the above reasoning. The probability of the occurrence of an earthquake (P_e) with
635 a M_w greater than or equal to the minimum magnitude of the fault is as follows:

$$636 \quad P_e = \begin{cases} 0, & d \leq 1 \text{ km} \\ d/d_{max}, & 1 \text{ km} < d \leq d_{max} \\ 1, & d > d_{max} \end{cases} \quad (6)$$

637 where d is the Joyner-Boore distance from a fault source. The maximum value of d
638 (d_{max}) is assumed to be controlled by the slip rate of the fault. For faults with slip
639 rates ≥ 1 mm/yr, we assume $d_{max} = L/2$ (L is the length along the strike, Fig. 2a); for
640 faults with slip rates of 0.3 - 1 mm/yr, $d_{max} = L/3$; and for faults with slip rates of ≤ 0.3
641 mm/yr, $d_{max} = L/4$. The rationale for varying d_{max} is given by a simple assumption: the
642 higher the slip rate is, the larger the deformation field and the higher the value of
643 d_{max} . This linear function has been applied around each fault, without differences
644 between footwall and hangingwall. We applied eq. (6) to the smoothed occurrence
645 rates of the distributed seismogenic sources. In Figure 8 we show the annual
646 cumulative MFD (Fig. 8a) and incremental annual MFD (Fig. 8c) computed for the
647 red bounded area in Figure 8b. Because we consider three fault source inputs, (red
648 lines in Fig.8): one using only TGR MFD; one using only CHG MFD; and one using
649 Mixed model MFD and because the MFDs of distributed seismicity grid points in the
650 vicinity of faults are modified with respect to the MFDs of these faults, we obtain
651 three different inputs of distributed seismicity, (blue lines in Fig. 8). These three
652 distributed seismogenic source inputs differ because the minimum magnitude of the
653 faults is $M_w 5.5$ in the TGR model, but this value depends on each fault source
654 dimension in the CHG and Mixed model. From $M_w = 4.5$ to $M_w = 5.5$ the complete
655 CPT15 is fully described by the MFD of the distributed source input. From $M_w = 5.5$
656 to $M_w = 6.3$ the total MFD (black lines in Fig. 8) computed using only TGR MFD is
657 higher than the MFD computed using only CHG and Mixed MFD, this because the
658 annual rates of occurrences of intermediate-magnitude events obtained with TGR
659 model are higher than the ones obtained with CHG and Mixed model, as shown in
660 the incremental annual MFD in Figure 8c. From $M_w = 6.4$ to $M_w = 7.3$ the total MFDs

Alessandro 6/10/y 15:57

Eliminato: two

Alessandro 6/10/y 15:57

Eliminato: .

Alessandro 6/10/y 15:57

Eliminato: and the other

Alessandro 6/10/y 15:57

Eliminato: CHR MFD,

Alessandro 6/10/y 15:57

Eliminato: two

Alessandro 6/10/y 15:57

Eliminato: .

Alessandro 6/10/y 15:57

Eliminato: two

Alessandro 6/10/y 15:57

Eliminato: model, as shown in Figure 8.

669 | computed using only CHG and Mixed MFD are higher the total MFD obtained with
670 | TGR model.

671 | Our approach allows incompleteness in the fault database to be bypassed, which is
672 | advantageous because all fault databases should be considered incomplete. In our
673 | approach, the seismicity is modified only in the vicinity of mapped faults. The
674 | remaining areas are fully described by the *distributed* input. With this approach, we
675 | do not define regions with reliable fault information, and the locations of currently
676 | unknown faults can be easily included when they are discovered in the future.

677 | 3. Results and Discussion

678 | To probabilistically obtain ground shaking, we assign the calculated seismicity rates,
679 | based on the Poisson hypothesis, to their pertinent geometries, i.e., individual 3D
680 | seismogenic sources for the *fault input* and point sources for the *distributed input*
681 | (Fig. 8). All the computations are performed using the OpenQuake Engine, an open
682 | source software developed recently with the purpose of providing seismic hazard
683 | and risk assessments, (Pagani et al., 2014). Moreover, it is widely recognized within
684 | the scientific community for its potential. The ground motion prediction equations
685 | (GMPE) of Akkar et al. (2013), Chiou et al., (2008), Faccioli et al., (2010) and Zhao
686 | et al., (2006) are used, because these GMPEs were selected in the ESHM13
687 | (Woessner et al., 2015) for active shallow crust. In addition, we used the GMPE
688 | proposed by Bindi et al. (2014) and calibrated using Italian data. We combined all
689 | GMPEs into a logic tree with the same weight of 0.2 for each branch. Note that these
690 | GMPEs use different distance metrics: the Joyner and Boore distance for Akkar et al.
691 | (2013), Bindi et al. (2014) and Chiou et al. (2008) and the closest rupture distance
692 | for Faccioli et al. (2010) and Zhao et al. (2006).

693 | The results of the fault source inputs, distributed source inputs, and aggregated
694 | model are expressed in terms of peak ground acceleration (PGA) for exceedance
695 | probabilities of 10% and 2% over 50 years, corresponding to return periods of 475
696 | and 2,475 years, respectively (Fig. 9).

697 | To explore the epistemic uncertainty associated with the MFDs of fault source inputs,
698 | we compared the seismic hazard levels obtained based on the TGR and CHG fault
699 | source inputs (left column in Fig. 9) using the TGR and CHG MFDs for all the fault

Alessandro 6/10/y 15:57

Eliminato: areas

Alessandro 6/10/y 15:57

Eliminato: PSH maps

Alessandro 6/10/y 15:57

Eliminato: (Global Earthquake Model, 2016) with a grid spacing of 0.05° in both latitude and longitude. We used this software because it is

Alessandro 6/10/y 15:57

Eliminato: by GEM

Alessandro 6/10/y 15:57

Eliminato: .

Alessandro 6/10/y 15:57

Eliminato: as suggested by

Alessandro 6/10/y 15:57

Eliminato: SHARE European project

Alessandro 6/10/y 15:57

Eliminato:).

Alessandro 6/10/y 15:57

Eliminato: The

Alessandro 6/10/y 15:57

Eliminato: used for each GMPE was

Alessandro 6/10/y 15:57

Eliminato: based on

Alessandro 6/10/y 15:57

Eliminato: distribution of activity rates over the range of magnitudes

715 sources (details in section 2.1.3). Although both models have the same seismic
716 moment release, the different MFDs generate clear differences. In fact, for 10%
717 exceedance probability in 50 yr, in the *TGR* model all faults contribute significantly to
718 the seismic hazard level, whereas in the *CHG* model, only a few faults located in the
719 central Apennines and Calabria contribute to the seismic hazard level. This
720 difference is due to the different shapes of the MFDs in the two models (Fig. 2c). As
721 shown in Figure 8, the amount of earthquakes with magnitudes between 5.5 and
722 approximately 6, which are likely the main contributors to these levels of seismic
723 hazard, is generally higher in the *TGR* model than in the *CHG* model. At a 2%
724 probability of exceedance in 50 years, all fault sources in the *CHG* contribute to the
725 seismic hazard level, but the absolute values are still generally higher in the *TGR*
726 model.

727 The *distributed input* (middle column in Fig. 9) depicts a more uniform shape of the
728 seismic hazard level than that of fault source inputs. A PGA value lower than 0.125 g
729 at a 10% probability of exceedance over 50 years and lower than 0.225 g at a 2%
730 probability of exceedance over 50 years encompass a large part of peninsular Italy
731 and Sicily. Two areas with high levels of ground shaking are located in the central
732 Apennines and northeastern Sicily.

733 The overall model, which was obtained by combining the fault and distributed source
734 inputs, is shown in the right column of Figure 9. Areas with comparatively high
735 seismic hazard levels, i.e., hazard levels greater than 0.225 g and greater than 0.45
736 g at 50-yr exceedance probabilities of 10% and 2%, respectively, are located
737 throughout the Apennines, in Calabria and in Sicily. The fault source inputs
738 contribute most to the total seismic hazard levels in the Apennines, Calabria and
739 eastern Sicily, where the highest PGA values are observed.

740 Figure 10 shows the ratios to the total seismic hazard level by the *fault* and
741 *distributed* source inputs at a specific site (L'Aquila, 42.400-13.400). Notably, in
742 Figure 10, *distributed* sources dominate the seismic hazard contribution at
743 exceedance probabilities greater than ~81% over 50 years, but the contribution of
744 *fault* sources cannot be neglected. Conversely, at exceedance probabilities of less
745 than ~10% in 50 years, the total hazard level is mainly associated with *fault* source
746 inputs. Moreover, note that the contributions are not based on deaggregation but are

Alessandro 6/10/y 15:57

Eliminato: .

Alessandro 6/10/y 15:57

Eliminato: percentage

Alessandro 6/10/y 15:57

Eliminato: hazards

Alessandro 6/10/y 15:57

Eliminato: low

Alessandro 6/10/y 15:57

Eliminato: of

Alessandro 6/10/y 15:57

Eliminato: a low value of

Alessandro 6/10/y 15:57

Eliminato: seismic hazard

Alessandro 6/10/y 15:57

Eliminato: created

Alessandro 6/10/y 15:57

Eliminato: contributions

756 | computed according to the percentage of each source input in the AFOE value of the
757 | combined model.

758 | Figure 11 presents seismic hazard maps for PGA at 10% and 2% exceedance
759 | probabilities in 50 years for *fault* sources, *distributed* sources and a combination of
760 | the two. These data were obtained using the above-described *Mixed* model, in which
761 | we selected the most “appropriate” MFD model (TGR or CHG) for each fault (as
762 | shown in Figure 3). The results of this model therefore have values between those of
763 | the two end-members shown in Figure 9.

764 | Figure 12 shows the *CHG*, *TGR* and *Mixed* model hazard curves of three sites
765 | (Cesena, L’Aquila and Crotona, Fig. 13c). As previously noted, the results of the
766 | *Mixed* model, due to the structure of the model, are between those of the *CHG* and
767 | *TGR* models. The relative positions of the hazard curves derived from the two end-
768 | member models and the *Mixed* model depend on the number of nearby fault sources
769 | that have been modelled using one of the MFD models and on the distance of the
770 | site from the faults. For example, in the case of the Crotona site, the majority of the
771 | fault sources in the *Mixed* model are modelled using the CHG MFD. Thus, the
772 | resulting hazard curve is similar to that of the *CHG* model. For the Cesena site, the
773 | three hazard curves overlap. Because the distance between Cesena and the closest
774 | fault sources is approximately 60 km, the impact of the fault input is less than the
775 | impact of the *distributed* source input. In this case, the choice of a particular MFD
776 | model has a limited impact on the modelling of *distributed* sources. Notably, for an
777 | annual frequency of exceedance (AFOE) higher than 10^{-4} , the *TGR* *fault* source
778 | input values are generally higher than those of the *CHG* source input, and the three
779 | models converge at AFOE lower than 10^{-4} , as shown for L’Aquila site. The resulting
780 | seismic hazard estimates depend on the assumed MFD model (*TGR* vs. *CHG*), and
781 | for the investigated range of AFOE, especially on the annual rates of occurrences of
782 | intermediate-magnitude events (5.5 to ~6.5, see Fig. 8). Therefore, the *TGR* model
783 | leads to the highest hazard values because this range of magnitude (5.5 to ~ 6.5)
784 | contributes the most to the hazard level.

785 | In Figure 13, we investigated the influences of the *Mixed* *fault* source inputs and the
786 | *Mixed* *distributed* source inputs on the total hazard level of the entire study area, as
787 | well as the spatial variability. The maps in Figure 13a show that the contribution of

Alessandro 6/10/y 15:57
Eliminato: PGAs

Alessandro 6/10/y 15:57
Eliminato: lower

Alessandro 6/10/y 15:57
Eliminato: <

Alessandro 6/10/y 15:57
Eliminato: .

Alessandro 6/10/y 15:57
Eliminato: CHG),

Alessandro 6/10/y 15:57
Eliminato: for

Alessandro 6/10/y 15:57
Eliminato:). Because we assume that the maximum magnitude is imposed by the fault geometry and that the seismic moment release is controlled by the slip rate

Alessandro 6/10/y 15:57
Formattato: Colore carattere: Automatico

Alessandro 6/10/y 15:57
Eliminato: in the hazard results

799 *fault* inputs to the total hazard level generally decreases as the exceedance
800 probability increases from 2% to 81% in 50 years. At a 2% probability of exceedance
801 in 50 years, the total hazard levels in the Apennines and eastern Sicily are mainly
802 related to faults, whereas at an 81% probability of exceedance in 50 years, the
803 contributions of *fault* inputs are high in local areas of central Italy and southern
804 Calabria.

805 Moreover, we examined the contributions of *fault* and *distributed* sources along three
806 E-W-oriented profiles in northern, central and southern Italy (Fig. 13b). In areas with
807 faults, the hazard level estimated by *fault* inputs is generally higher than that
808 estimated by the corresponding *distributed* source inputs. Notable exceptions are
809 present in areas proximal to slow-slipping active faults at an 81% probability of
810 exceedance in 50 years (profile A), such as those at the eastern and western
811 boundaries of the fault area in central Italy (profile B), and in areas where the
812 contribution of the *distributed* source input is equal to that of the *fault* input at a 10%
813 probability of exceedance in 50 years (eastern part of profile C).

814 The features depicted by the three profiles result from a combination of the slip rates
815 and spatial distributions of faults for *fault* source inputs. The proposed approach
816 requires a high level of expertise in active tectonics and cautious expert judgement
817 at many levels in the procedure. First, the seismic hazard estimate is based on the
818 definition of a segmentation model, which requires a series of rules based on
819 observations and empirical regression between earthquakes and the size of the
820 causative fault. New data might make it necessary to revise the rules or reconsider
821 the role of the segmentation. In some cases, expert judgement could permit
822 discrimination among different fault source models. Alternatively, all models should
823 be considered branches in a logic tree approach.

824 Moreover, we propose a fault seismicity input in which the MFD of each fault source
825 has been chosen based on an analysis of the occurrences of earthquakes that can
826 be tentatively or confidently assigned to a certain fault. To describe the fault activity,
827 we applied a probability density function to the magnitude, as commonly performed
828 in the literature: the TGR model, where the maximum magnitude is the upper
829 threshold and $M_w = 5.5$ is the lower threshold for all faults, and the characteristic
830 maximum magnitude model, which consists of a truncated normal distribution

Alessandro 6/10/y 15:57

Eliminato: Note that the contributions are not based on deaggregation but are computed according to the percentage of each source input in the AFOE value of the combined model.

Alessandro 6/10/y 15:57

Eliminato: This pattern should be considered a critical aspect of using fault models for PSH analysis. In fact, the

838 centred on the maximum magnitude. Other MFDs have been proposed to model the
839 earthquake recurrence of a fault. For example, Youngs and Coppersmith (1985)
840 proposed a modification to the truncated exponential model to allow for the
841 increased likelihood of characteristic events. However, we focused only on two
842 models, as we believe that instead of a “blind” or qualitative characterization of the
843 MFD of a fault source, future applications of statistical tests of the compatibility
844 between expected earthquake rates and observed historical seismicity could be used
845 as an objective method of identifying the optimal MFD of expected seismicity. As
846 shown in this analyses, fault sources, even if modelled by TGR or CHG MFD, are
847 able to match occurred seismicity for magnitude ~> 5.5 (see for example Fig. 8) and
848 so are complementary to other inputs that model seismicity using area sources or
849 smoothing approaches.

850 To focus on the general procedure for spatially integrating faults with sources
851 representing distributed (or off-fault) seismicity, we did not investigate the impact of
852 other smoothing procedures on the distributed sources, and we used fixed kernels
853 with a constant bandwidth (as in the works of Kagan and Jackson, 1994; Frankel et
854 al. 1997; Zechar and Jordan, 2010). The testing of adaptive bandwidths (e.g., Stock
855 and Smith, 2002; Helmstetter et al., 2006, 2007; Werner et al., 2010; Hiemer et al,
856 2014) or weighted combinations of both models has been reserved for future studies.

857
858 Finally, we compared, as shown in Figure 14, the 2013 European Seismic Hazard
859 Model (ESHM13) developed within the SHARE project, the current Italian national
860 seismic hazard map (MPS04) and the results of our model (Mixed model) using the
861 same GMPEs as used in this study. Specifically, for ESHM13, we compared the
862 results to the fault-based hazard map (FSBG model) that accounts for fault sources
863 and background seismicity. The figure shows how the impact of our fault sources is
864 more evident than in FSBG-ESHM13, and the comparison with MPS04 confirms a
865 similar pattern, but with some significant differences at the regional to local scales.

866
867 The strength of our approach lies in the integration of different levels of information
868 regarding the active faults in Italy, but the final result is unavoidably linked to the
869 quality of the relevant data. Our work focused on presenting and applying a new
870 approach for evaluating seismic hazards based on active faults and intentionally

Alessandro 6/10/y 15:57

Eliminato: 2011

872 avoided the introduction of uncertainties due to the use of different segmentation
873 rules or other slip rate values of faults. Moreover, the impact of ground motion
874 predictive models is important in seismic hazard assessment but beyond the scope
875 of this work. Future steps will be devoted to analysing these uncertainties and
876 evaluating their impacts on seismic hazard estimates.

877

878 4. Conclusions

879 We presented a seismogenic source model for Italy, which summarizes and
880 integrates the fault-based models developed within the last decade (Pace et al.,
881 2006).

882 The model proposed in this study combines fault source inputs based on over 110
883 faults grouped into 86 fault sources and distributed source inputs. For each fault
884 source, the maximum magnitude and its uncertainty were derived by applying
885 scaling relationships, and the rates of seismic activity were derived by applying slip
886 rates to seismic moment evaluations and balancing these seismic moments using
887 two MFD models.

888 To account for unknown faults, a distributed seismicity input was applied following
889 the well-known Frankel (1995) methodology to calculate seismicity parameters.

890 The fault sources and gridded distributed seismicity sources have been integrated
891 via a new approach based on the idea that deformation in the vicinity of an active
892 fault is concentrated along the fault and that the seismic activity in the surrounding
893 region is reduced. In particular, a distance-dependent linear weighting function has
894 been introduced to allow the contribution of distributed sources (in the magnitude
895 range overlapping the MFD of each fault source) to linearly decrease from 1 to 0 with
896 decreasing distance from a fault. The strength of our approach lies in the ability to
897 integrate different levels of available information for active faults that actually exist in
898 Italy (or elsewhere), but the final result is unavoidably linked to the quality of the
899 relevant data. We think that our seismogenic source model includes significant
900 advances in the use of integrated active fault and seismological data.

901 The probabilistically estimated ground shaking maps produced using our model
902 show a hazard pattern similar to that of the current maps at the national scale, but
903 some significant differences in hazard level are present at the regional to local scales

- Alessandro 6/10/y 15:57
Eliminato: our first national-scale PSH
- Alessandro 6/10/y 15:57
Eliminato: of
- Alessandro 6/10/y 15:57
Eliminato: PSH
- Alessandro 6/10/y 15:57
Eliminato: since
- Alessandro 6/10/y 15:57
Eliminato: publication of
- Alessandro 6/10/y 15:57
Eliminato: . in
- Alessandro 6/10/y 15:57
Eliminato: .

- Alessandro 6/10/y 15:57
Eliminato: The PSH

912 (Figure 13).

913 Moreover, the impact of using different MFD models to derive seismic activity rates
914 has on the hazard maps was investigated. The PGA values in the hazard maps
915 obtained with the *TGR* model are higher than those in the hazard maps based on the
916 *CHG* model. This difference is because the rates of earthquakes with magnitudes
917 from 5.5 to approximately 6 are generally higher in the *TGR* model than in the *CHG*
918 model. Moreover, the relative contributions of fault source inputs and distributed
919 source inputs have been identified in maps and profiles in three sectors of the study
920 area. These profiles show that the hazard level is generally higher where fault inputs
921 are used, and for high probabilities of exceedance, the contribution of *distributed*
922 inputs equals that of *fault* inputs.

923 Finally, the *Mixed* model was created by selecting the most appropriate MFD model
924 for each fault. All data, including the locations and parameters of fault sources, are
925 provided in the supplemental files of this paper.

926 It shall be noted that our new seismogenic source model is not intended to replace,
927 integrate or assess the current official national seismic hazard model of Italy. While
928 some aspects remain to be implemented in our approach (e.g., the integration of
929 reverse/thrust faults in the database, sensitivity tests for the distance-dependent
930 linear weighting function parameters, sensitivity tests for potential different
931 segmentation models, and fault source inputs that account for fault interactions), the
932 proposed model represents advancements in terms of input data (quantity and
933 quality) and methodology based on a decade of research in the field of fault-based
934 approaches to regional seismic hazard modelling.

935

936

937

938

939

940

941

942 **References**

943

944

Alessandro 6/10/y 15:57

Eliminato: that

Alessandro 6/10/y 15:57

Eliminato: generated by

Alessandro 6/10/y 15:57

Eliminato: generated by

Alessandro 6/10/y 15:57

Eliminato: This new PSH

949 Akinci, A., Galadini, F., Pantosti, D., Petersen, M., Malagnini, L., and Perkins, D.:
 950 Effect of Time Dependence on Probabilistic Seismic-Hazard Maps and
 951 Deaggregation for the Central Apennines, Italy, B Seismol Soc Am, 99, 585-
 952 610, 2009.

953 Akkar, S., Sandikkaya, M.A. , Bommer, J.J.: Empirical Ground-Motion Models for
 954 Point and Extended-Source Crustal Earthquake Scenarios in Europe and the
 955 Middle East, Bulletin of Earthquake Engineering, ISSN:1570-761X, 2013.

956 Benedetti, L., Manighetti, I., Gaudemer, Y., Finkel, R., Malavieille, J., Pou, K., Arnold,
 957 M., Aumaitre, G., Bourles, D., and Keddadouche, K.: Earthquake synchrony
 958 and clustering on Fucino faults (Central Italy) as revealed from in situ CI-36
 959 exposure dating, J Geophys Res-Sol Ea, 118, 4948-4974, 2013.

960 Bindi, D., Massa, M., Luzi, L., Ameri, G., Pacor, F., Puglia, R., and Augliera, P.: Pan-
 961 European ground-motion prediction equations for the average horizontal
 962 component of PGA, PGV, and 5%-damped PSA at spectral periods up to 3.0
 963 s using the RESORCE dataset (vol 12, pg 391, 2014), B Earthq Eng, 12, 431-
 964 448, 2014.

965 Boncio, P., Brozzetti, F. and Lavecchia G.: Architecture and seismotectonics of a
 966 regional Low-Angle Normal Fault zone in Central Italy. Tectonics, 19 (6),
 967 1038-1055, 2000.

968 Boncio, P., Lavecchia, G., and Pace, B.: Defining a model of 3D seismogenic
 969 sources for Seismic Hazard Assessment applications: The case of central
 970 Apennines (Italy), J Seismol, 8, 407-425, 2004.

971 Boncio, P., Pizzi, A., Cavuoto, G., Mancini, M., Piacentini, T., Miccadei, E., Cavinato,
 972 G. P., Piscitelli, S., Giocoli, A., Ferretti, G., De Ferrari, R., Gallipoli, M. R.,
 973 Mucciarelli, M., Di Fiore, V., Franceschini, A., Pergalani, F., Naso, G., and
 974 Macroarea, W. G.: Geological and geophysical characterisation of the
 975 Paganica - San Gregorio area after the April 6, 2009 L'Aquila earthquake (M-
 976 w 6.3, central Italy): implications for site response, B Geofis Teor Appl, 52,
 977 491-512, 2011.

978 Bull, J. M., Barnes, P. M., Lamarche, G., Sanderson, D. J., Cowie, P. A., Taylor, S.
 979 K., and Dix, J. K.: High-resolution record of displacement accumulation on an
 980 active normal fault: implications for models of slip accumulation during
 981 repeated earthquakes, J Struct Geol, 28, 1146-1166, 2006.

Alessandro 6/10/y 15:57

Spostato in giù [2]: Basili, R.,

Alessandro 6/10/y 15:57

Formattato: Italiano

Alessandro 6/10/y 15:57

Eliminato: Valensise, G., Vannoli, P., Burrato, P., Fracassi, U., Mariano, S., Tiberti, M. M. and Boschi, E.: The Database of Individual Seismogenic Sources (DISS), version 3: Summarizing 20 years of research on Italy's earthquake geology, Tectonophysics, 453, 20- 43, 2008. .

990 Chiou, B. S. J. and Youngs, R. R.: An NGA model for the average horizontal
 991 component of peak ground motion and response spectra, Earthq Spectra, 24,
 992 173-215, 2008.

993 Cornell, C.A.: Engineering seismic risk analysis, Bull. Seism. Soc. Am., 58,1583-
 994 1606, 1968.

995 Cowie, P. A., Vanneste, C., and Sornette, D.: Statistical Physics Model for the
 996 Spatiotemporal Evolution of Faults, J Geophys Res-Sol Ea, 98, 21809-21821,
 997 1993.

998

999 Cowie, P. A.: A healing-reloading feedback control on the growth rate of seismogenic
 1000 faults, J Struct Geol, 20, 1075-1087, 1998.

1001 Cowie, P. A., Underhill, J. R., Behn, M. D., Lin, J., and Gill, C. E.: Spatio-temporal
 1002 evolution of strain accumulation derived from multi-scale observations of Late
 1003 Jurassic rifting in the northern North Sea: A critical test of models for
 1004 lithospheric extension, Earth Planet Sc Lett, 234, 401-419, 2005.

1005 Cowie, P. A., Roberts, G. P., Bull, J. M., and Visini, F.: Relationships between fault
 1006 geometry, slip rate variability and earthquake recurrence in extensional
 1007 settings, Geophys J Int, 189, 143-160, 2012.

1008 D'amato, D., Pace, B., Di Nicola, L., Stuart, F.M., Visini, F., Azzaro, R., Branca, S.,
 1009 and Barfod, D.N.: Holocene slip rate variability along the Pernicana fault
 1010 system (Mt. Etna, Italy): Evidence from offset lava flows: GSA Bulletin,
 1011 doi:10.1130/B31510.1, 2016.

1012 Danciu, L., Şeşetyan, K., Demircioglu, M. et al.: The 2014 Earthquake Model of the
 1013 Middle East: seismogenic sources, Bull Earthquake Eng,
 1014 <https://doi.org/10.1007/s10518-017-0096-8>, 2017.

1015 Faccioli, E., Bianchini, A., and Villani, M.: New ground motion prediction equations
 1016 for $t > 1$ s and their influence on seismic hazard assessment, In: Proceedings
 1017 of the University of Tokyo symposium on long-period ground motion and
 1018 urban disaster mitigation, 2010.

1019 Ferranti, L., Palano, M., Cannavo, F., Mazzella, M. E., Oldow, J. S., Gueguen, E.,
 1020 Mattia, M., and Monaco, C.: Rates of geodetic deformation across active
 1021 faults in southern Italy, Tectonophysics, 621, 101-122, 2014.

Alessandro 6/10/y 15:57

Formattato: Tipo di carattere:Helvetica, Colore carattere: Automatico

Alessandro 6/10/y 15:57

Spostato (Inserimento) [3]

Alessandro 6/10/y 15:57

Eliminato: .: A healing-reloading feedback control on the growth rate of seismogenic faults, J Struct Geol, 20, 1075-1087, 1998

Alessandro 6/10/y 15:57

Eliminato: Cowie, P. A.,

Alessandro 6/10/y 15:57

Spostato in giù [4]: Roberts, G. P., Bull, J. M., and Visini, F.: Relationships between fault geometry, slip rate variability and earthquake recurrence in extensional settings, Geophys J Int, 189, 143-160, 2012. .

Alessandro 6/10/y 15:57

Spostato in su [3]: Vanneste, C., and Sornette, D.: Statistical Physics Model for the Spatiotemporal Evolution of Faults, J Geophys Res-Sol Ea, 98, 21809-21821, 1993

Alessandro 6/10/y 15:57

Spostato (inserimento) [4]

Alessandro 6/10/y 15:57

Eliminato: . .

1037 [Field, E. H., Jackson, D. D., and Dolan, J. F.: A mutually consistent seismic-hazard](#)
1038 [source model for southern California, B Seismol Soc Am, 89, 559-578, 1999.](#)
1039 [Field, E. H., Jordan, T. H., Page, M. T., Milner, K. R., Shaw, B. E., Dawson, T., Biasi,](#)
1040 [G. P., Parsons, T., Hardebeck, J. L., Michael, A. J., Weldon, R. J., Powers, P.](#)
1041 [M., Johnson, K. M., Zeng, Y., Bird, P., Felzer, K. R., van der Elst, N. J.,](#)
1042 [Madden, C., Arrowsmith, R., Werner, M. J., Thatcher, W. R., & Jackson, D.](#)
1043 [D.: A Synoptic View of the Third Uniform California Earthquake Rupture](#)
1044 [Forecast \(UCERF3\). Seismological Research Letters., doi:](#)
1045 [10.1785/0220170045](#), 2017.
1046 Field, E. H., Biasi, G. P., Bird, P., Dawson, T. E., Felzer, K. R., Jackson, D. D.,
1047 Johnson, K. M., Jordan, T. H., Madden, C., Michael, A. J., Milner, K. R., Page,
1048 M. T., Parsons, T., Powers, P. M., Shaw, B. E., Thatcher, W. R., Weldon, R.
1049 J., and Zeng, Y. H.: Long-Term Time-Dependent Probabilities for the Third
1050 Uniform California Earthquake Rupture Forecast (UCERF3), B Seismol Soc
1051 Am, 105, 511-543, 2015.
1052
1053 Finnegan, N. J., Schumer, R., and Finnegan, S.: A signature of transience in bedrock
1054 river incision rates over timescales of 10(4)-10(7) years, Nature, 505, 391-+,
1055 2014.
1056 Frankel, A.: Simulating Strong Motions of Large Earthquakes Using Recordings of
1057 Small Earthquakes - the Loma-Prieta Mainshock as a Test-Case, B Seismol
1058 Soc Am, 85, 1144-1160, 1995.
1059 Frankel, A., Mueller, C., Barnhard, T., Perkins, D., Leyendecker, E. V., Dickman, N.,
1060 Hanson, S., and Hopper, M.: Seismic-hazard maps for California, Nevada,
1061 and Western Arizona/Utah', U.S. Geological Survey Open-File Rept. 97-130,
1062 1997.
1063 Gallen, S. F., Pazzaglia, F. J., Wegmann, K. W., Pederson, J. L., and Gardner, T.
1064 W.: The dynamic reference frame of rivers and apparent transience in incision
1065 rates, Geology, 43, 623-626, 2015.
1066 Garcia-Mayordomo, J., Gaspar-Escribano, J. M., and Benito, B.: Seismic hazard
1067 assessment of the Province of Murcia (SE Spain): analysis of source
1068 contribution to hazard, J Seismol, 11, 453-471, 2007.

Alessandro 6/10/y 15:57

Spostato (inserimento) [5]

Alessandro 6/10/y 15:57

Formattato: Inglese (Regno Unito)

Alessandro 6/10/y 15:57

Formattato: Tipo di carattere:11 pt, Inglese (Stati Uniti)

Alessandro 6/10/y 15:57

Eliminato: Field, E.

Alessandro 6/10/y 15:57

Spostato in su [5]: H., Jackson, D. D., and Dolan, J. F.: A mutually consistent seismic-hazard source model for southern California, B Seismol Soc Am, 89, 559-578, 1999. .

1074 Gardner, J. K., Knopoff, L.: Is the sequence of earthquakes in Southern California,
 1075 with aftershocks removed, Poissonian?'. *Bulletin of the Seismological Society*
 1076 of America, 64, 1363-1367, 1974.

1077 Gardner, T. W., Jorgensen, D. W., Shuman, C., and Lemieux, C. R.: Geomorphic
 1078 and Tectonic Process Rates - Effects of Measured Time Interval, *Geology*, 15,
 1079 259-261, 1987.

1080 Gasperini P., Bernardini F., Valensise G. and Boschi E.: Defining Seismogenic
 1081 Sources from Historical Earthquake Felt Reports, *Bull. Seism. Soc. Am.*, 89,
 1082 94-110, 1999.

1083 Gunderson, K. L., Anastasio, D. J., Pazzaglia, F. J., and Picotti, V.: Fault slip rate
 1084 variability on 10(4)-10(5)yr timescales for the Salsomaggiore blind thrust fault,
 1085 Northern Apennines, Italy, *Tectonophysics*, 608, 356-365, 2013.

1086 Hanks, T. C., and Kanamori, H.: A moment magnitude scale, *Journal of Geophysics*
 1087 Research, 84, 2348–2350, 1979.

1088 Helmstetter, A., Kagan, Y. Y., and Jackson, D. D.: Comparison of short-term and
 1089 time-independent earthquake forecast models for southern California, *B*
 1090 *Seismol Soc Am*, 96, 90-106, 2006.

1091 Helmstetter, A., Kagan, Y. Y., and Jackson, D. D.: High-resolution time-independent
 1092 grid-based forecast for $M \leq 5$ earthquakes in California, *Seismol Res Lett*,
 1093 78, 78-86, 2007.

1094 Hiemer, S., Woessner, J., Basili, R., Danciu, L., Giardini, D., and Wiemer, S.: A
 1095 smoothed stochastic earthquake rate model considering seismicity and fault
 1096 moment release for Europe, *Geophysical Journal International*, Volume 198,
 1097 Pages 1159–1172, <https://doi.org/10.1093/gji/ggu186>, 2014.

1098 International Association of Seismology and Physics of the Earth's Interior (IASPEI):
 1099 Summary of Magnitude Working Group recommendations on standard
 1100 procedures for determining earthquake magnitudes from digital data,
 1101 [http://www.iaspei.org/](http://www.iaspei.org/commissions/CSOI/summary_of_WG_recommendations_2005.pdf)
 1102 [commissions/CSOI/summary_of_WG_recommendations_2005.pdf](http://www.iaspei.org/commissions/CSOI/summary_of_WG_recommendations_2005.pdf) (last
 1103 accessed December 2015), 2005.

1104 Kagan, Y. Y., Jackson D.D., and Geller, R.J.: Characteristic earthquake model,
 1105 1884–2011, R.I.P., *Seismol Res Lett*, 83, no. 6, 951– 953, 2012.

1106 Kagan, Y.

Alessandro 6/10/y 15:57

Eliminato: GEM: The OpenQuake-engine User Manual. Global Earthquake Model (GEM) Technical Report, doi: 10.13117/GEM.OPENQUAKE.MAN.ENGINE .1.9/01, 189 pages, 2016. -

Alessandro 6/10/y 15:57

Spostato (inserimento) [2]

Alessandro 6/10/y 15:57

Formattato: Italiano

Alessandro 6/10/y 15:57

Spostato in giù [6]: . Y.: Seismic moment distribution revisited: I. Statistical results, *Geophys J Int*, 148, 520-541, 2002. -

1115 [Kagan, Y. Y. and Knopoff, L.: Earthquake risk prediction as a stochastic process, Physics of the](#)
1116 [Earth and Planetary Interiors, 14, 97–108, 1977.](#)

1117 Kagan, Y. Y. and Jackson, D. D.: Long-Term Probabilistic Forecasting of
1118 Earthquakes, *J Geophys Res-Sol Ea*, 99, 13685-13700, 1994.

1119 [Kagan, Y. Y.: Seismic moment distribution revisited: I. Statistical results, Geophys J](#)
1120 [Int. 148, 520-541, 2002.](#)

1121 Kamer, Y. and Hiemer, S.: Data-driven spatial b value estimation with applications to
1122 California seismicity: To b or not to b, *J Geophys Res-Sol Ea*, 120, 5191-
1123 5214, 2015.

1124 King, G. C. P., Stein, R. S., and Lin, J.: Static Stress Changes and the Triggering of
1125 Earthquakes, *B Seismol Soc Am*, 84, 935-953, 1994.

1126 Kostrov, V. V.: Seismic moment and energy of earthquakes, and seismic flow of
1127 rock, *Physic of the Solid Earth*, 1, 23-44, 1974.

1128 Leonard, M.: Earthquake fault scaling: Self-consistent relating of rupture length,
1129 width, average displacement, and moment release. *Bulletin of the*
1130 *Seismological Society of America*, 100(5A), 1971- 1988, 2010.

1131 Machette, M.N.: Active, capable, and potentially active faults; a paleoseismic
1132 perspective, *J. Geodyn.*, 29, 387–392, 2000.

1133 Main, I.: Statistical physics, seismogenesis, and seismic hazard, *Rev Geophys*, 34,
1134 433-462, 1996.

1135 Mansfield, C. and Cartwright, J.: Fault growth by linkage: observations and
1136 implications from analogue models, *J Struct Geol*, 23, 745-763, 2001.

1137 Meletti, C., Visini, F., D'Amico, V., and Rovida A.: Seismic hazard in central Italy and
1138 the 2016 Amatrice earthquake, *Annals of Geophysics*, 59, doi:10.4401/ag-
1139 7248, 2016.

1140 McClymont, A. F., Villamor, P., and Green, A. G.: Assessing the contribution of off-
1141 fault deformation to slip-rate estimates within the Taupo Rift, New Zealand,
1142 using 3-D ground-penetrating radar surveying and trenching, *Terra Nova*, 21,
1143 446-451, 2009a.

1144 McClymont, A. F., Villamor, P., and Green, A. G.: Fault displacement accumulation
1145 and slip rate variability within the Taupo Rift (New Zealand) based on trench
1146 and 3-D ground-penetrating radar data, *Tectonics*, 28, 2009b.

1147 Nicol, A., Walsh, J. J., Watterson, J., and Underhill, J. R.: [Displacement rates of](#)
1148 [normal faults, Nature, 390, 157-159, 1997.](#)

Alessandro 6/10/y 15:57

Eliminato: Kagan, Y

Alessandro 6/10/y 15:57

Spostato (inserimento) [6]

Alessandro 6/10/y 15:57

Spostato (inserimento) [7]

1150 | [Nicol, A., Walsh, J.](#), Berryman, K., and Villamor, P.: Interdependence of fault
1151 | displacement rates and paleoearthquakes in an active rift, *Geology*, 34, 865-
1152 | 868, 2006.

1153 | Nicol, A., Walsh, J., Mouslopoulou, V., and Villamor, P.: Earthquake histories and
1154 | Holocene acceleration of fault displacement rates, *Geology*, 37, 911-914,
1155 | 2009.

1156 | Nicol, A., Walsh, J. J., Villamor, P., Seebeck, H., and Berryman, K. R.: Normal fault
1157 | interactions, paleoearthquakes and growth in an active rift, *J Struct Geol*, 32,
1158 | 1101-1113, 2010.

1159 | [x](#)

1160 | Ordaz, M. and Reyes, C.: Earthquake hazard in Mexico City: Observations versus
1161 | computations, *B Seismol Soc Am*, 89, 1379-1383, 1999.

1162 | Pace, B., [Peruzza, L., Lavecchia, G., and Boncio, P.](#): [Layered seismogenic source
1163 | model and probabilistic seismic-hazard analyses in central Italy](#), *B Seismol
1164 | Soc Am*, 96, 107-132, 2006.

1165 | [Pace, B.](#), Bocchini, G. M., and Boncio, P.: Do static stress changes of a moderate-
1166 | magnitude earthquake significantly modify the regional seismic hazard? Hints
1167 | from the L'Aquila 2009 normal-faulting earthquake (Mw 6.3, central Italy),
1168 | *Terra Nova*, 26, 430-439, 2014.

1169 | Pace, B., [▲](#)

1170 | Visini, F., and Peruzza, L.: FiSH: MATLAB Tools to Turn Fault Data into Seismic-
1171 | Hazard Models, *Seismol Res Lett*, 87, 374-386, 2016.

1172 | [Pagani, M., Monelli, D., Weatherill, G., Danciu, L., Crowley, H., Silva, V., Henshaw,
1173 | P., Butler, L., Nastasi, M., Panzeri, L., Simionato, M., and Vigano, D.](#):
1174 | [OpenQuake-engine: an open hazard \(and risk\) software for the Global
1175 | Earthquake Model](#), *Seismol Res Lett* 85:692–702. doi:10.1785/0220130087,
1176 | 2014.

1177 | Peruzza, L., and Pace B.: Sensitivity analysis for seismic source characteristics to
1178 | probabilistic seismic hazard assessment in central Apennines (Abruzzo area),
1179 | *Bollettino di Geofisica Teorica ed Applicata* 43, 79–100, 2002.

1180 | Peruzza, L., Pace, B., and Visini, F.: Fault-Based Earthquake Rupture Forecast in
1181 | Central Italy: Remarks after the L'Aquila M-w 6.3 Event, *B Seismol Soc Am*,
1182 | 101, 404-412, 2011.

Alessandro 6/10/y 15:57

Eliminato: Nicol, A., Walsh, J

Alessandro 6/10/y 15:57

Spostato in su [7]: . J., Watterson, J., and Underhill, J. R.: Displacement rates of normal faults, *Nature*, 390, 157-159, 1997. .

Alessandro 6/10/y 15:57

Spostato (inserimento) [8]

Alessandro 6/10/y 15:57

Spostato in su [8]: Peruzza, L., Lavecchia, G., and Boncio, P.: Layered seismogenic source model and probabilistic seismic-hazard analyses in central Italy, *B Seismol Soc Am*, 96, 107-132, 2006. . Pace, B.,

1193 Peruzza, L., Gee, R., Pace, B., Roberts, G., Scotti, O., Visini, F., Benedetti, L., and
1194 Pagani, M.: PSHA after a strong earthquake: hints for the recovery, *Annals of*
1195 *Geophysics*, 59, doi:10.4401/ag-7257, 2016

1196 Roberts, G. P., Cowie, P., Papanikolaou, I., and Michetti, A. M.: Fault scaling
1197 relationships, deformation rates and seismic hazards: an example from the
1198 Lazio-Abruzzo Apennines, central Italy, *J Struct Geol*, 26, 377-398, 2004.

1199 Roberts, G. P. and Michetti, A. M.: Spatial and temporal variations in growth rates
1200 along active normal fault systems: an example from The Lazio-Abruzzo
1201 Apennines, central Italy, *J Struct Geol*, 26, 339-376, 2004.

1202 Robinson, R., Nicol, A., Walsh, J. J., and Villamor, P.: Features of earthquake
1203 occurrence in a complex normal fault network: Results from a synthetic
1204 seismicity model of the Taupo Rift, New Zealand, *J Geophys Res-Sol Ea*, 114,
1205 2009.

1206 Rovida, A., Locati, M., Camassi, R., Lolli, B., and Gasperini P.: CPTI15, the 2015
1207 version of the Parametric Catalogue of Italian Earthquakes. Istituto Nazionale
1208 di Geofisica e Vulcanologia. doi:http://doi.org/10.6092/INGV.IT-CPTI15, 2016.

1209 Scotti, O., Clement, C., and Baumont, D.: Seismic hazard for design and verification
1210 of nuclear installations in France: regulatory context, debated issues and
1211 ongoing developments, *B Geofis Teor Appl*, 55, 135-148, 2014.

1212 Stein, R. S., King, G. C. P., and Lin, J.: Stress Triggering of the 1994 M=6.7
1213 Northridge, California, Earthquake by Its Predecessors, *Science*, 265, 1432-
1214 1435, 1994.

1215 Stirling, M., McVerry, G., Gerstenberger, M., Litchfield, N., Van Dissen, R.,
1216 Berryman, K., Barnes, P., Wallace, L., Villamor, P., Langridge, R., Lamarche,
1217 G., Nodder, S., Reyners, M., Bradley, B., Rhoades, D., Smith, W., Nicol, A.,
1218 Pettinga, J., Clark, K., and Jacobs, K.: National Seismic Hazard Model for
1219 New Zealand: 2010 Update, *B Seismol Soc Am*, 102, 1514-1542, 2012.

1220 Stock, C. and Smith, E. G. C.: Adaptive kernel estimation and continuous probability
1221 representation of historical earthquake catalogs, *B Seismol Soc Am*, 92, 904-
1222 912, 2002a.

1223 Stock, C. and Smith, E. G. C.: Comparison of seismicity models generated by
1224 different kernel estimations, *B Seismol Soc Am*, 92, 913-922, 2002b.

1225 Stucchi, M., Meletti, C., Montaldo, V., Crowley, H., Calvi, G. M., and Boschi, E.:
1226 Seismic Hazard Assessment (2003-2009) for the Italian Building Code, B
1227 Seismol Soc Am, 101, 1885-1911, 2011.

1228 Verdecchia, A. and Carena, S.: Coulomb stress evolution in a diffuse plate boundary:
1229 1400 years of earthquakes in eastern California and western Nevada, USA,
1230 Tectonics, 35, 1793-1811, 2016.

1231 Visini, F. and Pace, B.: Insights on a Key Parameter of Earthquake Forecasting, the
1232 Coefficient of Variation of the Recurrence Time, Using a Simple Earthquake
1233 Simulator, Seismol Res Lett, 85, 703-713, 2014.

1234 Weichert, D. H.: Estimation of the earthquake recurrence parameters for unequal
1235 observation periods for different magnitudes, Bulletin of the Seismological
1236 Society of America, 70, 1337-1346, 1980.

1237 Wells, D. L. and Coppersmith, K. J.: New Empirical Relationships among Magnitude,
1238 Rupture Length, Rupture Width, Rupture Area, and Surface Displacement, B
1239 Seismol Soc Am, 84, 974-1002, 1994.

1240 Werner, M. J., Helmstetter, A., Jackson, D. D., Kagan, Y. Y., and Wiemer, S.:
1241 Adaptively smoothed seismicity earthquake forecasts for Italy, Ann Geophys-
1242 Italy, 53, 107-116, 2010.

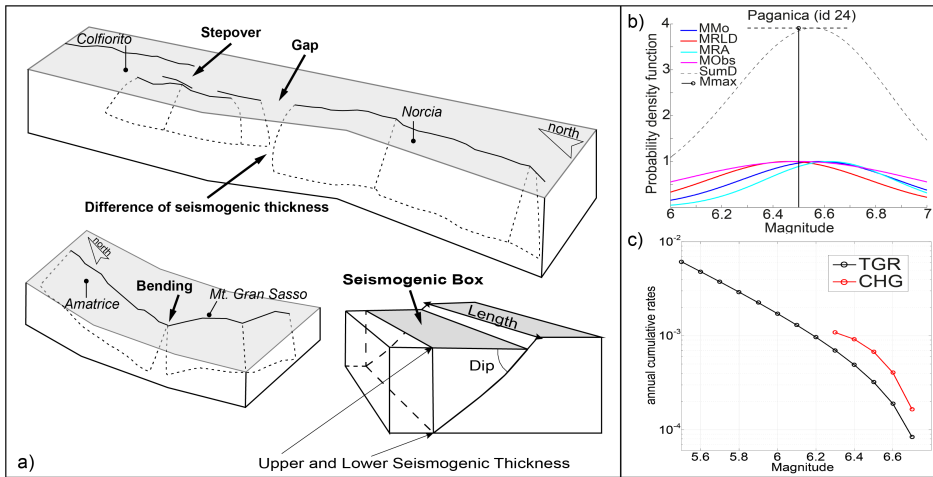
1243 Woessner, J., Laurentiu, D., Giardini, D., Crowley, H., Cotton, F., Grunthal, G.,
1244 Valensise, G., Arvidsson, R., Basili, R., Demircioglu, M. B., Hiemer, S.,
1245 Meletti, C., Musson, R. W., Rovida, A. N., Sesetyan, K., Stucchi, M., and
1246 Consortium, S.: The 2013 European Seismic Hazard Model: key components
1247 and results, B Earthq Eng, 13, 3553-3596, 2015.

1248 Youngs, R. R. and Coppersmith, K. J.: Implications of Fault Slip Rates and
1249 Earthquake Recurrence Models to Probabilistic Seismic Hazard Estimates, B
1250 Seismol Soc Am, 75, 939-964, 1985.

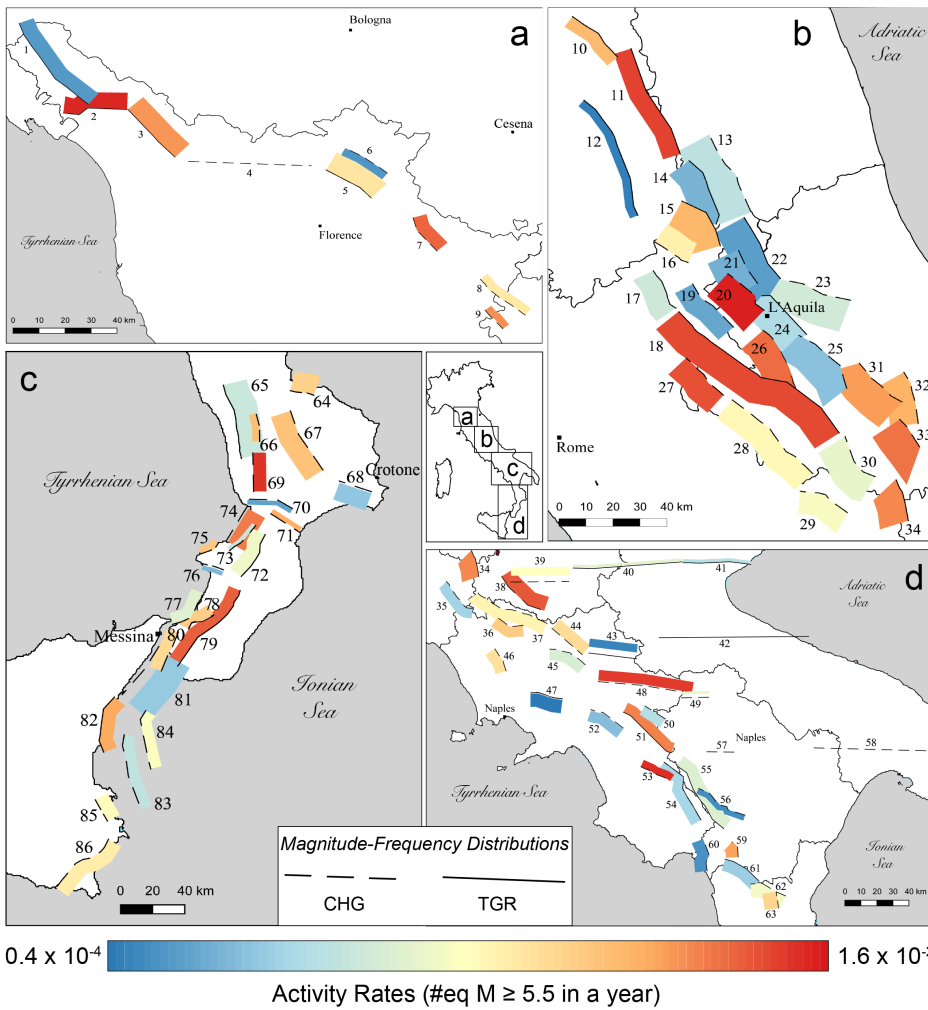
1251 Zechar, J. D. and Jordan, T. H.: Simple smoothed seismicity earthquake forecasts
1252 for Italy, Ann Geophys-Italy, 53, 99-105, 2010.

1253 Zhao, J. X., Zhang, J., Asano, A., Ohno, Y., Oouchi, T., Takahashi, T., Ogawa, H.,
1254 Irikura, K., Thio, H. K., Somerville, P. G., Fukushima, Y., and Fukushima, Y.:
1255 Attenuation relations of strong ground motion in Japan using site classification
1256 based on predominant period, B Seismol Soc Am, 96, 898-913, 2006.

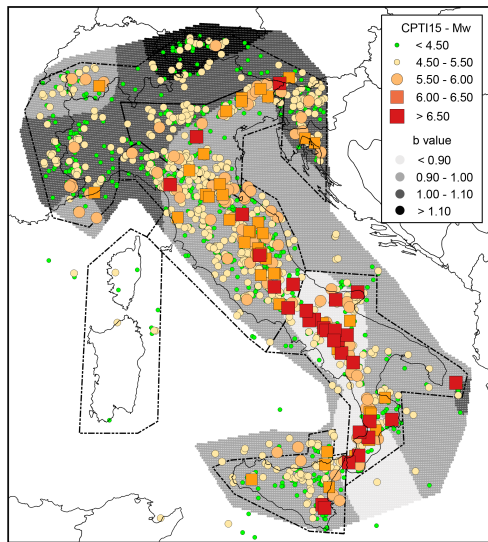
1257



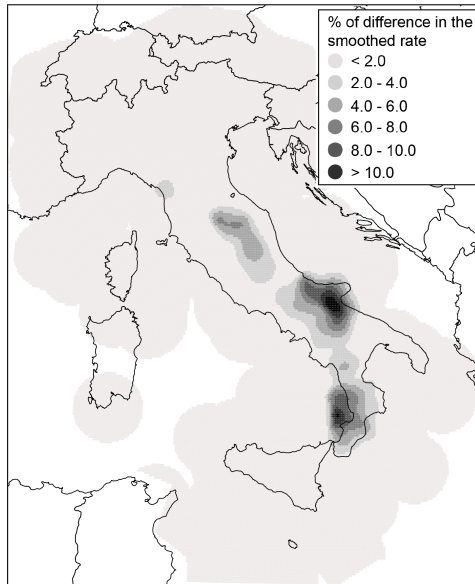
1264
 1265 Fig. 2 a) Conceptual model of active faults and segmentation rules adopted to define
 1266 a fault source and its planar projection, forming a seismogenic box [modified from
 1267 Boncio et al., 2004]. b) Example of FiSH code output (see Pace et al., 2016 for
 1268 details) for the Paganica fault source showing the magnitude estimates from
 1269 empirical relationships and observations, both of which are affected by uncertainties.
 1270 In this example, four magnitudes are estimated: MMo (blue line) is from the standard
 1271 formula (IASPEI, 2005); MRLD (red line) and MRA (cyan line) correspond to
 1272 estimates based on the maximum subsurface fault length and maximum rupture area
 1273 from the empirical relationships of Wells and Coppersmith (1994) for length and
 1274 area, respectively; and MObs (magenta line) is the largest observed moment
 1275 magnitude. The black dashed line represents the summed probability density curve
 1276 (SumD), the vertical black line represents the central value of the Gaussian fit of the
 1277 summed probability density curve (Mmax), and the horizontal black dashed line
 1278 represents its standard deviation (σ Mmax). The input values that were used to
 1279 obtain this output are provided in Table 1. c) Comparison of the magnitude–
 1280 frequency distributions of the Paganica source, which were obtained using the CHG
 1281 model (red line) and the TGR model (black line).



1282
 1283 Fig. 3 Maps showing the fault source inputs as seismogenic boxes (see Fig. 2a). The
 1284 colour scale indicates the activity rate. Solid and dashed lines (corresponding to the
 1285 uppermost edge of the fault) are used to highlight our choice between the two end-
 1286 members of the MFD model adopted in the so-called *Mixed* model.



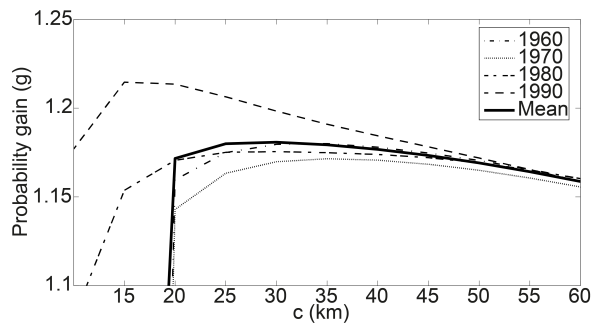
1287
 1288 Fig. 4 Historical earthquakes from the most recent version of the historical
 1289 parametric Italian catalogue (CPTI15, Rovida et al., 2016), the spatial variations in b-
 1290 values and the polygons defining the five macroseismic areas used to assess the
 1291 magnitude completeness intervals (Stucchi et al, 2011).



1292
 1293 Fig. 5 Differences in percentages between the two smoothed rates computed with
 1294 eq. (2) using the complete catalogue and the modified catalogue without events
 1295 associated with known active faults (TGR model)

Alessandro 6/10/y 15:57
 Eliminato: .

Alessandro 6/10/y 15:57
 Eliminato: produced by



1298

1299 Fig. 6 Probability gain per earthquake (see eq. 3) versus correlation distance c , used

1300 to determine the best radius for use in the smoothed seismicity approach (eq. 2)

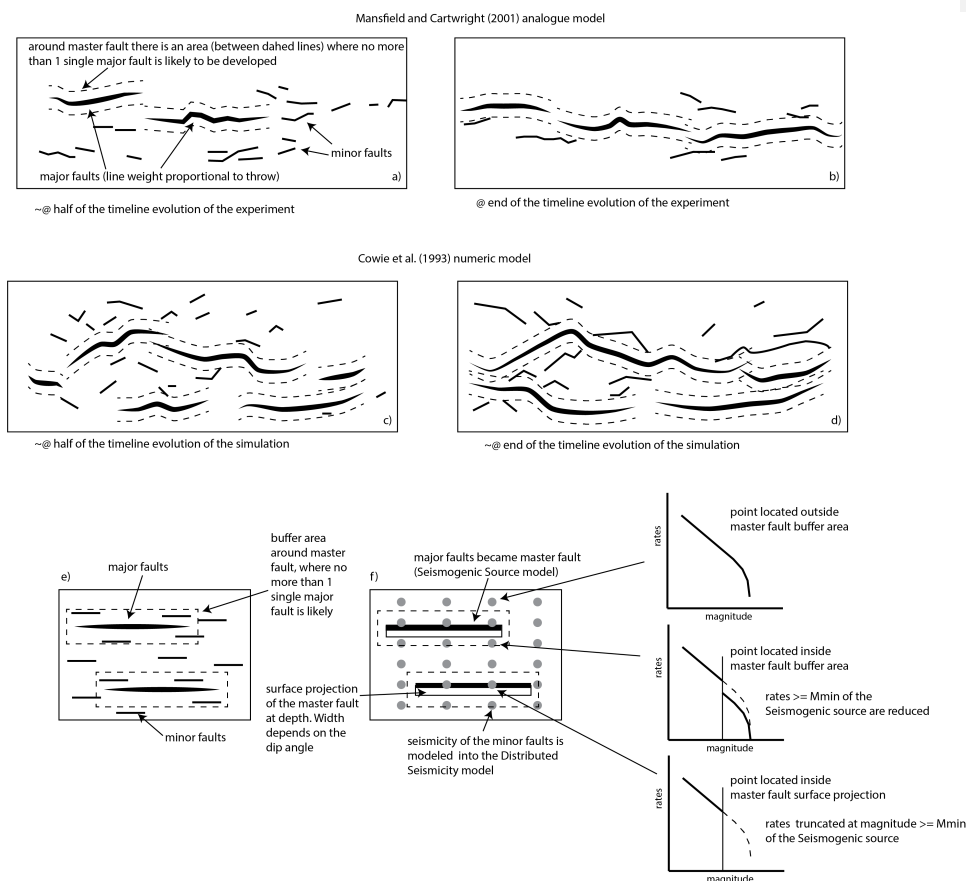
1301

1302

1303

1304

Alessandro 6/10/y 15:57
 Eliminato: highlighting



1306

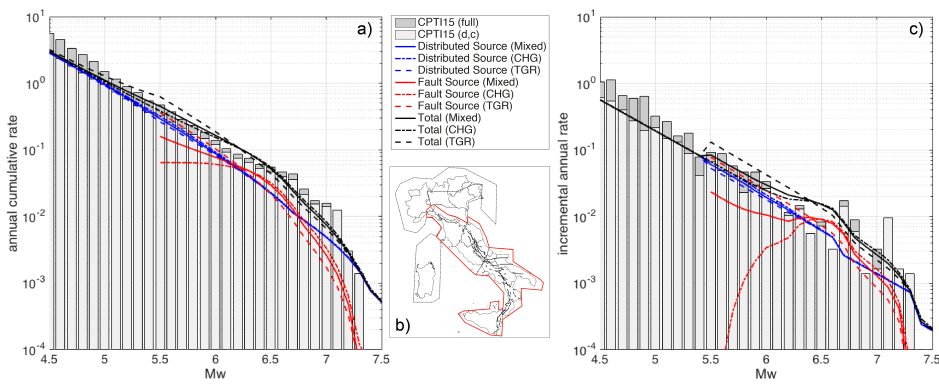
1307 | Fig. 7 Fault system evolution and its implications for our model. a) and b) Diagrams
 1308 from the Mansfield and Cartwright (2001) analogue experiment in two different
 1309 stages: the approximate midpoint of the sequence and the end of the sequence.
 1310 Areas exist around master faults where no more than a single major fault is likely to
 1311 develop. c) and d) Diagrams from numerical modelling conducted by Cowie et al.
 1312 (1993) in two different stages. This experiment shows the similar evolutionary features
 1313 of major and minor faults. e) and f) Application of the analogue and numerical
 1314 modelling of fault system evolution to the fault source input proposed in this paper. A
 1315 buffer area is drawn around each fault source, where it is unlikely for other major
 1316 faults to develop, accounting for the length and slip rate of the fault source. This
 1317 buffer area is useful for reducing or truncating the rates of expected distributed
 1318 seismicity based on the position of a distributed seismicity point with respect to the
 1319 buffer zone (see the text for details).

Alessandro 6/10/y 15:57

Eliminato: in

Alessandro 6/10/y 15:57

Eliminato: and it accounts



1322

1323

1324

1325

1326

1327

1328

1329

Fig. 8 a) Annual cumulative MFD and c) incremental annual MFD computed for the red bounded area in b). The rates have been computed using: (i) the full CPT115 catalogue; (ii) the declustered and complete catalogue (CPT115 (d, c) in the legend) obtained using the completeness magnitude thresholds over different periods of time given by Stucchi et al. (2011) for five large zones; (iii) the distributed sources; (iv) the fault sources; and (v) summing fault and distributed sources (Total).

Alessandro 6/10/y 15:57

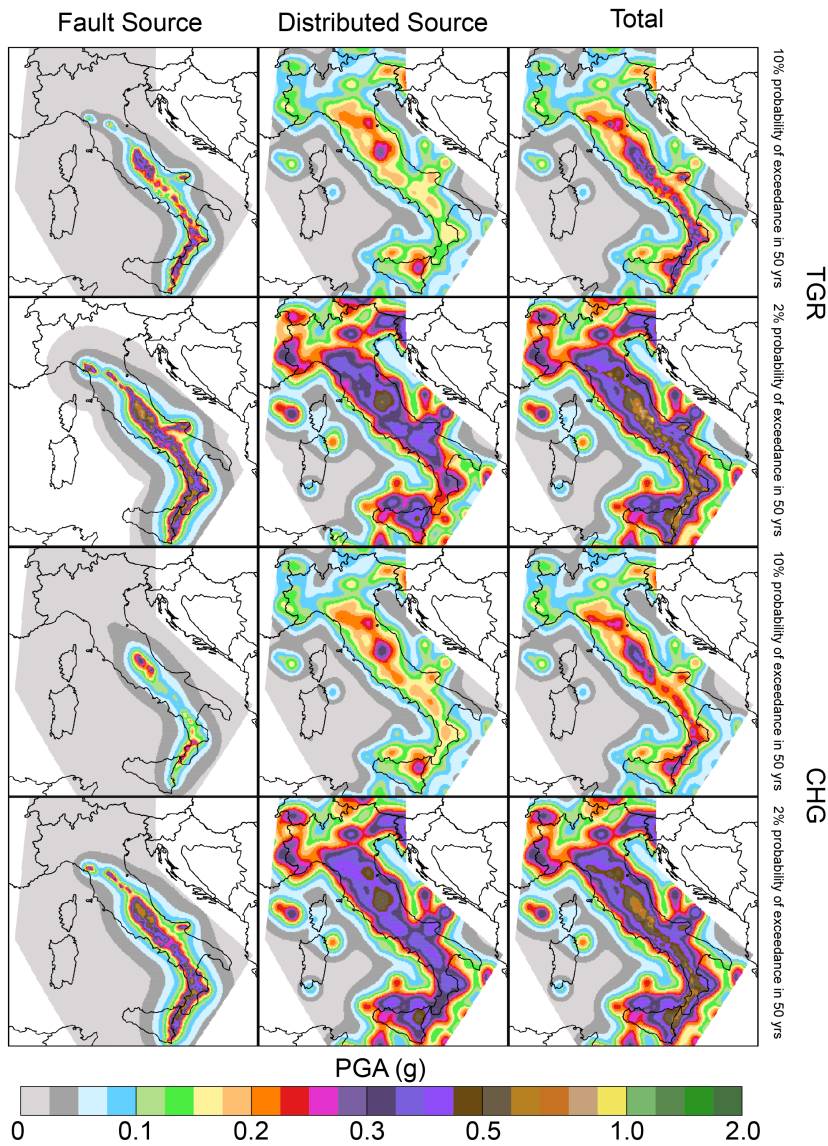
Eliminato: annual

Alessandro 6/10/y 15:57

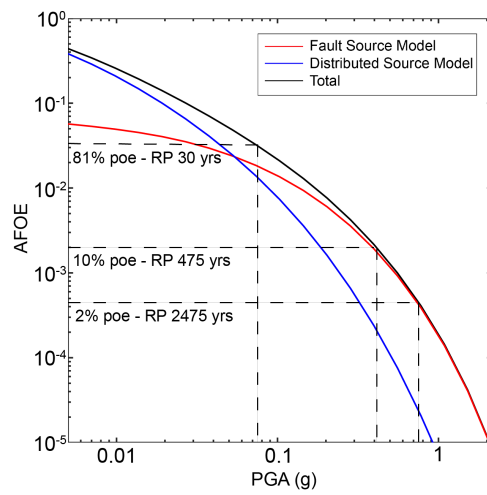
Eliminato: rate

Alessandro 6/10/y 15:57

Eliminato: rate



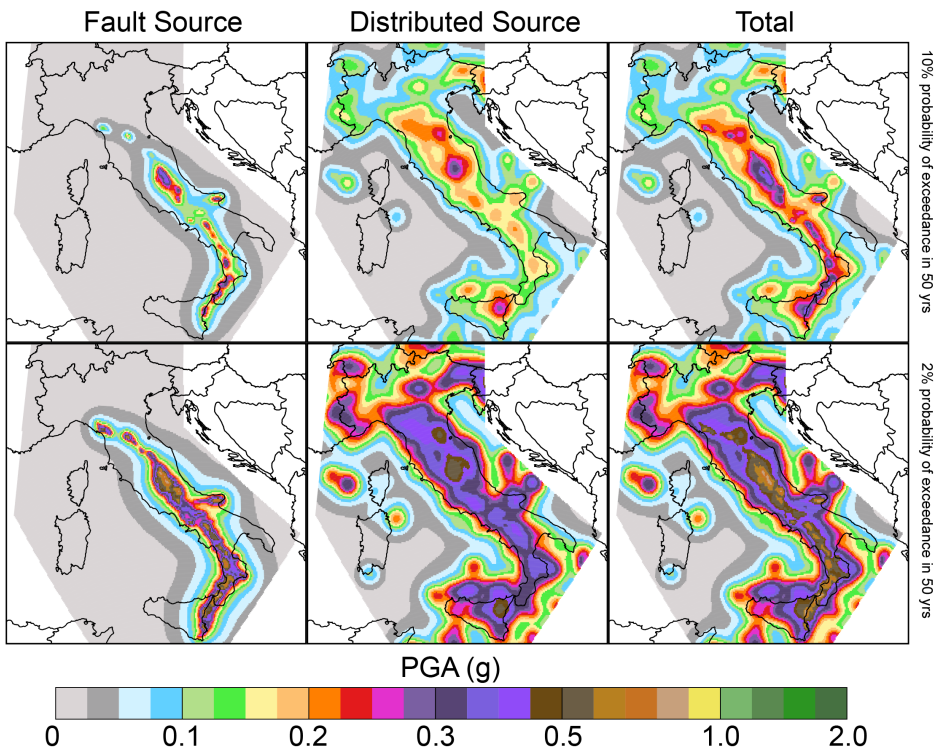
1333
 1334 Fig. 9 Seismic hazard maps for the *TGR* and *CHG* models expressed in terms of
 1335 peak ground acceleration (PGA) and computed for a latitude/longitude grid spacing
 1336 of 0.05° . The first and second rows show the fault source, distributed source and
 1337 total maps of the *TGR* model computed for 10% probability of exceedance in 50
 1338 years and 2% probability of exceedance in 50 years, corresponding to return periods
 1339 of 475 and 2475 years, respectively. The third and fourth rows show the same maps
 1340 for the *CHG* model.



1341

1342 Fig. 10 An example of the contribution to the total seismic hazard level (black line), in
 1343 terms of hazard curves, by the *fault* (red line) and *distributed* (blue line) source inputs
 1344 for one of the 45,602 grid points (L'Aquila, 42.400-13.400). The dashed lines
 1345 represent the 2%, 10% and 81% probabilities of exceedance (poes) in 50 years.

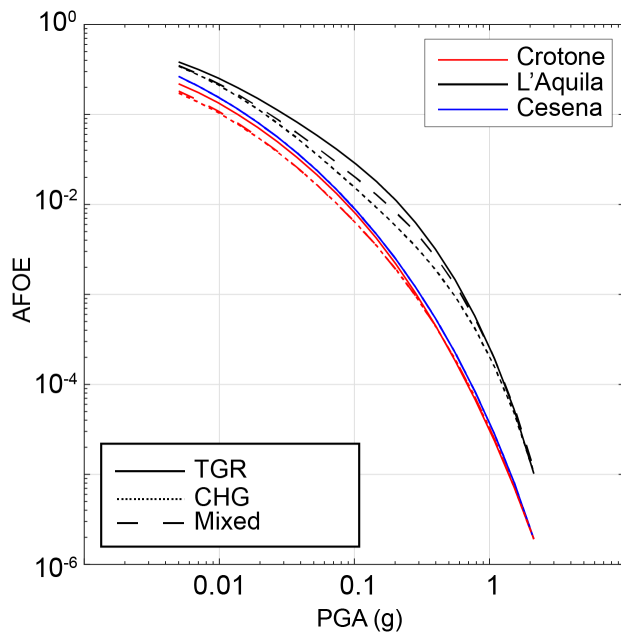
1346



1347

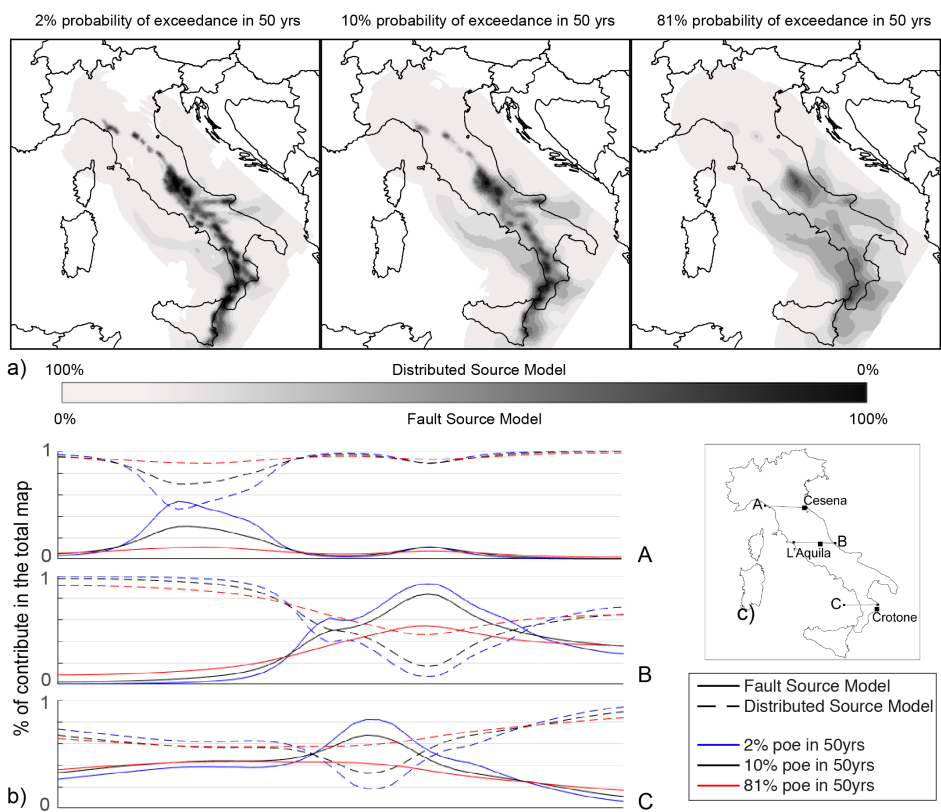
1348

1349 Fig. 11 Seismic hazard maps for the *Mixed* model. The first row shows the fault
 1350 source, distributed source and total maps computed for 10% probability of
 1351 exceedance in 50 years, and the second row shows the same maps but computed
 1352 for 2% probability of exceedance in 50 years, corresponding to return periods of 475
 1353 and 2475 years, respectively. The results are expressed in terms of peak ground
 1354 acceleration (PGA).



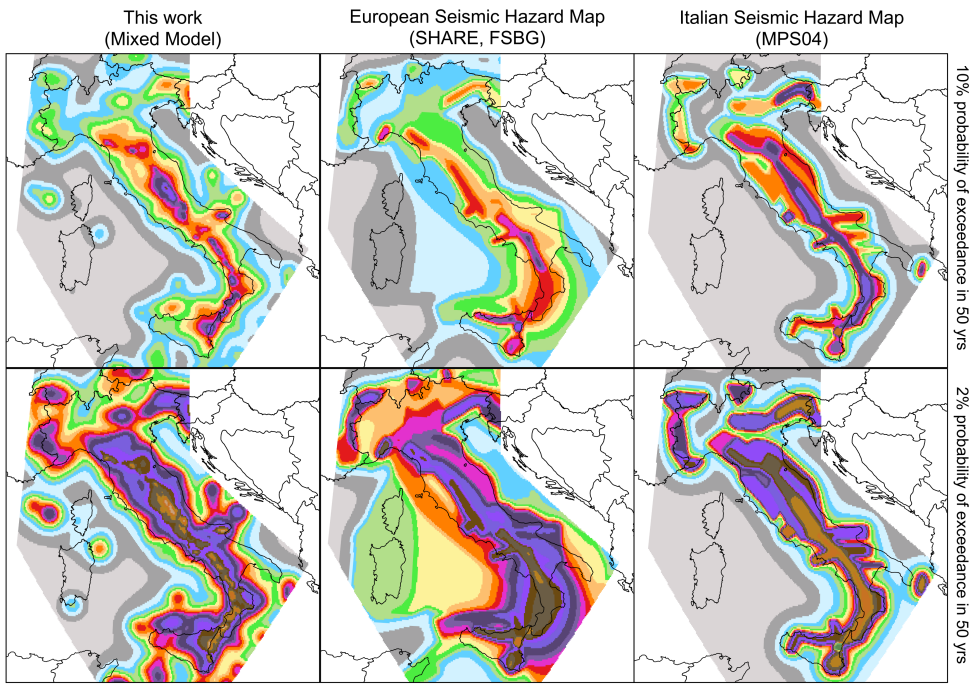
1355
 1356 Fig. 12 *CHG* (dotted line), *TGR* (solid line) and *Mixed* model (dashed line) hazard
 1357 curves for three sites (see Fig. 13 for the location): Cesena (red line), L'Aquila (black
 1358 line) and Crotone (blue line)
 1359

Alessandro 6/10/y 15:57
 Eliminato: :



1361
1362

1363 Fig. 13 a) Contribution maps of the Mixed *fault* and *distributed* source inputs to the
 1364 total hazard level for three probabilities of exceedance: 2%, 10% and 81%,
 1365 corresponding to return periods of 2475, 475 and 30 years, respectively. b)
 1366 Contributions of the Mixed *fault* (solid line) and *distributed* (dashed line) source
 1367 inputs along three profiles (A, B and C in Fig. 13c) for three probabilities of
 1368 exceedance: 2% (blue line), 10% (black line) and 81% (red line).



1369

1370 Fig. 14 Seismic hazard maps expressed in terms of Peak Ground Acceleration
 1371 (PGA) and computed for a latitude/longitude grid spacing of 0.05° based on **rock** site
 1372 conditions. The figure shows a comparison of our model (*Mixed* model, on the left),
 1373 the **ESHM13** model (FSBG logic tree branch, in the middle) and the current Italian
 1374 national seismic hazard map (MPS04, on the right). The same **combination of**
 1375 GMPEs (Akkar et al. 2013, Chiou et al., 2008, Faccioli et al., 2010 and Zhao et al.,
 1376 2006 and Bindi et al. 2014), were used for all models to obtain and compare the
 1377 maps.

1378

1379

1380

1381

1382

Alessandro 6/10/y 15:57

Eliminato: SHARE

ID	Fault Sources	L (km)	Dip (°)	Upper (km)	Lower (km)	SR _{min} (mm/yr)	SR _{max} (mm/yr)
1	Lunigiana	43.8	40	0	5	0.28	0.7
2	North Apuane Transfer	25.5	45	0	7	0.33	0.83
3	Garfagnana	26.9	30	0	4.5	0.35	0.57
4	Garfagnana Transfer	47.1	90	2	7	0.33	0.83
5	Mugello	21.0	40	0	7	0.33	0.83
6	Ronta	19.3	65	0	7	0.17	0.5
7	Poppi	17.1	40	0	4.5	0.33	0.83
8	Città di Castello	22.9	40	0	3	0.25	1.2
9	M.S.M. Tiberina	10.5	40	0	2.5	0.25	0.75
10	Gubbio	23.6	50	0	6	0.4	1.2
11	Colfiorito System	45.9	50	0	8	0.25	0.9
12	Umbra Valley	51.1	55	0	4.5	0.4	1.2
13	Vettore-Bove	35.4	50	0	15	0.2	1.05
14	Nottoria-Preci	29.0	50	0	12	0.2	1
15	Cascia-Cittareale	24.3	50	0	13.5	0.2	1
16	Leonessa	14.9	55	0	12	0.1	0.7
17	Rieti	17.6	50	0	10	0.25	0.6
18	Fucino	82.3	50	0	13	0.3	1.6
19	Sella di Corno	23.1	60	0	13	0.35	0.7
20	Pizzoli-Pettino	21.3	50	0	14	0.3	1
21	Monte Reale	15.1	50	0	14	0.25	0.9
22	Gorzano	28.1	50	0	15	0.2	1
23	Gran Sasso	28.4	50	0	15	0.35	1.2
24	Paganica	23.7	50	0	14	0.4	0.9
25	Middle Aternum Valley	29.1	50	0	14	0.15	0.45
26	Campo Felice-Ovindoli	26.2	50	0	13	0.2	1.6
27	Carsoli	20.5	50	0	11	0.35	0.6
28	Liri	42.5	50	0	11	0.3	1.26
29	Sora	20.4	50	0	11	0.15	0.45
30	Marsicano	20.0	50	0	13	0.25	1.2
31	Sulmona	22.6	50	0	15	0.6	1.35
32	Maiella	21.4	55	0	15	0.7	1.6
33	Aremogna C.Miglia	13.1	50	0	15	0.1	0.6
34	Barrea	17.1	55	0	13	0.2	1
35	Cassino	24.6	60	0	11	0.25	0.5
36	Ailano-Piedimonte	17.6	60	0	12	0.15	0.35
37	Matese	48.3	60	0	13	0.2	1.9
38	Bojano	35.5	55	0	13	0.2	0.9
39	Frosolone	36.1	70	11	25	0.35	0.93
40	Ripabottoni-San Severo	68.3	85	6	25	0.1	0.5
41	Mattinata	42.3	85	0	25	0.7	1
42	Castelluccio dei Sauri	93.2	90	11	22	0.1	0.5
43	Ariano Irpino	30.1	70	11	25	0.35	0.93
44	Tammaro	25.0	60	0	13	0.35	0.93
45	Benevento	25.0	55	0	10	0.35	0.93
46	Volturno	15.7	60	1	13	0.23	0.57
47	Avella	20.5	55	1	13	0.2	0.7
48	Ufita-Bisaccia	59.0	64	1.5	15	0.35	0.93

49	Melfi	17.2	80	12	22	0.1	0.5
50	Irpinia Antithetic	15.0	60	0	11	0.2	0.53
51	Irpinia	39.7	65	0	14	0.3	2.5
52	Vulturara	23.7	60	1	13	0.2	0.35
53	Alburni	20.4	60	0	8	0.35	0.7
54	Caggiano-Diano Valley	46.0	60	0	12	0.35	1.15
55	Pergola-Maddalena	50.6	60	0	12	0.20	0.93
56	Agri	34.9	50	5	15	0.8	1.3
57	Potenza	17.8	90	15	21	0.1	0.5
58	Palagianello	73.3	90	13	22	0.1	0.5
59	Monte Alpi	10.9	60	0	13	0.35	0.9
60	Maratea	21.6	60	0	13	0.46	0.7
61	Mercure	25.8	60	0	13	0.2	0.6
62	Pollino	23.8	60	0	15	0.22	0.58
63	Castrovillari	10.3	60	0	15	0.2	1.15
64	Rossano	14.9	60	0	22	0.5	0.6
65	Crati West	49.7	45	0	15	0.84	1.4
66	Crati East	18.4	60	0	8	0.75	1.45
67	Lakes	43.6	60	0	22	0.75	1.45
68	Fuscalto	21.1	60	2	22	0.75	1.45
69	Piano Lago-Decollatura	25.0	60	1	15	0.23	0.57
70	Catanzaro North	29.5	80	3	20	0.75	1.45
71	Catanzaro South	21.3	80	3	20	0.75	1.45
72	Serre	31.6	60	0	15	0.7	1.15
73	Vibo	23.0	80	0	15	0.75	1.45
74	Sant'Eufemia Gulf	24.8	40	1	11	0.11	0.3
75	Capo Vaticano	13.7	60	0	8	0.75	1.45
76	Coccorino	13.3	70	3	11	0.75	1.45
77	Scilla	29.7	60	0	13	0.8	1.5
78	Sant'Eufemia	19.2	60	0	13	0.75	1.45
79	Cittanova-Armo	63.8	60	0	13	0.45	1.45
80	Reggio Calabria	27.2	60	0	13	0.7	2
81	Taormina	38.7	30	3	13	0.9	2.6
82	Acireale	39.4	60	0	15	1.15	2.3
83	Western Ionian	50.1	65	0	15	0.75	1.45
84	Eastern Ionian	39.3	65	0	15	0.75	1.45
85	Climiti	15.7	60	0	15	0.75	1.45
86	Avola	46.9	60	0	16	0.8	1.6

1385

1386 Table 1 Geometric Parameters of the Fault Sources. L, along-strike length; Dip,
1387 inclination angle of the fault plane; Upper and Lower, the thickness bounds of the
1388 local seismogenic layer; SRmin and SRmax, the **minimum and maximum** slip rates
1389 assigned to the sources using the references available (see the supplemental files);
1390 and *ID*, the fault number identifier.

1391

ID	Fault Sources	Historical Earthquakes				Instrumental Earthquakes		
		yyyy/mm/dd	I_{Max}	I_0	M_w	sD	yyyy/mm/dd	M_w
1	Lunigiana	1481/05/07	VIII	VIII	5.6	0.4		
		1834/02/14	IX	IX	6.0	0.1		
2	North Apuane Transfer	1837/04/11	X	IX	5.9	0.1		
3	Garfagnana	1740/03/06	VIII	VIII	5.6	0.2		
		1920/09/07	X	X	6.5	0.1		
4	Garfagnana Transfer							
5	Mugello	1542/06/13	IX	IX	6.0	0.2		
		1919/06/29	X	X	6.4	0.1		
6	Ronta							
7	Poppi							
8	Città di Castello	1269			5.7			
		1389/10/18	IX	IX	6	0.5		
		1458/04/26	VIII-IX	VIII-IX	5.8	0.5		
		1789/09/30	IX	IX	5.9	0.1		
9	M.S.M. Tiberina	1352/12/25	IX	IX	6.3	0.2		
		1917/04/26	IX-X	IX-X	6.0	0.1		
10	Gubbio						1984/04/29	5.6
11	Colfiorito System	1279/04/30	X	IX	6.2	0.2	1997/09/26	5.7
		1747/04/17	IX	IX	6.1	0.1	1997/09/26	6
		1751/07/27	X	X	6.4	0.1		
12	Umbra Valley	1277		VIII	5.6	0.5		
		1832/01/13	X	X	6.4	0.1		
		1854/02/12	VIII	VIII	5.6	0.3		
13	Vettore-Bove						2016/10/30	6.5
14	Nottoria-Preci	1328/12/01	X	X	6.5	0.3	1979/09/19	5.8
		1703/01/14	XI	XI	6.9	0.1		
		1719/06/27	VIII	VIII	5.6	0.3		
		1730/05/12	IX	IX	6.0	0.1		
		1859/08/22	VIII-IX	VIII-IX	5.7	0.3		
		1879/02/23	VIII	VIII	5.6	0.3		
15	Cascia-Cittareale	1599/11/06	IX	IX	6.1	0.2		
		1916/11/16	VIII	VIII	5.5	0.1		
16	Leonessa							
17	Rieti	1298/12/01	X	IX-X	6.3	0.5		
		1785/10/09	VIII-IX	VIII-IX	5.8	0.2		
18	Fucino	1349/09/09	IX	IX	6.3	0.1		
		1904/02/24	IX	VIII-IX	5.7	0.1		
		1915/01/13	XI	XI	7	0.1		
19	Sella di Corno							
20	Pizzoli-Pettino	1703/02/02	X	X	6.7	0.1		
21	Monte Reale							
22	Gorzano	1639/10/07	X	IX-X	6.2	0.2		
		1646/04/28	IX	IX	5.9	0.4		
23	Gran Sasso							
24	Paganica	1315/12/03	VIII	VIII	5.6	0.5	2009/06/04	6.3
		1461/11/27	X	X	6.5	0.5		
25	Middle Aternum Valley							
26	Campo Felice-Ovindoli							
27	Carsoli							
28	Liri							
29	Sora	1654/07/24	X	IX-X	6.3	0.2		
30	Marsicano							
31	Sulmona							
32	Maiella							
33	Aremogna C. Miglia							
34	Barrea						1984/05/07	5.9
35	Cassino							
36	Ailano-Piedimonte							
37	Matese	1349/09/09	X-XI	X	6.8	0.2		

38	Bojano	1805/07/26	X	X	6.7	0.1		
39	Frosolone	1456/12/05	XI	XI	7	0.1		
40	Ripabottoni-San Severo	1627/07/30	X	X	6.7	0.1	2002/10/31	5.7
		1647/05/05	VII-VIII	VII-VIII	5.7	0.4		
		1657/01/29	IX-X	VIII-IX	6.0	0.2		
41	Mattinata	1875/12/06	VIII	VIII	5.9	0.1		
		1889/12/08	VII	VII	5.5	0.1		
		1948/08/18	VII-VIII	VII-VIII	5.6	0.1		
42	Castelluccio dei Sauri	1361/07/17	X	IX	6	0.5		
		1560/05/11	VIII	VIII	5.7	0.5		
		1731/03/20	IX	IX	6.3	0.1		
43	Ariano Irpino	1456/12/05			6.9	0.1		
		1962/08/21	IX	IX	6.2	0.1		
44	Tammaro	1688/06/05	XI	XI	7	0.1		
45	Benevento							
46	Volturno							
47	Avella	1499/12/05	VIII	VIII	5.6	0.5		
48	Ufita-Bisaccia	1732/11/29	X-XI	X-XI	6.8	0.1		
		1930/07/23	X	X	6.7	0.1		
49	Melfi	1851/08/14	X	X	6.5	0.1		
50	Irpinia Antithetic							
51	Irpinia	1466/01/15	VIII-IX	VIII-IX	6.0	0.2	1980/11/23	6.8
		1692/03/04	VIII	VIII	5.9	0.4		
		1694/09/08	X	X	6.7	0.1		
		1853/04/09	IX	VIII	5.6	0.2		
52	Volturara							
53	Alburni							
54	Caggiano-Diano Valley	1561/07/31	IX-X	X	6.3	0.1		
55	Pergola-Maddalena	1857/12/16			6.5			
		1857/12/16			6.3			
56	Agri							
57	Potenza	1273/12/18	VIII-IX	VIII-IX	5.8	0.5	1990/05/05	5.8
58	Palagianello							
59	Monte Alpi							
60	Maratea							
61	Mercure	1708/01/26	VIII-IX	VIII	5.6	0.6	1998/09/09	5.5
62	Pollino							
63	Castrovillari							
64	Rossano	1836/04/25	X	IX	6.2	0.2		

65	Crati West	1184/05/24	IX	IX	6.8	0.3
1870/10/04		X	IX-X	6.2	0.1	
1886/03/06		VII-VIII	VII-VIII	5.6	0.3	
66	Crati East	1767/07/14	VIII-IX	VIII-IX	5.9	0.2
1835/10/12		X	IX	5.9	0.3	
67	Lakes	1638/06/08	X	X	6.8	0.1
68	Fuscalto	1832/03/08	X	X	6.6	0.1
69	Piano Lago-Decollatura					
70	Catanzaro North	1638/03/27			6.6	
71	Catanzaro South	1626/04/04	X	IX	6.1	0.4
72	Serre	1659/11/05	X	X	6.6	0.1
1743/12/07		IX-X	VIII-IX	5.9	0.2	
1783/02/07		X-XI	X-XI	6.7	0.1	
1791/10/13		IX	IX	6.1	0.1	
73	Vibo					
74	Sant'Eufemia Gulf	1905/09/08	X-XI	X-XI	7	0.1
75	Capo Vaticano					
76	Coccorino	1928/03/07	VIII	VII-VIII	5.9	0.1
77	Scilla					
78	Sant'Eufemia	1894/11/16	IX	IX	6.1	0.1
79	Cittanova-Armo	1509/02/25	IX	VIII	5.6	0.4
1783/02/05		XI	XI	7.1	0.1	
80	Reggio Calabria					
81	Taormina	1908/12/28	XI	XI	7.1	0.2
82	Acireale	1818/02/20	IX-X	IX-X	6.3	0.1
83	Western Ionian	1693/01/11	XI	XI	7.3	0.1
84	Eastern Ionian					
85	Climiti					
86	Avola					

1392

1393 Table 2 Earthquake-Source Association Adopted for Fault Sources. I_{Max} , maximum
1394 intensity; I_0 , epicentral intensity; M_w , moment magnitude; and sD, standard deviation
1395 of the moment magnitude. For references, see the supplemental files.

1 **Integrating faults and past earthquakes into a probabilistic seismic hazard**
2 **model for peninsular Italy**

3

4 Alessandro Valentini¹, Francesco Visini² and Bruno Pace¹

5 ¹ DiSPUTer, Università degli Studi “Gabriele d’Annunzio”, Chieti, Italy

6 ² Istituto Nazionale di Geofisica e Vulcanologia, L’Aquila, Italy

7

8 **Abstract**

9

10 *Italy is one of the most seismically active countries in Europe. Moderate to strong earthquakes, with*
11 *magnitudes of up to ~7, have been historically recorded for many active faults. Currently,*
12 *probabilistic seismic hazard assessments in Italy are mainly based on area source models, in which*
13 *seismicity is modelled using a number of seismotectonic zones and the occurrence of earthquakes is*
14 *assumed uniform. However, in the past decade, efforts have increasingly been directed towards using*
15 *fault sources in seismic hazard models to obtain more detailed and potentially more realistic patterns*
16 *of ground motion. In our model, we used two categories of earthquake sources. The first involves*
17 *active faults, and fault slip rates were used to quantify the seismic activity rate. We produced an*
18 *inventory of all fault sources with details of their geometric, kinematic and energetic properties. The*
19 *associated parameters were used to compute the total seismic moment rate of each fault. We*
20 *evaluated the magnitude-frequency distribution (MFD) of each fault source using two models: a*
21 *characteristic Gaussian model centred on the maximum magnitude and a Truncated Gutenberg-*
22 *Richter model. The second earthquake source category involves distributed seismicity, and a fixed-*
23 *radius smoothed approach and a historical catalogue were used to evaluate seismic activity. Under*
24 *the assumption that deformation is concentrated along faults, we combined the MFD derived from the*
25 *geometry and slip rates of active faults with the MFD from the spatially smoothed earthquake sources*
26 *and assumed that the smoothed seismic activity in the vicinity of an active fault gradually decreases*
27 *by a fault size-driven factor. Additionally, we computed horizontal peak ground acceleration maps for*
28 *return periods of 475 and 2,475 yrs. Although the ranges and gross spatial distributions of the*
29 *expected accelerations obtained here are comparable to those obtained through methods involving*
30 *seismic catalogues and classical zonation models, the spatial pattern of the hazard maps obtained*
31 *with our model is far more detailed. Our model is characterized by areas that are more hazardous*
32 *and that correspond to mapped active faults, while previous models yield expected accelerations that*
33 *are almost uniformly distributed across large regions. In addition, we conducted sensitivity tests to*

34 *determine the impact on the hazard results of the earthquake rates derived from two MFD models for*
35 *faults and to determine the relative contributions of faults versus distributed seismic activity. We*
36 *believe that our model represents advancements in terms of the input data (quantity and quality) and*
37 *methodology used in the field of fault-based regional seismic hazard modelling in Italy.*
38

39 **1. Introduction**

40 In this paper, we present the results of a new probabilistic seismic hazard (PSH)
41 model for Italy that includes significant advances in the use of integrated active fault
42 and seismological data. The use of active faults as an input for PSH analysis is a
43 consolidated approach in many countries characterized by high strain rates and
44 seismic releases, as shown, for example, by Field et al. (2015) in California and
45 Stirling et al. (2012) in New Zealand. However, in recent years, active fault data have
46 also been successfully integrated into PSH assessments in regions with moderate-
47 to-low strain rates, such as SE Spain (e.g., Garcia-Mayordomo et al., 2007), France
48 (e.g., Scotti et al., 2014), and central Italy (e.g., Peruzza et al., 2011).

49 In Europe, a working group of the European Seismological Commission, named
50 *Fault2SHA*, is discussing fault-based seismic hazard modelling
51 (<https://sites.google.com/site/linkingfaultpsha/home>). The working group, born to
52 motivate exchanges between field geologists, fault modellers and seismic hazard
53 practitioners, organizes workshops, conference sessions, and special issues and
54 stimulates collaborations between researchers. The work we are presenting here
55 stems from the activities of the *Fault2SHA* working group.

56 Combining active faults and background sources is one of the main issues in this
57 type of approach. Although the methodology remains far from identifying a standard
58 procedure, common approaches combine active faults and background sources by
59 applying a threshold magnitude, generally between 5.5 and 7, above which
60 seismicity is modelled as occurring on faults and below which seismicity is modelled
61 via a smoothed approach (e.g., Akinci et al., 2009), area sources (e.g., the so-called
62 FSBG model in SHARE; Woessner et al., 2015) or a combination of the two (Field et
63 al., 2015; Pace et al., 2006).

64 Another important issue in the use of active faults in PSHA is assigning the “correct”
65 magnitude-frequency distribution (MFD) to the fault sources. Gutenberg-Richter (GR)

66 and characteristic earthquake models are commonly used, and the choice
67 sometimes depends on the knowledge of the fault and data availability. Often, the
68 choice of the “appropriate” MFD for each fault source is a difficult task because
69 palaeoseismological studies are scarce, and it is often difficult to establish clear
70 relationships between mapped faults and historical seismicity. Recently, Field et al.
71 (2017) discussed the effects and complexity of the choice, highlighting how often the
72 GR model results are not consistent with data; however, in other cases,
73 uncharacteristic behaviour, with rates smaller than the maximum, are possible. The
74 discussion is open (see for example the discussion by Kagan et al., 2012) and far
75 from being solved with the available observations, including both seismological
76 and/or geological/paleoseismological observations. In this work, we explore the
77 calculations of these two MFDs, a characteristic Gaussian model and a Truncated
78 Gutenberg-Richter model, to explore the epistemic uncertainties and to consider a
79 *Mixed model* as a so-called “expert judgement” model. This approach is useful for
80 comparative analysis, and which we assigned one of the two MFDs to each fault
81 source. The rationale of the choice of the MFD of each fault source is explained in
82 detail later in this paper. However, this approach obviously does not solve the issue,
83 and the choice of MFD remains an open question in fault-based PSHA.

84 In Italy, the current national PSH model for building code (Stucchi et al., 2011) is
85 based on area sources and the classical Cornell approach (Cornell, 1968), in which
86 the occurrence of earthquakes is assumed uniform in the defined seismotectonic
87 zones. However, we believe that more efforts must be directed towards using
88 geological data (e.g., fault sources and paleoseismological information) in PSH
89 models to obtain detailed patterns of ground motion, extend the observational time
90 required to capture the recurrence of large-magnitude events and improve the
91 reliability of seismic hazard assessments. In fact, as highlighted by the 2016-2017
92 seismic sequences in central Italy, a zone-based PSH is not able to model local
93 spatial variations in ground motion (Meletti et al., 2016), whereas a fault-based
94 model can provide insights for aftershock time-dependent PSH analysis (Peruzza et
95 al., 2016). In conclusion, even if the main purpose of this work is to integrate active
96 faults into hazard calculations for the Italian territory, this study does not represent
97 an official update of the seismic hazard model of Italy.

98

99 **2. Source Inputs**

100 Two earthquake-source inputs are considered in this work. The first is a fault source
101 input that is based on active faults and uses the geometries and slip rates of known
102 active faults to compute activity rates over a certain range of magnitude. The second
103 is a classical smoothed approach that accounts for the rates of expected
104 earthquakes with a minimum moment magnitude (M_w) of 4.5 but excludes
105 earthquakes associated with known faults based on a modified earthquake
106 catalogue. Note that our PSH model requires the combination of the two source
107 inputs related to the locations of expected seismicity rates into a single model.
108 Therefore, these two earthquake-source inputs are not independent but
109 complementary, in both the magnitude and frequency distribution, and together
110 account for all seismicity in Italy.

111 In the following subsections, we describe the two source inputs and how they are
112 combined in the PSH model.

113 **2.1 Fault Source Input**

114 In seismic hazard assessment, an active fault is a structure that exhibits evidence of
115 activity in the late Quaternary (i.e., in the past 125 kyr), has a demonstrable or
116 potential capability of generating major earthquakes and is capable of future
117 reactivation (see Machette, 2000 for a discussion on terminology). The evidence of
118 Quaternary activity can be geomorphological and/or paleoseismological when
119 activation information from instrumental seismic sequences and/or association to
120 historical earthquakes is not available. Fault source inputs are useful for seismic
121 hazard studies, and we compiled a database for Italy via the analysis and synthesis
122 of neotectonic and seismotectonic data from approximately 90 published studies of
123 110 faults across Italy. Our database included, but was not limited to, the Database
124 of Individual Seismogenic Sources (DISS vers. 3.2.0, <http://diss.rm.ingv.it/diss/>),
125 which is already available for Italy. It is important to highlight that the DISS is
126 currently composed of two main categories of seismogenic sources: individual and
127 composite sources. The latter are defined by the DISS' authors as "*simplified and
128 three-dimensional representation of a crustal fault containing an unspecified number
129 of seismogenic sources that cannot be singled out. Composite seismogenic sources
130 are not associated with a specific set of earthquakes or earthquake distribution*", and

131 therefore are not useful for our PSHA approach; the former is “a *simplified and three-*
132 *dimensional representation of a rectangular fault plane. Individual seismogenic*
133 *sources are assumed to exhibit characteristic behaviour with respect to rupture*
134 *length/width and expected magnitude*” ([http://diss.rm.ingv.it/diss/index.php/about/13-](http://diss.rm.ingv.it/diss/index.php/about/13-introduction)
135 [introduction](http://diss.rm.ingv.it/diss/index.php/about/13-introduction)). Even if in agreement with our approach, we note that some of the
136 individual seismogenic sources in the DISS are based on geological and
137 paleoseismological information, and many others used the *Boxer* code (Gasperini et
138 al., 1999) to calculate the epicentre, moment magnitude, size and orientation of a
139 seismic source from observed macroseismic intensities. We carefully analysed the
140 individual sources and some related issues: (i) the lack of updating of the geological
141 information of some individual sources and (ii) the nonconformity between the input
142 data used by DISS in *Boxer* and the latest historical seismicity (CPTI15) and
143 macroseismic intensity (DBMI15) publications. Thus, we performed a full review of
144 the fault database. We then compiled a fault source database as a synthesis of
145 works published over the past twenty years, including DISS, using all updated and
146 available geological, paleoseismological and seismological data (see the
147 supplemental files for a complete list of references). We consider our database as
148 complete as possible in terms of individual seismogenic sources, and it contains all
149 the parameters necessary to construct an input dataset for fault-based PSHA.

150 The resulting database of normal and strike-slip active and seismogenic faults in
151 peninsular Italy (Fig. 1, Tables 1 and 2; see the supplemental files) includes all the
152 available geometric, kinematic, slip rate and earthquake source-related information.
153 In the case of missing data regarding the geometric parameters of dip and rake, we
154 assumed typical dip and rake values of 60° and -90° , respectively, for normal faults
155 and 90° and 0° or 180° , respectively, for strike-slip faults. In this paper, only normal
156 and strike-slip faults are used as fault source inputs. We decided not to include thrust
157 faults in the present study because, with the methodology proposed in this study (as
158 discussed later in the text), the maximum size of a single-rupture segment must be
159 defined, and segmentation criteria have not been established for large thrust zones.
160 Moreover, our method uses slip rates to derive active seismicity rates, and sufficient
161 knowledge of these values is not available for thrust faults in Italy. Because some
162 areas of Italy, such as the NW sector of the Alps, Po Valley, the offshore sector of
163 the central Adriatic Sea, and SW Sicily, may be excluded by this limitation, we are

164 considering an update to our approach to include thrust faults and volcanic sources
165 in a future study. The upper and lower boundaries of the seismogenic layer are
166 mainly derived from the analysis of Stucchi et al. (2011) of the Italian national
167 seismic hazard model and locally refined by more detailed studies (Boncio et al.,
168 2011; Peruzza et al., 2011; Ferranti et al., 2014).

169 Based on the compiled database, we explored three main issues associated with
170 defining a fault source input: the slip rate evaluation, the segmentation model and
171 the expected seismicity rate calculation.

172 *2.1.1 Slip rates*

173 Slip rates control fault-based seismic hazards (Main, 1996, Roberts et al., 2004; Bull
174 et al., 2006; Visini and Pace, 2014) and reflect the velocities of the mechanisms that
175 operate during continental deformation (e.g., Cowie et al., 2005). Moreover, long-
176 term observations of faults in various tectonic contexts have shown that slip rates
177 vary in space and time (e.g., Bull et al., 2006; Nicol et al., 2006, 2010, McClymont et
178 al., 2009; Gunderson et al., 2013; Benedetti et al., 2013, D'Amato et al., 2016), and
179 numerical simulations (e.g., Robinson et al., 2009; Cowie et al., 2012; Visini and
180 Pace, 2014) suggest that variability mainly occurs in response to interactions
181 between adjacent faults. Therefore, understanding the temporal variability in fault slip
182 rates is a key point in understanding the earthquake recurrence rates and their
183 variability.

184 In this work, we used the mean of the minimum and maximum slip rate values listed
185 in Table 1 and assumed that it is representative of the long-term behaviour (over the
186 past 15 ky in the Apennines). These values were derived from approximately 65
187 available neotectonics, palaeoseismology and seismotectonics papers (see the
188 supplemental files). To evaluate the long-term slip rate, which is representative of the
189 average slip behaviour, and its variability over time, we used slip rates determined in
190 different ways and at different time scales (e.g., at the decadal scale based on
191 geodetic data or at longer scales based on the displacement of Holocene or Plio-
192 Pleistocene horizons). Because a direct comparison of slip rates over different time
193 intervals obtained by different methods may be misleading (Nicol et al., 2009), we
194 cannot exclude the possibility that epistemic uncertainties could affect the original

195 data in some cases. The discussion of these possible biases and their evaluation via
196 statistically derived approaches (e.g., Gardner et al., 1987; Finnegan et al., 2014;
197 Gallen et al., 2015) is beyond the scope of this paper and will be explored in future
198 work. Moreover, we are assuming that slip rate values used are representative of
199 seismic movements, and aseismic factors are not taken into account. Therefore, we
200 believe that investigating the effect of this assumption could be another issue
201 explored in future work; for example, by differentiating between aseismic slip factors
202 in different tectonic contexts.

203 Because 28 faults had no measured slip (or throw) rate (Fig. 1a), we proposed a
204 statistically derived approach to assign a slip rate to these faults. Based on the slip
205 rate spatial distribution shown in Figure 1b, we subdivided the fault database into
206 three large regions—the Northern Apennines, Central-Southern Apennines and
207 Calabria-Sicilian coast—and analysed the slip rate distribution in these three areas. In
208 Figure 1b, the slip rates tend to increase from north to south. The fault slip rates in
209 the Northern Apennines range from 0.3 to 0.8 mm/yr, with the most common ranging
210 from approximately 0.5-0.6 mm/yr; the slip rates in the Central-Southern Apennines
211 range from 0.3 to 1.0, and the most common rate is approximately 0.3 mm/yr; and
212 the slip rates in the southern area (Calabria and Sicily) range from 0.9 to 1.8, with
213 the most common being approximately 0.9 mm/yr.

214 The first step in assigning an average slip rate and a range of variability to the faults
215 with unknown values is to identify the most representative distribution among known
216 probability density functions using the slip rate data from each of the three areas. We
217 test five well-known probability density functions (*Weibull*, *normal*, *exponential*,
218 *Inverse Gaussian* and *gamma*) against mean slip rate observations. The resulting
219 function with the highest log-likelihood is the *normal* function in all three areas. Thus,
220 the mean value of the *normal* distribution is assigned to the faults with unknown
221 values. We assign a value of 0.58 mm/yr to faults in the northern area, 0.64 mm/yr to
222 faults in the Central-Southern area, and 1.10 mm/yr to faults in the Calabria-Sicilian
223 area. To assign a range of slip rate variability to each of the three areas, we test the
224 same probability density functions against slip rate variability observations. Similar to
225 the mean slip rate, the probability density function with the highest log-likelihood is
226 the *normal* function in all three areas. We assign a value of 0.25 mm/yr to the faults

227 in the northern area, 0.29 mm/yr to the faults in the Central-Southern area, and 0.35
228 mm/yr to the faults in the Calabria-Sicilian area.

229

230 2.1.2 Segmentation rules for delineating fault sources

231 An important issue in the definition of a fault source input is the formulation of
232 segmentation rules. In fact, the question of whether structural segment boundaries
233 along multisegment active faults act as persistent barriers to a single rupture is
234 critical to defining the maximum seismogenic potential of fault sources. In our case,
235 the rationale behind the definition of a fault source is based on the assumption that
236 the geometric and kinematic features of a fault source are expressions of its
237 seismogenic potential and that its dimensions are compatible for hosting major (M_w
238 ≥ 5.5) earthquakes. Therefore, a fault source is considered a fault or an ensemble of
239 faults that slip together during an individual major earthquake. A fault source is
240 defined by a *seismogenic master fault* and its surface projection (Fig. 2a).
241 *Seismogenic master faults* are separated from each other by first-order structural or
242 geometrical complexities. Following the suggestions by Boncio et al. (2004) and
243 Field et al. (2015), we imposed the following segmentation rules in our case study: (i)
244 4-km fault gaps among aligned structures; (ii) intersections with cross structures
245 (often transfer faults) extending 4 km along strike and oriented at nearly right angles
246 to the intersecting faults; (iii) overlapping or underlapping en echelon arrangements
247 with separations between faults of 4 km; (iv) bending $\geq 60^\circ$ for more than 4 km; (v)
248 average slip rate variability along a strike greater than or equal to 50%; and (vi)
249 changes in seismogenic thickness greater than 5 km among aligned structures.
250 Example applications of the above rules are illustrated in Figure 2a.

251 By applying the above rules to our fault database, the 110 faults yielded 86 fault
252 sources: 9 strike-slip sources and 77 normal-slip sources. The longest fault source is
253 *Castelluccio dei Sauri* (fault number (*id in Table 1*) 42, $L = 93.2$ km), and the shortest
254 is *Castrovillari* (*id* 63, $L = 10.3$ km). The mean length is 30 km. The dip angle varies
255 from 30° to 90° , and 70% of the fault sources have dip angles between 50° and 60° .
256 The mean value of seismogenic thickness (ST) is approximately 12 km. The source
257 with the largest ST is *Mattinata* (*id* 41, $ST = 25$ km), and the source with the thinnest

258 ST is *Monte Santa Maria Tiberina* (id 9, ST = 2.5 km) due to the presence of an east-
259 dipping low angle normal fault, the Alto-Tiberina Fault (Boncio et al., 2000), located a
260 few kilometres west of the Monte Santa Maria Tiberina fault. Observed values of
261 maximum magnitude (M_w) have been assigned to 35 fault sources (based on Table
262 2), and the values vary from 5.90 to 7.32. The fault source inputs are shown in
263 Figure 3.

264

265 2.1.3 Expected seismicity rates

266 Each fault source is characterized by data, such as kinematic, geometry and slip rate
267 information, that we use as inputs for the FiSH code (Pace et al., 2016) to calculate
268 the global budget of the seismic moment rate allowed by the structure. This
269 calculation is based on predefined size-magnitude relationships in terms of the
270 maximum magnitude (M_{max}) and the associated mean recurrence time (T_{mean}). Table
271 1 summarizes the geometric parameters used as FiSH input parameters for each
272 fault source (seismogenic box) shown in Figure 3. To evaluate M_{max} of each source,
273 according to Pace et al., (2016) we first computed and then combined up to five M_{max}
274 values (see the example of the Paganica fault source in Fig. 2b, details in Pace et
275 al., 2016). Specifically, these five M_{max} values are as follows: MMO based on the
276 calculated scalar seismic moment (M_0) and the application of the standard formula
277 $M_w = 2/3 (\log M_0 - 9.1)$ (Hanks and Kanamori, 1979; IASPEI, 2005); two magnitude
278 values using the Wells and Coppersmith (1994) empirical relationships for the
279 maximum subsurface rupture length (MRLD) and maximum rupture area (MRA); a
280 value that corresponds to the maximum observed magnitude (MObs), if available;
281 and a value (MASP, ASP for aspect ratio) computed by reducing the fault length
282 input if the aspect ratio (W/L) is smaller than the value evaluated by the relation
283 between the aspect ratio and rupture length of observed earthquake ruptures, as
284 derived by Peruzza and Pace (2002) (not in the case of Paganica in Fig. 2b).
285 Although incorrect to consider MObs a possible M_{max} value and treat it the same as
286 other estimations, in some cases, it was useful to constrain the seismogenic
287 potentials of individual seismogenic sources. As an example, for the *Irpinia Fault* (id
288 51 in Tables 1 and 2), the characteristics of the 1980 earthquake ($M_w \sim 6.9$) can be
289 used to evaluate M_{max} via comparison with the M_{max} derived from scaling
290 relationships. In such cases, we (i) calculated the maximum expected magnitude

291 (M_{max1}) and the relative uncertainties using only the scaling relationships and (ii)
292 compared the maximum of observed magnitudes of the earthquakes potentially
293 associated with the fault. If MObs was within the range of $M_{max} \pm 1$ standard
294 deviation, we considered the value and recalculated a new M_{max} (M_{max2}) with a new
295 uncertainty. If MObs was larger than M_{max1} , we reviewed the fault geometry and/or
296 the earthquake-source association.

297 Because all the empirical relationships, as well as observed historical and recent
298 magnitudes of earthquakes, are affected by uncertainties, the *MomentBalance* (MB)
299 portion of the FiSH code (Pace et al., 2016) was used to account for these
300 uncertainties. MB computes a probability density function for each magnitude
301 derived from empirical relationships or observations and summarizes the results as a
302 maximum magnitude value with a standard deviation. The uncertainties in the
303 empirical scaling relationship are taken from the studies of Wells and Coppersmith
304 (1994), Peruzza and Pace (2002) and Leonard (2010). Currently, the uncertainty in
305 magnitude associated with the seismic moment is fixed and set to 0.3, whereas the
306 catalogue defines the uncertainty in MObs. Moreover, to combine the evaluated
307 maximum magnitudes, MB creates a probability curve for each magnitude by
308 assuming a normal distribution (Fig. 2). We assumed an untruncated normal
309 distribution of magnitudes at both sides. MB successively sums the probability
310 density curves and fits the summed curve to a normal distribution to obtain the mean
311 of the maximum magnitude M_{max} and its standard deviation.

312 Thus, a unique M_{max} with a standard deviation is computed for each source, and this
313 value represents the maximum rupture that is allowed by the fault geometry and the
314 rheological properties.

315 Finally, to obtain the mean recurrence time of M_{max} (i.e., T_{mean}), we use the criterion
316 of “segment seismic moment conservation” proposed by Field et al. (1999). This
317 criterion divides the seismic moment that corresponds to M_{max} by the moment rate
318 for given a slip rate:

319
$$T_{mean} = \frac{1}{Char_Rate} = \frac{10^{1.5 M_{max} 9.1}}{\mu VLW} \quad (1)$$

320 where T_{mean} is the mean recurrence time in years, Char_Rate is the annual mean
321 rate of occurrence, M_{max} is the computed mean maximum magnitude, μ is the shear
322 modulus, V is the average long-term slip rate, and L and W are geometrical
323 parameters of the fault along-strike rupture length and downdip width, respectively.
324 This approach was used for both MFDs in this study, and, in particular, we evaluated
325 M_{max} and T_{mean} based on the fault geometry and the slip rate of each individual
326 source. Additionally, we calculated the total expected seismic moment rate using
327 equation 1. Then, we partitioned the total expected seismic moment rate based on a
328 range given by $M_{\text{max}} \pm 1$ standard deviation following a Gaussian distribution.
329 After the fault source is entered as input, the seismic moment rate is calculated, M_{max}
330 (Fig. 2b) and T_{mean} are defined for each source, we computed the MFDs of expected
331 seismicity. For each fault source, we use two “end-member” MFD models: (i) a
332 *Characteristic Gaussian (CHG)* model, a symmetric Gaussian curve (applied to the
333 incremental MFD values) centred on the M_{max} value of each fault with a range of
334 magnitudes equal to 1-sigma, and (ii) a *Truncated Gutenberg-Richter (TGR, Ordaz,*
335 *1999; Kagan, 2002)* model, with M_{max} as the upper threshold and $M_w = 5.5$ as the
336 minimum threshold for all sources. The b-values are constant and equal to 1.0 for all
337 faults, and they are obtained by the interpolation of earthquake data from the CPTI15
338 catalogue, as single-source events are insufficient for calculating the required
339 statistics. The a-values were computed with the ActivityRate tool of the FiSH code.
340 ActivityRate balances the total expected seismic moment rate with the seismic
341 moment rate that was obtained based on M_{max} and T_{mean} (details in Pace et al.,
342 2016). In Figure 2c, we show an example of the expected seismicity rates in terms of
343 the annual cumulative rates for the Paganica source using the two above-described
344 MFDs.
345 Finally, we create a so-called “expert judgement” model, called the *Mixed* model, to
346 determine the MFD for each fault source based on the earthquake-source
347 associations. In this case, we decided that if an earthquake assigned to a fault
348 source (see Table 2 for earthquake-source associations) has a magnitude lower than
349 the magnitude range in the curve of the *CHG* model distribution, the *TGR* model is
350 applied to that fault source. Otherwise, the *CHG* model, which peaks at the
351 calculated M_{max} , is applied. Of course, errors in this approach can originate from the
352 misallocation of historical earthquakes, and we cannot exclude the possibility that
353 potentially active faults responsible for historical earthquakes have not yet been

354 mapped. The MFD model assigned to each fault source in our *Mixed* model is shown
355 in Figure 3.

356

357 **2.2 Distributed Source Inputs**

358 Introducing distributed earthquakes into the PSH model is necessary because
359 researchers have not been able to identify a causative source (i.e., a mapped fault)
360 for important earthquakes in the historical catalogue. This lack of correlation between
361 earthquakes and faults may be related to (i) interseismic strain accumulation in areas
362 between major faults, (ii) earthquakes occurring on unknown or blind faults, (iii)
363 earthquakes occurring on unmapped faults characterized by slip rates lower than the
364 rates of erosional processes, and/or (iv) the general lack of surface ruptures
365 associated with faults generating $M_w < 5.5$ earthquakes.

366 We used the historical catalogue of earthquakes (CPTI15; Rovida et al., 2016; Fig.
367 4) to model the occurrence of moderate-to-large ($M_w \geq 4.5$) earthquakes. The
368 catalogue consists of 4,427 events and covers approximately the last one thousand
369 years from 01/01/1005 to 28/12/2014. Before using the catalogue, we removed all
370 events not considered mainshocks via a declustering filter (Gardner and Knopoff,
371 1977). This process resulted in a complete catalogue composed of 1,839
372 independent events. Moreover, to avoid any artificial effects related to double
373 counting due to the use of two seismicity sources, i.e., the fault sources and the
374 distributed seismicity sources, we removed events associated with known active
375 faults from the CPTI15 earthquake catalogue. If the causative fault of an earthquake
376 is known, that earthquake does not need to be included in the seismicity smoothing
377 procedure. The earthquake-source association is based on neotectonics,
378 palaeoseismology and seismotectonics papers (see the supplemental files) and, in a
379 few cases, macroseismic intensity maps. In Table 2, we listed the earthquakes with
380 known causative fault sources. The differences in the smoothed rates given by eq.
381 (2) using the complete and modified catalogues are shown in Figure 5.

382 We applied the standard methodology developed by Frankel (1995) to estimate the
383 density of seismicity in a grid with latitudinal and longitudinal spacing of 0.05° . The
384 smoothed rate of events in each cell i is determined as follows:

385
$$n_i = \frac{\sum_j n_j e^{-\frac{\Delta_{ij}^2}{c^2}}}{\sum_j e^{-\frac{\Delta_{ij}^2}{c^2}}} \quad (2)$$

386 where n_i is the cumulative rate of earthquakes with magnitudes greater than the
 387 completeness magnitude M_c in each cell i of the grid and Δ_{ij} is the distance between
 388 the centres of grid cells i and j . The parameter c is the correlation distance. The sum
 389 is calculated in cells j within a distance of $3c$ of cell i .

390 To compute earthquake rates, we adopted the completeness magnitude thresholds
 391 over different periods given by Stucchi et al. (2011) for five large zones (Fig. 4).

392 To optimize the smoothing distance Δ in eq. (2), we divided the earthquake
 393 catalogue into four 10-yr disjoint learning and target periods from the 1960s to the
 394 1990s. For each pair of learning and target catalogues, we used the probability gain
 395 per earthquake to find the optimal smoothing distance (Kagan and Knopoff, 1977;
 396 Helmstetter et al., 2007). After assuming a spatially uniform earthquake density
 397 model as a reference model, the probability gain per earthquake G of a candidate
 398 model relative to a reference model is given by the following equation:

399
$$G = \exp\left(\frac{L-L_0}{N}\right) \quad (3)$$

400 where N is the number of events in the target catalogue and L and L_0 are the joint
 401 log-likelihoods of the candidate model and reference model, respectively. Under the
 402 assumption of a Poisson earthquake distribution, the joint log-likelihood of a model is
 403 given as follows:

404
$$L = \sum_{i_x=1}^{N_x} \sum_{j_y=1}^{N_y} \log p [\lambda(i_x, i_y), \omega] \quad (4)$$

405 where p is the Poisson probability, λ is the spatial density, ω is the number of
 406 observed events during the target period, and the parameters i_x and i_y denote each
 407 corresponding longitude-latitude cell.

408 Figure 6 shows that for the four different pairs of learning-target catalogues, the
 409 optimal smoothing distance c ranges from 30-40 km. Finally, the mean of all the

410 probability gains per earthquake yields a maximum smoothing distance of 30 km
411 (Fig. 6), which is then used in eq. (2).

412 The b-value of the GR distribution is calculated on a regional basis using the
413 maximum-likelihood method of Weichert (1980), which allows multiple periods with
414 varying completeness levels to be combined. Following the approach recently
415 proposed by Kamer and Hiemer (2015), we used a penalized likelihood-based
416 method for the spatial estimation of the GR b-values based on the Voronoi
417 tessellation of space without tectonic dependency. The whole Italian territory has
418 been divided into a grid with a longitude/latitude spacing of 0.05° , and the centres of
419 the grid cells represent the possible centres of Voronoi polygons. We vary the
420 number of Voronoi polygons, N_v , from 3 to 50, generating 1000 tessellations for
421 each N_v . The summed log-likelihood of each obtained tessellation is compared with
422 the log-likelihood given by the simplest model (prior model) obtained using the entire
423 earthquake dataset. We find that 673 random realizations led to better performance
424 than the prior model. Thus, we calculate an ensemble model using these 673
425 solutions, and the mean b-value of each grid node is shown in Figure 4.

426 The maximum magnitude M_{max} assigned to each node of the grid, the nodal planes
427 and the depths have been taken from the SHARE European project (Woessner et
428 al., 2015). The SHARE project evaluated the maximum magnitudes of large areas of
429 Europe based on a joint procedure involving historical observations and tectonic
430 regionalization. We adopted the lowest of the maximum magnitudes proposed by
431 SHARE, but evaluating the impact of different maximum magnitudes is beyond the
432 scope of this work.

433 Finally, the rates of expected seismicity for each node of the grid are assumed to
434 follow the TGR model (Kagan 2002):

$$435 \quad \lambda(M) = \lambda_0 \frac{\exp(-\beta M) - \exp(-\beta M_u)}{\exp(-\beta M_0) - \exp(-\beta M_u)} \quad (5)$$

436 where the magnitude (M) is in the range of M_0 (minimum magnitude) to M_u (upper or
437 maximum magnitude); otherwise $\lambda(M)$ is 0. Additionally, λ_0 is the smoothed rate of
438 earthquakes at $M_w = 4.5$ and $\beta = b \ln(10)$.

439 **2.3 Combining Fault and Distributed Sources**

440 To combine the two source inputs, we introduced a distance-dependent linear
441 weighting function, such that the contribution from the distributed sources linearly
442 decreases from 1 to 0 with decreasing distance from the fault. The expected
443 seismicity rates of the distributed sources start at $M_w = 4.5$, which is lower than the
444 minimum magnitude of the fault sources, and the weighting function is only
445 applicable in the magnitude range overlapping the MFD of each fault. This weighting
446 function is based on the assumption that faults tend to modify the surrounding
447 deformation field (Fig. 7), and this assumption is explained in detail later in this
448 paper.

449 During fault system evolution, the increase in the size of a fault through linking with
450 other faults results in an increase in displacement that is proportional to the quantity
451 of strain accommodated by the fault (Kostrov, 1974). Under a constant regional
452 strain rate, the activity of arranged across strike must eventually decrease (Nicol et
453 al., 1997; Cowie, 1998; Roberts et al., 2004). Using an analogue modelling,
454 Mansfield and Cartwright (2001) showed that faults grow via cycles of overlap, relay
455 formation, breaching and linkage between neighbouring segments across a wide
456 range of scales. During the evolution of a system, the merging of neighbour faults,
457 mostly along the strike, results in the formation of major faults, which are associated
458 with the majority of displacement. These major faults are surrounded by minor faults,
459 which are associated with lower degrees of displacement. To highlight the spatial
460 patterns of major and minor faults, Figures 7a and 7b present diagrams from the
461 Mansfield and Cartwright (2001) experiment in two different stages: the approximate
462 midpoint of the sequence and the end of the sequence. Numerical modelling
463 performed by Cowie et al. (1993) yielded similar evolutionary features for major and
464 minor faults. The numerical fault simulation of Cowie et al. (1993) was able to
465 reproduce the development of a normal fault system from the early nucleation stage,
466 including interactions with adjacent faults, to full linkage and the formation of a large
467 through fault. The model also captures the increase in the displacement rate of a
468 large linked fault. In Figures 7c and 7d, we focus on two stages of the simulation
469 (from Cowie et al., 1993): the stage in which the fault segments have formed and
470 some have become linked and the final stage of the simulation.

471 Notably, the spatial distributions of major and minor faults are very similar in the
472 experiments of both Mansfield and Cartwright (2001) and Cowie et al. (1993), as
473 shown in Figures 7a-d. Developments during the early stage of major fault formation
474 appear to control the location and evolution of future faults, with some areas where
475 no major faults develop. The long-term evolution of a fault system is the
476 consequence of the progressive cumulative effects of the slip history, i.e.,
477 earthquake occurrence, of each fault. Large earthquakes are generally thought to
478 produce static and dynamic stress changes in the surrounding areas (King et al.,
479 1994; Stein, 1999; Pace et al., 2014; Verdecchia and Carena, 2016). Static stress
480 changes produce areas of negative stress, also known as shadow zones, and
481 positive stress zones. The spatial distributions of decreases (unloading) and
482 increases (loading) in stress during the long-term slip history of faults likely influence
483 the distance across strike between major faults. Thus, given a known major active
484 fault geometrically capable of hosting a $M_w \geq 5.5$ earthquake, the possibility that a
485 future $M_w \geq 5.5$ earthquake will occur in the vicinity of the fault, but is not caused by
486 that fault, should decrease as the distance from the fault decreases. Conversely,
487 earthquakes with magnitudes lower than 5.5 and those due to slip along minor faults
488 are likely to occur everywhere within a fault system, including in proximity to a major
489 fault.

490 In Figure 7e, we illustrate the results of the analogue and numerical modelling of
491 fault system evolution and indicate the areas around major faults where it is unlikely
492 that other major faults develop. In Figure 7f, we show the next step in moving from
493 geologic and structural considerations. In this step, we combine fault sources and
494 distributed seismicity source inputs, which serve as inputs for the PSH model. Fault
495 sources are used to model major faults and are represented by a master fault (i.e.,
496 one or more major faults) and its projection at the surface. Distributed seismicity is
497 used to model seismicity associated with minor, unknown or unmapped faults.
498 Depending on the positions of distributed seismicity points with respect to the buffer
499 zones around major faults, the rates of expected distributed seismicity remain
500 unmodified or decrease and can even reach zero.

501 Specifically, we introduced a slip rate and a distance-weighted linear function based
502 on the above reasoning. The probability of the occurrence of an earthquake (P_e) with
503 a M_w greater than or equal to the minimum magnitude of the fault is as follows:

$$Pe = \begin{cases} 0, & d \leq 1 \text{ km} \\ d/d_{max}, & 1 \text{ km} < d \leq d_{max} \\ 1, & d > d_{max} \end{cases} \quad (6)$$

505 where d is the Joyner-Boore distance from a fault source. The maximum value of d
506 (d_{max}) is controlled by the slip rate of the fault. For faults with slip rates ≥ 1 mm/yr, we
507 assume $d_{max} = L/2$ (L is the length along the strike, Fig. 2a); for faults with slip rates
508 of 0.3 - 1 mm/yr, $d_{max} = L/3$; and for faults with slip rates of ≤ 0.3 mm/yr, $d_{max} = L/4$.
509 The rationale for varying d_{max} is given by a simple assumption: the higher the slip
510 rate is, the larger the deformation field and the higher the value of d_{max} . We applied
511 eq. (6) to the smoothed occurrence rates of the distributed seismogenic sources.
512 Because we consider two fault source inputs, one using only TGR MFD and the
513 other only CHR MFD, and because the MFDs of distributed seismicity grid points in
514 the vicinity of faults are modified with respect to the MFDs of these faults, we obtain
515 two different inputs of distributed seismicity. These two distributed seismogenic
516 source inputs differ because the minimum magnitude of the faults is Mw 5.5 in the
517 TGR model, but this value depends on each fault source dimension in the CHG
518 model, as shown in Figure 8.

519 Our approach allows incompleteness in the fault database to be bypassed, which is
520 advantageous because all fault databases should be considered incomplete. In our
521 approach, the seismicity is modified only in the vicinity of mapped faults. The
522 remaining areas are fully described by the *distributed* input. With this approach, we
523 do not define areas with reliable fault information, and the locations of currently
524 unknown faults can be easily included when they are discovered in the future.

525 **3. Results and Discussion**

526 To obtain PSH maps, we assign the calculated seismicity rates, based on the
527 Poisson hypothesis, to their pertinent geometries, i.e., individual 3D seismogenic
528 sources for the *fault input* and point sources for the *distributed input* (Fig. 8). All the
529 computations are performed using the OpenQuake Engine (Global Earthquake
530 Model, 2016) with a grid spacing of 0.05° in both latitude and longitude. We used this
531 software because it is open source software developed recently by GEM with the
532 purpose of providing seismic hazard and risk assessments. Moreover, it is widely
533 recognized within the scientific community for its potential. The ground motion

534 prediction equations (GMPE) of Akkar et al. (2013), Chiou et al., (2008), Faccioli et
535 al., (2010) and Zhao et al., (2006) are used, as suggested by the SHARE European
536 project (Woessner et al., 2015). In addition, we used the GMPE proposed by Bindi et
537 al. (2014) and calibrated using Italian data. We combined all GMPEs into a logic tree
538 with the same weight of 0.2 for each branch. The distance used for each GMPE was
539 the Joyner and Boore distance for Akkar et al. (2013), Bindi et al. (2014) and Chiou
540 et al. (2008) and the closest rupture distance for Faccioli et al. (2010) and Zhao et al.
541 (2006).

542 The results of the fault source inputs, distributed source inputs, and aggregated
543 model are expressed in terms of peak ground acceleration (PGA) based on
544 exceedance probabilities of 10% and 2% over 50 years, corresponding to return
545 periods of 475 and 2,475 years, respectively (Fig. 9).

546 To explore the epistemic uncertainty associated with the distribution of activity rates
547 over the range of magnitudes of fault source inputs, we compared the seismic
548 hazard levels obtained based on the TGR and CHG fault source inputs (left column
549 in Fig. 9) using the TGR and CHG MFDs for all the fault sources (details in section
550 2.1.3). Although both models have the same seismic moment release, the different
551 MFDs generate clear differences. In fact, in the *TGR* model, all faults contribute
552 significantly to the seismic hazard level, whereas in the *CHG* model, only a few faults
553 located in the central Apennines and Calabria contribute to the seismic hazard level.
554 This difference is due to the different shapes of the MFDs in the two models (Fig.
555 2c). As shown in Figure 8, the percentage of earthquakes with magnitudes between
556 5.5 and approximately 6, which are likely the main contributors to these levels of
557 seismic hazards, is generally higher in the *TGR* model than in the *CHG* model. At a
558 2% probability of exceedance in 50 years, all fault sources in the CHG contribute to
559 the seismic hazard level, but the absolute values are still generally higher in the *TGR*
560 model.

561 The *distributed input* (middle column in Fig. 9) depicts a more uniform shape of the
562 seismic hazard level than that of fault source inputs. A low PGA value of 0.125 g at a
563 10% probability of exceedance over 50 years and a low value of 0.225 g at a 2%
564 probability of exceedance over 50 years encompass a large part of peninsular Italy

565 and Sicily. Two areas with high seismic hazard levels are located in the central
566 Apennines and northeastern Sicily.

567 The overall model, which was created by combining the fault and distributed source
568 inputs, is shown in the right column of Figure 9. Areas with comparatively high
569 seismic hazard levels, i.e., hazard levels greater than 0.225 g and greater than 0.45
570 g at 50-yr exceedance probabilities of 10% and 2%, respectively, are located
571 throughout the Apennines, in Calabria and in Sicily. The fault source inputs
572 contribute most to the total seismic hazard levels in the Apennines, Calabria and
573 eastern Sicily, where the highest PGA values are observed.

574 Figure 10 shows the contributions to the total seismic hazard level by the *fault* and
575 *distributed* source inputs at a specific site (L'Aquila, 42.400-13.400). Notably, in
576 Figure 10, *distributed* sources dominate the seismic hazard contribution at
577 exceedance probabilities greater than ~81% over 50 years, but the contribution of
578 *fault* sources cannot be neglected. Conversely, at exceedance probabilities of less
579 than ~10% in 50 years, the total hazard level is mainly associated with *fault* source
580 inputs.

581 Figure 11 presents seismic hazard maps for PGAs at 10% and 2% exceedance
582 probabilities in 50 years for *fault* sources, *distributed* sources and a combination of
583 the two. These data were obtained using the above-described *Mixed* model, in which
584 we selected the most "appropriate" MFD model (TGR or CHG) for each fault (as
585 shown in Figure 3). The results of this model therefore have values between those of
586 the two end-members shown in Figure 9.

587 Figure 12 shows the *CHG*, *TGR* and *Mixed* model hazard curves of three sites
588 (Cesena, L'Aquila and Crotone, Fig. 13c). As previously noted, the results of the
589 *Mixed* model, due to the structure of the model, are between those of the *CHG* and
590 *TGR* models. The relative positions of the hazard curves derived from the two end-
591 member models and the *Mixed* model depend on the number of nearby fault sources
592 that have been modelled using one of the MFD models and on the distance of the
593 site from the faults. For example, in the case of the Crotone site, the majority of the
594 fault sources in the *Mixed* model are modelled using the CHG MFD. Thus, the
595 resulting hazard curve is similar to that of the *CHG* model. For the Cesena site, the

596 three hazard curves overlap. Because the distance between Cesena and the closest
597 fault sources is approximately 60 km, the impact of the fault input is less than the
598 impact of the *distributed* source input. In this case, the choice of a particular MFD
599 model has a limited impact on the modelling of *distributed* sources. Notably, for an
600 annual frequency of exceedance (*AFOE*) lower than 10^{-4} , the *TGR fault* source input
601 values are generally higher than those of the *CHG* source input, and the three
602 models converge at $AFOE < 10^{-4}$. The resulting seismic hazard estimates depend on
603 the assumed MFD model (*TGR* vs. *CHG*), especially for intermediate-magnitude
604 events (5.5 to ~6.5). Because we assume that the maximum magnitude is imposed
605 by the fault geometry and that the seismic moment release is controlled by the slip
606 rate, the *TGR* model leads to the highest hazard values because this range of
607 magnitude contributes the most to the hazard level.

608 In Figure 13, we investigated the influences of the Mixed *fault* source inputs and the
609 Mixed *distributed* source inputs on the total hazard level of the entire study area, as
610 well as the variability in the hazard results. The maps in Figure 13a show that the
611 contribution of *fault* inputs to the total hazard level generally decreases as the
612 exceedance probability increases from 2% to 81% in 50 years. At a 2% probability of
613 exceedance in 50 years, the total hazard levels in the Apennines and eastern Sicily
614 are mainly related to faults, whereas at an 81% probability of exceedance in 50
615 years, the contributions of *fault* inputs are high in local areas of central Italy and
616 southern Calabria.

617 Moreover, we examined the contributions of *fault* and *distributed* sources along three
618 E-W-oriented profiles in northern, central and southern Italy (Fig. 13b). Note that the
619 contributions are not based on deaggregation but are computed according to the
620 percentage of each source input in the *AFOE* value of the combined model. In areas
621 with faults, the hazard level estimated by *fault* inputs is generally higher than that
622 estimated by the corresponding *distributed* source inputs. Notable exceptions are
623 present in areas proximal to slow-slipping active faults at an 81% probability of
624 exceedance in 50 years (profile A), such as those at the eastern and western
625 boundaries of the fault area in central Italy (profile B), and in areas where the
626 contribution of the *distributed* source input is equal to that of the *fault* input at a 10%
627 probability of exceedance in 50 years (eastern part of profile C).

628 The features depicted by the three profiles result from a combination of the slip rates
629 and spatial distributions of faults for *fault* source inputs. This pattern should be
630 considered a critical aspect of using fault models for PSH analysis. In fact, the
631 proposed approach requires a high level of expertise in active tectonics and cautious
632 expert judgement at many levels in the procedure. First, the seismic hazard estimate
633 is based on the definition of a segmentation model, which requires a series of rules
634 based on observations and empirical regression between earthquakes and the size
635 of the causative fault. New data might make it necessary to revise the rules or
636 reconsider the role of the segmentation. In some cases, expert judgement could
637 permit discrimination among different fault source models. Alternatively, all models
638 should be considered branches in a logic tree approach.

639 Moreover, we propose a fault seismicity input in which the MFD of each fault source
640 has been chosen based on an analysis of the occurrences of earthquakes that can
641 be tentatively or confidently assigned to a certain fault. To describe the fault activity,
642 we applied a probability density function to the magnitude, as commonly performed
643 in the literature: the TGR model, where the maximum magnitude is the upper
644 threshold and $M_w = 5.5$ is the lower threshold for all faults, and the characteristic
645 maximum magnitude model, which consists of a truncated normal distribution
646 centred on the maximum magnitude. Other MFDs have been proposed to model the
647 earthquake recurrence of a fault. For example, Youngs and Coppersmith (1985)
648 proposed a modification to the truncated exponential model to allow for the
649 increased likelihood of characteristic events. However, we focused only on two
650 models, as we believe that instead of a “blind” or qualitative characterization of the
651 MFD of a fault source, future applications of statistical tests of the compatibility
652 between expected earthquake rates and observed historical seismicity could be used
653 as an objective method of identifying the optimal MFD of expected seismicity.

654 To focus on the general procedure for spatially integrating faults with sources
655 representing distributed (or off-fault) seismicity, we did not investigate the impact of
656 other smoothing procedures on the distributed sources, and we used fixed kernels
657 with a constant bandwidth (as in the works of Kagan and Jackson, 1994; Frankel et
658 al. 1997; Zechar and Jordan, 2010). The testing of adaptive bandwidths (e.g., Stock

659 and Smith, 2002; Helmstetter et al., 2006, 2007; Werner et al., 2011) or weighted
660 combinations of both models has been reserved for future studies.

661

662 Finally, we compared, as shown in Figure 14, the 2013 European Seismic Hazard
663 Model (ESHM13) developed within the SHARE project, the current Italian national
664 seismic hazard map (MPS04) and the results of our model (Mixed model) using the
665 same GMPEs as used in this study. Specifically, for ESHM13, we compared the
666 results to the fault-based hazard map (FSBG model) that accounts for fault sources
667 and background seismicity. The figure shows how the impact of our fault sources is
668 more evident than in FSBG-ESHM13, and the comparison with MPS04 confirms a
669 similar pattern, but with some significant differences at the regional to local scales.

670

671 The strength of our approach lies in the integration of different levels of information
672 regarding the active faults in Italy, but the final result is unavoidably linked to the
673 quality of the relevant data. Our work focused on presenting and applying a new
674 approach for evaluating seismic hazards based on active faults and intentionally
675 avoided the introduction of uncertainties due to the use of different segmentation
676 rules or other slip rate values of faults. Moreover, the impact of ground motion
677 predictive models is important in seismic hazard assessment but beyond the scope
678 of this work. Future steps will be devoted to analysing these uncertainties and
679 evaluating their impacts on seismic hazard estimates.

680

681 **4. Conclusions**

682 We presented our first national-scale PSH model of Italy, which summarizes and
683 integrates the fault-based PSH models developed since the publication of Pace et al.
684 in 2006.

685 The model proposed in this study combines fault source inputs based on over 110
686 faults grouped into 86 fault sources and distributed source inputs. For each fault
687 source, the maximum magnitude and its uncertainty were derived by applying
688 scaling relationships, and the rates of seismic activity were derived by applying slip
689 rates to seismic moment evaluations and balancing these seismic moments using
690 two MFD models.

691 To account for unknown faults, a distributed seismicity input was applied following
692 the well-known Frankel (1995) methodology to calculate seismicity parameters.

693 The fault sources and distributed sources have been integrated via a new approach
694 based on the idea that deformation in the vicinity of an active fault is concentrated
695 along the fault and that the seismic activity in the surrounding region is reduced. In
696 particular, a distance-dependent linear weighting function has been introduced to
697 allow the contribution of distributed sources (in the magnitude range overlapping the
698 MFD of each fault source) to linearly decrease from 1 to 0 with decreasing distance
699 from a fault. The strength of our approach lies in the ability to integrate different
700 levels of available information for active faults that actually exist in Italy (or
701 elsewhere), but the final result is unavoidably linked to the quality of the relevant
702 data.

703 The PSH maps produced using our model show a hazard pattern similar to that of
704 the current maps at the national scale, but some significant differences in hazard
705 level are present at the regional to local scales (Figure 13).

706 Moreover, the impact that using different MFD models to derive seismic activity rates
707 has on the hazard maps was investigated. The PGA values in the hazard maps
708 generated by the *TGR* model are higher than those in the hazard maps generated by
709 the *CHG* model. This difference is because the rates of earthquakes with
710 magnitudes from 5.5 to approximately 6 are generally higher in the *TGR* model than
711 in the *CHG* model. Moreover, the relative contributions of fault source inputs and
712 distributed source inputs have been identified in maps and profiles in three sectors of
713 the study area. These profiles show that the hazard level is generally higher where
714 fault inputs are used, and for high probabilities of exceedance, the contribution of
715 *distributed* inputs equals that of *fault* inputs.

716 Finally, the *Mixed* model was created by selecting the most appropriate MFD model
717 for each fault. All data, including the locations and parameters of fault sources, are
718 provided in the supplemental files of this paper.

719 This new PSH model is not intended to replace, integrate or assess the current
720 official national seismic hazard model of Italy. While some aspects remain to be
721 implemented in our approach (e.g., the integration of reverse/thrust faults in the
722 database, sensitivity tests for the distance-dependent linear weighting function
723 parameters, sensitivity tests for potential different segmentation models, and fault
724 source inputs that account for fault interactions), the proposed model represents

725 advancements in terms of input data (quantity and quality) and methodology based
726 on a decade of research in the field of fault-based approaches to regional seismic
727 hazard modelling.

728

729

730

731

732

733

734

735 **References**

736

737

738 Akinci, A., Galadini, F., Pantosti, D., Petersen, M., Malagnini, L., and Perkins, D.:
739 Effect of Time Dependence on Probabilistic Seismic-Hazard Maps and
740 Deaggregation for the Central Apennines, Italy, *B Seismol Soc Am*, 99, 585-
741 610, 2009.

742 Akkar, S., Sandikkaya, M.A. , Bommer, J.J.: Empirical Ground-Motion Models for
743 Point and Extended-Source Crustal Earthquake Scenarios in Europe and the
744 Middle East, *Bulletin of Earthquake Engineering*, ISSN:1570-761X, 2013.

745 Basili, R., Valensise, G., Vannoli, P., Burrato, P., Fracassi, U., Mariano, S., Tiberti,
746 M. M. and Boschi, E.: The Database of Individual Seismogenic Sources
747 (DISS), version 3: Summarizing 20 years of research on Italy's earthquake
748 geology, *Tectonophysics*, 453, 20- 43, 2008.

749 Benedetti, L., Manighetti, I., Gaudemer, Y., Finkel, R., Malavieille, J., Pou, K., Arnold,
750 M., Aumaitre, G., Bourles, D., and Keddadouche, K.: Earthquake synchrony
751 and clustering on Fucino faults (Central Italy) as revealed from in situ Cl-36
752 exposure dating, *J Geophys Res-Sol Ea*, 118, 4948-4974, 2013.

753 Bindi, D., Massa, M., Luzi, L., Ameri, G., Pacor, F., Puglia, R., and Augliera, P.: Pan-
754 European ground-motion prediction equations for the average horizontal
755 component of PGA, PGV, and 5%-damped PSA at spectral periods up to 3.0
756 s using the RESORCE dataset (vol 12, pg 391, 2014), *B Earthq Eng*, 12, 431-
757 448, 2014.

758 Boncio, P., Brozzetti, F. and Lavecchia G.: Architecture and seismotectonics of a
759 regional Low-Angle Normal Fault zone in Central Italy. *Tectonics*, 19 (6),
760 1038-1055, 2000.

761 Boncio, P., Lavecchia, G., and Pace, B.: Defining a model of 3D seismogenic
762 sources for Seismic Hazard Assessment applications: The case of central
763 Apennines (Italy), *J Seismol*, 8, 407-425, 2004.

764 Boncio, P., Pizzi, A., Cavuoto, G., Mancini, M., Piacentini, T., Miccadei, E., Cavinato,
765 G. P., Piscitelli, S., Giocoli, A., Ferretti, G., De Ferrari, R., Gallipoli, M. R.,
766 Mucciarelli, M., Di Fiore, V., Franceschini, A., Pergalani, F., Naso, G., and
767 Macroarea, W. G.: Geological and geophysical characterisation of the
768 Paganica - San Gregorio area after the April 6, 2009 L'Aquila earthquake (M-
769 w 6.3, central Italy): implications for site response, *B Geofis Teor Appl*, 52,
770 491-512, 2011.

771 Bull, J. M., Barnes, P. M., Lamarche, G., Sanderson, D. J., Cowie, P. A., Taylor, S.
772 K., and Dix, J. K.: High-resolution record of displacement accumulation on an
773 active normal fault: implications for models of slip accumulation during
774 repeated earthquakes, *J Struct Geol*, 28, 1146-1166, 2006.

775 Chiou, B. S. J. and Youngs, R. R.: An NGA model for the average horizontal
776 component of peak ground motion and response spectra, *Earthq Spectra*, 24,
777 173-215, 2008.

778 Cornell, C.A.: Engineering seismic risk analysis, *Bull. Seism. Soc. Am.*, 58,1583-
779 1606, 1968.

780 Cowie, P. A.: A healing-reloading feedback control on the growth rate of seismogenic
781 faults, *J Struct Geol*, 20, 1075-1087, 1998.

782 Cowie, P. A., Roberts, G. P., Bull, J. M., and Visini, F.: Relationships between fault
783 geometry, slip rate variability and earthquake recurrence in extensional
784 settings, *Geophys J Int*, 189, 143-160, 2012.

785 Cowie, P. A., Underhill, J. R., Behn, M. D., Lin, J., and Gill, C. E.: Spatio-temporal
786 evolution of strain accumulation derived from multi-scale observations of Late
787 Jurassic rifting in the northern North Sea: A critical test of models for
788 lithospheric extension, *Earth Planet Sc Lett*, 234, 401-419, 2005.

789 Cowie, P. A., Vanneste, C., and Sornette, D.: Statistical Physics Model for the
790 Spatiotemporal Evolution of Faults, *J Geophys Res-Sol Ea*, 98, 21809-21821,
791 1993.

792 D'amato, D., Pace, B., Di Nicola, L., Stuart, F.M., Visini, F., Azzaro, R., Branca, S.,
793 and Barfod, D.N.: Holocene slip rate variability along the Pernicana fault
794 system (Mt. Etna, Italy): Evidence from offset lava flows: *GSA Bulletin*,
795 doi:10.1130/B31510.1, 2016.

796 Faccioli, E., Bianchini, A., and Villani, M.: New ground motion prediction equations
797 for $t > 1$ s and their influence on seismic hazard assessment, In: *Proceedings*
798 *of the University of Tokyo symposium on long-period ground motion and*
799 *urban disaster mitigation*, 2010.

800 Ferranti, L., Palano, M., Cannavo, F., Mazzella, M. E., Oldow, J. S., Gueguen, E.,
801 Mattia, M., and Monaco, C.: Rates of geodetic deformation across active
802 faults in southern Italy, *Tectonophysics*, 621, 101-122, 2014.

803 Field, E. H., Biasi, G. P., Bird, P., Dawson, T. E., Felzer, K. R., Jackson, D. D.,
804 Johnson, K. M., Jordan, T. H., Madden, C., Michael, A. J., Milner, K. R., Page,
805 M. T., Parsons, T., Powers, P. M., Shaw, B. E., Thatcher, W. R., Weldon, R.
806 J., and Zeng, Y. H.: Long-Term Time-Dependent Probabilities for the Third
807 Uniform California Earthquake Rupture Forecast (UCERF3), *B Seismol Soc*
808 *Am*, 105, 511-543, 2015.

809 Field, E. H., Jackson, D. D., and Dolan, J. F.: A mutually consistent seismic-hazard
810 source model for southern California, *B Seismol Soc Am*, 89, 559-578, 1999.

811 Finnegan, N. J., Schumer, R., and Finnegan, S.: A signature of transience in bedrock
812 river incision rates over timescales of $10(4)$ - $10(7)$ years, *Nature*, 505, 391-+,
813 2014.

814 Frankel, A.: Simulating Strong Motions of Large Earthquakes Using Recordings of
815 Small Earthquakes - the Loma-Prieta Mainshock as a Test-Case, *B Seismol*
816 *Soc Am*, 85, 1144-1160, 1995.

817 Frankel, A., Mueller, C., Barnhard, T., Perkins, D., Leyendecker, E. V., Dickman, N.,
818 Hanson, S., and Hopper, M.: Seismic-hazard maps for California, Nevada,
819 and Western Arizona/Utah', *U.S. Geological Survey Open-File Rept.* 97-130,
820 1997.

821 Gallen, S. F., Pazzaglia, F. J., Wegmann, K. W., Pederson, J. L., and Gardner, T.
822 W.: The dynamic reference frame of rivers and apparent transience in incision
823 rates, *Geology*, 43, 623-626, 2015.

824 Garcia-Mayordomo, J., Gaspar-Escribano, J. M., and Benito, B.: Seismic hazard
825 assessment of the Province of Murcia (SE Spain): analysis of source
826 contribution to hazard, *J Seismol*, 11, 453-471, 2007.

827 Gardner, J. K., Knopoff, L.: Is the sequence of earthquakes in Southern California,
828 with aftershocks removed, Poissonian?'. *Bulletin of the Seismological Society*
829 *of America*, 64, 1363-1367, 1974.

830 Gardner, T. W., Jorgensen, D. W., Shuman, C., and Lemieux, C. R.: Geomorphic
831 and Tectonic Process Rates - Effects of Measured Time Interval, *Geology*, 15,
832 259-261, 1987.

833 Gasperini P., Bernardini F., Valensise G. and Boschi E.: Defining Seismogenic
834 Sources from Historical Earthquake Felt Reports, *Bull. Seism. Soc. Am.*, 89,
835 94-110, 1999.

836 GEM: The OpenQuake-engine User Manual. Global Earthquake Model (GEM)
837 Technical Report, doi: 10.13117/GEM.OPENQUAKE.MAN.ENGINE.1.9/01,
838 189 pages, 2016.

839 Gunderson, K. L., Anastasio, D. J., Pazzaglia, F. J., and Picotti, V.: Fault slip rate
840 variability on 10(4)-10(5)yr timescales for the Salsomaggiore blind thrust fault,
841 Northern Apennines, Italy, *Tectonophysics*, 608, 356-365, 2013.

842 Hanks, T. C., and Kanamori, H.: A moment magnitude scale, *Journal of Geophysics*
843 *Research*, 84, 2348–2350, 1979.

844 Helmstetter, A., Kagan, Y. Y., and Jackson, D. D.: Comparison of short-term and
845 time-independent earthquake forecast models for southern California, *B*
846 *Seismol Soc Am*, 96, 90-106, 2006.

847 Helmstetter, A., Kagan, Y. Y., and Jackson, D. D.: High-resolution time-independent
848 grid-based forecast for $M \leq 5$ earthquakes in California, *Seismol Res Lett*,
849 78, 78-86, 2007.

850 International Association of Seismology and Physics of the Earth's Interior (IASPEI):
851 Summary of Magnitude Working Group recommendations on standard
852 procedures for determining earthquake magnitudes from digital data,
853 <http://www.iaspei.org/>

854 commissions/CSOI/summary_of_WG_recommendations_2005.pdf (last
855 accessed December 2015), 2005.

856 Kagan, Y. Y.: Seismic moment distribution revisited: I. Statistical results, *Geophys J*
857 *Int*, 148, 520-541, 2002.

858 Kagan, Y., and Knopoff, L.: Earthquake risk prediction as a stochastic process,
859 *Physics of the Earth and Planetary Interiors*, 14, 97–108, 1977.

860 Kagan, Y. Y. and Jackson, D. D.: Long-Term Probabilistic Forecasting of
861 Earthquakes, *J Geophys Res-Sol Ea*, 99, 13685-13700, 1994.

862 Kamer, Y. and Hiemer, S.: Data-driven spatial b value estimation with applications to
863 California seismicity: To b or not to b, *J Geophys Res-Sol Ea*, 120, 5191-
864 5214, 2015.

865 King, G. C. P., Stein, R. S., and Lin, J.: Static Stress Changes and the Triggering of
866 Earthquakes, *B Seismol Soc Am*, 84, 935-953, 1994.

867 Kostrov, V. V.: Seismic moment and energy of earthquakes, and seismic flow of
868 rock, *Physic of the Solid Earth*, 1, 23-44, 1974.

869 Leonard, M.: Earthquake fault scaling: Self-consistent relating of rupture length,
870 width, average displacement, and moment release. *Bulletin of the*
871 *Seismological Society of America*, 100(5A), 1971- 1988, 2010.

872 Machette, M.N.: Active, capable, and potentially active faults; a paleoseismic
873 perspective, *J. Geodyn.*, 29, 387–392, 2000.

874 Main, I.: Statistical physics, seismogenesis, and seismic hazard, *Rev Geophys*, 34,
875 433-462, 1996.

876 Mansfield, C. and Cartwright, J.: Fault growth by linkage: observations and
877 implications from analogue models, *J Struct Geol*, 23, 745-763, 2001.

878 Meletti, C., Visini, F., D'Amico, V., and Rovida A.: Seismic hazard in central Italy and
879 the 2016 Amatrice earthquake, *Annals of Geophysics*, 59, doi:10.4401/ag-
880 7248, 2016.

881 McClymont, A. F., Villamor, P., and Green, A. G.: Assessing the contribution of off-
882 fault deformation to slip-rate estimates within the Taupo Rift, New Zealand,
883 using 3-D ground-penetrating radar surveying and trenching, *Terra Nova*, 21,
884 446-451, 2009a.

885 McClymont, A. F., Villamor, P., and Green, A. G.: Fault displacement accumulation
886 and slip rate variability within the Taupo Rift (New Zealand) based on trench
887 and 3-D ground-penetrating radar data, *Tectonics*, 28, 2009b.

888 Nicol, A., Walsh, J., Berryman, K., and Villamor, P.: Interdependence of fault
889 displacement rates and paleoearthquakes in an active rift, *Geology*, 34, 865-
890 868, 2006.

891 Nicol, A., Walsh, J., Mouslopoulou, V., and Villamor, P.: Earthquake histories and
892 Holocene acceleration of fault displacement rates, *Geology*, 37, 911-914,
893 2009.

894 Nicol, A., Walsh, J. J., Villamor, P., Seebeck, H., and Berryman, K. R.: Normal fault
895 interactions, paleoearthquakes and growth in an active rift, *J Struct Geol*, 32,
896 1101-1113, 2010.

897 Nicol, A., Walsh, J. J., Watterson, J., and Underhill, J. R.: Displacement rates of
898 normal faults, *Nature*, 390, 157-159, 1997.

899 Ordaz, M. and Reyes, C.: Earthquake hazard in Mexico City: Observations versus
900 computations, *B Seismol Soc Am*, 89, 1379-1383, 1999.

901 Pace, B., Bocchini, G. M., and Boncio, P.: Do static stress changes of a moderate-
902 magnitude earthquake significantly modify the regional seismic hazard? Hints
903 from the L'Aquila 2009 normal-faulting earthquake (Mw 6.3, central Italy),
904 *Terra Nova*, 26, 430-439, 2014.

905 Pace, B., Peruzza, L., Lavecchia, G., and Boncio, P.: Layered seismogenic source
906 model and probabilistic seismic-hazard analyses in central Italy, *B Seismol
907 Soc Am*, 96, 107-132, 2006.

908 Pace, B., Visini, F., and Peruzza, L.: FiSH: MATLAB Tools to Turn Fault Data into
909 Seismic-Hazard Models, *Seismol Res Lett*, 87, 374-386, 2016.

910 Peruzza, L., and Pace B.: Sensitivity analysis for seismic source characteristics to
911 probabilistic seismic hazard assessment in central Apennines (Abruzzo area),
912 *Bollettino di Geofisica Teorica ed Applicata* 43, 79–100, 2002.

913 Peruzza, L., Pace, B., and Visini, F.: Fault-Based Earthquake Rupture Forecast in
914 Central Italy: Remarks after the L'Aquila M-w 6.3 Event, *B Seismol Soc Am*,
915 101, 404-412, 2011.

916 Peruzza, L., Gee, R., Pace, B., Roberts, G., Scotti, O., Visini, F., Benedetti, L., and
917 Pagani, M.: PSHA after a strong earthquake: hints for the recovery, *Annals of
918 Geophysics*, 59, doi:10.4401/ag-7257, 2016

919 Roberts, G. P., Cowie, P., Papanikolaou, I., and Michetti, A. M.: Fault scaling
920 relationships, deformation rates and seismic hazards: an example from the
921 Lazio-Abruzzo Apennines, central Italy, *J Struct Geol*, 26, 377-398, 2004.

922 Roberts, G. P. and Michetti, A. M.: Spatial and temporal variations in growth rates
923 along active normal fault systems: an example from The Lazio-Abruzzo
924 Apennines, central Italy, *J Struct Geol*, 26, 339-376, 2004.

925 Robinson, R., Nicol, A., Walsh, J. J., and Villamor, P.: Features of earthquake
926 occurrence in a complex normal fault network: Results from a synthetic
927 seismicity model of the Taupo Rift, New Zealand, *J Geophys Res-Sol Ea*, 114,
928 2009.

929 Rovida, A., Locati, M., Camassi, R., Lolli, B., and Gasperini P.: CPTI15, the 2015
930 version of the Parametric Catalogue of Italian Earthquakes. Istituto Nazionale
931 di Geofisica e Vulcanologia. doi:<http://doi.org/10.6092/INGV.IT-CPTI15>, 2016.

932 Scotti, O., Clement, C., and Baumont, D.: Seismic hazard for design and verification
933 of nuclear installations in France: regulatory context, debated issues and
934 ongoing developments, *B Geofis Teor Appl*, 55, 135-148, 2014.

935 Stein, R. S., King, G. C. P., and Lin, J.: Stress Triggering of the 1994 M=6.7
936 Northridge, California, Earthquake by Its Predecessors, *Science*, 265, 1432-
937 1435, 1994.

938 Stirling, M., McVerry, G., Gerstenberger, M., Litchfield, N., Van Dissen, R.,
939 Berryman, K., Barnes, P., Wallace, L., Villamor, P., Langridge, R., Lamarche,
940 G., Nodder, S., Reyners, M., Bradley, B., Rhoades, D., Smith, W., Nicol, A.,
941 Pettinga, J., Clark, K., and Jacobs, K.: National Seismic Hazard Model for
942 New Zealand: 2010 Update, *B Seismol Soc Am*, 102, 1514-1542, 2012.

943 Stock, C. and Smith, E. G. C.: Adaptive kernel estimation and continuous probability
944 representation of historical earthquake catalogs, *B Seismol Soc Am*, 92, 904-
945 912, 2002a.

946 Stock, C. and Smith, E. G. C.: Comparison of seismicity models generated by
947 different kernel estimations, *B Seismol Soc Am*, 92, 913-922, 2002b.

948 Stucchi, M., Meletti, C., Montaldo, V., Crowley, H., Calvi, G. M., and Boschi, E.:
949 Seismic Hazard Assessment (2003-2009) for the Italian Building Code, *B*
950 *Seismol Soc Am*, 101, 1885-1911, 2011.

951 Verdecchia, A. and Carena, S.: Coulomb stress evolution in a diffuse plate boundary:
952 1400 years of earthquakes in eastern California and western Nevada, USA,
953 *Tectonics*, 35, 1793-1811, 2016.

954 Visini, F. and Pace, B.: Insights on a Key Parameter of Earthquake Forecasting, the
955 Coefficient of Variation of the Recurrence Time, Using a Simple Earthquake
956 Simulator, *Seismol Res Lett*, 85, 703-713, 2014.

957 Weichert, D. H: Estimation of the earthquake recurrence parameters for unequal
958 observation periods for different magnitudes, *Bulletin of the Seismological*
959 *Society of America*, 70, 1337-1346, 1980.

960 Wells, D. L. and Coppersmith, K. J.: New Empirical Relationships among Magnitude,
961 Rupture Length, Rupture Width, Rupture Area, and Surface Displacement, *B*
962 *Seismol Soc Am*, 84, 974-1002, 1994.

963 Werner, M. J., Helmstetter, A., Jackson, D. D., Kagan, Y. Y., and Wiemer, S.:
964 Adaptively smoothed seismicity earthquake forecasts for Italy, *Ann Geophys-*
965 *Italy*, 53, 107-116, 2010.

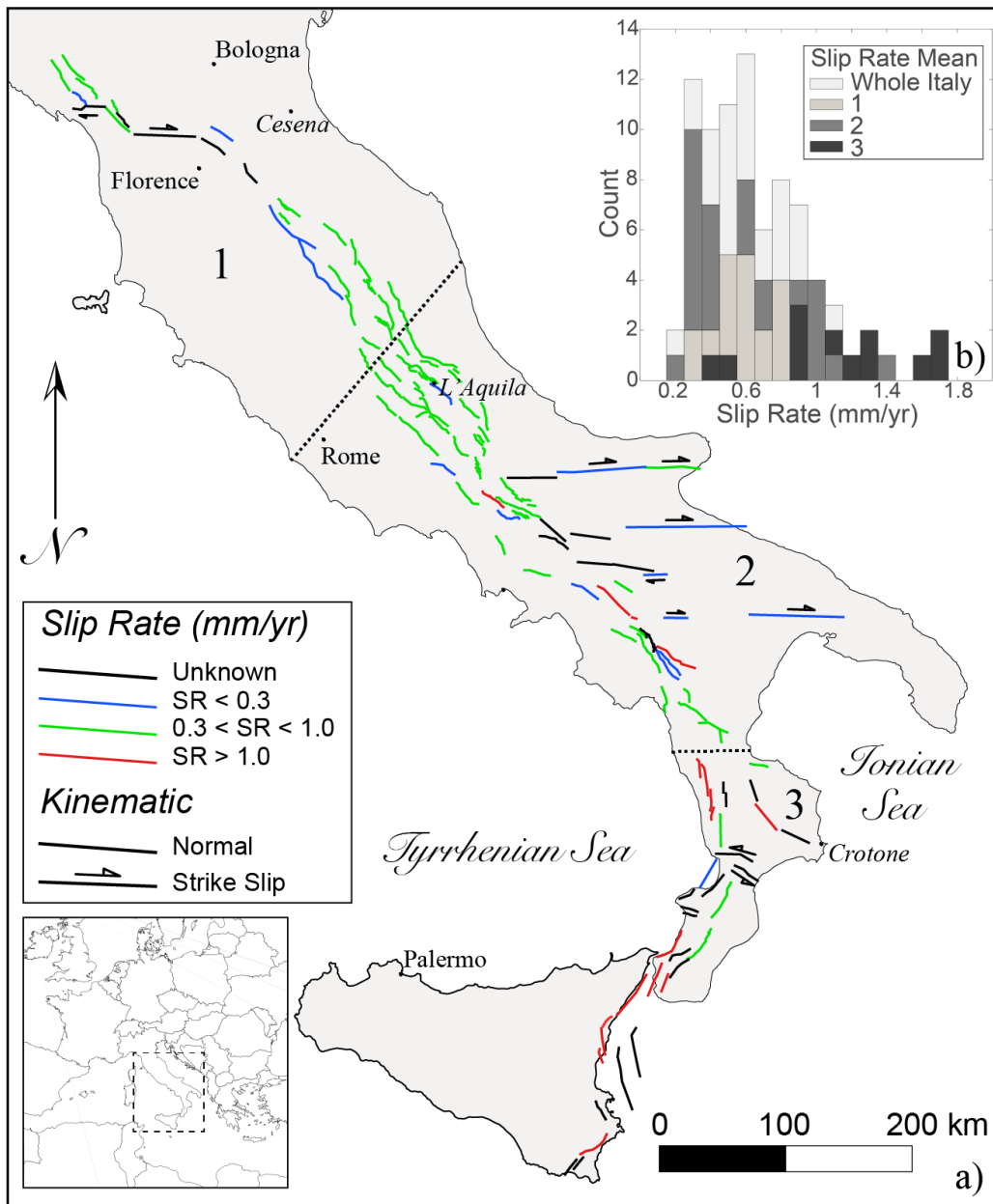
966 Woessner, J., Laurentiu, D., Giardini, D., Crowley, H., Cotton, F., Grunthal, G.,
967 Valensise, G., Arvidsson, R., Basili, R., Demircioglu, M. B., Hiemer, S.,
968 Meletti, C., Musson, R. W., Rovida, A. N., Sesetyan, K., Stucchi, M., and
969 Consortium, S.: The 2013 European Seismic Hazard Model: key components
970 and results, *B Earthq Eng*, 13, 3553-3596, 2015.

971 Youngs, R. R. and Coppersmith, K. J.: Implications of Fault Slip Rates and
972 Earthquake Recurrence Models to Probabilistic Seismic Hazard Estimates, *B*
973 *Seismol Soc Am*, 75, 939-964, 1985.

974 Zechar, J. D. and Jordan, T. H.: Simple smoothed seismicity earthquake forecasts
975 for Italy, *Ann Geophys-Italy*, 53, 99-105, 2010.

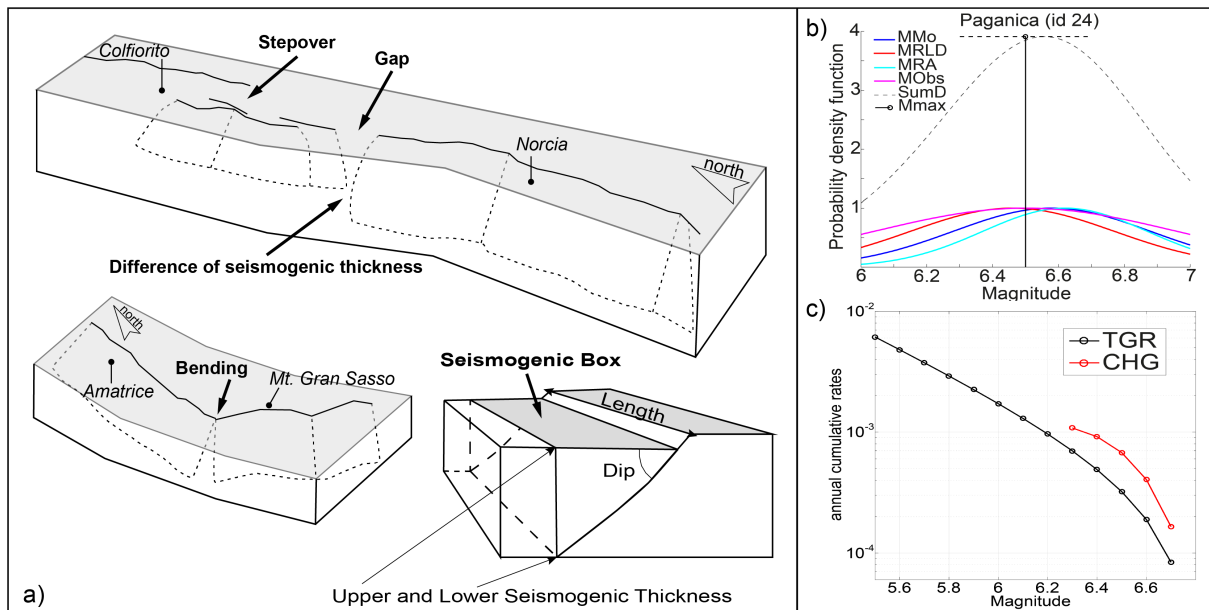
976 Zhao, J. X., Zhang, J., Asano, A., Ohno, Y., Oouchi, T., Takahashi, T., Ogawa, H.,
977 Irikura, K., Thio, H. K., Somerville, P. G., Fukushima, Y., and Fukushima, Y.:
978 Attenuation relations of strong ground motion in Japan using site classification
979 based on predominant period, *B Seismol Soc Am*, 96, 898-913, 2006.

980



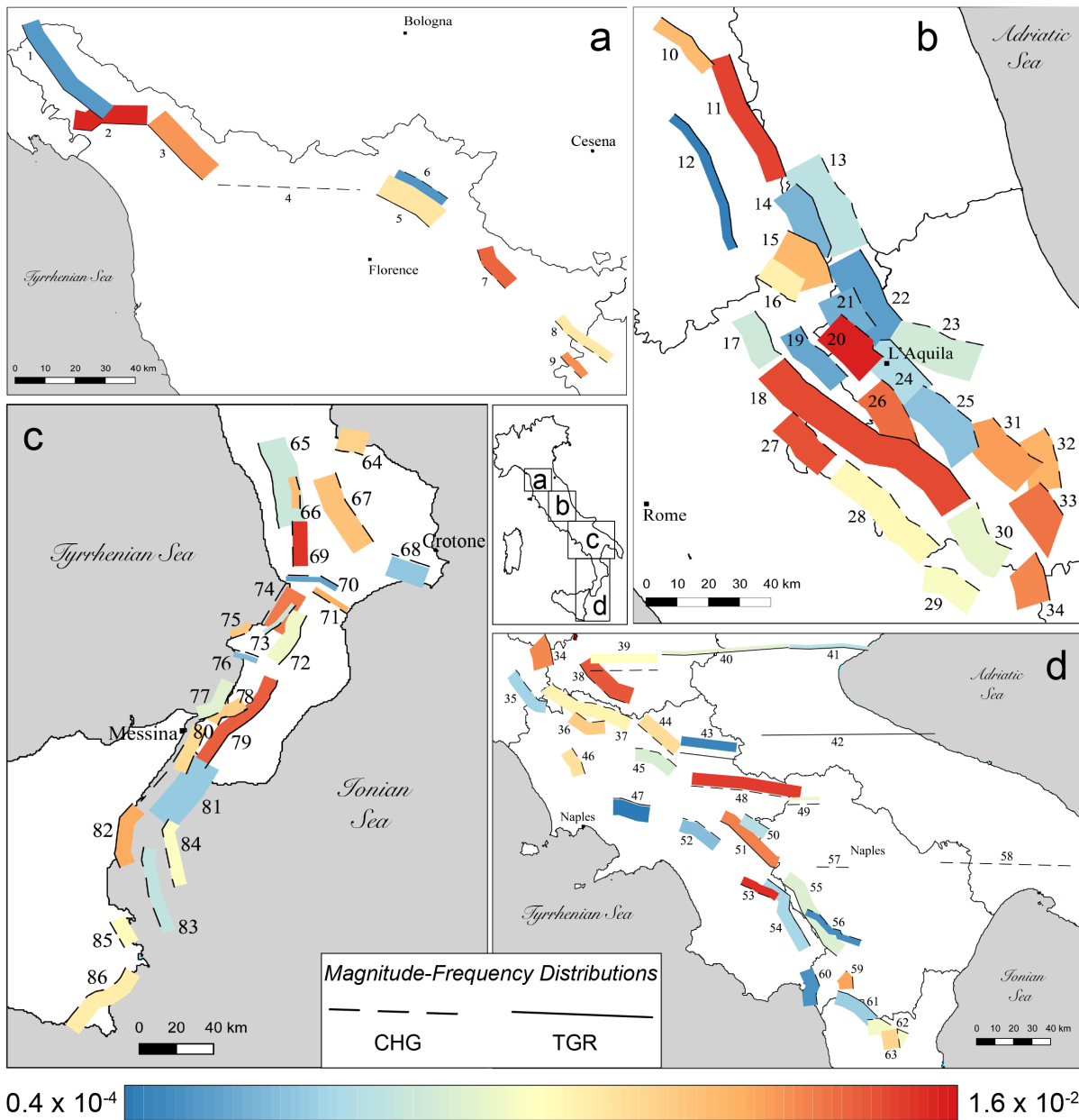
981

982 Fig. 1 a) Map of normal and strike-slip active faults used in this study. The colour
 983 scale indicates the slip rate. b) Histogram of the slip rate distribution in the entire
 984 study area and in three subsectors. The numbers 1, 2 and 3 represent the Northern
 985 Apennines, Central-Southern Apennines and Calabria-Sicilian coast regions,
 986 respectively. The dotted black lines are the boundaries of the regions.



987

988 Fig. 2 a) Conceptual model of active faults and segmentation rules adopted to define
 989 a fault source and its planar projection, forming a seismogenic box [modified from
 990 Boncio et al., 2004]. b) Example of FiSH code output (see Pace et al., 2016 for
 991 details) for the Paganica fault source showing the magnitude estimates from
 992 empirical relationships and observations, both of which are affected by uncertainties.
 993 In this example, four magnitudes are estimated: M_{Mo} (blue line) is from the standard
 994 formula (IASPEI, 2005); M_{RDL} (red line) and M_{RA} (cyan line) correspond to
 995 estimates based on the maximum subsurface fault length and maximum rupture area
 996 from the empirical relationships of Wells and Coppersmith (1994) for length and
 997 area, respectively; and M_{Obs} (magenta line) is the largest observed moment
 998 magnitude. The black dashed line represents the summed probability density curve
 999 (SumD), the vertical black line represents the central value of the Gaussian fit of the
 1000 summed probability density curve (M_{max}), and the horizontal black dashed line
 1001 represents its standard deviation (σ M_{max}). The input values that were used to obtain
 1002 this output are provided in Table 1. c) Comparison of the magnitude–frequency
 1003 distributions of the Paganica source, which were obtained using the CHG model (red
 1004 line) and the TGR model (black line).



0.4 x 10⁻⁴ 1.6 x 10⁻²

Activity Rates (#eq $M \geq 5.5$ in a year)

1005

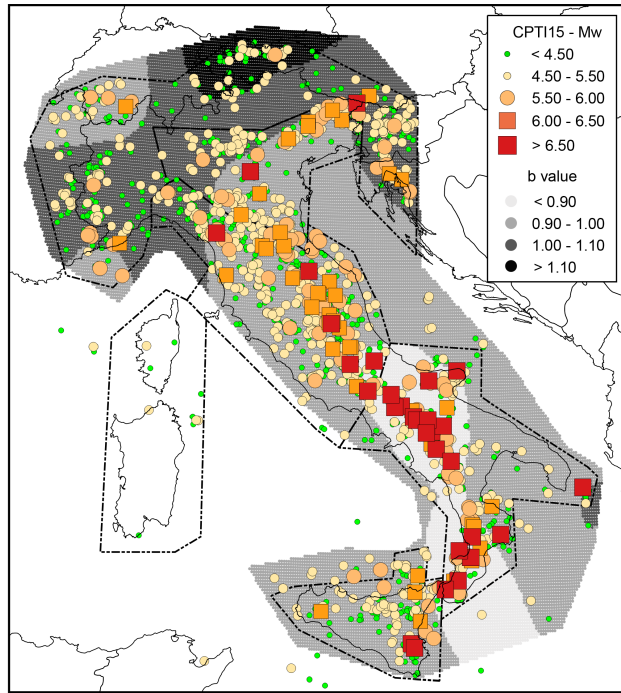
1006

1007

1008

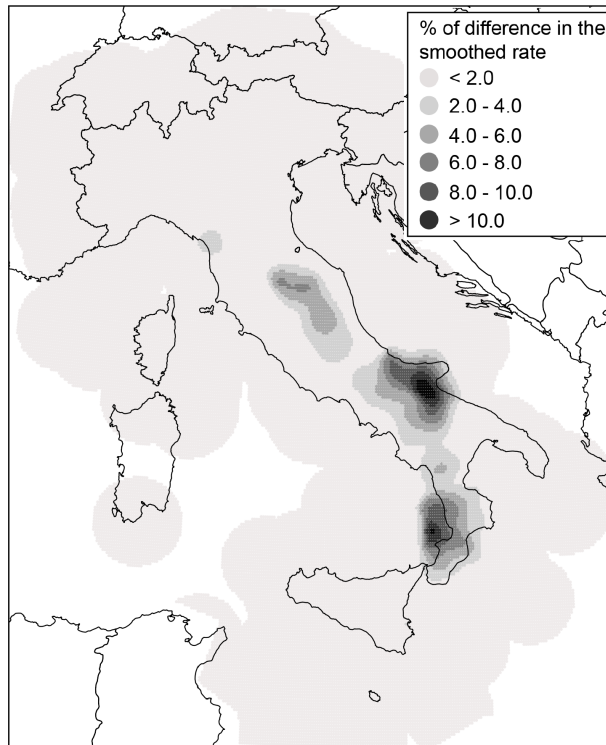
1009

Fig. 3 Maps showing the fault source inputs as seismicogenic boxes (see Fig. 2a). The colour scale indicates the activity rate. Solid and dashed lines (corresponding to the uppermost edge of the fault) are used to highlight our choice between the two end-members of the MFD model adopted in the so-called *Mixed* model.



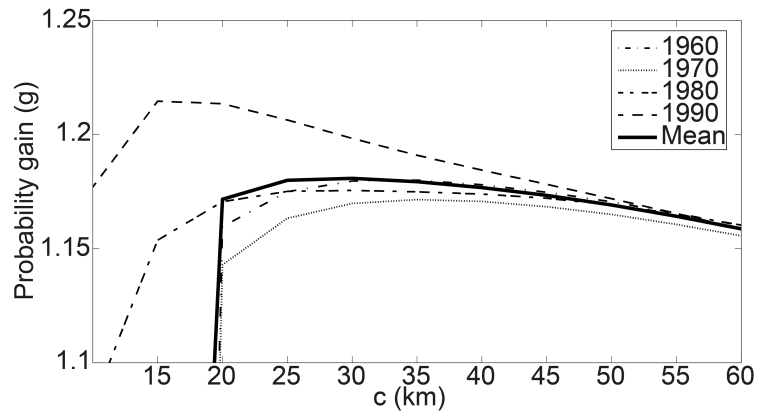
1010

1011 Fig. 4 Historical earthquakes from the most recent version of the historical
 1012 parametric Italian catalogue (CPTI15, Rovida et al., 2016), the spatial variations in b-
 1013 values and the polygons defining the five macroseismic areas used to assess the
 1014 magnitude intervals.



1015

1016 Fig. 5 Differences in percentages between the two smoothed rates produced by eq.
 1017 (2) using the complete catalogue and the modified catalogue without events
 1018 associated with known active faults (*TGR* model)



1019

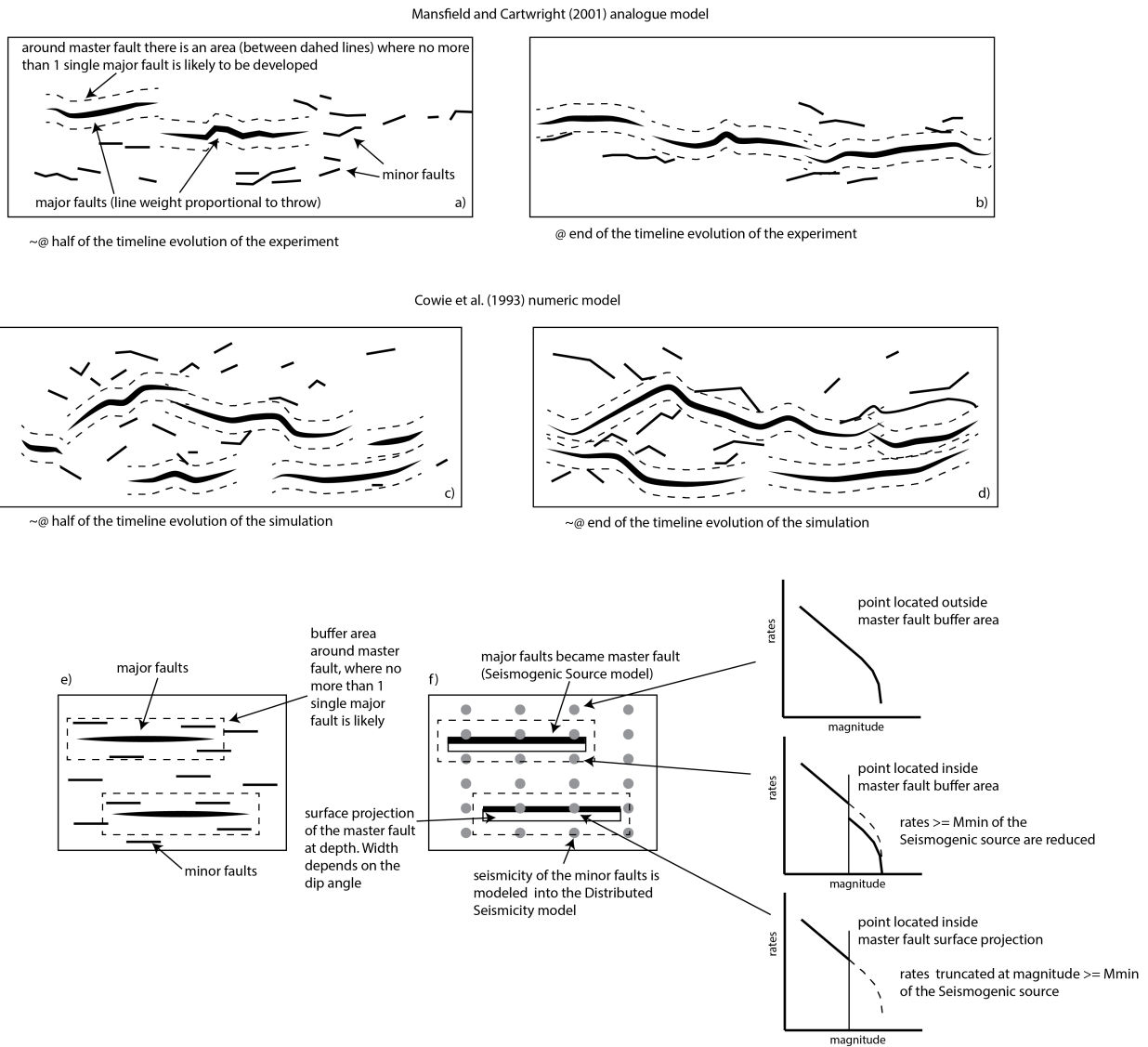
1020 Fig. 6 Probability gain per earthquake (see eq. 3) versus correlation distance c ,
 1021 highlighting the best radius for use in the smoothed seismicity approach (eq. 2)

1022

1023

1024

1025



1026

1027

1028

1029

1030

1031

1032

1033

1034

1035

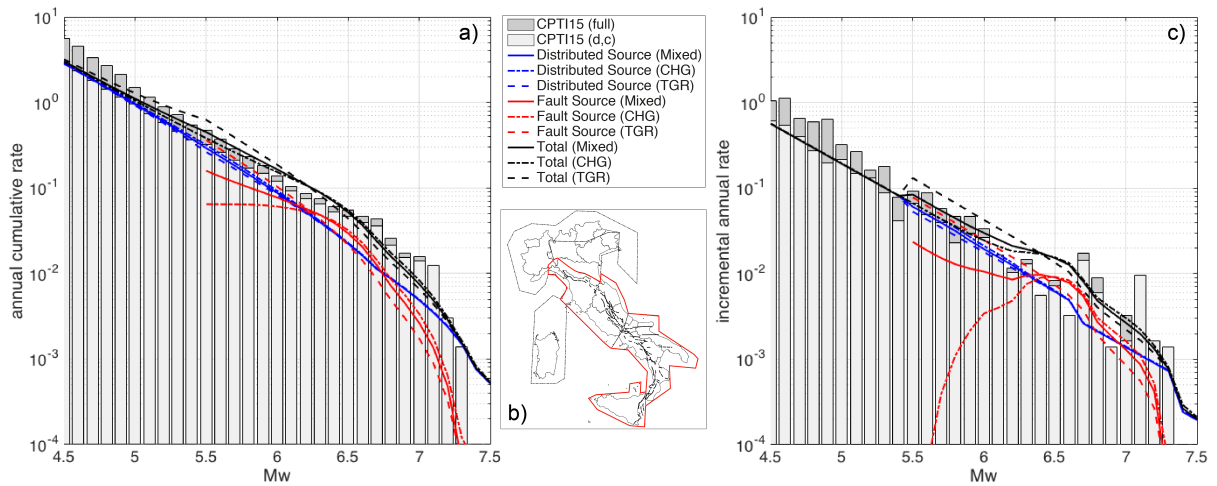
1036

1037

1038

1039

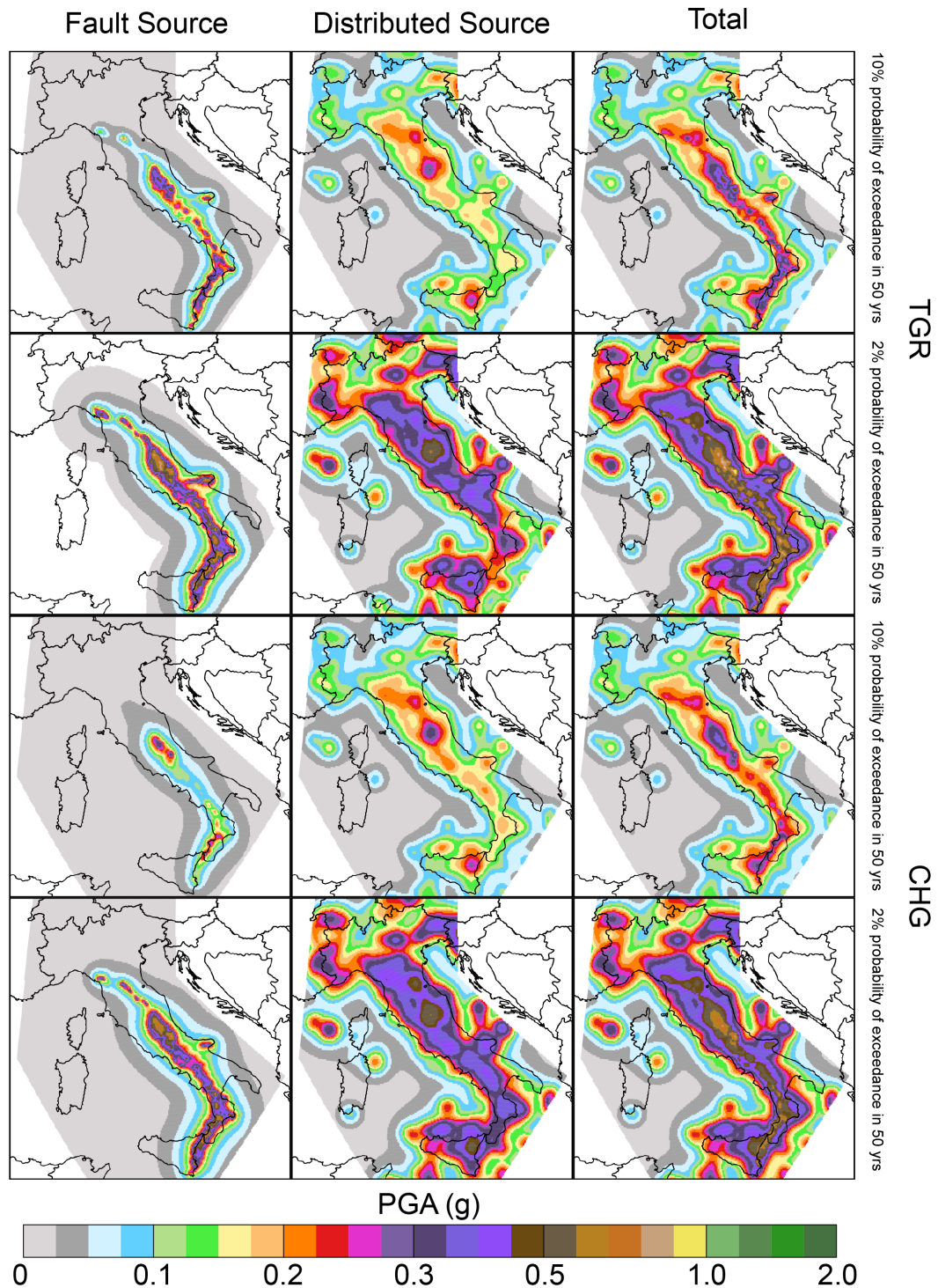
Fig. 7 Fault system evolution and implications in our model. a) and b) Diagrams from the Mansfield and Cartwright (2001) analogue experiment in two different stages: the approximate midpoint of the sequence and the end of the sequence. Areas exist around master faults where no more than a single major fault is likely to develop. c) and d) Diagrams from numerical modelling conducted by Cowie et al. (1993) in two different stages. This experiment shows the similar evolutionary features of major and minor faults. e) and f) Application of the analogue and numeric modelling of fault system evolution to the fault source input proposed in this paper. A buffer area is drawn around each fault source, where it is unlikely for other major faults to develop, and it accounts for the length and slip rate of the fault source. This buffer area is useful for reducing or truncating the rates of expected distributed seismicity based on the position of a distributed seismicity point with respect to the buffer zone (see the text for details).



1040

1041 Fig. 8 a) annual cumulative rate and c) incremental annual rate computed for the red
 1042 bounded area in b). The rates have been computed using: (i) the full CPTI15
 1043 catalogue; (ii) the declustered and complete catalogue (CPTI15 (d, c) in the legend)
 1044 obtained using the completeness magnitude thresholds over different periods of time
 1045 given by Stucchi et al. (2011) for five large zones; (iii) the distributed sources; (iv) the
 1046 fault sources; and (v) summing fault and distributed sources (Total).

1047



1048

1049

1050

1051

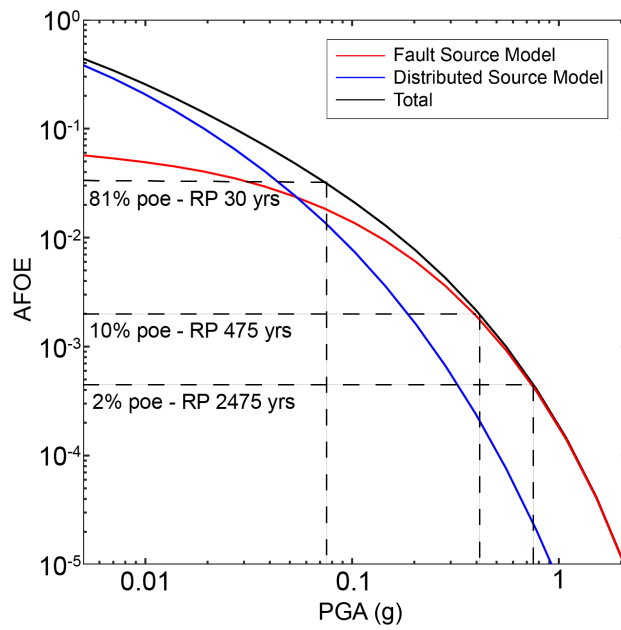
1052

1053

1054

1055

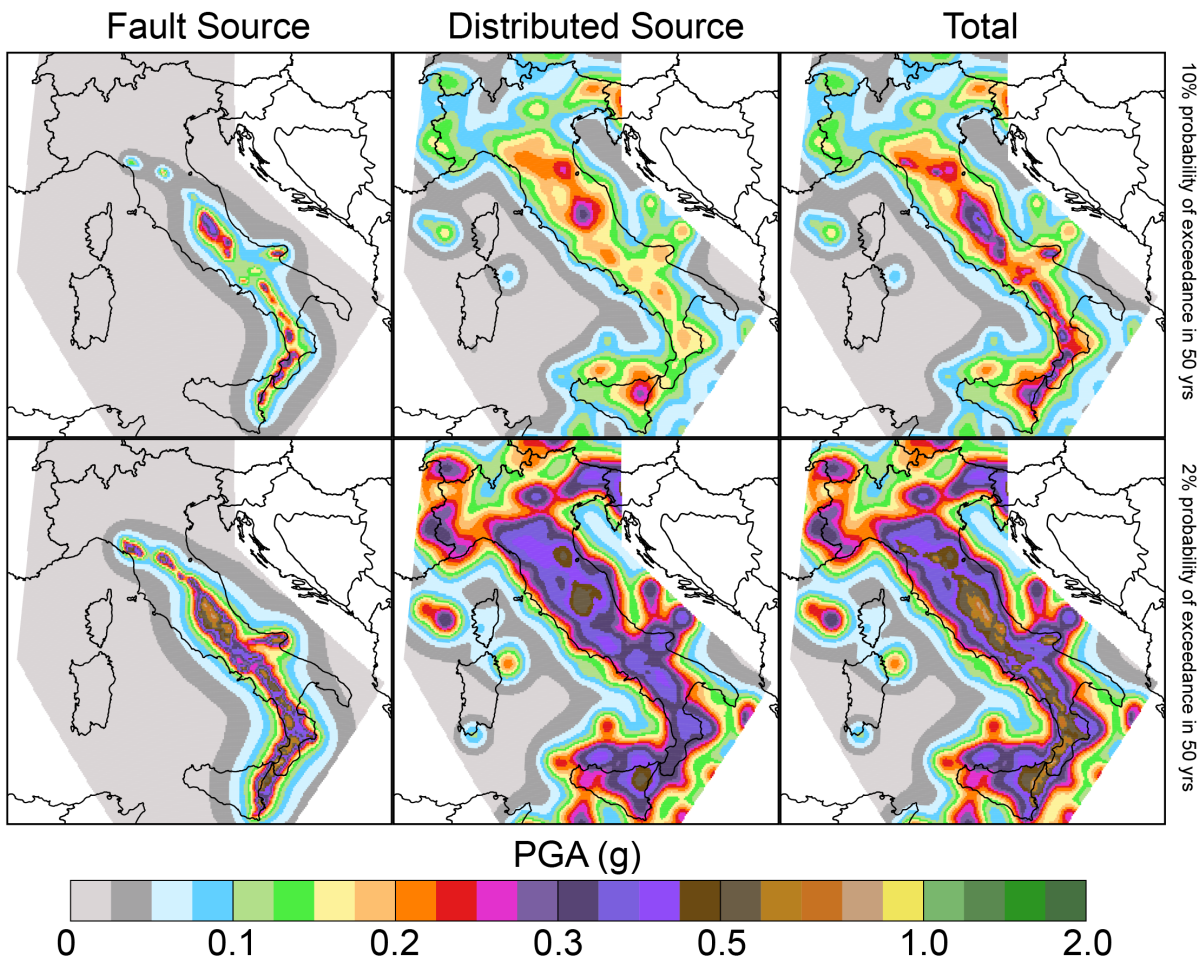
Fig. 9 Seismic hazard maps for the *TGR* and *CHG* models expressed in terms of peak ground acceleration (PGA) and computed for a latitude/longitude grid spacing of 0.05° . The first and second rows show the fault source, distributed source and total maps of the *TGR* model computed for 10% probability of exceedance in 50 years and 2% probability of exceedance in 50 years, corresponding to return periods of 475 and 2475 years, respectively. The third and fourth rows show the same maps for the *CHG* model.



1056

1057 Fig. 10 An example of the contribution to the total seismic hazard level (black line), in
 1058 terms of hazard curves, by the *fault* (red line) and *distributed* (blue line) source inputs
 1059 for one of the 45,602 grid points (L'Aquila, 42.400-13.400). The dashed lines
 1060 represent the 2%, 10% and 81% probabilities of exceedance (poes) in 50 years.

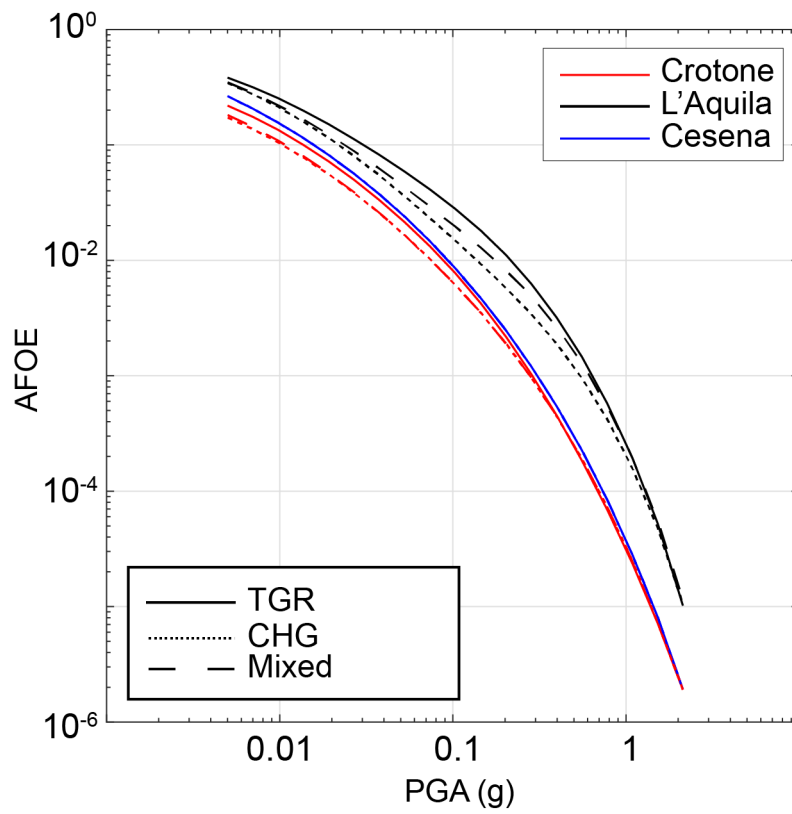
1061



1062

1063

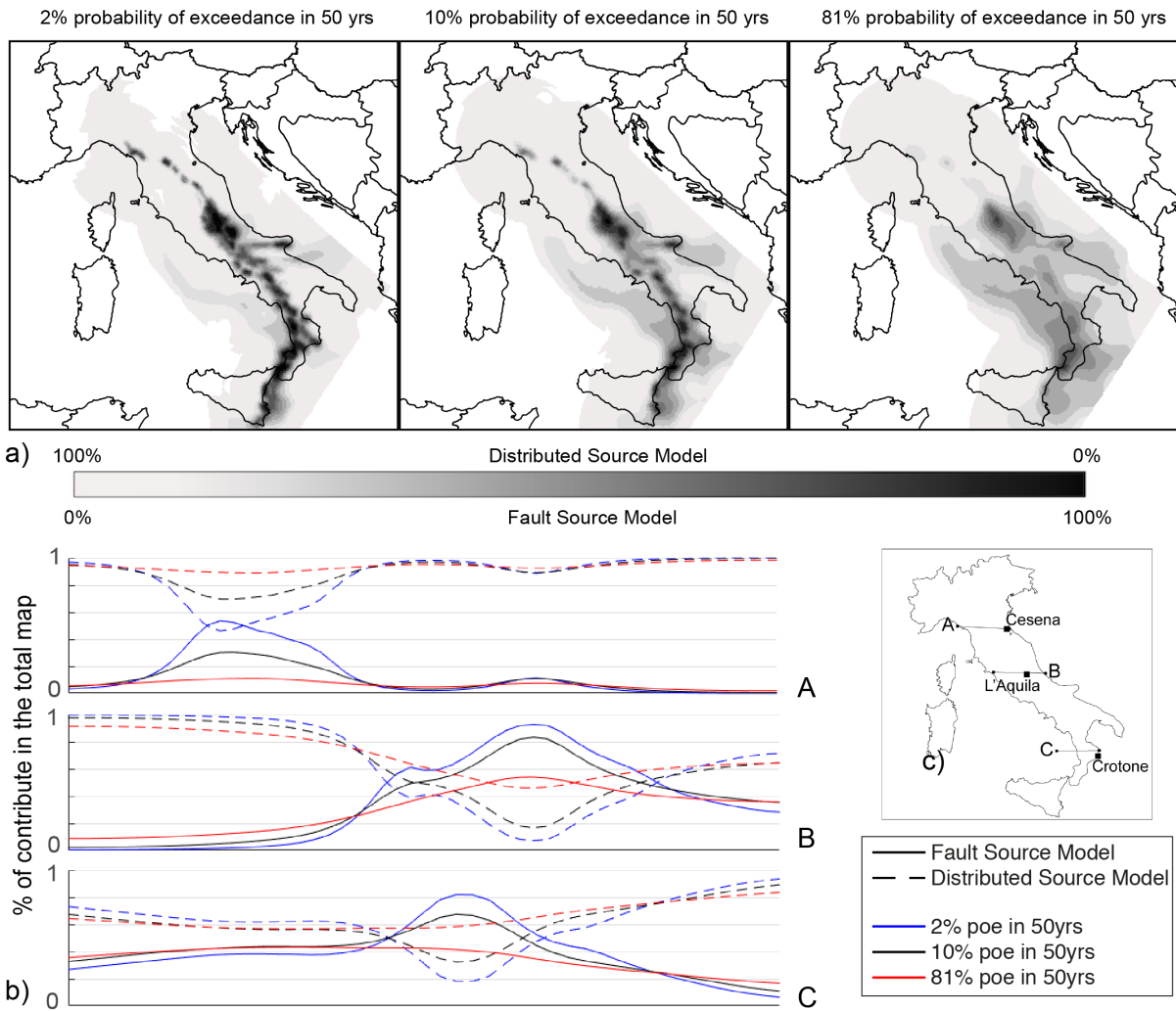
1064 Fig. 11 Seismic hazard maps for the *Mixed* model. The first row shows the fault
 1065 source, distributed source and total maps computed for 10% probability of
 1066 exceedance in 50 years, and the second row shows the same maps but computed
 1067 for 2% probability of exceedance in 50 years, corresponding to return periods of 475
 1068 and 2475 years, respectively. The results are expressed in terms of peak ground
 1069 acceleration (PGA).



1070

1071 Fig. 12 *CHG* (dotted line), *TGR* (solid line) and *Mixed* model (dashed line) hazard
 1072 curves for three sites: Cesena (red line), L'Aquila (black line) and Crotone (blue line)

1073



1074

1075

1076

1077

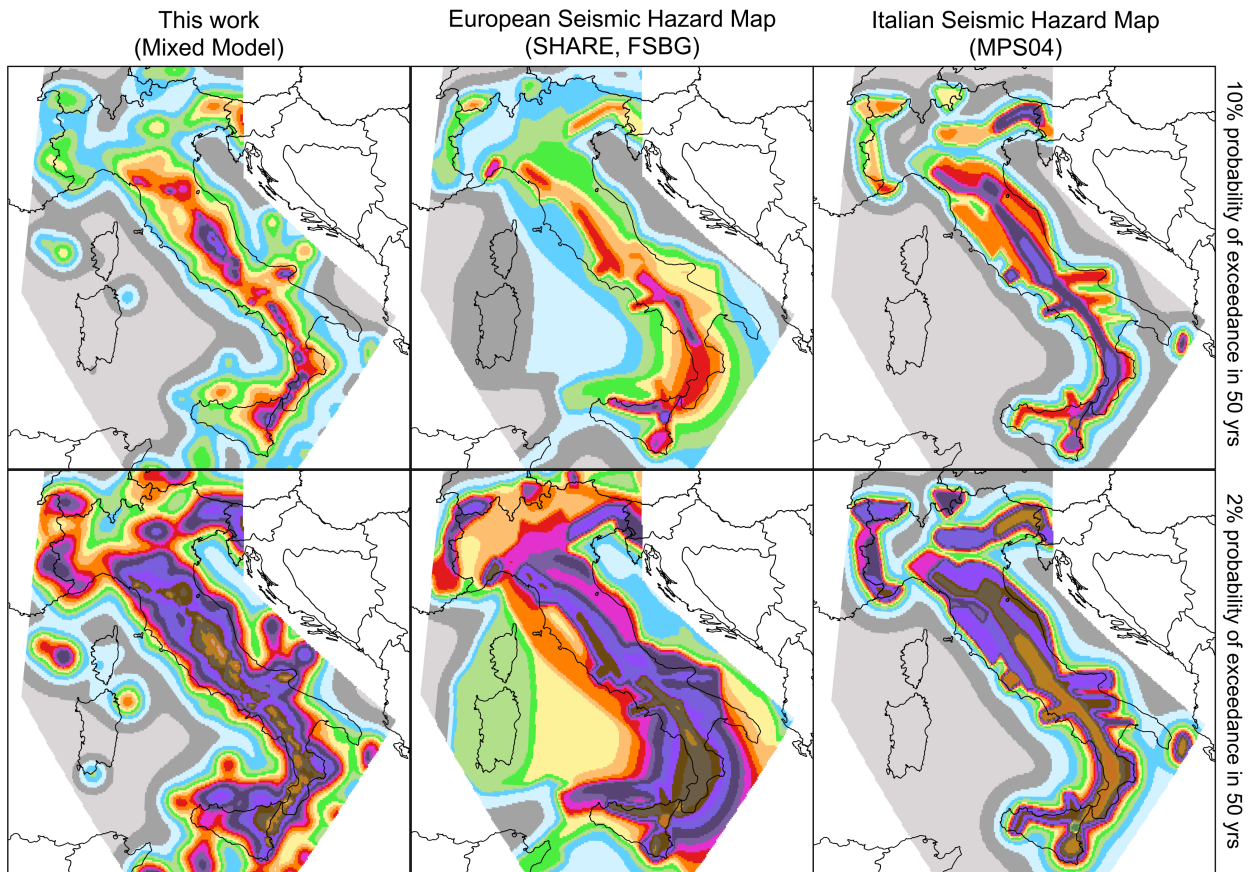
1078

1079

1080

1081

Fig. 13 a) Contribution maps of the Mixed *fault* and *distributed* source inputs to the total hazard level for three probabilities of exceedance: 2%, 10% and 81%, corresponding to return periods of 2475, 475 and 30 years, respectively. b) Contributions of the Mixed *fault* (solid line) and *distributed* (dashed line) source inputs along three profiles (A, B and C in Fig. 13c) for three probabilities of exceedance: 2% (blue line), 10% (black line) and 81% (red line).



1082

1083 Fig. 14 Seismic hazard maps expressed in terms of Peak Ground Acceleration
 1084 (PGA) and computed for a latitude/longitude grid spacing of 0.05° based on site
 1085 conditions. The figure shows a comparison of our model (*Mixed* model, on the left),
 1086 the SHARE model (FSBG logic tree branch, in the middle) and the current Italian
 1087 national seismic hazard map (MPS04, on the right). The same GMPEs (Akkar et al.
 1088 2013, Chiou et al., 2008, Faccioli et al., 2010 and Zhao et al., 2006 and Bindi et al.
 1089 2014), were used for all models to obtain and compare the maps.

1090

1091

1092

1093

1094

1095

ID	Fault Sources	L (km)	Dip (°)	Upper (km)	Lower (km)	SR _{min} (mm/yr)	SR _{max} (mm/yr)
1	Lunigiana	43.8	40	0	5	0.28	0.7
2	North Apuane Transfer	25.5	45	0	7	0.33	0.83
3	Garfagnana	26.9	30	0	4.5	0.35	0.57
4	Garfagnana Transfer	47.1	90	2	7	0.33	0.83
5	Mugello	21.0	40	0	7	0.33	0.83
6	Ronta	19.3	65	0	7	0.17	0.5
7	Poppi	17.1	40	0	4.5	0.33	0.83
8	Città di Castello	22.9	40	0	3	0.25	1.2
9	M.S.M. Tiberina	10.5	40	0	2.5	0.25	0.75
10	Gubbio	23.6	50	0	6	0.4	1.2
11	Colfiorito System	45.9	50	0	8	0.25	0.9
12	Umbra Valley	51.1	55	0	4.5	0.4	1.2
13	Vettore-Bove	35.4	50	0	15	0.2	1.05
14	Nottoria-Preci	29.0	50	0	12	0.2	1
15	Cascia-Cittareale	24.3	50	0	13.5	0.2	1
16	Leonessa	14.9	55	0	12	0.1	0.7
17	Rieti	17.6	50	0	10	0.25	0.6
18	Fucino	82.3	50	0	13	0.3	1.6
19	Sella di Corno	23.1	60	0	13	0.35	0.7
20	Pizzoli-Pettino	21.3	50	0	14	0.3	1
21	Monteale	15.1	50	0	14	0.25	0.9
22	Gorzano	28.1	50	0	15	0.2	1
23	Gran Sasso	28.4	50	0	15	0.35	1.2
24	Paganica	23.7	50	0	14	0.4	0.9
25	Middle Aternum Valley	29.1	50	0	14	0.15	0.45
26	Campo Felice-Ovindoli	26.2	50	0	13	0.2	1.6
27	Carsoli	20.5	50	0	11	0.35	0.6
28	Liri	42.5	50	0	11	0.3	1.26
29	Sora	20.4	50	0	11	0.15	0.45
30	Marsicano	20.0	50	0	13	0.25	1.2
31	Sulmona	22.6	50	0	15	0.6	1.35
32	Maiella	21.4	55	0	15	0.7	1.6
33	Aremogna C.Miglia	13.1	50	0	15	0.1	0.6
34	Barrea	17.1	55	0	13	0.2	1
35	Cassino	24.6	60	0	11	0.25	0.5
36	Ailano-Piedimonte	17.6	60	0	12	0.15	0.35
37	Matese	48.3	60	0	13	0.2	1.9
38	Bojano	35.5	55	0	13	0.2	0.9
39	Frosolone	36.1	70	11	25	0.35	0.93
40	Ripabottoni-San Severo	68.3	85	6	25	0.1	0.5
41	Mattinata	42.3	85	0	25	0.7	1
42	Castelluccio dei Sauri	93.2	90	11	22	0.1	0.5
43	Ariano Irpino	30.1	70	11	25	0.35	0.93
44	Tammaro	25.0	60	0	13	0.35	0.93
45	Benevento	25.0	55	0	10	0.35	0.93
46	Volturno	15.7	60	1	13	0.23	0.57
47	Avella	20.5	55	1	13	0.2	0.7
48	Ufita-Bisaccia	59.0	64	1.5	15	0.35	0.93
49	Melfi	17.2	80	12	22	0.1	0.5
50	Irpinia Antithetic	15.0	60	0	11	0.2	0.53

51	Irpinia	39.7	65	0	14	0.3	2.5
52	Volturara	23.7	60	1	13	0.2	0.35
53	Alburni	20.4	60	0	8	0.35	0.7
54	Caggiano-Diano Valley	46.0	60	0	12	0.35	1.15
55	Pergola-Maddalena	50.6	60	0	12	0.20	0.93
56	Agri	34.9	50	5	15	0.8	1.3
57	Potenza	17.8	90	15	21	0.1	0.5
58	Palagianello	73.3	90	13	22	0.1	0.5
59	Monte Alpi	10.9	60	0	13	0.35	0.9
60	Maratea	21.6	60	0	13	0.46	0.7
61	Mercure	25.8	60	0	13	0.2	0.6
62	Pollino	23.8	60	0	15	0.22	0.58
63	Castrovillari	10.3	60	0	15	0.2	1.15
64	Rossano	14.9	60	0	22	0.5	0.6
65	Crati West	49.7	45	0	15	0.84	1.4
66	Crati East	18.4	60	0	8	0.75	1.45
67	Lakes	43.6	60	0	22	0.75	1.45
68	Fuscalto	21.1	60	2	22	0.75	1.45
69	Piano Lago-Decollatura	25.0	60	1	15	0.23	0.57
70	Catanzaro North	29.5	80	3	20	0.75	1.45
71	Catanzaro South	21.3	80	3	20	0.75	1.45
72	Serre	31.6	60	0	15	0.7	1.15
73	Vibo	23.0	80	0	15	0.75	1.45
74	Sant'Eufemia Gulf	24.8	40	1	11	0.11	0.3
75	Capo Vaticano	13.7	60	0	8	0.75	1.45
76	Coccorino	13.3	70	3	11	0.75	1.45
77	Scilla	29.7	60	0	13	0.8	1.5
78	Sant'Eufemia	19.2	60	0	13	0.75	1.45
79	Cittanova-Armo	63.8	60	0	13	0.45	1.45
80	Reggio Calabria	27.2	60	0	13	0.7	2
81	Taormina	38.7	30	3	13	0.9	2.6
82	Acireale	39.4	60	0	15	1.15	2.3
83	Western Ionian	50.1	65	0	15	0.75	1.45
84	Eastern Ionian	39.3	65	0	15	0.75	1.45
85	Climiti	15.7	60	0	15	0.75	1.45
86	Avola	46.9	60	0	16	0.8	1.6

1096

1097 Table 1 Geometric Parameters of the Fault Sources. L, along-strike length; Dip,
1098 inclination angle of the fault plane; Upper and Lower, the thickness bounds of the
1099 local seismogenic layer; SRmin and SRmax, the slip rates assigned to the sources
1100 using the references available (see the supplemental files); and *ID*, the fault number
1101 identifier.

1102

ID	Fault Sources	Historical Earthquakes				Instrumental Earthquakes		
		yyyy/mm/dd	I_{Max}	I_0	M_w	sD	yyyy/mm/dd	M_w
1	Lunigiana	1481/05/07	VIII	VIII	5.6	0.4		
		1834/02/14	IX	IX	6.0	0.1		
2	North Apuane Transfer	1837/04/11	X	IX	5.9	0.1		
3	Garfagnana	1740/03/06	VIII	VIII	5.6	0.2		
		1920/09/07	X	X	6.5	0.1		
4	Garfagnana Transfer							
5	Mugello	1542/06/13	IX	IX	6.0	0.2		
		1919/06/29	X	X	6.4	0.1		
6	Ronta							
7	Poppi							
8	Città di Castello	1269			5.7			
		1389/10/18	IX	IX	6	0.5		
		1458/04/26	VIII-IX	VIII-IX	5.8	0.5		
		1789/09/30	IX	IX	5.9	0.1		
9	M.S.M. Tiberina	1352/12/25	IX	IX	6.3	0.2		
		1917/04/26	IX-X	IX-X	6.0	0.1		
10	Gubbio						1984/04/29	5.6
11	Colfiorito System	1279/04/30	X	IX	6.2	0.2	1997/09/26	5.7
		1747/04/17	IX	IX	6.1	0.1	1997/09/26	6
		1751/07/27	X	X	6.4	0.1		
12	Umbra Valley	1277		VIII	5.6	0.5		
		1832/01/13	X	X	6.4	0.1		
		1854/02/12	VIII	VIII	5.6	0.3		
13	Vettore-Bove						2016/10/30	6.5
14	Nottoria-Preci	1328/12/01	X	X	6.5	0.3	1979/09/19	5.8
		1703/01/14	XI	XI	6.9	0.1		
		1719/06/27	VIII	VIII	5.6	0.3		
		1730/05/12	IX	IX	6.0	0.1		
		1859/08/22	VIII-IX	VIII-IX	5.7	0.3		
		1879/02/23	VIII	VIII	5.6	0.3		
15	Cascia-Cittareale	1599/11/06	IX	IX	6.1	0.2		
		1916/11/16	VIII	VIII	5.5	0.1		
16	Leonessa							
17	Rieti	1298/12/01	X	IX-X	6.3	0.5		
		1785/10/09	VIII-IX	VIII-IX	5.8	0.2		
18	Fucino	1349/09/09	IX	IX	6.3	0.1		
		1904/02/24	IX	VIII-IX	5.7	0.1		
		1915/01/13	XI	XI	7	0.1		
19	Sella di Corno							
20	Pizzoli-Pettino	1703/02/02	X	X	6.7	0.1		
21	Monte Reale							
22	Gorzano	1639/10/07	X	IX-X	6.2	0.2		
		1646/04/28	IX	IX	5.9	0.4		
23	Gran Sasso							
24	Paganica	1315/12/03	VIII	VIII	5.6	0.5	2009/06/04	6.3
		1461/11/27	X	X	6.5	0.5		
25	Middle Aternum Valley							
26	Campo Felice-Ovindoli							
27	Carsoli							
28	Liri							
29	Sora	1654/07/24	X	IX-X	6.3	0.2		
30	Marsicano							
31	Sulmona							
32	Maiella							
33	Aremogna C.Miglia							
34	Barrea						1984/05/07	5.9
35	Cassino							
36	Ailano-Piedimonte							
37	Matese	1349/09/09	X-XI	X	6.8	0.2		

38	Bojano	1805/07/26	X	X	6.7	0.1		
39	Frosolone	1456/12/05	XI	XI	7	0.1		
40	Ripabottoni-San Severo	1627/07/30	X	X	6.7	0.1	2002/10/31	5.7
		1647/05/05	VII-VIII	VII-VIII	5.7	0.4		
		1657/01/29	IX-X	VIII-IX	6.0	0.2		
41	Mattinata	1875/12/06	VIII	VIII	5.9	0.1		
		1889/12/08	VII	VII	5.5	0.1		
		1948/08/18	VII-VIII	VII-VIII	5.6	0.1		
42	Castelluccio dei Sauri	1361/07/17	X	IX	6	0.5		
		1560/05/11	VIII	VIII	5.7	0.5		
		1731/03/20	IX	IX	6.3	0.1		
43	Ariano Irpino	1456/12/05			6.9	0.1		
		1962/08/21	IX	IX	6.2	0.1		
44	Tammaro	1688/06/05	XI	XI	7	0.1		
45	Benevento							
46	Volturno							
47	Avella	1499/12/05	VIII	VIII	5.6	0.5		
48	Ufita-Bisaccia	1732/11/29	X-XI	X-XI	6.8	0.1		
		1930/07/23	X	X	6.7	0.1		
49	Melfi	1851/08/14	X	X	6.5	0.1		
50	Irpinia Antithetic							
51	Irpinia	1466/01/15	VIII-IX	VIII-IX	6.0	0.2	1980/11/23	6.8
		1692/03/04	VIII	VIII	5.9	0.4		
		1694/09/08	X	X	6.7	0.1		
		1853/04/09	IX	VIII	5.6	0.2		
52	Volturara							
53	Alburni							
54	Caggiano-Diano Valley	1561/07/31	IX-X	X	6.3	0.1		
55	Pergola-Maddalena	1857/12/16			6.5			
		1857/12/16			6.3			
56	Agri							
57	Potenza	1273/12/18	VIII-IX	VIII-IX	5.8	0.5	1990/05/05	5.8
58	Palagianello							
59	Monte Alpi							
60	Maratea							
61	Mercure	1708/01/26	VIII-IX	VIII	5.6	0.6	1998/09/09	5.5
62	Pollino							
63	Castrovillari							
64	Rossano	1836/04/25	X	IX	6.2	0.2		

65	Crati West	1184/05/24	IX	IX	6.8	0.3
		1870/10/04	X	IX-X	6.2	0.1
		1886/03/06	VII-VIII	VII-VIII	5.6	0.3
66	Crati East	1767/07/14	VIII-IX	VIII-IX	5.9	0.2
		1835/10/12	X	IX	5.9	0.3
67	Lakes	1638/06/08	X	X	6.8	0.1
68	Fuscalto	1832/03/08	X	X	6.6	0.1
69	Piano Lago-Decollatura					
70	Catanzaro North	1638/03/27			6.6	
71	Catanzaro South	1626/04/04	X	IX	6.1	0.4
72	Serre	1659/11/05	X	X	6.6	0.1
		1743/12/07	IX-X	VIII-IX	5.9	0.2
		1783/02/07	X-XI	X-XI	6.7	0.1
		1791/10/13	IX	IX	6.1	0.1
73	Vibo					
74	Sant'Eufemia Gulf	1905/09/08	X-XI	X-XI	7	0.1
75	Capo Vaticano					
76	Coccorino	1928/03/07	VIII	VII-VIII	5.9	0.1
77	Scilla					
78	Sant'Eufemia	1894/11/16	IX	IX	6.1	0.1
79	Cittanova-Armo	1509/02/25	IX	VIII	5.6	0.4
		1783/02/05	XI	XI	7.1	0.1
80	Reggio Calabria					
81	Taormina	1908/12/28	XI	XI	7.1	0.2
82	Acireale	1818/02/20	IX-X	IX-X	6.3	0.1
83	Western Ionian	1693/01/11	XI	XI	7.3	0.1
84	Eastern Ionian					
85	Climiti					
86	Avola					

1103

1104 Table 2 Earthquake-Source Association Adopted for Fault Sources. I_{Max} , maximum
1105 intensity; I_0 , epicentral intensity; M_w , moment magnitude; and sD, standard deviation
1106 of the moment magnitude. For references, see the supplemental files.

Integrating faults and past earthquakes into a probabilistic seismic hazard model for peninsular Italy

3

4 Alessandro Valentini¹, Francesco Visini² and Bruno Pace¹





5 ¹ DiSPUTer, Università degli Studi “Gabriele d’Annunzio”, Chieti, Italy

6 ² Istituto Nazionale di Geofisica e Vulcanologia, L’Aquila, Italy

7

8 **Abstract**

9

10 *Italy is one of the most seismically active countries in Europe. Moderate to strong earthquakes, with*
11 *magnitudes of up to ~7, have been historically recorded for many active faults. Currently,*
12 *probabilistic seismic hazard assessments in Italy are mainly based on area source models, in which*
13 *seismicity is modelled using a number of seismotectonic zones and the occurrence of earthquakes is*
14 *assumed uniform. However, in the past decade, efforts have increasingly been directed towards using*
15 *fault sources in seismic hazard models to obtain more detailed and potentially more realistic patterns*
16 *of ground motion. In our model, we used two categories of earthquake sources. The first involves*
17 *active faults, and  slip rates were used to quantify the seismic activity rate. We produced an*
18 *inventory of all fault sources with details of their geometric, kinematic and energetic properties. The*
19 *associated parameters were used to compute the total seismic moment rate of each fault. We*
20 *evaluated the magnitude-frequency distribution (MFD) of each fault source using two models: a*
21 *characteristic Gaussian model centred  the maximum magnitude and a Truncated Gutenberg-*
22 *Richter model. The second earthquake source category involves  tributed seismicity, and  fixed-*
23 *radius smoothed approach and a historical catalogue were used to evaluate seismic activity. Under*
24 *the assumption that deformation is concentrated along faults, we combined the MFD derived from the*
25 *geometry and slip rates of active faults with the MFD from the spatially smoothed earthquake sources*
26 *and assumed that the smoothed seismic activity in the vicinity of an active fault gradually decreases*
27 *by a fault size-driven factor. Additionally, we computed horizontal peak ground acceleration maps for*
28 *return periods of 475 and 2,475 yrs. Although the ranges and gross spatial distributions of the*
29 *expected accelerations obtained here are comparable to those obtained through methods involving*
30 *seismic catalogues and classical zonation models, the spatial pattern of the hazard maps obtained*
31 *with our model is far more detailed. Our model is characterized by areas that are more hazardous*
32 *and that correspond to mapped active faults, while previous models yield expected accelerations that*
33 *are almost uniformly distributed across large regions. In addition, we conducted sensitivity tests to*

34 *determine the impact on the hazard results of the earthquake rates derived from two MFD models for*
35 *faults and to determine the relative contributions of faults versus distributed seismic activity. We*
36 *believe that our model represents advancements in terms of the input data (quantity and quality) and*
37 *methodology used in the field of fault-based regional seismic hazard modelling in Italy.*
38


39 **1. Introduction**





40 In this paper, we present the results of ~~a new probabilistic seismic hazard (PSH)~~
41 ~~model~~ for Italy that includes **significant advances** in the use of integrated active fault
42 and seismological data. The use of active faults as an input for ~~PSH~~ analysis is a
43 consolidated approach in many countries characterized by high strain rates and
44 seismic releases, as shown, for example, by Field et al. (2015) in California and
45 Stirling et al. (2012) in New Zealand. ~~However~~ in recent years, active fault data have
46 also been successfully integrated into ~~PSH assessments~~ in regions with moderate-
47 to-low strain rates, such as SE Spain (e.g., Garcia-Mayordomo et al., 2007), France
48 (e.g., Scotti et al., 2014), and central Italy (e.g., Peruzza et al., 2011).

49 In Europe, a working group of the European Seismological Commission, named
50 **Fault2SHA**, is **discussing** **fault-based** **seismic** **hazard** **modelling**
51 (<https://sites.google.com/site/linkingfaultpsha/home>). The working group, born to
52 **motivate exchanges between field geologists, fault modellers and seismic hazard**
53 **practitioners, organizes workshops, conference sessions, and special issues and**
54 **stimulates collaborations between researchers. The work we are presenting here**
55 **stems from the activities of the *Fault2SHA* working group.**

56 Combining active faults and background sources is **one of the main issues** in this
57 type of approach. Although the methodology remains far from identifying a standard
58 procedure, common approaches combine active faults and background sources by
59 applying a threshold magnitude, generally between 5.5 and 7, above which
60 seismicity is modelled as occurring on faults and below which seismicity is modelled
61 via a **smoothed approach** (e.g., Akinci et al., 2009), area sources (e.g., the so-called
62 FSBG model in ~~SHARE~~ Woessner et al., 2015) or a combination of the two (Field et
63 al., 2015; Pace et al., 2006).

64 Another important **issue** in the use of active faults in ~~PSHA~~ is ~~assigning the “correct”~~
65 ~~magnitude-frequency distribution (MFD) to the fault sources.~~ Gutenberg-Richter (GR)

66 and characteristic earthquake models are commonly used, and the choice
67 sometimes depends on the knowledge of the fault and data availability. Often, the
68 choice of the “appropriate” MFD for each fault source is a difficult task because
69 palaeoseismological studies are scarce, and it is often difficult to establish clear
70 relationships between mapped faults and historical seismicity. Recently, Field et al.
71 (2017) discussed the effects and complexity of the choice, highlighting how often the
72 GR model results are not consistent with data; however, in other cases,
73 uncharacteristic behaviour, with rates smaller than the maximum, are possible. The
74 discussion is open (see for example the discussion by Kagan et al., 2012) and far
75 from being solved with the available observations, including both seismological
76 and/or geological/paleoseismological observations. In this work, we explore the
77 calculations of these two MFDs, a characteristic Gaussian model and a Truncated
78 Gutenberg-Richter model, to explore the epistemic uncertainties and to consider a
79 *Mixed model* as a so-called “expert judgement” model. This approach is useful for
80 comparative analysis, and which we assigned one of the two MFDs to each fault
81 source. The rationale of the choice of the MFD of each fault source is explained in
82 detail later in this paper. However, this approach obviously does  **not solve the issue,**
83 and the choice of MFD remains an open question in fault-based PSHA.

84 In Italy, the current national PSH model for building code (Stucchi et al., 2011) is
85 based on area sources and the classical Cornell approach (Cornell, 1968), in which
86 the occurrence of earthquakes is assumed uniform in the defined seismotectonic
87 zones. However, we believe that more efforts must be directed towards using
88 geological data (e.g., fault sources and paleoseismological information) in **PSH**
89 **model**  to obtain detailed patterns of ground motion, extend the observational time
90 required to capture the recurrence of large-magnitude events and improve the
91 reliability of seismic hazard assessments. In fact, as highlighted by the 2016-2017
 seismic sequences in central Italy, a zone-based **PSH**  is not **able to model local**
93 **spatial variations in ground motion** (Meletti et al., 2016), whereas a fault-based
94 model can provide insights for aftershock time-dependent **PSH**  analysis (Peruzza et
95 al., 2016). In conclusion, even if the main purpose of this work is to integrate active
96 faults into hazard calculations for the Italian territory, this study does not represent
97 an official update of the seismic hazard model of Italy.

98

99 2. Source Inputs


100 Two earthquake-source inputs are considered in this work. The first is a ~~fault source~~
101 ~~input that is based on~~ active faults and uses the geometries and slip rates of known
102 active faults to compute activity rates over a certain range of magnitude. The second
103 is a classical smoothed approach that accounts for the rates of expected
104 earthquakes with a minimum moment magnitude (M_w) of 4.5 but excludes
105 earthquakes associated with known faults based on a modified earthquake
106 catalogue. Note that our ~~PSH~~ model requires the combination of the two source
107 inputs related to the locations of expected seismicity rates into a ~~single model~~
108 Therefore, these two earthquake-source inputs are not independent but
109 complementary, in both the magnitude and frequency distribution, and together
110 account for all seismicity in Italy.

111 In the following subsections, we describe the two source inputs and how they are
112 combined in the ~~PSH~~ model.


113 2.1 Fault Source Input

114 In seismic hazard assessment, an active fault is a structure that exhibits evidence of
115 activity in the late Quaternary (i.e., in the past 125 kyr), has a demonstrable or
116 potential capability of generating major earthquakes and is capable of future
117 reactivation (see Machette, 2000 for a discussion on terminology). The evidence of
118 Quaternary activity can be geomorphological and/or paleoseismological when
119 activation information from instrumental seismic sequences and/or association to
120 historical earthquakes is not available. Fault source ~~input~~ are useful for seismic
121 hazard studies, and we compiled a database for Italy via the analysis and synthesis
122 of neotectonic and seismotectonic data from approximately 90 published studies of
123 110 faults across Italy. Our database included, but was not limited to, the Database
124 of Individual Seismogenic Sources (DISS vers. 3.2.0, <http://diss.rm.ingv.it/diss/>),
125 which is already available for Italy. It is important to highlight that the DISS is
126 currently composed of two main categories of seismogenic sources: individual and
127 composite sources. The latter are defined by the DISS' authors as "*simplified and*
128 *three-dimensional representation of a crustal fault containing an unspecified number*
129 *of seismogenic sources that cannot be singled out. Composite seismogenic sources*
130 *are not associated with a specific set of earthquakes or earthquake distribution*", and

131 therefore are not useful for our PSHA approach; the former is “a *simplified and three-*
132 *dimensional representation of a rectangular fault plane. Individual seismogenic*
133 *sources are assumed to exhibit characteristic behaviour with respect to rupture*
134 *length/width and expected magnitude*” ([http://diss.rm.ingv.it/diss/index.php/about/13-](http://diss.rm.ingv.it/diss/index.php/about/13-introduction)
135 [introduction](http://diss.rm.ingv.it/diss/index.php/about/13-introduction)). Even if in agreement with our approach, we note that some of the
136 individual seismogenic sources in the DISS are based on geological and
137 paleoseismological information, and many others used the *Boxer* code (Gasperini et
138 al., 1999) to calculate the epicentre, moment magnitude, size and orientation of a
139 seismic source from observed macroseismic intensities. We carefully analysed the
140 individual sources and some related issues: (i) the lack of updating of the geological
141 information of some individual sources and (ii) the nonconformity between the input
142 data used by DISS in *Boxer* and the latest historical seismicity (CPTI15) and
143 macroseismic intensity (DBMI15) publications. Thus, we performed a full review of
144 the fault database. We then compiled a fault source database as a synthesis of
145 works published over the past twenty years, including DISS, using all updated and
146 available geological, paleoseismological and seismological data (see the
147 supplemental files for a complete list of references). We consider our database as
148 complete as possible in terms of individual seismogenic sources, and it contains all
149 the parameters necessary to construct an input dataset for fault-based PSHA.


150 The resulting database of normal and strike-slip active and seismogenic faults in
151 peninsular Italy (Fig. 1, Tables 1 and 2; see the supplemental files) includes all the
152 available geometric, kinematic, slip rate and earthquake source-related information.
153 In the case of missing data regarding the geometric parameters of dip and rake, we
154 assumed typical dip and rake values of 60° and -90° , respectively, for normal faults
155 and 90° and 0° or 180° , respectively, for strike-slip faults. In this paper, only normal
156 and strike-slip faults are used as fault source inputs. We decided not to include thrust
157 faults in the present study because, with the methodology proposed in this study (as
158 discussed later in the text), the maximum size of a single-rupture segment must be
159 defined, and segmentation criteria have not been established for large thrust zones.
160 Moreover, our method uses ~~slip rate~~  to derive active seismicity rates, and sufficient
161 knowledge of these values is not available for thrust faults in Italy. Because some
162 areas of Italy, such as the NW sector of the Alps, Po Valley, the offshore sector of
163 the central Adriatic Sea, and SW Sicily, may be excluded by this limitation, we are

164 considering an update to our approach to include thrust faults and volcanic sources
165 in a future study. The upper and lower boundaries of the seismogenic layer are
166 mainly derived from the analysis of Stucchi et al. (2011) of the Italian national
167 seismic hazard model and locally refined by more detailed studies (Boncio et al.,
168 2011; Peruzza et al., 2011; Ferranti et al., 2014).

169 Based on the compiled database, we explored three main  associated with
170 defining a fault source input: the slip rate evaluation, the segmentation model and
171 the expected seismicity rate calculation.

172 *2.1.1 Slip rates*

173 Slip rates control fault-based seismic hazards (Main, 1996, Roberts et al., 2004; Bull
174 et al., 2006; Visini and Pace, 2014) and reflect the velocities of the mechanisms that
175 operate during continental deformation (e.g., Cowie et al., 2005). Moreover, long-
176 term observations of faults in various tectonic contexts have shown that slip rates
177 vary in space and time (e.g., Bull et al., 2006; Nicol et al., 2006, 2010, McClymont et
178 al., 2009; Gunderson et al., 2013; Benedetti et al., 2013, D'Amato et al., 2016), and
179 numerical simulations (e.g., Robinson et al., 2009; Cowie et al., 2012; Visini and
180 Pace, 2014) suggest that variability mainly occurs in response to interactions
181 between adjacent faults. Therefore, understanding the temporal variability in fault slip
182 rates is a key point in understanding the earthquake recurrence rates and their
183 variability.

184 In this work, we used the mean of the minimum and maximum slip rate values listed
185 in Table 1 and assumed that it is representative of the long-term behaviour (over the
186 past 15 ky in the Apennines). These values were derived from approximately 65
187 available neotectonics, palaeoseismology and seismotectonics papers (see the
188 supplemental files). To evaluate the long-term slip rate, which is representative of the
189 average slip behaviour, and its variability over time, we used slip rates determined in
190 different ways and at different time scales (e.g., at the decadal scale based on
191 geodetic data or at longer scales based on the displacement of Holocene or Plio-
192 Pleistocene horizons). Because a direct comparison of slip rates over different time
193 intervals obtained by different methods may be misleading (Nicol et al., 2009), we
194 cannot exclude the possibility  **that epistemic uncertainties** could affect the original

195 data in some cases. The discussion of these possible biases and their evaluation via
196 statistically derived approaches (e.g., Gardner et al., 1987; Finnegan et al., 2014;
197 Gallen et al., 2015) is beyond the scope of this paper and will be explored in future
198 work. Moreover, we are assuming that slip rate values used are representative of
199 seismic movements, and aseismic factors are not taken into account. Therefore, we
200 believe that investigating the effect of this assumption could be another issue
201 explored in future work; for example, by differentiating between aseismic slip factors
202 in different tectonic contexts.

203 Because 28 faults had no measured slip (or throw) rate (Fig. 1a), we proposed a
204 statistically derived approach to assign a slip rate to these faults. Based on the slip
205 rate spatial distribution shown in Figure 1b, we subdivided the fault database into
206 three large regions—the Northern Apennines, Central-Southern Apennines and
207 Calabria-Sicilian coast—and analysed the slip rate distribution in these three areas. In
208 Figure 1b, the slip rates tend to increase from north to south. The fault slip rates in
209 the Northern Apennines range from 0.3 to 0.8 mm/yr, with the most common ranging
210 from approximately 0.5-0.6 mm/yr; the slip rates in the Central-Southern Apennines
211 range from 0.3 to 1.0, and the most common rate is approximately 0.3 mm/yr; and
212 the slip rates in the southern area (Calabria and Sicily) range from 0.9 to 1.8, with
213 the most common being approximately 0.9 mm/yr.

214 The first step in assigning an average slip rate and a range of variability to the faults
215 with unknown values is to identify the most representative distribution among known
216 probability density functions using the slip rate data from each of the three areas. We
217 test five well-known probability density functions (*Weibull*, *normal*, *exponential*,
218 *Inverse Gaussian* and *gamma*) against mean slip rate observations. The resulting
219 function with the highest log-likelihood is the *normal* function in all three areas. Thus,
220 the mean value of the *normal* distribution is assigned to the faults with unknown
221 values. We assign a value of 0.58 mm/yr to faults in the northern area, 0.64 mm/yr to
222 faults in the Central-Southern area, and 1.10 mm/yr to faults in the Calabria-Sicilian
223 area. To assign a range of slip rate variability to each of the three areas, we test the
224 same probability density functions against slip rate variability observations. Similar to
225 the mean slip rate, the probability density function with the highest log-likelihood is
226 the *normal* function in all three areas. We assign a value of 0.25 mm/yr to the faults

227 in the northern area, 0.29 mm/yr to the faults in the Central-Southern area, and 0.35
228 mm/yr to the faults in the Calabria-Sicilian area.

229

230 2.1.2 Segmentation rules for delineating fault sources

231 An important issue in the definition of a fault source input is the formulation of
232 segmentation rules. In fact, the question of whether structural segment boundaries
233 along multisegment active faults act as persistent barriers to a single rupture is
234 critical to defining the maximum seismogenic potential of fault sources. In our case,
235 the rationale behind the definition of a fault source is based on the assumption that
236 the geometric and kinematic features of a fault source are expressions of its
237 seismogenic potential and that its dimensions are compatible for hosting major (M_w
238 ≥ 5.5) earthquakes. Therefore, a fault source is considered a fault or an ensemble of
239 faults that slip together during an individual major earthquake. A fault source is
240 defined by a *seismogenic master fault* and its surface projection (Fig. 2a).
241 *Seismogenic master faults* are separated from each other by first-order structural or
242 geometrical complexities. Following the suggestions by Boncio et al. (2004) and
243 Field et al. (2015), we imposed the following segmentation rules in our case study: (i)
244 4-km fault gaps among aligned structures; (ii) intersections with cross structures
245 (often transfer faults) extending 4 km along strike and oriented at nearly right angles
246 to the intersecting faults; (iii) overlapping or underlapping en echelon arrangements
247 with separations between faults of 4 km; (iv) bending $\geq 60^\circ$ for more than 4 km; (v)
248 average slip rate variability along a strike greater than or equal to 50%; and (vi)
249 changes in seismogenic thickness greater than 5 km among aligned structures.
250 Example applications of the above rules are illustrated in Figure 2a.


251 By applying the above rules to our fault database, the 110 faults yielded 86 fault
252 sources: 9 strike-slip sources and 77 normal-slip sources. The longest fault source is
253 *Castelluccio dei Sauri* (fault number (*id in Table 1*) 42, $L = 93.2$ km), and the shortest
254 is *Castrovillari* (*id* 63, $L = 10.3$ km). The mean length is 30 km. The dip angle varies
255 from 30° to 90° , and 70% of the fault sources have dip angles between 50° and 60° .
256 The mean value of seismogenic thickness (ST) is approximately 12 km. The source
257 with the largest ST is *Mattinata* (*id* 41, $ST = 25$ km), and the source with the thinnest

258 ST is *Monte Santa Maria Tiberina* (id 9, ST = 2.5 km) due to the presence of an east-
259 dipping low angle normal fault, the Alto-Tiberina Fault (Boncio et al., 2000), located a
260 few kilometres west of the Monte Santa Maria Tiberina fault. Observed values of
261 maximum magnitude (M_w) have been assigned to 35 fault sources (based on Table
262 2), and the values vary from 5.90 to 7.32. The fault source inputs are shown in
263 Figure 3.

264

265 2.1.3 Expected seismicity rates

266 Each fault source is characterized by data, such as kinematic, geometry and slip rate
267 information, that we use as inputs for the FiSH code (Pace et al., 2016) to calculate
268 the global budget of the seismic moment rate allowed by the structure. This
269 calculation is based on predefined size-magnitude relationships in terms of the
270 maximum magnitude (M_{max}) and the associated mean recurrence time (T_{mean}). Table
271 1 summarizes the geometric parameters used as FiSH input parameters for each
272 fault source (seismogenic box) shown in Figure 3. To evaluate M_{max} of each source,
273 according to Pace et al., (2016) we first computed and then combined up to five M_{max}
274 values (see the example of the Paganica fault source in Fig. 2b, details in Pace et
275 al., 2016). Specifically, these five M_{max} values are as follows: MMO based on the
276 calculated scalar seismic moment (M_0) and the application of the standard formula
277 $M_w = 2/3 (\log M_0 - 9.1)$ (Hanks and Kanamori, 1979; IASPEI, 2005); two magnitude
278 values using the Wells and Coppersmith (1994) empirical relationships for the
279 maximum subsurface rupture length (MRLD) and maximum rupture area (MRA); a
280 value that corresponds to the maximum observed magnitude (MObs), if available;
281 and a value (MASP, ASP for aspect ratio) computed by reducing the fault length
282 input if the aspect ratio (W/L) is smaller than the value evaluated by the relation
283 between the aspect ratio and rupture length of observed earthquake ruptures, as
284 derived by Peruzza and Pace (2002) (not in the case of Paganica in Fig. 2b).

285  Although incorrect to consider MObs a possible M_{max} value and treat it the same as
286 other estimations, in some cases, it was useful to constrain the seismogenic
287 potentials of individual seismogenic sources. As an example, for the *Irpinia Fault* (id
288 51 in Tables 1 and 2), the characteristics of the 1980 earthquake ($M_w \sim 6.9$) can be
289 used to evaluate M_{max} via comparison with the M_{max} derived from scaling
290 relationships. In such cases, we (i) calculated the maximum expected magnitude

291 (M_{max1}) and the relative uncertainties using only the scaling relationships and (ii)
292 compared the maximum of observed magnitudes of the earthquakes potentially
293 associated with the fault. If M_{Obs} was within the range of $M_{max} \pm 1$ standard
294 deviation, we considered the value and recalculated a new M_{max} (M_{max2}) with a new
295 uncertainty. If M_{Obs} was larger than M_{max1} , we reviewed the fault geometry and/or
296 the earthquake-source association.

297 Because all the empirical relationships, as well as observed historical and recent
298 magnitudes of earthquakes, are affected by uncertainties, the *MomentBalance* (MB)
299 portion of the FiSH code (Pace et al., 2016) was used to account for these
300 uncertainties. MB computes a ~~probability density function~~ for each magnitude
301 derived from empirical relationships or observations and summarizes the results as a
302 maximum magnitude value with a standard deviation. The uncertainties in the
303 empirical scaling relationship are taken from the studies of Wells and Coppersmith
304 (1994), Peruzza and Pace (2002) and Leonard (2010). Currently, the uncertainty in
305 magnitude associated with the seismic moment is fixed and set to 0.3, whereas the
306 catalogue defines the uncertainty in M_{Obs} . Moreover, to combine the evaluated
307 maximum magnitudes, MB creates a probability curve for each magnitude by
308 assuming a normal distribution (Fig. 2). We assumed an untruncated normal
309 distribution of magnitudes at both sides. MB successively sums the probability
310 density curves and fits the summed curve to a normal distribution to obtain the mean
311 of the maximum magnitude M_{max} and its standard deviation.

312 Thus, a unique M_{max} with a standard deviation is computed for each source, and this
313 value represents the maximum rupture that is allowed by the fault geometry and the
314 rheological properties.

315 Finally, to obtain the mean recurrence time of M_{max} (i.e., T_{mean}), we use the criterion
316 of “segment seismic moment conservation” proposed by Field et al. (1999). This
317 criterion divides the seismic moment that corresponds to M_{max} by the moment rate
318 for given a slip rate:

319
$$T_{mean} = \frac{1}{Char_Rate} = \frac{10^{1.5 M_{max} 9.1}}{\mu VLW} \quad (1)$$

320 where T_{mean} is the mean recurrence time in years, **Char_Rate** is the annual mean
321 rate of occurrence, M_{max} is the computed mean maximum magnitude, μ is the shear
322 modulus, V is the average long-term slip rate, and L and W are geometrical
323 parameters of the fault along-strike rupture length and downdip width, respectively.
324 This approach was used for both MFDs in this study, and, in particular, we evaluated
325 M_{max} and T_{mean} based on the fault geometry and the slip rate of each individual
326 source. Additionally, we calculated the total expected seismic moment rate using
327 equation 1. Then, we partitioned the total expected seismic moment rate based on a
328 range given by $M_{\text{max}} \pm 1$ standard deviation following a Gaussian distribution.
329 After the fault source is entered as input, the seismic moment rate is calculated, M_{max}
330 (Fig. 2b) and T_{mean} are defined for each source, we computed the MFDs of expected
331 seismicity. For each fault source, we use two “end-member” MFD models: (i) a
332 *Characteristic Gaussian (CHG)* model, a symmetric Gaussian curve (applied to the
333 incremental MFD values) centred on the M_{max} value of each fault with a range of
334 magnitudes equal to 1-sigma, and (ii) a *Truncated Gutenberg-Richter (TGR, Ordaz,*
335 *1999; Kagan, 2002)* model, with M_{max} as the upper threshold and $M_w = 5.5$ as the
336 minimum threshold for all sources. **The b-values are constant and equal to 1.0 for all**
337 **faults, and they are obtained by the interpolation of earthquake data from the CPTI15**
338 **catalogue, as single-source events are insufficient for calculating the required**
339 **statistics.** The a-values were computed with the ActivityRate tool of the FiSH code.
340 **ActivityRate balances the total expected seismic moment rate with the seismic**
341 **moment rate that was obtained based on M_{max} and T_{mean} (details in Pace et al.,**
342 **2016).** In Figure 2c, we show an example of the expected seismicity rates in terms of
343 the annual cumulative rates for the Paganica source using the two above-described
344 MFDs.
345 **Finally, we create a so-called “expert judgement” model, called the *Mixed* model, to**
346 **determine the MFD for each fault source based on the earthquake-source**
347 **associations. In this case, we decided that if an earthquake assigned to a fault**
348 **source (see Table 2 for earthquake-source associations) has a magnitude lower than**
349 **the magnitude range in the curve of the *CHG* model distribution, the *TGR* model is**
350 **applied to that fault source. Otherwise, the *CHG* model, which peaks at the**
351 **calculated M_{max} , is applied.** Of course, errors in this approach can originate from the
352 misallocation of historical earthquakes, and we cannot exclude the possibility that
353 potentially active faults responsible for historical earthquakes have not yet been

354 mapped. The MFD model assigned to each fault source in our *Mixed* model is shown
355 in Figure 3.

356

357 **2.2 Distributed Source Inputs**

358 Introducing distributed earthquakes into the [PSH](#) model is necessary because
359 researchers have not been able to identify a causative source (i.e., a mapped fault)
360 for important earthquakes in the historical catalogue. This lack of correlation between
361 earthquakes and faults may be related to (i) interseismic strain accumulation in areas
362 between major faults, (ii) earthquakes occurring on unknown or blind faults, (iii)
363 earthquakes occurring on unmapped faults characterized by slip rates lower than the
364 rates of erosional processes, and/or (iv) the general lack of surface ruptures
365 associated with faults generating $M_w < 5.5$ earthquakes.

366 We used the historical catalogue of earthquakes (CPTI15; Rovida et al., 2016; Fig.
367 4) to model the occurrence of moderate-to-large ($M_w \geq 4.5$) earthquakes. The
368 catalogue consists of 4,427 events and covers approximately the last one thousand
369 years from 01/01/1005 to 28/12/2014. Before using the catalogue, we removed all
370 events not considered mainshocks via a declustering filter (Gardner and Knopoff,
371 1977). This process resulted in a complete catalogue composed of 1,839
372 independent events. Moreover, to avoid any artificial effects related to double
373 counting due to the use of two seismicity sources, i.e., the fault sources and the
374 distributed seismicity sources, we removed events associated with known active
375 faults from the CPTI15 earthquake catalogue. If the causative fault of an earthquake
376 is known, that earthquake does not need to be included in the seismicity smoothing
377 procedure. The earthquake-source association is based on neotectonics,
378 palaeoseismology and seismotectonics papers (see the supplemental files) and, in a
379 few cases, macroseismic intensity maps. In Table 2, we listed the earthquakes with
380 known causative fault sources. The differences in the smoothed rates given by eq.
381 (2) using the complete and modified catalogues are shown in Figure 5.

382 We applied the standard methodology developed by Frankel (1995) to estimate the
383 density of seismicity in a grid with latitudinal and longitudinal spacing of 0.05° . The
384 smoothed rate of events in each cell i is determined as follows:

385
$$n_i = \frac{\sum_j n_j e^{-\frac{\Delta_{ij}^2}{c^2}}}{\sum_j e^{-\frac{\Delta_{ij}^2}{c^2}}} \quad (2)$$

386 where n_i is the cumulative rate of earthquakes with magnitudes greater than the
 387 completeness magnitude M_c in each cell i of the grid and Δ_{ij} is the distance between
 388 the centres of grid cells i and j . The parameter c is the correlation distance. The sum
 389 is calculated in cells j within a distance of $3c$ of cell i .

390 To compute earthquake rates, we adopted the completeness magnitude thresholds
 391 over different periods given by Stucchi et al. (2011) for five large zones (Fig. 4).

392 To optimize the smoothing distance Δ in eq. (2), we divided the earthquake
 393 catalogue into four 10-yr disjoint learning and target periods from the 1960s to the
 394 1990s. For each pair of learning and target catalogues, we used the probability gain
 395 per earthquake to find the optimal smoothing distance (Kagan and Knopoff, 1977;
 396 Helmstetter et al., 2007). After assuming a spatially uniform earthquake density
 397 model as a reference model, the probability gain per earthquake G of a candidate
 398 model relative to a reference model is given by the following equation:

399
$$G = \exp\left(\frac{L-L_0}{N}\right) \quad (3)$$

400 where N is the number of events in the target catalogue and L and L_0 are the joint
 401 log-likelihoods of the candidate model and reference model, respectively. Under the
 402 assumption of a Poisson earthquake distribution, the joint log-likelihood of a model is
 403 given as follows:

404
$$L = \sum_{i_x=1}^{N_x} \sum_{j_y=1}^{N_y} \log p [\lambda(i_x, i_y), \omega] \quad (4)$$

405 where p is the Poisson probability, λ is the spatial density, ω is the number of
 406 observed events during the target period, and the parameters i_x and i_y denote each
 407 corresponding longitude-latitude cell.

408 Figure 6 shows that for the four different pairs of learning-target catalogues, the
 409 optimal smoothing distance c ranges from 30-40 km. Finally, the mean of all the

410 probability gains per earthquake yields a maximum smoothing distance of 30 km
411 (Fig. 6), which is then used in eq. (2).

412 The b-value of the GR distribution is calculated on a regional basis using the
413 maximum-likelihood method of Weichert (1980), which allows multiple periods with
414 varying completeness levels to be combined. Following the approach recently
415 proposed by Kamer and Hiemer (2015), we used a penalized likelihood-based
416 method for the spatial estimation of the GR b-values based on the Voronoi
417 tessellation of space without tectonic dependency. The whole Italian territory has
418 been divided into a grid with a longitude/latitude spacing of 0.05° , and the centres of
419 the grid cells represent the possible centres of Voronoi polygons. We vary the
420 number of Voronoi polygons, N_v , from 3 to 50, generating 1000 tessellations for
421 each N_v . The summed log-likelihood of each obtained tessellation is compared with
422 the log-likelihood given by the simplest model (prior model) obtained using the entire
423 earthquake dataset. We find that 673 random realizations led to better performance
424 than the prior model. Thus, we calculate an ensemble model using these 673
425 solutions, and the mean b-value of each grid node is shown in Figure 4.

426 The maximum magnitude M_{max} assigned to each node of the grid, the nodal planes
427 and the depths have been taken from the SHARE European project (Woessner et
428 al., 2015). The SHARE project evaluated the maximum magnitudes of large areas of
429 Europe based on a joint procedure involving historical observations and tectonic
430 regionalization. We adopted the lowest of the maximum magnitudes proposed by
431 SHARE, but evaluating the impact of different maximum magnitudes is beyond the
432 scope of this work.

433 Finally, the rates of expected seismicity for each node of the grid are assumed to
434 follow the TGR model (Kagan 2002):

$$435 \quad \lambda(M) = \lambda_0 \frac{\exp(-\beta M) - \exp(-\beta M_u)}{\exp(-\beta M_0) - \exp(-\beta M_u)} \quad (5)$$

436 where the magnitude (M) is in the range of M_0 (minimum magnitude) to M_u (upper or
437 maximum magnitude); otherwise $\lambda(M)$ is 0. Additionally, λ_0 is the smoothed rate of
438 earthquakes at $M_w = 4.5$ and $\beta = b \ln(10)$.

439 **2.3 Combining Fault and Distributed Sources**

440 To combine the two source inputs, we introduced a distance-dependent linear
441 weighting function, such that the contribution from the distributed sources linearly
442 decreases from 1 to 0 with decreasing distance from the fault. The expected
443 seismicity rates of the distributed sources start at $M_w = 4.5$, which is lower than the
444 minimum magnitude of the fault sources, and the weighting function is only
445 applicable in the magnitude range overlapping the MFD of each fault. This weighting
446 function is based on the assumption that faults tend to modify the surrounding
447 deformation field (Fig. 7), and this assumption is explained in detail later in this
448 paper.

449 During fault system evolution, the increase in the size of a fault through linking with
450 other faults results in an increase in displacement that is proportional to the quantity
451 of strain accommodated by the fault (Kostrov, 1974). Under a constant regional
452 strain rate, the activity of arranged across strike must eventually decrease (Nicol et
453 al., 1997; Cowie, 1998; Roberts et al., 2004). Using an analogue modelling,
454 Mansfield and Cartwright (2001) showed that faults grow via cycles of overlap, relay
455 formation, breaching and linkage between neighbouring segments across a wide
456 range of scales. During the evolution of a system, the merging of neighbour faults,
457 mostly along the strike, results in the formation of major faults, which are associated
458 with the majority of displacement. These major faults are surrounded by minor faults,
459 which are associated with lower degrees of displacement. To highlight the spatial
460 patterns of major and minor faults, Figures 7a and 7b present diagrams from the
461 Mansfield and Cartwright (2001) experiment in two different stages: the approximate
462 midpoint of the sequence and the end of the sequence. Numerical modelling
463 performed by Cowie et al. (1993) yielded similar evolutionary features for major and
464 minor faults. The numerical fault simulation of Cowie et al. (1993) was able to
465 reproduce the development of a normal fault system from the early nucleation stage,
466 including interactions with adjacent faults, to full linkage and the formation of a large
467 through fault. The model also captures the increase in the displacement rate of a
468 large linked fault. In Figures 7c and 7d, we focus on two stages of the simulation
469 (from Cowie et al., 1993): the stage in which the fault segments have formed and
470 some have become linked and the final stage of the simulation.

471 Notably, the spatial distributions of major and minor faults are very similar in the
472 experiments of both Mansfield and Cartwright (2001) and Cowie et al. (1993), as
473 shown in Figures 7a-d. Developments during the early stage of major fault formation
474 appear to control the location and evolution of future faults, with some areas where
475 no major faults develop. The long-term evolution of a fault system is the
476 consequence of the progressive cumulative effects of the slip history, i.e.,
477 earthquake occurrence, of each fault. Large earthquakes are generally thought to
478 produce static and dynamic stress changes in the surrounding areas (King et al.,
479 1994; Stein, 1999; Pace et al., 2014; Verdecchia and Carena, 2016). Static stress
480 changes produce areas of negative stress, also known as shadow zones, and
481 positive stress zones. The spatial distributions of decreases (unloading) and
482 increases (loading) in stress during the long-term slip history of faults likely influence
483 the distance across strike between major faults. Thus, given a known major active
484 fault geometrically capable of hosting a $M_w \geq 5.5$ earthquake, the possibility that a
485 future $M_w \geq 5.5$ earthquake will occur in the vicinity of the fault, but is not caused by
486 that fault, should decrease as the distance from the fault decreases. Conversely,
487 earthquakes with magnitudes lower than 5.5 and those due to slip along minor faults
488 are likely to occur everywhere within a fault system, including in proximity to a major
489 fault.

490 In Figure 7e, we illustrate the results of the analogue and numerical modelling of
491 fault system evolution and indicate the areas around major faults where it is unlikely
492 that other major faults develop. In Figure 7f, we show the next step in moving from
493 geologic and structural considerations. In this step, we combine fault sources and
494 distributed seismicity source inputs, which serve as inputs for the PSH model. Fault
495 sources are used to model major faults and are represented by a master fault (i.e.,
496 one or more major faults) and its projection at the surface. Distributed seismicity is
497 used to model seismicity associated with minor, unknown or unmapped faults.
498 Depending on the positions of distributed seismicity points with respect to the buffer
499 zones around major faults, the rates of expected distributed seismicity remain
500 unmodified or decrease and can even reach zero.

501 Specifically, we introduced a slip rate and a distance-weighted linear function based
502 on the above reasoning. The probability of the occurrence of an earthquake (P_e) with
503 a M_w greater than or equal to the minimum magnitude of the fault is as follows:

$$Pe = \begin{cases} 0, & d \leq 1 \text{ km} \\ d/d_{max}, & 1 \text{ km} < d \leq d_{max} \\ 1, & d > d_{max} \end{cases} \quad (6)$$

505 where d is the Joyner-Boore distance from a fault source. The maximum value of d
 506 (d_{max}) is controlled by the slip rate of the fault. For faults with slip rates ≥ 1 mm/yr, we
 507 assume $d_{max} = L/2$ (L is the length along the strike, Fig. 2a); for faults with slip rates
 508 of 0.3 - 1 mm/yr, $d_{max} = L/3$; and for faults with slip rates of ≤ 0.3 mm/yr, $d_{max} = L/4$.
 509 The rationale for varying d_{max} is given by a simple assumption: the higher the slip
 510 rate is, the larger the deformation field and the higher the value of d_{max} . We applied
 511 eq. (6) to the smoothed occurrence rates of the distributed seismogenic sources.
 512 Because we consider two fault source inputs, one using only TGR MFD and the
 513 other only CHR MFD, and because the MFDs of distributed seismicity grid points in
 514 the vicinity of faults are modified with respect to the MFDs of these faults, we obtain
 515 two different inputs of distributed seismicity. These two distributed seismogenic
 516 source inputs differ because the minimum magnitude of the faults is Mw 5.5 in the
 517 TGR model, but this value depends on each fault source dimension in the CHG
 518 model, as shown in Figure 8.

519 Our approach allows incompleteness in the fault database to be bypassed, which is
 520 advantageous because all fault databases should be considered incomplete. In our
 521 approach, the seismicity is modified only in the vicinity of mapped faults. The
 522 remaining areas are fully described by the *distributed* input. With this approach, we
 523 do not define areas with reliable fault information, and the locations of currently
 524 unknown faults can be easily included when they are discovered in the future.

525 3. Results and Discussion

526 To ~~obtain PSH map~~ we assign the calculated seismicity rates, based on the
 527 Poisson hypothesis, to their pertinent geometries, i.e., individual 3D seismogenic
 528 sources for the *fault input* and point sources for the *distributed input* (Fig. 8). All the
 529 computations are performed using the OpenQuake Engine (Global Earthquake
 530 Model, 2016) with a grid spacing of 0.05° in both latitude and longitude. We used this
 531 software because it is open source software developed recently by GEM with the
 532 purpose of providing seismic hazard and risk assessments. Moreover, it is widely
 533 recognized within the scientific community for its potential. The ground motion

534 prediction equations (GMPE) of Akkar et al. (2013), Chiou et al., (2008), Faccioli et
535 al., (2010) and Zhao et al., (2006) are used, ~~as suggested by the SHARE European~~
536 ~~project~~ (Woessner et al., 2015). In addition, we used the GMPE proposed by Bindi et
537 al. (2014) and calibrated using Italian data. We combined all GMPEs into a logic tree
538 with the same weight of 0.2 for each branch. The distance used for each GMPE was
539 the Joyner and Boore distance for Akkar et al. (2013), Bindi et al. (2014) and Chiou
540 et al. (2008) and the closest rupture distance for Faccioli et al. (2010) and Zhao et al.
541 (2006).

542 The results of the fault source inputs, distributed source inputs, and aggregated
543 model are expressed in terms of peak ground acceleration (PGA) based on
544 exceedance probabilities of 10% and 2% over 50 years, corresponding to return
545 periods of 475 and 2,475 years, respectively (Fig. 9).

546 To explore the epistemic uncertainty associated with the distribution of activity rates
547 over the range of magnitudes of fault source inputs, we compared the seismic
548 hazard levels obtained based on the TGR and CHG fault source inputs (left column
549 in Fig. 9) using the TGR and CHG MFDs for all the fault sources (details in section
550 2.1.3). Although both models have the same seismic moment release, the different
551 MFDs generate clear differences. In fact, in the *TGR* model, all faults contribute
552 significantly to the seismic hazard level, whereas in the *CHG* model, only a few faults
553 located in the central Apennines and Calabria contribute to the seismic hazard level.
554 This difference is due to the different shapes of the MFDs in the two models (Fig.
555 2c). As shown in Figure 8, the percentage of earthquakes with magnitudes between
556 5.5 and approximately 6, which are likely the main contributors to these levels of
557 seismic hazards, is generally higher in the *TGR* model than in the *CHG* model. At a
558 2% probability of exceedance in 50 years, all fault sources in the CHG contribute to
559 the seismic hazard level, but the absolute values are still generally higher in the *TGR*
560 model.

561 The *distributed input* (middle column in Fig. 9) depicts a more uniform shape of the
562 seismic hazard level than that of fault source inputs. A low PGA value of 0.125 g at a
563 10% probability of exceedance over 50 years and a low value of 0.225 g at a 2%
564 probability of exceedance over 50 years encompass a large part of peninsular Italy

565 and Sicily. Two areas with high seismic hazard levels are located in the central
566 Apennines and northeastern Sicily.

567 The overall model, which was created by combining the fault and distributed source
568 inputs, is shown in the right column of Figure 9. Areas with comparatively high
569 seismic hazard levels, i.e., hazard levels greater than 0.225 g and greater than 0.45
570 g at 50-yr exceedance probabilities of 10% and 2%, respectively, are located
571 throughout the Apennines, in Calabria and in Sicily. The fault source inputs
572 contribute most to the total seismic hazard levels in the Apennines, Calabria and
573 eastern Sicily, where the highest PGA values are observed.

574 Figure 10 shows the contributions to the total seismic hazard level by the *fault* and
575 *distributed* source inputs at a specific site (L'Aquila, 42.400-13.400). Notably, in
576 Figure 10, *distributed* sources dominate the seismic hazard contribution at
577 exceedance probabilities greater than ~81% over 50 years, but the contribution of
578 *fault* sources cannot be neglected. Conversely, at exceedance probabilities of less
579 than ~10% in 50 years, the total hazard level is mainly associated with *fault* source
580 inputs.

581 Figure 11 presents seismic hazard maps for PGAs at 10% and 2% exceedance
582 probabilities in 50 years for *fault* sources, *distributed* sources and a combination of
583 the two. These data were obtained using the above-described *Mixed* model, in which
584 we selected the most "appropriate" MFD model (TGR or CHG) for each fault (as
585 shown in Figure 3). The results of this model therefore have values between those of
586 the two end-members shown in Figure 9.

587 Figure 12 shows the *CHG*, *TGR* and *Mixed* model hazard curves of three sites
588 (Cesena, L'Aquila and Crotone, Fig. 13c). As previously noted, the results of the
589 *Mixed* model, due to the structure of the model, are between those of the *CHG* and
590 *TGR* models. The relative positions of the hazard curves derived from the two end-
591 member models and the *Mixed* model depend on the number of nearby fault sources
592 that have been modelled using one of the MFD models and on the distance of the
593 site from the faults. For example, in the case of the Crotone site, the majority of the
594 fault sources in the *Mixed* model are modelled using the CHG MFD. Thus, the
595 resulting hazard curve is similar to that of the *CHG* model. For the Cesena site, the

596 three hazard curves overlap. Because the distance between Cesena and the closest
597 fault sources is approximately 60 km, the impact of the fault input is less than the
598 impact of the *distributed* source input. In this case, the choice of a particular MFD
599 model has a limited impact on the modelling of *distributed* sources. Notably, for an
600 annual frequency of exceedance (*AFOE*) lower than 10^{-4} , the *TGR fault* source input
601 values are generally higher than those of the *CHG* source input, and the three
602 models converge at $AFOE < 10^{-4}$. The resulting seismic hazard estimates depend on
603 the assumed MFD model (*TGR* vs. *CHG*), especially for intermediate-magnitude
604 events (5.5 to ~6.5). Because we assume that the maximum magnitude is imposed
605 by the fault geometry and that the seismic moment release is controlled by the slip
606 rate, the *TGR* model leads to the highest hazard values because this range of
607 magnitude contributes the most to the hazard level.

608 In Figure 13, we investigated the influences of the Mixed *fault* source inputs and the
609 Mixed *distributed* source inputs on the total hazard level of the entire study area, as
610 well as the variability in the hazard results. The maps in Figure 13a show that the
611 contribution of *fault* inputs to the total hazard level generally decreases as the
612 exceedance probability increases from 2% to 81% in 50 years. At a 2% probability of
613 exceedance in 50 years, the total hazard levels in the Apennines and eastern Sicily
614 are mainly related to faults, whereas at an 81% probability of exceedance in 50
615 years, the contributions of *fault* inputs are high in local areas of central Italy and
616 southern Calabria.

617 Moreover, we examined the contributions of *fault* and *distributed* sources along three
618 E-W-oriented profiles in northern, central and southern Italy (Fig. 13b). Note that the
619 contributions are not based on deaggregation but are computed according to the
620 percentage of each source input in the *AFOE* value of the combined model. In areas
621 with faults, the hazard level estimated by *fault* inputs is generally higher than that
622 estimated by the corresponding *distributed* source inputs. Notable exceptions are
623 present in areas proximal to slow-slipping active faults at an 81% probability of
624 exceedance in 50 years (profile A), such as those at the eastern and western
625 boundaries of the fault area in central Italy (profile B), and in areas where the
626 contribution of the *distributed* source input is equal to that of the *fault* input at a 10%
627 probability of exceedance in 50 years (eastern part of profile C).

628 The features depicted by the three profiles result from a combination of the slip rates
629 and spatial distributions of faults for *fault* source inputs. This pattern should be
630 considered a critical aspect of using fault models for PSH analysis. In fact, the
631 proposed approach requires a high level of expertise in active tectonics and cautious
632 expert judgement at many levels in the procedure. First, the seismic hazard estimate
633 is based on the definition of a segmentation model, which requires a series of rules
634 based on observations and empirical regression between earthquakes and the size
635 of the causative fault. New data might make it necessary to revise the rules or
636 reconsider the role of the segmentation. In some cases, expert judgement could
637 permit discrimination among different fault source models. Alternatively, all models
638 should be considered branches in a logic tree approach.

639 Moreover, we propose a fault seismicity input in which the MFD of each fault source
640 has been chosen based on an analysis of the occurrences of earthquakes that can
641 be tentatively or confidently assigned to a certain fault. To describe the fault activity,
642 we applied a probability density function to the magnitude, as commonly performed
643 in the literature: the TGR model, where the maximum magnitude is the upper
644 threshold and $M_w = 5.5$ is the lower threshold for all faults, and the characteristic
645 maximum magnitude model, which consists of a truncated normal distribution
646 centred on the maximum magnitude. Other MFDs have been proposed to model the
647 earthquake recurrence of a fault. For example, Youngs and Coppersmith (1985)
648 proposed a modification to the truncated exponential model to allow for the
649 increased likelihood of characteristic events. However, we focused only on two
650 models, as we believe that instead of a “blind” or qualitative characterization of the
651 MFD of a fault source, future applications of statistical tests of the compatibility
652 between expected earthquake rates and observed historical seismicity could be used
653 as an objective method of identifying the optimal MFD of expected seismicity.

654 To focus on the general procedure for spatially integrating faults with sources
655 representing distributed (or off-fault) seismicity, we did not investigate the impact of
656 other smoothing procedures on the distributed sources, and we used fixed kernels
657 with a constant bandwidth (as in the works of Kagan and Jackson, 1994; Frankel et
658 al. 1997; Zechar and Jordan, 2010). The testing of adaptive bandwidths (e.g., Stock



and Smith, 2002; Helmstetter et al., 2006, 2007; Werner et al., 2011) or weighted combinations of both models has been reserved for future studies.

661

662 Finally, we compared, as shown in Figure 14, the 2013 European Seismic Hazard
663 Model (ESHM13) developed within the SHARE project, the current Italian national
664 seismic hazard map (MPS04) and the results of our model (Mixed model) using the
665 same GMPEs as used in this study. Specifically, for ESHM13, we compared the
666 results to the fault-based hazard map (FSBG model) that accounts for fault sources
667 and background seismicity. The figure shows how the impact of our fault sources is
668 more evident than in FSBG-ESHM13, and the comparison with MPS04 confirms a
669 similar pattern, but with some significant differences at the regional to local scales.

670

671 The strength of our approach lies in the integration of different levels of information
672 regarding the active faults in Italy, but the final result is unavoidably linked to the
673 quality of the relevant data. Our work focused on presenting and applying a new
674 approach for evaluating seismic hazards based on active faults and intentionally
675 avoided the introduction of uncertainties due to the use of different segmentation
676 rules or other slip rate values of faults. Moreover, the impact of ground motion
677 predictive models is important in seismic hazard assessment but beyond the scope
678 of this work. Future steps will be devoted to analysing these uncertainties and
679 evaluating their impacts on seismic hazard estimates.

680

681 4. Conclusions

682 We presented ~~our first national scale PSH model of Italy~~, which summarizes and
683 integrates the fault-based PSH models ~~developed since the publication of Pace et al.~~
684 ~~in 2006.~~

685 The model proposed in this study combines fault source inputs based on over 110
686 faults grouped into 86 fault sources and distributed source inputs. For each fault
687 source, the maximum magnitude and its uncertainty were derived by applying
688 scaling relationships, and the rates of seismic activity were derived by applying slip
689 rates to seismic moment evaluations and balancing these seismic moments using
690 two MFD models.

691 To account for unknown faults, a distributed seismicity input was applied following
692 the well-known Frankel (1995) methodology to calculate seismicity parameters.

693 The fault sources and distributed sources have been integrated via a new approach
694 based on the idea that deformation in the vicinity of an active fault is concentrated
695 along the fault and that the seismic activity in the surrounding region is reduced. In
696 particular, a distance-dependent linear weighting function has been introduced to
697 allow the contribution of distributed sources (in the magnitude range overlapping the
698 MFD of each fault source) to linearly decrease from 1 to 0 with decreasing distance
699 from a fault. The strength of our approach lies in the ability to integrate different
700 levels of available information for active faults that actually exist in Italy (or
701 elsewhere), but the final result is unavoidably linked to the quality of the relevant
702 data.

703 The PSH maps produced using our model show a hazard pattern similar to that of
704 the current maps at the national scale, but some significant differences in hazard
705 level are present at the regional to local scales (Figure 13).

706 Moreover, the impact that using different MFD models to derive seismic activity rates
707 has on the hazard maps was investigated. The PGA values in the hazard maps
708 generated by the *TGR* model are higher than those in the hazard maps generated by
709 the *CHG* model. This difference is because the rates of earthquakes with
710 magnitudes from 5.5 to approximately 6 are generally higher in the *TGR* model than
711 in the *CHG* model. Moreover, the relative contributions of fault source inputs and
712 distributed source inputs have been identified in maps and profiles in three sectors of
713 the study area. These profiles show that the hazard level is generally higher where

714 fault inputs are used, and for high probabilities of exceedance, the contribution of
715 distributed inputs equals that of fault inputs.

716 Finally, the *Mixed* model was created by selecting the most appropriate MFD model
717 for each fault. All data, including the locations and parameters of fault sources, are
718 provided in the supplemental files of this paper.

719 This new PSH model is not intended to replace, integrate or assess the current
720 official national seismic hazard model of Italy. While some aspects remain to be
721 implemented in our approach (e.g., the integration of reverse/thrust faults in the
722 database, sensitivity tests for the distance-dependent linear weighting function
723 parameters, sensitivity tests for potential different segmentation models, and fault
724 source inputs that account for fault interactions), the proposed model represents

725 advancements in terms of input data (quantity and quality) and methodology based
726 on a decade of research in the field of fault-based approaches to regional seismic
727 hazard modelling.

728

729

730

731

732

733

734

735 **References**

736

737

738 Akinci, A., Galadini, F., Pantosti, D., Petersen, M., Malagnini, L., and Perkins, D.:
739 Effect of Time Dependence on Probabilistic Seismic-Hazard Maps and
740 Deaggregation for the Central Apennines, Italy, *B Seismol Soc Am*, 99, 585-
741 610, 2009.

742 Akkar, S., Sandikkaya, M.A. , Bommer, J.J.: Empirical Ground-Motion Models for
743 Point and Extended-Source Crustal Earthquake Scenarios in Europe and the
744 Middle East, *Bulletin of Earthquake Engineering*, ISSN:1570-761X, 2013.

745 Basili, R., Valensise, G., Vannoli, P., Burrato, P., Fracassi, U., Mariano, S., Tiberti,
746 M. M. and Boschi, E.: The Database of Individual Seismogenic Sources
747 (DISS), version 3: Summarizing 20 years of research on Italy's earthquake
748 geology, *Tectonophysics*, 453, 20- 43, 2008.

749 Benedetti, L., Manighetti, I., Gaudemer, Y., Finkel, R., Malavieille, J., Pou, K., Arnold,
750 M., Aumaitre, G., Bourles, D., and Keddadouche, K.: Earthquake synchrony
751 and clustering on Fucino faults (Central Italy) as revealed from in situ ³⁶Cl-
752 exposure dating, *J Geophys Res-Sol Ea*, 118, 4948-4974, 2013.

753 Bindi, D., Massa, M., Luzi, L., Ameri, G., Pacor, F., Puglia, R., and Augliera, P.: Pan-
754 European ground-motion prediction equations for the average horizontal
755 component of PGA, PGV, and 5%-damped PSA at spectral periods up to 3.0
756 s using the RESORCE dataset (vol 12, pg 391, 2014), *B Earthq Eng*, 12, 431-
757 448, 2014.

758 Boncio, P., Brozzetti, F. and Lavecchia G.: Architecture and seismotectonics of a
759 regional Low-Angle Normal Fault zone in Central Italy. *Tectonics*, 19 (6),
760 1038-1055, 2000.

761 Boncio, P., Lavecchia, G., and Pace, B.: Defining a model of 3D seismogenic
762 sources for Seismic Hazard Assessment applications: The case of central
763 Apennines (Italy), *J Seismol*, 8, 407-425, 2004.

764 Boncio, P., Pizzi, A., Cavuoto, G., Mancini, M., Piacentini, T., Miccadei, E., Cavinato,
765 G. P., Piscitelli, S., Giocoli, A., Ferretti, G., De Ferrari, R., Gallipoli, M. R.,
766 Mucciarelli, M., Di Fiore, V., Franceschini, A., Pergalani, F., Naso, G., and
767 Macroarea, W. G.: Geological and geophysical characterisation of the
768 Paganica - San Gregorio area after the April 6, 2009 L'Aquila earthquake (M-
769 w 6.3, central Italy): implications for site response, *B Geofis Teor Appl*, 52,
770 491-512, 2011.

771 Bull, J. M., Barnes, P. M., Lamarche, G., Sanderson, D. J., Cowie, P. A., Taylor, S.
772 K., and Dix, J. K.: High-resolution record of displacement accumulation on an
773 active normal fault: implications for models of slip accumulation during
774 repeated earthquakes, *J Struct Geol*, 28, 1146-1166, 2006.

775 Chiou, B. S. J. and Youngs, R. R.: An NGA model for the average horizontal
776 component of peak ground motion and response spectra, *Earthq Spectra*, 24,
777 173-215, 2008.

778 Cornell, C.A.: Engineering seismic risk analysis, *Bull. Seism. Soc. Am.*, 58,1583-
779 1606, 1968.

780 Cowie, P. A.: A healing-reloading feedback control on the growth rate of seismogenic
781 faults, *J Struct Geol*, 20, 1075-1087, 1998.

782 Cowie, P. A., Roberts, G. P., Bull, J. M., and Visini, F.: Relationships between fault
783 geometry, slip rate variability and earthquake recurrence in extensional
784 settings, *Geophys J Int*, 189, 143-160, 2012.

785 Cowie, P. A., Underhill, J. R., Behn, M. D., Lin, J., and Gill, C. E.: Spatio-temporal
786 evolution of strain accumulation derived from multi-scale observations of Late
787 Jurassic rifting in the northern North Sea: A critical test of models for
788 lithospheric extension, *Earth Planet Sc Lett*, 234, 401-419, 2005.

789 Cowie, P. A., Vanneste, C., and Sornette, D.: Statistical Physics Model for the
790 Spatiotemporal Evolution of Faults, *J Geophys Res-Sol Ea*, 98, 21809-21821,
791 1993.

792 D'amato, D., Pace, B., Di Nicola, L., Stuart, F.M., Visini, F., Azzaro, R., Branca, S.,
793 and Barfod, D.N.: Holocene slip rate variability along the Pernicana fault
794 system (Mt. Etna, Italy): Evidence from offset lava flows: *GSA Bulletin*,
795 doi:10.1130/B31510.1, 2016.

796 Faccioli, E., Bianchini, A., and Villani, M.: New ground motion prediction equations
797 for $t > 1$ s and their influence on seismic hazard assessment, In: *Proceedings*
798 *of the University of Tokyo symposium on long-period ground motion and*
799 *urban disaster mitigation*, 2010.

800 Ferranti, L., Palano, M., Cannavo, F., Mazzella, M. E., Oldow, J. S., Gueguen, E.,
801 Mattia, M., and Monaco, C.: Rates of geodetic deformation across active
802 faults in southern Italy, *Tectonophysics*, 621, 101-122, 2014.

803 Field, E. H., Biasi, G. P., Bird, P., Dawson, T. E., Felzer, K. R., Jackson, D. D.,
804 Johnson, K. M., Jordan, T. H., Madden, C., Michael, A. J., Milner, K. R., Page,
805 M. T., Parsons, T., Powers, P. M., Shaw, B. E., Thatcher, W. R., Weldon, R.
806 J., and Zeng, Y. H.: Long-Term Time-Dependent Probabilities for the Third
807 Uniform California Earthquake Rupture Forecast (UCERF3), *B Seismol Soc*
808 *Am*, 105, 511-543, 2015.

809 Field, E. H., Jackson, D. D., and Dolan, J. F.: A mutually consistent seismic-hazard
810 source model for southern California, *B Seismol Soc Am*, 89, 559-578, 1999.

811 Finnegan, N. J., Schumer, R., and Finnegan, S.: A signature of transience in bedrock
812 river incision rates over timescales of $10(4)$ - $10(7)$ years, *Nature*, 505, 391-+,
813 2014.

814 Frankel, A.: Simulating Strong Motions of Large Earthquakes Using Recordings of
815 Small Earthquakes - the Loma-Prieta Mainshock as a Test-Case, *B Seismol*
816 *Soc Am*, 85, 1144-1160, 1995.

817 Frankel, A., Mueller, C., Barnhard, T., Perkins, D., Leyendecker, E. V., Dickman, N.,
818 Hanson, S., and Hopper, M.: Seismic-hazard maps for California, Nevada,
819 and Western Arizona/Utah', *U.S. Geological Survey Open-File Rept.* 97-130,
820 1997.

821 Gallen, S. F., Pazzaglia, F. J., Wegmann, K. W., Pederson, J. L., and Gardner, T.
822 W.: The dynamic reference frame of rivers and apparent transience in incision
823 rates, *Geology*, 43, 623-626, 2015.

824 Garcia-Mayordomo, J., Gaspar-Escribano, J. M., and Benito, B.: Seismic hazard
825 assessment of the Province of Murcia (SE Spain): analysis of source
826 contribution to hazard, *J Seismol*, 11, 453-471, 2007.

827 Gardner, J. K., Knopoff, L.: Is the sequence of earthquakes in Southern California,
828 with aftershocks removed, Poissonian?'. *Bulletin of the Seismological Society*
829 *of America*, 64, 1363-1367, 1974.

830 Gardner, T. W., Jorgensen, D. W., Shuman, C., and Lemieux, C. R.: Geomorphic
831 and Tectonic Process Rates - Effects of Measured Time Interval, *Geology*, 15,
832 259-261, 1987.

833 Gasperini P., Bernardini F., Valensise G. and Boschi E.: Defining Seismogenic
834 Sources from Historical Earthquake Felt Reports, *Bull. Seism. Soc. Am.*, 89,
835 94-110, 1999.

836 GEM: The OpenQuake-engine User Manual. Global Earthquake Model (GEM)
837 Technical Report, doi: 10.13117/GEM.OPENQUAKE.MAN.ENGINE.1.9/01,
838 189 pages, 2016.

839 Gunderson, K. L., Anastasio, D. J., Pazzaglia, F. J., and Picotti, V.: Fault slip rate
840 variability on 10(4)-10(5)yr timescales for the Salsomaggiore blind thrust fault,
841 Northern Apennines, Italy, *Tectonophysics*, 608, 356-365, 2013.

842 Hanks, T. C., and Kanamori, H.: A moment magnitude scale, *Journal of Geophysics*
843 *Research*, 84, 2348–2350, 1979.

844 Helmstetter, A., Kagan, Y. Y., and Jackson, D. D.: Comparison of short-term and
845 time-independent earthquake forecast models for southern California, *B*
846 *Seismol Soc Am*, 96, 90-106, 2006.

847 Helmstetter, A., Kagan, Y. Y., and Jackson, D. D.: High-resolution time-independent
848 grid-based forecast for $M \leq 5$ earthquakes in California, *Seismol Res Lett*,
849 78, 78-86, 2007.

850 International Association of Seismology and Physics of the Earth's Interior (IASPEI):
851 Summary of Magnitude Working Group recommendations on standard
852 procedures for determining earthquake magnitudes from digital data,
853 <http://www.iaspei.org/>

854 commissions/CSOI/summary_of_WG_recommendations_2005.pdf (last
855 accessed December 2015), 2005.

856 Kagan, Y. Y.: Seismic moment distribution revisited: I. Statistical results, *Geophys J*
857 *Int*, 148, 520-541, 2002.

858 Kagan, Y., and Knopoff, L.: Earthquake risk prediction as a stochastic process,
859 *Physics of the Earth and Planetary Interiors*, 14, 97–108, 1977.

860 Kagan, Y. Y. and Jackson, D. D.: Long-Term Probabilistic Forecasting of
861 Earthquakes, *J Geophys Res-Sol Ea*, 99, 13685-13700, 1994.

862 Kamer, Y. and Hiemer, S.: Data-driven spatial b value estimation with applications to
863 California seismicity: To b or not to b, *J Geophys Res-Sol Ea*, 120, 5191-
864 5214, 2015.

865 King, G. C. P., Stein, R. S., and Lin, J.: Static Stress Changes and the Triggering of
866 Earthquakes, *B Seismol Soc Am*, 84, 935-953, 1994.

867 Kostrov, V. V.: Seismic moment and energy of earthquakes, and seismic flow of
868 rock, *Physic of the Solid Earth*, 1, 23-44, 1974.

869 Leonard, M.: Earthquake fault scaling: Self-consistent relating of rupture length,
870 width, average displacement, and moment release. *Bulletin of the*
871 *Seismological Society of America*, 100(5A), 1971- 1988, 2010.

872 Machette, M.N.: Active, capable, and potentially active faults; a paleoseismic
873 perspective, *J. Geodyn.*, 29, 387–392, 2000.

874 Main, I.: Statistical physics, seismogenesis, and seismic hazard, *Rev Geophys*, 34,
875 433-462, 1996.

876 Mansfield, C. and Cartwright, J.: Fault growth by linkage: observations and
877 implications from analogue models, *J Struct Geol*, 23, 745-763, 2001.

878 Meletti, C., Visini, F., D'Amico, V., and Rovida A.: Seismic hazard in central Italy and
879 the 2016 Amatrice earthquake, *Annals of Geophysics*, 59, doi:10.4401/ag-
880 7248, 2016.

881 McClymont, A. F., Villamor, P., and Green, A. G.: Assessing the contribution of off-
882 fault deformation to slip-rate estimates within the Taupo Rift, New Zealand,
883 using 3-D ground-penetrating radar surveying and trenching, *Terra Nova*, 21,
884 446-451, 2009a.

885 McClymont, A. F., Villamor, P., and Green, A. G.: Fault displacement accumulation
886 and slip rate variability within the Taupo Rift (New Zealand) based on trench
887 and 3-D ground-penetrating radar data, *Tectonics*, 28, 2009b.

888 Nicol, A., Walsh, J., Berryman, K., and Villamor, P.: Interdependence of fault
889 displacement rates and paleoearthquakes in an active rift, *Geology*, 34, 865-
890 868, 2006.

891 Nicol, A., Walsh, J., Mouslopoulou, V., and Villamor, P.: Earthquake histories and
892 Holocene acceleration of fault displacement rates, *Geology*, 37, 911-914,
893 2009.

894 Nicol, A., Walsh, J. J., Villamor, P., Seebeck, H., and Berryman, K. R.: Normal fault
895 interactions, paleoearthquakes and growth in an active rift, *J Struct Geol*, 32,
896 1101-1113, 2010.

897 Nicol, A., Walsh, J. J., Watterson, J., and Underhill, J. R.: Displacement rates of
898 normal faults, *Nature*, 390, 157-159, 1997.

899 Ordaz, M. and Reyes, C.: Earthquake hazard in Mexico City: Observations versus
900 computations, *B Seismol Soc Am*, 89, 1379-1383, 1999.

901 Pace, B., Bocchini, G. M., and Boncio, P.: Do static stress changes of a moderate-
902 magnitude earthquake significantly modify the regional seismic hazard? Hints
903 from the L'Aquila 2009 normal-faulting earthquake (Mw 6.3, central Italy),
904 *Terra Nova*, 26, 430-439, 2014.

905 Pace, B., Peruzza, L., Lavecchia, G., and Boncio, P.: Layered seismogenic source
906 model and probabilistic seismic-hazard analyses in central Italy, *B Seismol
907 Soc Am*, 96, 107-132, 2006.

908 Pace, B., Visini, F., and Peruzza, L.: FiSH: MATLAB Tools to Turn Fault Data into
909 Seismic-Hazard Models, *Seismol Res Lett*, 87, 374-386, 2016.

910 Peruzza, L., and Pace B.: Sensitivity analysis for seismic source characteristics to
911 probabilistic seismic hazard assessment in central Apennines (Abruzzo area),
912 *Bollettino di Geofisica Teorica ed Applicata* 43, 79–100, 2002.

913 Peruzza, L., Pace, B., and Visini, F.: Fault-Based Earthquake Rupture Forecast in
914 Central Italy: Remarks after the L'Aquila M-w 6.3 Event, *B Seismol Soc Am*,
915 101, 404-412, 2011.

916 Peruzza, L., Gee, R., Pace, B., Roberts, G., Scotti, O., Visini, F., Benedetti, L., and
917 Pagani, M.: PSHA after a strong earthquake: hints for the recovery, *Annals of
918 Geophysics*, 59, doi:10.4401/ag-7257, 2016

919 Roberts, G. P., Cowie, P., Papanikolaou, I., and Michetti, A. M.: Fault scaling
920 relationships, deformation rates and seismic hazards: an example from the
921 Lazio-Abruzzo Apennines, central Italy, *J Struct Geol*, 26, 377-398, 2004.

922 Roberts, G. P. and Michetti, A. M.: Spatial and temporal variations in growth rates
923 along active normal fault systems: an example from The Lazio-Abruzzo
924 Apennines, central Italy, *J Struct Geol*, 26, 339-376, 2004.

925 Robinson, R., Nicol, A., Walsh, J. J., and Villamor, P.: Features of earthquake
926 occurrence in a complex normal fault network: Results from a synthetic
927 seismicity model of the Taupo Rift, New Zealand, *J Geophys Res-Sol Ea*, 114,
928 2009.

929 Rovida, A., Locati, M., Camassi, R., Lolli, B., and Gasperini P.: CPTI15, the 2015
930 version of the Parametric Catalogue of Italian Earthquakes. Istituto Nazionale
931 di Geofisica e Vulcanologia. doi:<http://doi.org/10.6092/INGV.IT-CPTI15>, 2016.

932 Scotti, O., Clement, C., and Baumont, D.: Seismic hazard for design and verification
933 of nuclear installations in France: regulatory context, debated issues and
934 ongoing developments, *B Geofis Teor Appl*, 55, 135-148, 2014.

935 Stein, R. S., King, G. C. P., and Lin, J.: Stress Triggering of the 1994 M=6.7
936 Northridge, California, Earthquake by Its Predecessors, *Science*, 265, 1432-
937 1435, 1994.

938 Stirling, M., McVerry, G., Gerstenberger, M., Litchfield, N., Van Dissen, R.,
939 Berryman, K., Barnes, P., Wallace, L., Villamor, P., Langridge, R., Lamarche,
940 G., Nodder, S., Reyners, M., Bradley, B., Rhoades, D., Smith, W., Nicol, A.,
941 Pettinga, J., Clark, K., and Jacobs, K.: National Seismic Hazard Model for
942 New Zealand: 2010 Update, *B Seismol Soc Am*, 102, 1514-1542, 2012.

943 Stock, C. and Smith, E. G. C.: Adaptive kernel estimation and continuous probability
944 representation of historical earthquake catalogs, *B Seismol Soc Am*, 92, 904-
945 912, 2002a.

946 Stock, C. and Smith, E. G. C.: Comparison of seismicity models generated by
947 different kernel estimations, *B Seismol Soc Am*, 92, 913-922, 2002b.

948 Stucchi, M., Meletti, C., Montaldo, V., Crowley, H., Calvi, G. M., and Boschi, E.:
949 Seismic Hazard Assessment (2003-2009) for the Italian Building Code, *B*
950 *Seismol Soc Am*, 101, 1885-1911, 2011.

951 Verdecchia, A. and Carena, S.: Coulomb stress evolution in a diffuse plate boundary:
952 1400 years of earthquakes in eastern California and western Nevada, USA,
953 *Tectonics*, 35, 1793-1811, 2016.

954 Visini, F. and Pace, B.: Insights on a Key Parameter of Earthquake Forecasting, the
955 Coefficient of Variation of the Recurrence Time, Using a Simple Earthquake
956 Simulator, *Seismol Res Lett*, 85, 703-713, 2014.

957 Weichert, D. H: Estimation of the earthquake recurrence parameters for unequal
958 observation periods for different magnitudes, *Bulletin of the Seismological*
959 *Society of America*, 70, 1337-1346, 1980.

960 Wells, D. L. and Coppersmith, K. J.: New Empirical Relationships among Magnitude,
961 Rupture Length, Rupture Width, Rupture Area, and Surface Displacement, *B*
962 *Seismol Soc Am*, 84, 974-1002, 1994.

963 Werner, M. J., Helmstetter, A., Jackson, D. D., Kagan, Y. Y., and Wiemer, S.:
964 Adaptively smoothed seismicity earthquake forecasts for Italy, *Ann Geophys-*
965 *Italy*, 53, 107-116, 2010.

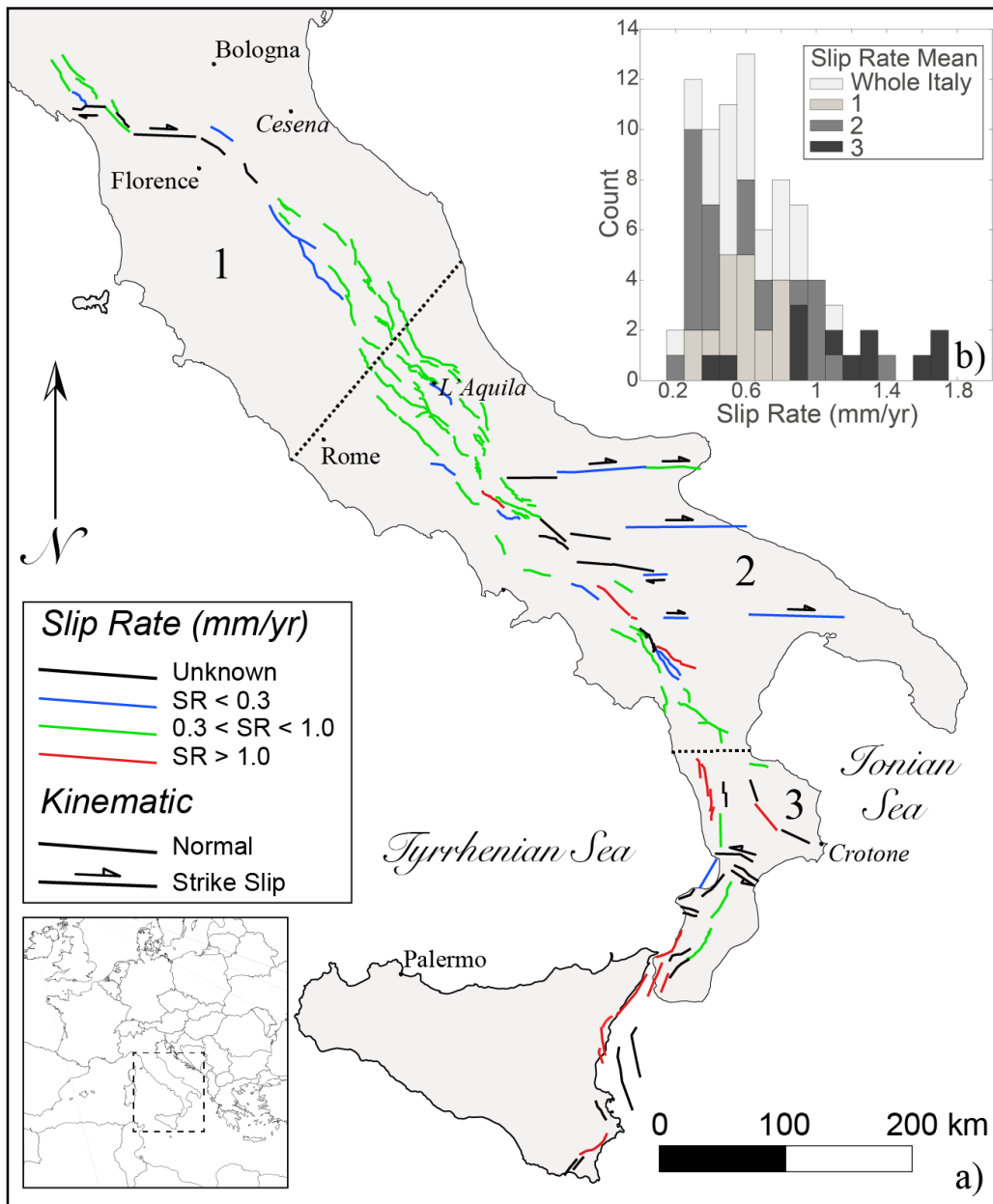
966 Woessner, J., Laurentiu, D., Giardini, D., Crowley, H., Cotton, F., Grunthal, G.,
967 Valensise, G., Arvidsson, R., Basili, R., Demircioglu, M. B., Hiemer, S.,
968 Meletti, C., Musson, R. W., Rovida, A. N., Sesetyan, K., Stucchi, M., and
969 Consortium, S.: The 2013 European Seismic Hazard Model: key components
970 and results, *B Earthq Eng*, 13, 3553-3596, 2015.

971 Youngs, R. R. and Coppersmith, K. J.: Implications of Fault Slip Rates and
972 Earthquake Recurrence Models to Probabilistic Seismic Hazard Estimates, *B*
973 *Seismol Soc Am*, 75, 939-964, 1985.

974 Zechar, J. D. and Jordan, T. H.: Simple smoothed seismicity earthquake forecasts
975 for Italy, *Ann Geophys-Italy*, 53, 99-105, 2010.

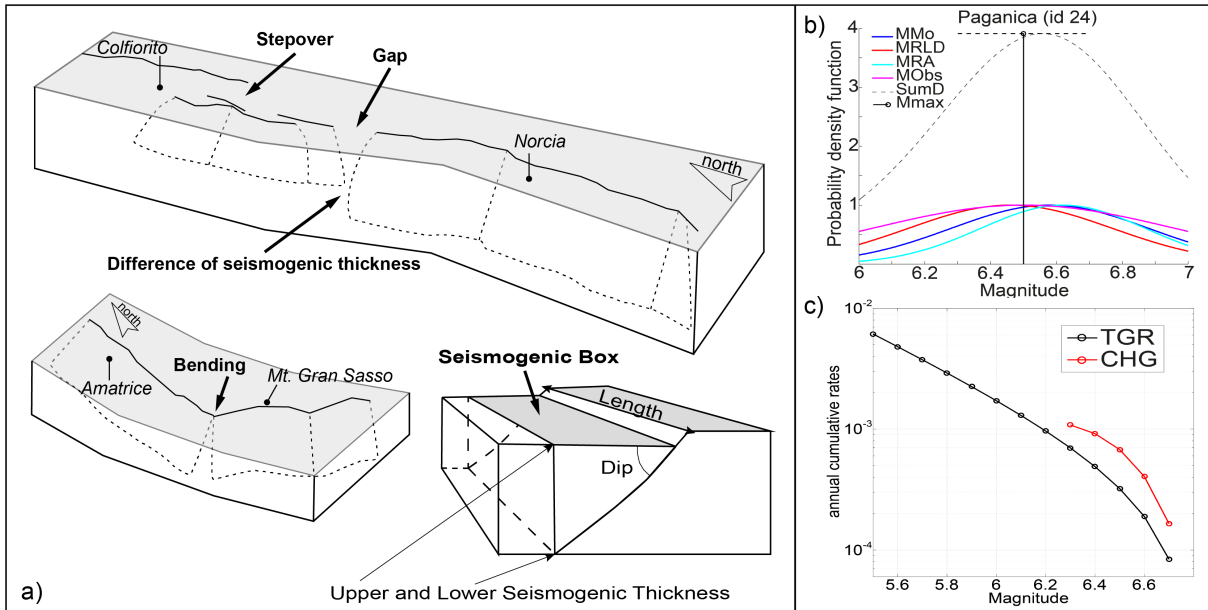
976 Zhao, J. X., Zhang, J., Asano, A., Ohno, Y., Oouchi, T., Takahashi, T., Ogawa, H.,
977 Irikura, K., Thio, H. K., Somerville, P. G., Fukushima, Y., and Fukushima, Y.:
978 Attenuation relations of strong ground motion in Japan using site classification
979 based on predominant period, *B Seismol Soc Am*, 96, 898-913, 2006.

980



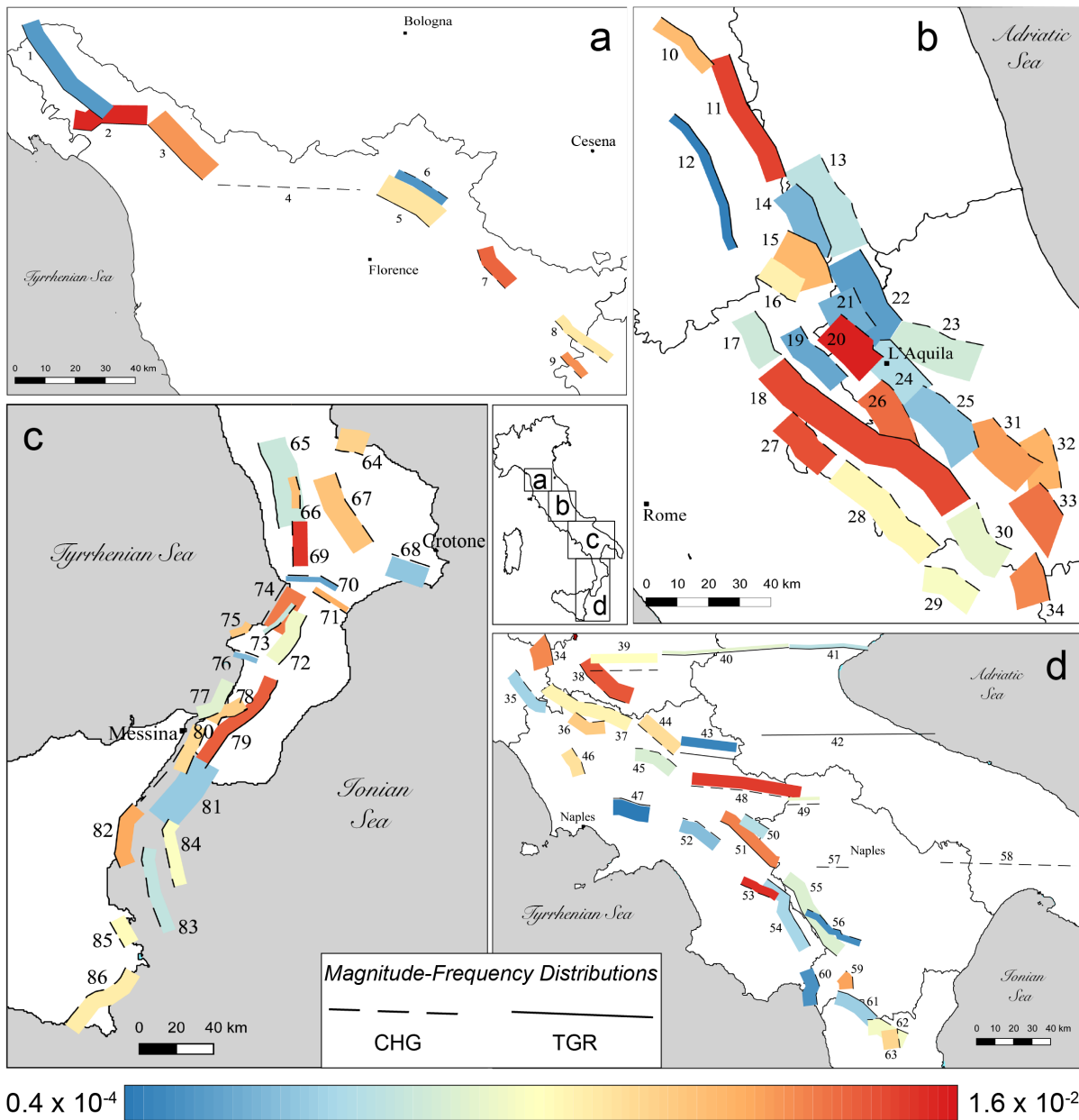
981

982 Fig. 1 a) Map of normal and strike-slip active faults used in this study. The colour
 983 scale indicates the slip rate. b) Histogram of the slip rate distribution in the entire
 984 study area and in three subsectors. The numbers 1, 2 and 3 represent the Northern
 985 Apennines, Central-Southern Apennines and Calabria-Sicilian coast regions,
 986 respectively. The dotted black lines are the boundaries of the regions.



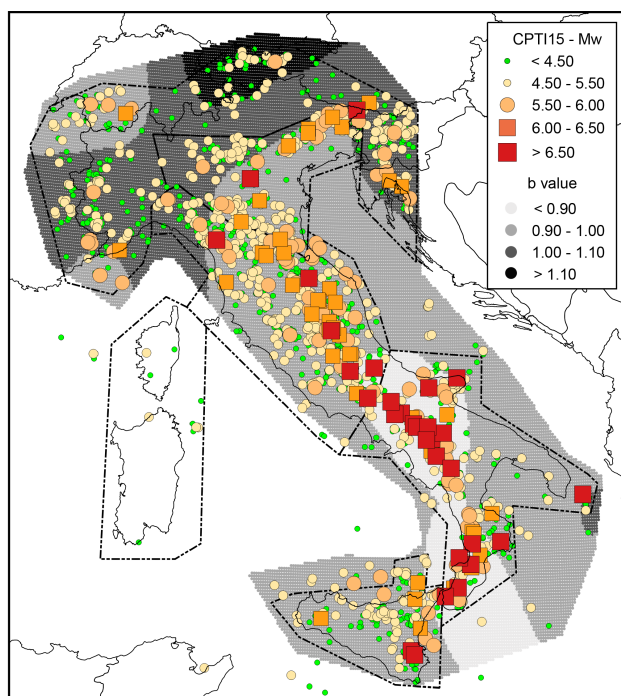
987

988 Fig. 2 a) Conceptual model of active faults and segmentation rules adopted to define
 989 a fault source and its planar projection, forming a seismogenic box [modified from
 990 Boncio et al., 2004]. b) Example of FiSH code output (see Pace et al., 2016 for
 991 details) for the Paganica fault source showing the magnitude estimates from
 992 empirical relationships and observations, both of which are affected by uncertainties.
 993 In this example, four magnitudes are estimated: M_{Mo} (blue line) is from the standard
 994 formula (IASPEI, 2005); M_{RDL} (red line) and M_{RA} (cyan line) correspond to
 995 estimates based on the maximum subsurface fault length and maximum rupture area
 996 from the empirical relationships of Wells and Coppersmith (1994) for length and
 997 area, respectively; and M_{Obs} (magenta line) is the largest observed moment
 998 magnitude. The black dashed line represents the summed probability density curve
 999 (SumD), the vertical black line represents the central value of the Gaussian fit of the
 1000 summed probability density curve (M_{max}), and the horizontal black dashed line
 1001 represents its standard deviation (σ M_{max}). The input values that were used to obtain
 1002 this output are provided in Table 1. c) Comparison of the magnitude–frequency
 1003 distributions of the Paganica source, which were obtained using the CHG model (red
 1004 line) and the TGR model (black line).

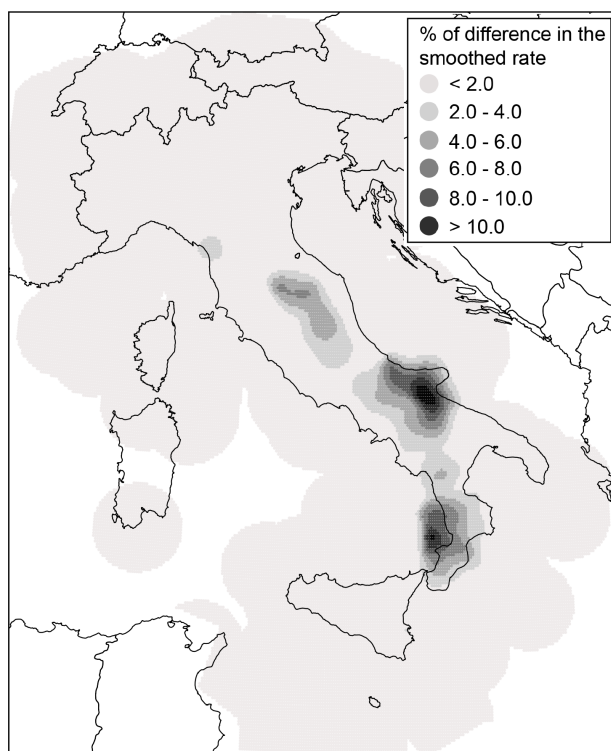


1005
1006
1007
1008
1009

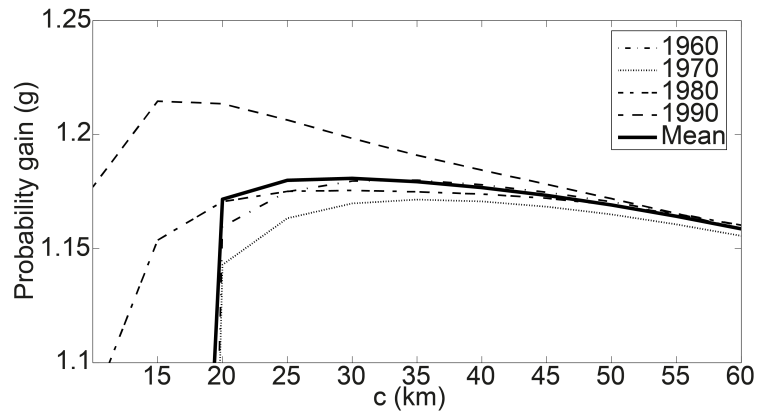
Fig. 3 Maps showing the fault source inputs as seismogenic boxes (see Fig. 2a). The colour scale indicates the activity rate. Solid and dashed lines (corresponding to the uppermost edge of the fault) are used to highlight our choice between the two end-members of the MFD model adopted in the so-called *Mixed* model.



1010
 1011 Fig. 4 Historical earthquakes from the most recent version of the historical
 1012 parametric Italian catalogue (CPTI15, Rovida et al., 2016), the spatial variations in b-
 1013 values and the polygons defining the five macroseismic areas used to assess the
 1014 magnitude intervals.



1015
 1016 Fig. 5 Differences in percentages between the two smoothed rates produced by eq.
 1017 (2) using the complete catalogue and the modified catalogue without events
 1018 associated with known active faults (*TGR* model)



1019

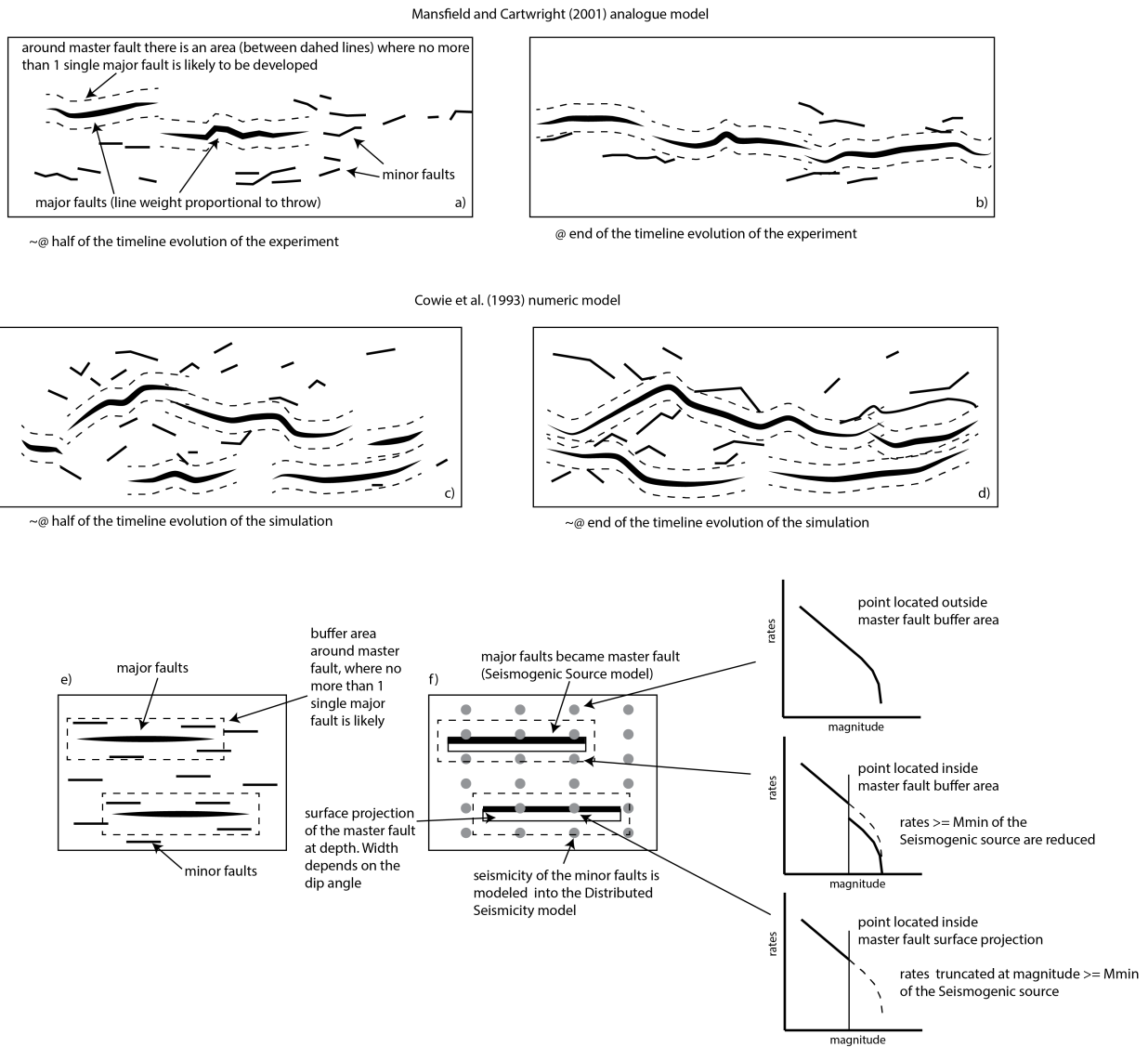
1020 Fig. 6 Probability gain per earthquake (see eq. 3) versus correlation distance c ,
 1021 highlighting the best radius for use in the smoothed seismicity approach (eq. 2)

1022

1023

1024

1025



1026

1027

1028

1029

1030

1031

1032

1033

1034

1035

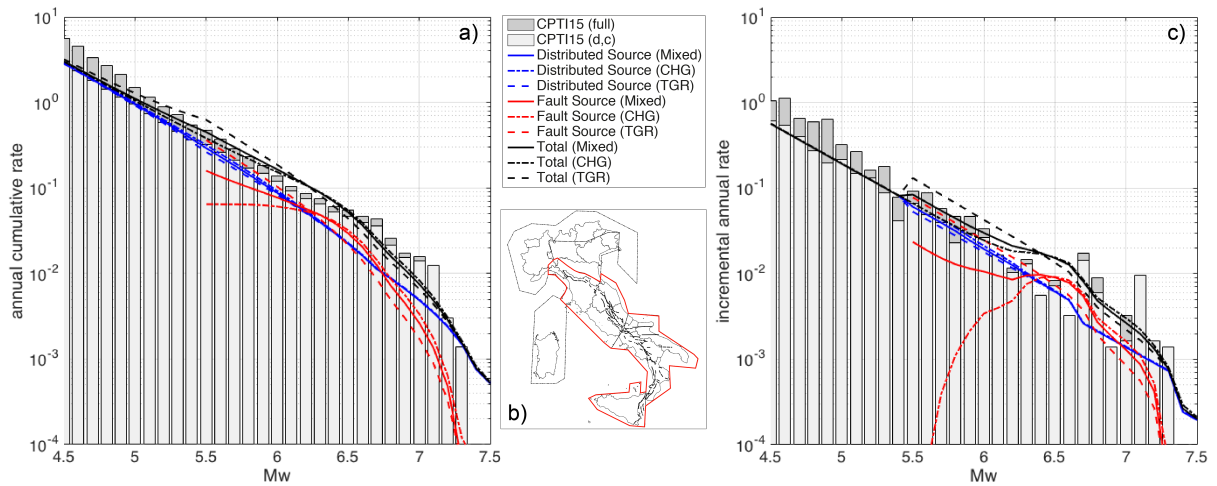
1036

1037

1038

1039

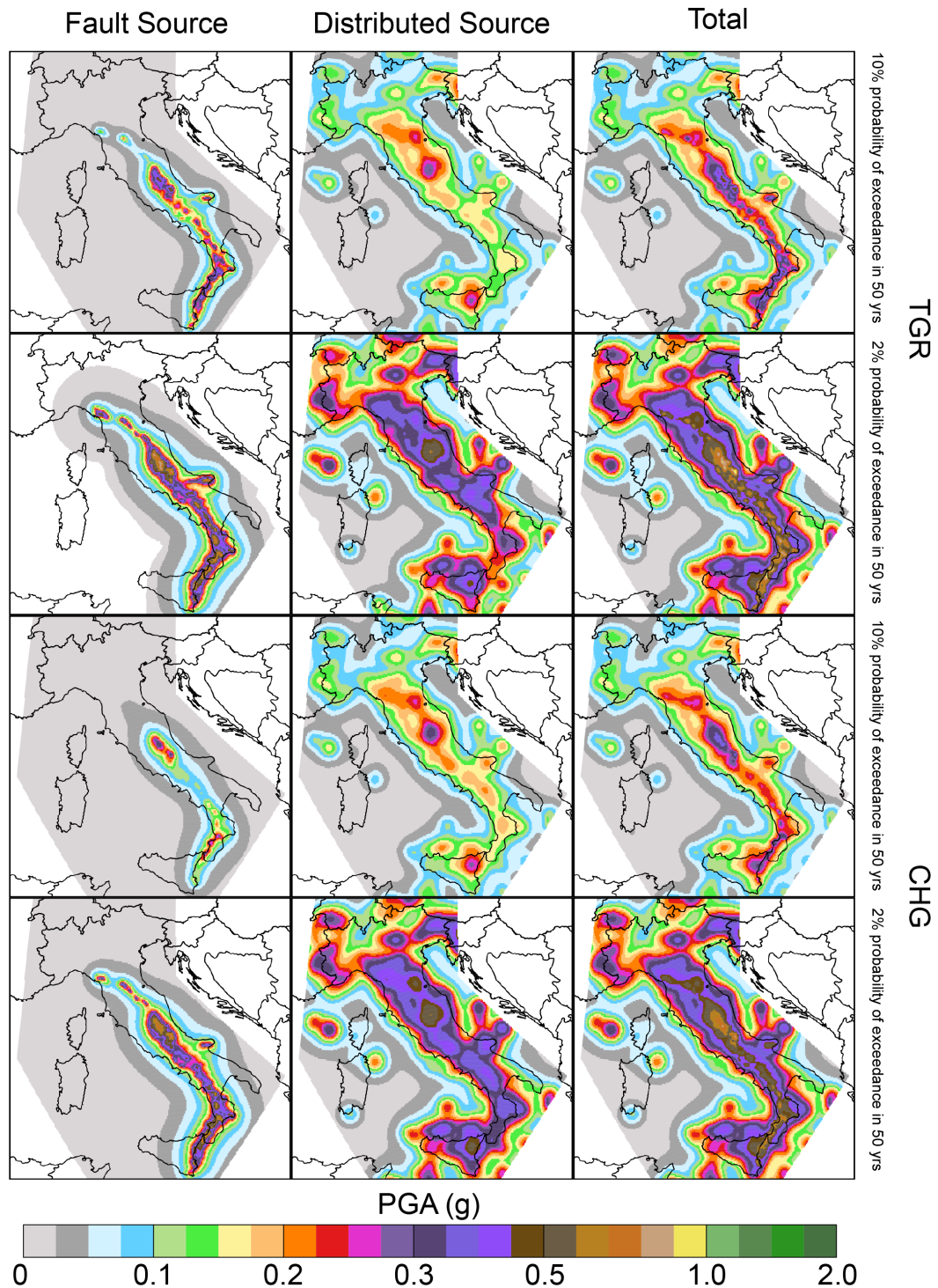
Fig. 7 Fault system evolution and implications in our model. a) and b) Diagrams from the Mansfield and Cartwright (2001) analogue experiment in two different stages: the approximate midpoint of the sequence and the end of the sequence. Areas exist around master faults where no more than a single major fault is likely to develop. c) and d) Diagrams from numerical modelling conducted by Cowie et al. (1993) in two different stages. This experiment shows the similar evolutionary features of major and minor faults. e) and f) Application of the analogue and numeric modelling of fault system evolution to the fault source input proposed in this paper. A buffer area is drawn around each fault source, where it is unlikely for other major faults to develop, and it accounts for the length and slip rate of the fault source. This buffer area is useful for reducing or truncating the rates of expected distributed seismicity based on the position of a distributed seismicity point with respect to the buffer zone (see the text for details).



1040

1041 Fig. 8 a) annual cumulative rate and c) incremental annual rate computed for the red
 1042 bounded area in b). The rates have been computed using: (i) the full CPTI15
 1043 catalogue; (ii) the declustered and complete catalogue (CPTI15 (d, c) in the legend)
 1044 obtained using the completeness magnitude thresholds over different periods of time
 1045 given by Stucchi et al. (2011) for five large zones; (iii) the distributed sources; (iv) the
 1046 fault sources; and (v) summing fault and distributed sources (Total).

1047



1048

1049

1050

1051

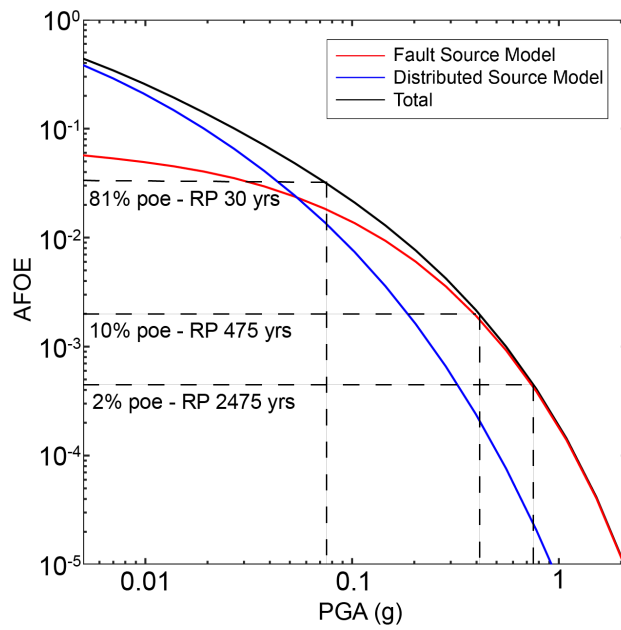
1052

1053

1054

1055

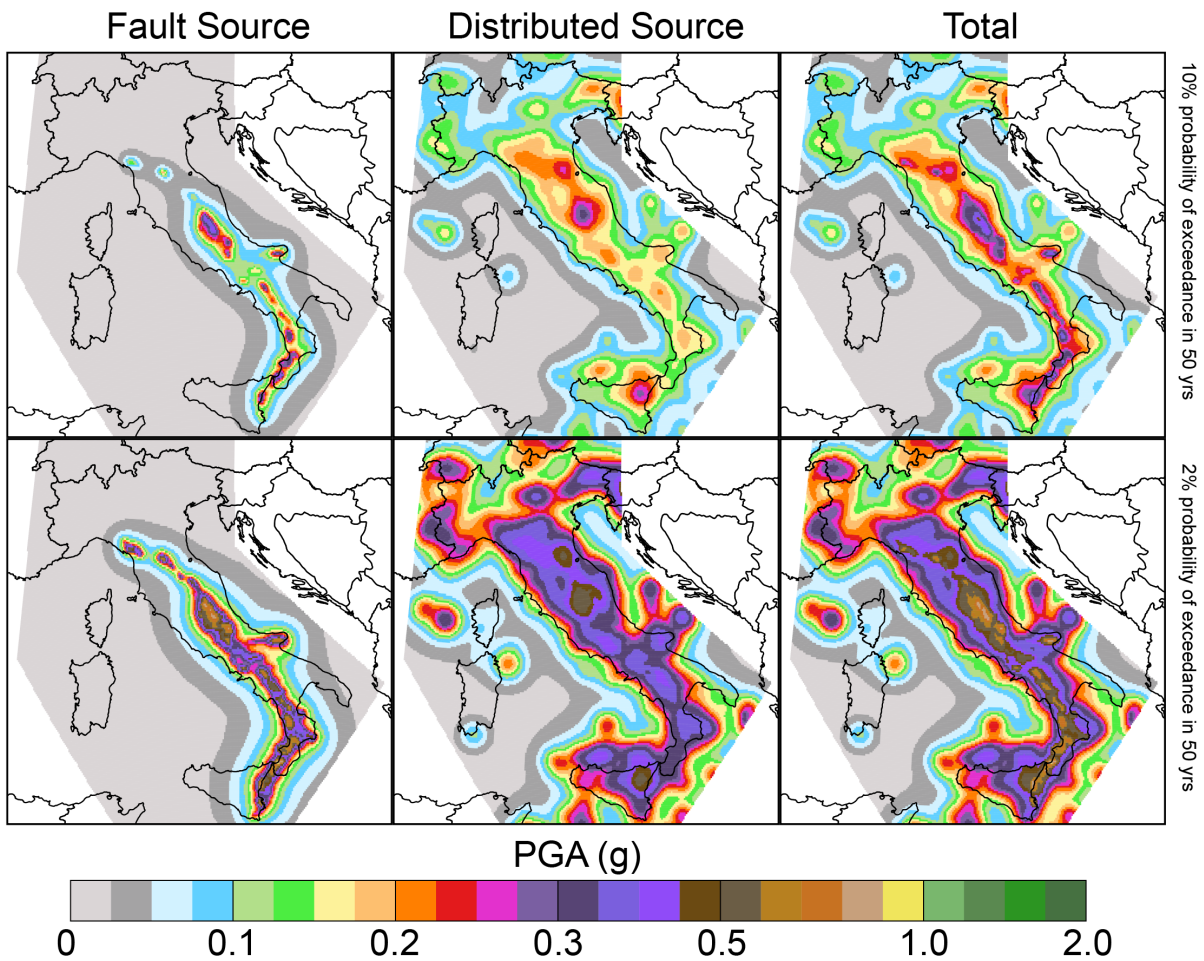
Fig. 9 Seismic hazard maps for the *TGR* and *CHG* models expressed in terms of peak ground acceleration (PGA) and computed for a latitude/longitude grid spacing of 0.05° . The first and second rows show the fault source, distributed source and total maps of the *TGR* model computed for 10% probability of exceedance in 50 years and 2% probability of exceedance in 50 years, corresponding to return periods of 475 and 2475 years, respectively. The third and fourth rows show the same maps for the *CHG* model.



1056

1057 Fig. 10 An example of the contribution to the total seismic hazard level (black line), in
 1058 terms of hazard curves, by the *fault* (red line) and *distributed* (blue line) source inputs
 1059 for one of the 45,602 grid points (L'Aquila, 42.400-13.400). The dashed lines
 1060 represent the 2%, 10% and 81% probabilities of exceedance (poes) in 50 years.

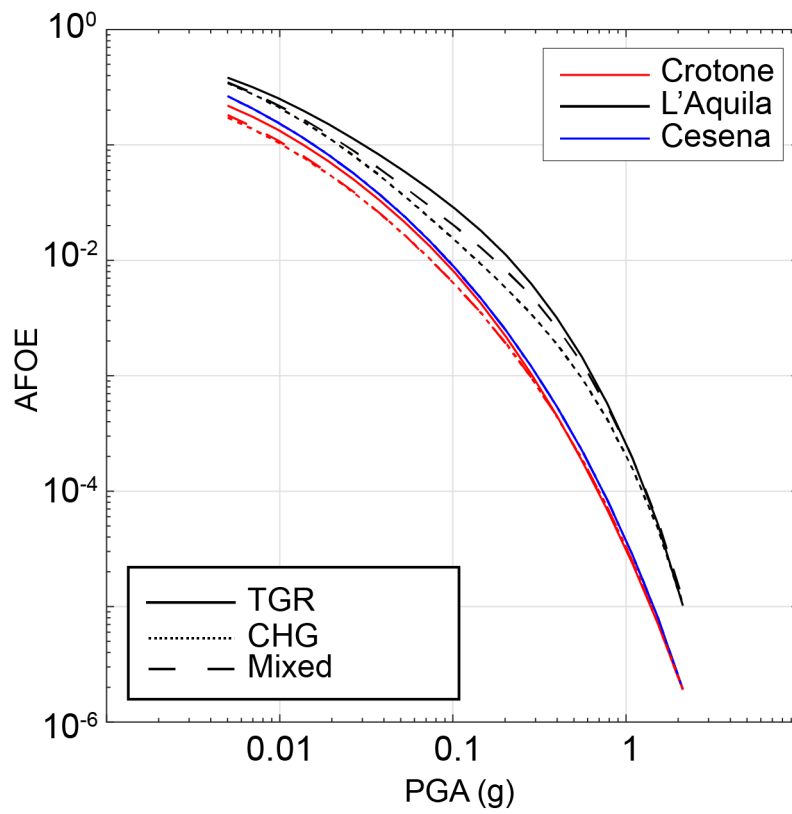
1061



1062

1063

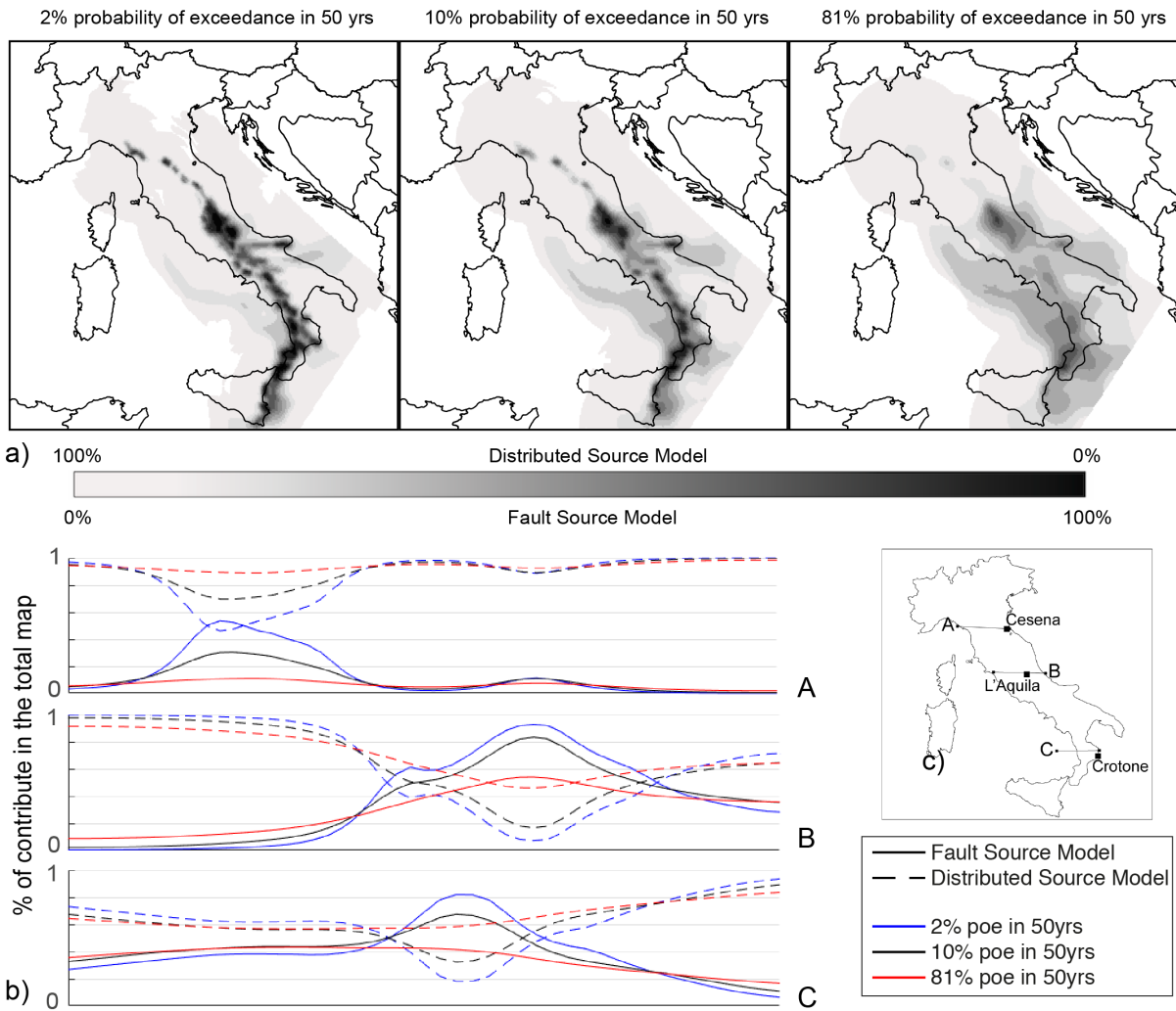
1064 Fig. 11 Seismic hazard maps for the *Mixed* model. The first row shows the fault
 1065 source, distributed source and total maps computed for 10% probability of
 1066 exceedance in 50 years, and the second row shows the same maps but computed
 1067 for 2% probability of exceedance in 50 years, corresponding to return periods of 475
 1068 and 2475 years, respectively. The results are expressed in terms of peak ground
 1069 acceleration (PGA).



1070

1071 Fig. 12 *CHG* (dotted line), *TGR* (solid line) and *Mixed* model (dashed line) hazard
 1072 curves for three sites: Cesena (red line), L'Aquila (black line) and Crotone (blue line)

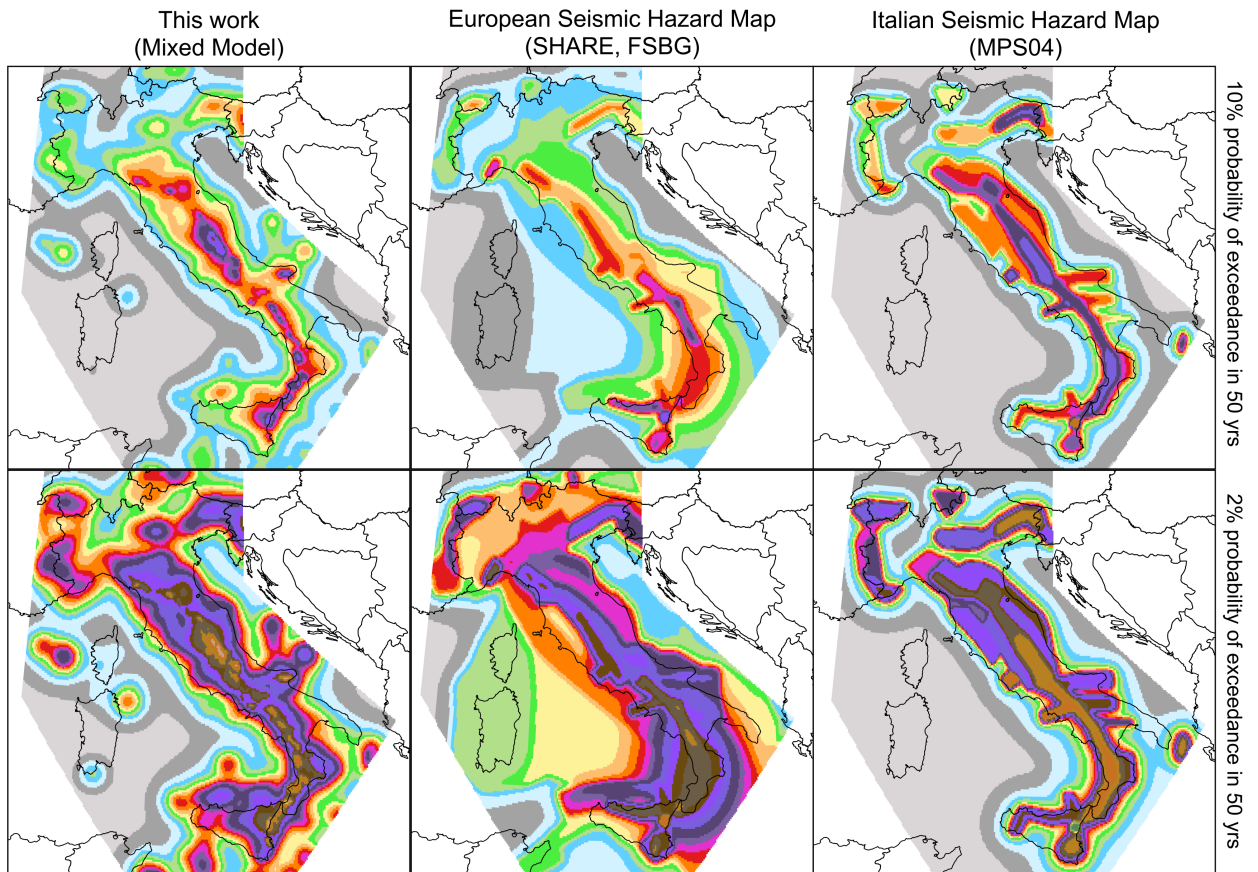
1073



1074

1075

1076 Fig. 13 a) Contribution maps of the Mixed *fault* and *distributed* source inputs to the
 1077 total hazard level for three probabilities of exceedance: 2%, 10% and 81%,
 1078 corresponding to return periods of 2475, 475 and 30 years, respectively. b)
 1079 Contributions of the Mixed *fault* (solid line) and *distributed* (dashed line) source
 1080 inputs along three profiles (A, B and C in Fig. 13c) for three probabilities of
 1081 exceedance: 2% (blue line), 10% (black line) and 81% (red line).



1082

1083 Fig. 14 Seismic hazard maps expressed in terms of Peak Ground Acceleration
 1084 (PGA) and computed for a latitude/longitude grid spacing of 0.05° based on site
 1085 conditions. The figure shows a comparison of our model (*Mixed* model, on the left),
 1086 the SHARE model (FSBG logic tree branch, in the middle) and the current Italian
 1087 national seismic hazard map (MPS04, on the right). The same GMPEs (Akkar et al.
 1088 2013, Chiou et al., 2008, Faccioli et al., 2010 and Zhao et al., 2006 and Bindi et al.
 1089 2014), were used for all models to obtain and compare the maps.

1090

1091

1092

1093

1094

1095

ID	Fault Sources	L (km)	Dip (°)	Upper (km)	Lower (km)	SR _{min} (mm/yr)	SR _{max} (mm/yr)
1	Lunigiana	43.8	40	0	5	0.28	0.7
2	North Apuane Transfer	25.5	45	0	7	0.33	0.83
3	Garfagnana	26.9	30	0	4.5	0.35	0.57
4	Garfagnana Transfer	47.1	90	2	7	0.33	0.83
5	Mugello	21.0	40	0	7	0.33	0.83
6	Ronta	19.3	65	0	7	0.17	0.5
7	Poppi	17.1	40	0	4.5	0.33	0.83
8	Città di Castello	22.9	40	0	3	0.25	1.2
9	M.S.M. Tiberina	10.5	40	0	2.5	0.25	0.75
10	Gubbio	23.6	50	0	6	0.4	1.2
11	Colfiorito System	45.9	50	0	8	0.25	0.9
12	Umbra Valley	51.1	55	0	4.5	0.4	1.2
13	Vettore-Bove	35.4	50	0	15	0.2	1.05
14	Nottoria-Preci	29.0	50	0	12	0.2	1
15	Cascia-Cittareale	24.3	50	0	13.5	0.2	1
16	Leonessa	14.9	55	0	12	0.1	0.7
17	Rieti	17.6	50	0	10	0.25	0.6
18	Fucino	82.3	50	0	13	0.3	1.6
19	Sella di Corno	23.1	60	0	13	0.35	0.7
20	Pizzoli-Pettino	21.3	50	0	14	0.3	1
21	Monteale	15.1	50	0	14	0.25	0.9
22	Gorzano	28.1	50	0	15	0.2	1
23	Gran Sasso	28.4	50	0	15	0.35	1.2
24	Paganica	23.7	50	0	14	0.4	0.9
25	Middle Aternum Valley	29.1	50	0	14	0.15	0.45
26	Campo Felice-Ovindoli	26.2	50	0	13	0.2	1.6
27	Carsoli	20.5	50	0	11	0.35	0.6
28	Liri	42.5	50	0	11	0.3	1.26
29	Sora	20.4	50	0	11	0.15	0.45
30	Marsicano	20.0	50	0	13	0.25	1.2
31	Sulmona	22.6	50	0	15	0.6	1.35
32	Maiella	21.4	55	0	15	0.7	1.6
33	Aremogna C.Miglia	13.1	50	0	15	0.1	0.6
34	Barrea	17.1	55	0	13	0.2	1
35	Cassino	24.6	60	0	11	0.25	0.5
36	Ailano-Piedimonte	17.6	60	0	12	0.15	0.35
37	Matese	48.3	60	0	13	0.2	1.9
38	Bojano	35.5	55	0	13	0.2	0.9
39	Frosolone	36.1	70	11	25	0.35	0.93
40	Ripabottoni-San Severo	68.3	85	6	25	0.1	0.5
41	Mattinata	42.3	85	0	25	0.7	1
42	Castelluccio dei Sauri	93.2	90	11	22	0.1	0.5
43	Ariano Irpino	30.1	70	11	25	0.35	0.93
44	Tammaro	25.0	60	0	13	0.35	0.93
45	Benevento	25.0	55	0	10	0.35	0.93
46	Volturno	15.7	60	1	13	0.23	0.57
47	Avella	20.5	55	1	13	0.2	0.7
48	Ufita-Bisaccia	59.0	64	1.5	15	0.35	0.93
49	Melfi	17.2	80	12	22	0.1	0.5
50	Irpinia Antithetic	15.0	60	0	11	0.2	0.53

51	Irpinia	39.7	65	0	14	0.3	2.5
52	Volturara	23.7	60	1	13	0.2	0.35
53	Alburni	20.4	60	0	8	0.35	0.7
54	Caggiano-Diano Valley	46.0	60	0	12	0.35	1.15
55	Pergola-Maddalena	50.6	60	0	12	0.20	0.93
56	Agri	34.9	50	5	15	0.8	1.3
57	Potenza	17.8	90	15	21	0.1	0.5
58	Palagianello	73.3	90	13	22	0.1	0.5
59	Monte Alpi	10.9	60	0	13	0.35	0.9
60	Maratea	21.6	60	0	13	0.46	0.7
61	Mercure	25.8	60	0	13	0.2	0.6
62	Pollino	23.8	60	0	15	0.22	0.58
63	Castrovillari	10.3	60	0	15	0.2	1.15
64	Rossano	14.9	60	0	22	0.5	0.6
65	Crati West	49.7	45	0	15	0.84	1.4
66	Crati East	18.4	60	0	8	0.75	1.45
67	Lakes	43.6	60	0	22	0.75	1.45
68	Fuscalto	21.1	60	2	22	0.75	1.45
69	Piano Lago-Decollatura	25.0	60	1	15	0.23	0.57
70	Catanzaro North	29.5	80	3	20	0.75	1.45
71	Catanzaro South	21.3	80	3	20	0.75	1.45
72	Serre	31.6	60	0	15	0.7	1.15
73	Vibo	23.0	80	0	15	0.75	1.45
74	Sant'Eufemia Gulf	24.8	40	1	11	0.11	0.3
75	Capo Vaticano	13.7	60	0	8	0.75	1.45
76	Coccorino	13.3	70	3	11	0.75	1.45
77	Scilla	29.7	60	0	13	0.8	1.5
78	Sant'Eufemia	19.2	60	0	13	0.75	1.45
79	Cittanova-Armo	63.8	60	0	13	0.45	1.45
80	Reggio Calabria	27.2	60	0	13	0.7	2
81	Taormina	38.7	30	3	13	0.9	2.6
82	Acireale	39.4	60	0	15	1.15	2.3
83	Western Ionian	50.1	65	0	15	0.75	1.45
84	Eastern Ionian	39.3	65	0	15	0.75	1.45
85	Climiti	15.7	60	0	15	0.75	1.45
86	Avola	46.9	60	0	16	0.8	1.6

1096

1097 Table 1 Geometric Parameters of the Fault Sources. L, along-strike length; Dip,
1098 inclination angle of the fault plane; Upper and Lower, the thickness bounds of the
1099 local seismogenic layer; SRmin and SRmax, the slip rates assigned to the sources
1100 using the references available (see the supplemental files); and *ID*, the fault number
1101 identifier.

1102

ID	Fault Sources	Historical Earthquakes				Instrumental Earthquakes		
		yyyy/mm/dd	I_{Max}	I_0	M_w	sD	yyyy/mm/dd	M_w
1	Lunigiana	1481/05/07	VIII	VIII	5.6	0.4		
		1834/02/14	IX	IX	6.0	0.1		
2	North Apuane Transfer	1837/04/11	X	IX	5.9	0.1		
3	Garfagnana	1740/03/06	VIII	VIII	5.6	0.2		
		1920/09/07	X	X	6.5	0.1		
4	Garfagnana Transfer							
5	Mugello	1542/06/13	IX	IX	6.0	0.2		
		1919/06/29	X	X	6.4	0.1		
6	Ronta							
7	Poppi							
8	Città di Castello	1269			5.7			
		1389/10/18	IX	IX	6	0.5		
		1458/04/26	VIII-IX	VIII-IX	5.8	0.5		
		1789/09/30	IX	IX	5.9	0.1		
9	M.S.M. Tiberina	1352/12/25	IX	IX	6.3	0.2		
		1917/04/26	IX-X	IX-X	6.0	0.1		
10	Gubbio						1984/04/29	5.6
11	Colfiorito System	1279/04/30	X	IX	6.2	0.2	1997/09/26	5.7
		1747/04/17	IX	IX	6.1	0.1	1997/09/26	6
		1751/07/27	X	X	6.4	0.1		
12	Umbra Valley	1277		VIII	5.6	0.5		
		1832/01/13	X	X	6.4	0.1		
		1854/02/12	VIII	VIII	5.6	0.3		
13	Vettore-Bove						2016/10/30	6.5
14	Nottoria-Preci	1328/12/01	X	X	6.5	0.3	1979/09/19	5.8
		1703/01/14	XI	XI	6.9	0.1		
		1719/06/27	VIII	VIII	5.6	0.3		
		1730/05/12	IX	IX	6.0	0.1		
		1859/08/22	VIII-IX	VIII-IX	5.7	0.3		
		1879/02/23	VIII	VIII	5.6	0.3		
15	Cascia-Cittareale	1599/11/06	IX	IX	6.1	0.2		
		1916/11/16	VIII	VIII	5.5	0.1		
16	Leonessa							
17	Rieti	1298/12/01	X	IX-X	6.3	0.5		
		1785/10/09	VIII-IX	VIII-IX	5.8	0.2		
18	Fucino	1349/09/09	IX	IX	6.3	0.1		
		1904/02/24	IX	VIII-IX	5.7	0.1		
		1915/01/13	XI	XI	7	0.1		
19	Sella di Corno							
20	Pizzoli-Pettino	1703/02/02	X	X	6.7	0.1		
21	Monte Reale							
22	Gorzano	1639/10/07	X	IX-X	6.2	0.2		
		1646/04/28	IX	IX	5.9	0.4		
23	Gran Sasso							
24	Paganica	1315/12/03	VIII	VIII	5.6	0.5	2009/06/04	6.3
		1461/11/27	X	X	6.5	0.5		
25	Middle Aternum Valley							
26	Campo Felice-Ovindoli							
27	Carsoli							
28	Liri							
29	Sora	1654/07/24	X	IX-X	6.3	0.2		
30	Marsicano							
31	Sulmona							
32	Maiella							
33	Aremogna C.Miglia							
34	Barrea						1984/05/07	5.9
35	Cassino							
36	Ailano-Piedimonte							
37	Matese	1349/09/09	X-XI	X	6.8	0.2		

38	Bojano	1805/07/26	X	X	6.7	0.1		
39	Frosolone	1456/12/05	XI	XI	7	0.1		
40	Ripabottoni-San Severo	1627/07/30	X	X	6.7	0.1	2002/10/31	5.7
		1647/05/05	VII-VIII	VII-VIII	5.7	0.4		
		1657/01/29	IX-X	VIII-IX	6.0	0.2		
41	Mattinata	1875/12/06	VIII	VIII	5.9	0.1		
		1889/12/08	VII	VII	5.5	0.1		
		1948/08/18	VII-VIII	VII-VIII	5.6	0.1		
42	Castelluccio dei Sauri	1361/07/17	X	IX	6	0.5		
		1560/05/11	VIII	VIII	5.7	0.5		
		1731/03/20	IX	IX	6.3	0.1		
43	Ariano Irpino	1456/12/05			6.9	0.1		
		1962/08/21	IX	IX	6.2	0.1		
44	Tammaro	1688/06/05	XI	XI	7	0.1		
45	Benevento							
46	Volturno							
47	Avella	1499/12/05	VIII	VIII	5.6	0.5		
48	Ufita-Bisaccia	1732/11/29	X-XI	X-XI	6.8	0.1		
		1930/07/23	X	X	6.7	0.1		
49	Melfi	1851/08/14	X	X	6.5	0.1		
50	Irpinia Antithetic							
51	Irpinia	1466/01/15	VIII-IX	VIII-IX	6.0	0.2	1980/11/23	6.8
		1692/03/04	VIII	VIII	5.9	0.4		
		1694/09/08	X	X	6.7	0.1		
		1853/04/09	IX	VIII	5.6	0.2		
52	Volturara							
53	Alburni							
54	Caggiano-Diano Valley	1561/07/31	IX-X	X	6.3	0.1		
55	Pergola-Maddalena	1857/12/16			6.5			
		1857/12/16			6.3			
56	Agri							
57	Potenza	1273/12/18	VIII-IX	VIII-IX	5.8	0.5	1990/05/05	5.8
58	Palagianello							
59	Monte Alpi							
60	Maratea							
61	Mercure	1708/01/26	VIII-IX	VIII	5.6	0.6	1998/09/09	5.5
62	Pollino							
63	Castrovillari							
64	Rossano	1836/04/25	X	IX	6.2	0.2		

65	Crati West	1184/05/24	IX	IX	6.8	0.3
		1870/10/04	X	IX-X	6.2	0.1
		1886/03/06	VII-VIII	VII-VIII	5.6	0.3
66	Crati East	1767/07/14	VIII-IX	VIII-IX	5.9	0.2
		1835/10/12	X	IX	5.9	0.3
67	Lakes	1638/06/08	X	X	6.8	0.1
68	Fuscalto	1832/03/08	X	X	6.6	0.1
69	Piano Lago-Decollatura					
70	Catanzaro North	1638/03/27			6.6	
71	Catanzaro South	1626/04/04	X	IX	6.1	0.4
72	Serre	1659/11/05	X	X	6.6	0.1
		1743/12/07	IX-X	VIII-IX	5.9	0.2
		1783/02/07	X-XI	X-XI	6.7	0.1
		1791/10/13	IX	IX	6.1	0.1
73	Vibo					
74	Sant'Eufemia Gulf	1905/09/08	X-XI	X-XI	7	0.1
75	Capo Vaticano					
76	Coccorino	1928/03/07	VIII	VII-VIII	5.9	0.1
77	Scilla					
78	Sant'Eufemia	1894/11/16	IX	IX	6.1	0.1
79	Cittanova-Armo	1509/02/25	IX	VIII	5.6	0.4
		1783/02/05	XI	XI	7.1	0.1
80	Reggio Calabria					
81	Taormina	1908/12/28	XI	XI	7.1	0.2
82	Acireale	1818/02/20	IX-X	IX-X	6.3	0.1
83	Western Ionian	1693/01/11	XI	XI	7.3	0.1
84	Eastern Ionian					
85	Climiti					
86	Avola					

1103

1104 Table 2 Earthquake-Source Association Adopted for Fault Sources. I_{Max} , maximum
1105 intensity; I_0 , epicentral intensity; M_w , moment magnitude; and sD, standard deviation
1106 of the moment magnitude. For references, see the supplemental files.

1 **Integrating faults and past earthquakes into a probabilistic seismic hazard**
2 **model for peninsular Italy**

3

4 Alessandro Valentini¹, Francesco Visini² and Bruno Pace¹

5 ¹ DiSPUTer, Università degli Studi “Gabriele d’Annunzio”, Chieti, Italy

6 ² Istituto Nazionale di Geofisica e Vulcanologia, L’Aquila, Italy

7

8 **Abstract**

9

10 *Italy is one of the most seismically active countries in Europe. Moderate to strong earthquakes, with*
11 *magnitudes of up to ~7, have been historically recorded for many active faults. Currently,*
12 *probabilistic seismic hazard assessments in Italy are mainly based on area source models, in which*
13 *seismicity is modelled using a number of seismotectonic zones and the occurrence of earthquakes is*
14 *assumed uniform. However, in the past decade, efforts have increasingly been directed towards using*
15 *fault sources in seismic hazard models to obtain more detailed and potentially more realistic patterns*
16 *of ground motion. In our model, we used two categories of earthquake sources. The first involves*
17 *active faults, and fault slip rates were used to quantify the seismic activity rate. We produced an*
18 *inventory of all fault sources with details of their geometric, kinematic and energetic properties. The*
19 *associated parameters were used to compute the total seismic moment rate of each fault. We*
20 *evaluated the magnitude-frequency distribution (MFD) of each fault source using two models: a*
21 *characteristic Gaussian model centred on the maximum magnitude and a Truncated Gutenberg-*
22 *Richter model. The second earthquake source category involves distributed seismicity, and a fixed-*
23 *radius smoothed approach and a historical catalogue were used to evaluate seismic activity. Under*
24 *the assumption that deformation is concentrated along faults, we combined the MFD derived from the*
25 *geometry and slip rates of active faults with the MFD from the spatially smoothed earthquake sources*
26 *and assumed that the smoothed seismic activity in the vicinity of an active fault gradually decreases*
27 *by a fault size-driven factor. Additionally, we computed horizontal peak ground acceleration maps for*
28 *return periods of 475 and 2,475 yrs. Although the ranges and gross spatial distributions of the*
29 *expected accelerations obtained here are comparable to those obtained through methods involving*
30 *seismic catalogues and classical zonation models, the spatial pattern of the hazard maps obtained*
31 *with our model is far more detailed. Our model is characterized by areas that are more hazardous*
32 *and that correspond to mapped active faults, while previous models yield expected accelerations that*
33 *are almost uniformly distributed across large regions. In addition, we conducted sensitivity tests to*

34 *determine the impact on the hazard results of the earthquake rates derived from two MFD models for*
35 *faults and to determine the relative contributions of faults versus distributed seismic activity. We*
36 *believe that our model represents advancements in terms of the input data (quantity and quality) and*
37 *methodology used in the field of fault-based regional seismic hazard modelling in Italy.*
38

39 **1. Introduction**

40 In this paper, we present the results of a new probabilistic seismic hazard (PSH)
41 model for Italy that includes significant advances in the use of integrated active fault
42 and seismological data. The use of active faults as an input for PSH analysis is a
43 consolidated approach in many countries characterized by high strain rates and
44 seismic releases, as shown, for example, by Field et al. (2015) in California and
45 Stirling et al. (2012) in New Zealand. However, in recent years, active fault data have
46 also been successfully integrated into PSH assessments in regions with moderate-
47 to-low strain rates, such as SE Spain (e.g., Garcia-Mayordomo et al., 2007), France
48 (e.g., Scotti et al., 2014), and central Italy (e.g., Peruzza et al., 2011).

49 In Europe, a working group of the European Seismological Commission, named
50 *Fault2SHA*, is discussing fault-based seismic hazard modelling
51 (<https://sites.google.com/site/linkingfaultpsha/home>). The working group, born to
52 motivate exchanges between field geologists, fault modellers and seismic hazard
53 practitioners, organizes workshops, conference sessions, and special issues and
54 stimulates collaborations between researchers. The work we are presenting here
55 stems from the activities of the *Fault2SHA* working group.

56 Combining active faults and background sources is one of the main issues in this
57 type of approach. Although the methodology remains far from identifying a standard
58 procedure, common approaches combine active faults and background sources by
59 applying a threshold magnitude, generally between 5.5 and 7, above which
60 seismicity is modelled as occurring on faults and below which seismicity is modelled
61 via a smoothed approach (e.g., Akinci et al., 2009), area sources (e.g., the so-called
62 FSBG model in SHARE; Woessner et al., 2015) or a combination of the two (Field et
63 al., 2015; Pace et al., 2006).

64 Another important issue in the use of active faults in PSHA is assigning the “correct”
65 magnitude-frequency distribution (MFD) to the fault sources. Gutenberg-Richter (GR)



66 and characteristic earthquake models are commonly used, and the choice
67 sometimes depends on the knowledge of the fault and data availability. Often, the
68 choice of the “appropriate” MFD for each fault source is a difficult task because
69 palaeoseismological studies are scarce, and it is often difficult to establish clear
70 relationships between mapped faults and historical seismicity. Recently, Field et al.
71 (2017) discussed the effects and complexity of the choice, highlighting how often the
72 GR model results are not consistent with data; however, in other cases,
73 uncharacteristic behaviour, with rates smaller than the maximum, are possible. The
74 discussion is open (see for example the discussion by Kagan et al., 2012) and far
75 from being solved with the available observations, including both seismological
76 and/or geological/paleoseismological observations. In this work, we explore the
77 calculations of these two MFDs, a characteristic Gaussian model and a Truncated
78 Gutenberg-Richter model, to explore the epistemic uncertainties and to consider a
79 *Mixed model* as a so-called “expert judgement” model. This approach is useful for
80 comparative analysis, and which we assigned one of the two MFDs to each fault
81 source. The rationale of the choice of the MFD of each fault source is explained in
82 detail later in this paper. However, this approach obviously does not solve the issue,
83 and the choice of MFD remains an open question in fault-based PSHA.

84 In Italy, the current national PSH model for building code (Stucchi et al., 2011) is
85 based on area sources and the classical Cornell approach (Cornell, 1968), in which
86 the occurrence of earthquakes is assumed uniform in the defined seismotectonic
87 zones. However, we believe that more efforts must be directed towards using
88 geological data (e.g., fault sources and paleoseismological information) in PSH
89 models to obtain detailed patterns of ground motion, extend the observational time
90 required to capture the recurrence of large-magnitude events and improve the
91 reliability of seismic hazard assessments. In fact, as highlighted by the 2016-2017
92 seismic sequences in central Italy, a zone-based PSH is not able to model local
93 spatial variations in ground motion (Meletti et al., 2016), whereas a fault-based
94 model can provide insights for aftershock time-dependent PSH analysis (Peruzza et
95 al., 2016). In conclusion, even if the main purpose of this work is to integrate active
96 faults into hazard calculations for the Italian territory, this study does not represent
97 an official update of the seismic hazard model of Italy.

98

99 **2. Source Inputs**

100 Two earthquake-source inputs are considered in this work. The first is a fault source
101 input that is based on active faults and uses the geometries and slip rates of known
102 active faults to compute activity rates over a certain range of magnitude.^SThe second
103 is a classical smoothed approach that accounts for the rates of expected
104 earthquakes with a minimum moment magnitude (M_w) of 4.5 but excludes
105 earthquakes associated with known faults based on a modified earthquake
106 catalogue. Note that our PSH model requires the combination of the two source
107 inputs related to the locations of expected seismicity rates into a single model.
108 Therefore, these two earthquake-source inputs are not independent but
109 complementary, in both the magnitude and frequency distribution, and together
110 account for all seismicity in Italy.

111 In the following subsections, we describe the two source inputs and how they are
112 combined in the PSH model.

113 **2.1 Fault Source Input**

114 In seismic hazard assessment, an active fault is a structure that exhibits evidence of
115 activity in the late Quaternary (i.e., in the past 125 kyr), has a demonstrable or
116 potential capability of generating major earthquakes and is capable of future
117 reactivation (see Machette, 2000 for a discussion on terminology). The evidence of
118 Quaternary activity can be geomorphological and/or paleoseismological when
119 activation information from instrumental seismic sequences and/or association to
120 historical earthquakes is not available. Fault source inputs are useful for seismic
121 hazard studies, and we compiled a database for Italy via the analysis and synthesis
122 of neotectonic and seismotectonic data from approximately 90 published studies of
123 110 faults across Italy. Our database included, but was not limited to, the Database
124 of Individual Seismogenic Sources (DISS vers. 3.2.0, <http://diss.rm.ingv.it/diss/>),
125 which is already available for Italy. It is important to highlight that the DISS is
126 currently composed of two main categories of seismogenic sources: individual and
127 composite sources. The latter are defined by the DISS' authors as "*simplified and
128 three-dimensional representation of a crustal fault containing an unspecified number
129 of seismogenic sources that cannot be singled out. Composite seismogenic sources
130 are not associated with a specific set of earthquakes or earthquake distribution*", and

131 therefore are not useful for our PSHA approach; the former is “a *simplified and three-*
132 *dimensional representation of a rectangular fault plane. Individual seismogenic*
133 *sources are assumed to exhibit characteristic behaviour with respect to rupture*
134 *length/width and expected magnitude*” ([http://diss.rm.ingv.it/diss/index.php/about/13-](http://diss.rm.ingv.it/diss/index.php/about/13-introduction)
135 [introduction](http://diss.rm.ingv.it/diss/index.php/about/13-introduction)). Even if in agreement with our approach, we note that some of the
136 individual seismogenic sources in the DISS are based on geological and
137 paleoseismological information, and many others used the *Boxer* code (Gasperini et
138 al., 1999) to calculate the epicentre, moment magnitude, size and orientation of a
139 seismic source from observed macroseismic intensities. We carefully analysed the
140 individual sources and some related issues: (i) the lack of updating of the geological
141 information of some individual sources and (ii) the nonconformity between the input
142 data used by DISS in *Boxer* and the latest historical seismicity (CPTI15) and
143 macroseismic intensity (DBMI15) publications. Thus, we performed a full review of
144 the fault database. We then compiled a fault source database as a synthesis of
145 works published over the past twenty years, including DISS, using all updated and
146 available geological, paleoseismological and seismological data (see the
147 supplemental files for a complete list of references). We consider our database as
148 complete as possible in terms of individual seismogenic sources, and it contains all
149 the parameters necessary to construct an input dataset for fault-based PSHA.

150 The resulting database of normal and strike-slip active and seismogenic faults in
151 peninsular Italy (Fig. 1, Tables 1 and 2; see the supplemental files) includes all the
152 available geometric, kinematic, slip rate and earthquake source-related information.
153 In the case of missing data regarding the geometric parameters of dip and rake, we
154 assumed typical dip and rake values of 60° and -90° , respectively, for normal faults
155 and 90° and 0° or 180° , respectively, for strike-slip faults. In this paper, only normal
156 and strike-slip faults are used as fault source inputs. We decided not to include thrust
157 faults in the present study because, with the methodology proposed in this study (as
158 discussed later in the text), the maximum size of a single-rupture segment must be
159 defined, and segmentation criteria have not been established for large thrust zones.
160 Moreover, our method uses slip rates to derive active seismicity rates, and sufficient
161 knowledge of these values is not available for thrust faults in Italy. Because some
162 areas of Italy, such as the NW sector of the Alps, Po Valley, the offshore sector of
163 the central Adriatic Sea, and SW Sicily, may be excluded by this limitation, we are

164 considering an update to our approach to include thrust faults and volcanic sources
165 in a future study. The upper and lower boundaries of the seismogenic layer are
166 mainly derived from the analysis of Stucchi et al. (2011) of the Italian national
167 seismic hazard model and locally refined by more detailed studies (Boncio et al.,
168 2011; Peruzza et al., 2011; Ferranti et al., 2014).

169 Based on the compiled database, we explored three main issues associated with
170 defining a fault source input: the slip rate evaluation, the segmentation model and
171 the expected seismicity rate calculation.

172 *2.1.1 Slip rates*

173 Slip rates control fault-based seismic hazards (Main, 1996, Roberts et al., 2004; Bull
174 et al., 2006; Visini and Pace, 2014) and reflect the velocities of the mechanisms that
175 operate during continental deformation (e.g., Cowie et al., 2005). Moreover, long-
176 term observations of faults in various tectonic contexts have shown that slip rates
177 vary in space and time (e.g., Bull et al., 2006; Nicol et al., 2006, 2010, McClymont et
178 al., 2009; Gunderson et al., 2013; Benedetti et al., 2013, D'Amato et al., 2016), and
179 numerical simulations (e.g., Robinson et al., 2009; Cowie et al., 2012; Visini and
180 Pace, 2014) suggest that variability mainly occurs in response to interactions
181 between adjacent faults. Therefore, understanding the temporal variability in fault slip
182 rates is a key point in understanding the earthquake recurrence rates and their
183 variability.

184 In this work, we used the mean of the minimum and maximum slip rate values listed
185 in Table 1 and assumed that it is representative of the long-term behaviour (over the
186 past 15 ky in the Apennines). These values were derived from approximately 65
187 available neotectonics, palaeoseismology and seismotectonics papers (see the
188 supplemental files). To evaluate the long-term slip rate, which is representative of the
189 average slip behaviour, and its variability over time, we used slip rates determined in
190 different ways and at different time scales (e.g., at the decadal scale based on
191 geodetic data or at longer scales based on the displacement of Holocene or Plio-
192 Pleistocene horizons). Because a direct comparison of slip rates over different time
193 intervals obtained by different methods may be misleading (Nicol et al., 2009), we
194 cannot exclude the possibility that epistemic uncertainties could affect the original



195 data in some cases. The discussion of these possible biases and their evaluation via
196 statistically derived approaches (e.g., Gardner et al., 1987; Finnegan et al., 2014;
197 Gallen et al., 2015) is beyond the scope of this paper and will be explored in future
198 work. Moreover, we are assuming that slip rate values used are representative of
199 seismic movements, and aseismic factors are not taken into account. Therefore, we
200 believe that investigating the effect of this assumption could be another issue
201 explored in future work; for example, by differentiating between aseismic slip factors
202 in different tectonic contexts.


203 Because 28 faults had no measured slip (or throw) rate (Fig. 1a), we proposed a
204 statistically derived approach to assign a slip rate to these faults. Based on the slip
205 rate spatial distribution shown in Figure 1b, we subdivided the fault database into
206 three large regions—the Northern Apennines, Central-Southern Apennines and
207 Calabria-Sicilian coast—and analysed the slip rate distribution in these three areas. In
208 Figure 1b, the slip rates tend to increase from north to south. The fault slip rates in
209 the Northern Apennines range from 0.3 to 0.8 mm/yr, with the most common ranging
210 from approximately 0.5-0.6 mm/yr; the slip rates in the Central-Southern Apennines
211 range from 0.3 to 1.0, and the most common rate is approximately 0.3 mm/yr; and
212 the slip rates in the southern area (Calabria and Sicily) range from 0.9 to 1.8, with
213 the most common being approximately 0.9 mm/yr.

214 The first step in assigning an average slip rate and a range of variability to the faults
215 with unknown values is to identify the most representative distribution among known
216 probability density functions using the slip rate data from each of the three areas. We
217 test five well-known probability density functions (*Weibull*, *normal*, *exponential*,
218 *Inverse Gaussian* and *gamma*) against mean slip rate observations. The resulting
219 function with the highest log-likelihood is the *normal* function in all three areas. Thus,
220 the mean value of the *normal* distribution is assigned to the faults with unknown
221 values. We assign a value of 0.58 mm/yr to faults in the northern area, 0.64 mm/yr to
222 faults in the Central-Southern area, and 1.10 mm/yr to faults in the Calabria-Sicilian
223 area. To assign a range of slip rate variability to each of the three areas, we test the
224 same probability density functions against slip rate variability observations. Similar to
225 the mean slip rate, the probability density function with the highest log-likelihood is
226 the *normal* function in all three areas. We assign a value of 0.25 mm/yr to the faults

227 in the northern area, 0.29 mm/yr to the faults in the Central-Southern area, and 0.35
228 mm/yr to the faults in the Calabria-Sicilian area.

229

230 2.1.2 Segmentation rules for delineating fault sources

231 An important issue in the definition of a fault source input is the formulation of
232 segmentation rules. In fact, the question of whether structural segment boundaries
233 along multisegment active faults act as persistent barriers to a single rupture is
234 critical to defining the maximum seismogenic potential of fault sources. In our case,
235 the rationale behind the definition of a fault source is based on the assumption that
236 the geometric and kinematic features of a fault source are expressions of its
237 seismogenic potential and that its dimensions are compatible for hosting major (M_w
238 ≥ 5.5) earthquakes. Therefore, a fault source is ~~is considered~~  fault or an ensemble of
239 faults that slip together during an individual major earthquake. A fault source is
240 defined by a *seismogenic master fault* and its surface projection (Fig. 2a).
241 *Seismogenic master faults* are separated from each other by first-order structural or
242 geometrical complexities. Following the suggestions by Boncio et al. (2004) and
243 Field et al. (2015), we imposed the following segmentation rules in our case study: (i)
244 4-km fault gaps among aligned structures; (ii) intersections with cross structures
245 (often transfer faults) extending 4 km along strike and oriented at nearly right angles
246 to the intersecting faults; (iii) overlapping or underlapping en echelon arrangements
247 with separations between faults of 4 km; (iv) bending $\geq 60^\circ$ for more than 4 km; (v)
248 average slip rate variability along a strike greater than or equal to 50%; and (vi)
249 changes in seismogenic thickness greater than 5 km among aligned structures.
250 Example applications of the above rules are illustrated in Figure 2a.

251 By applying the above rules to our fault database, the 110 faults yielded 86 fault
252 sources: 9 strike-slip sources and 77 normal-slip sources. The longest fault source is
253 *Castelluccio dei Sauri* (fault number (*id in Table 1*) 42, $L = 93.2$ km), and the shortest
254 is *Castrovillari* (*id* 63, $L = 10.3$ km). The mean length is 30 km. The dip angle varies
255 from 30° to 90° , and 70% of the fault sources have dip angles between 50° and 60° .
256 The mean value of seismogenic thickness (ST) is approximately 12 km. The source
257 with the largest ST is *Mattinata* (*id* 41, $ST = 25$ km), and the source with the thinnest

258 ST is *Monte Santa Maria Tiberina* (id 9, ST = 2.5 km) due to the presence of an east-
259 dipping low angle normal fault, the Alto-Tiberina Fault (Boncio et al., 2000), located a
260 few kilometres west of the Monte Santa Maria Tiberina fault. Observed values of
261 maximum magnitude (M_w) have been assigned to 35 fault sources (based on Table
262 2), and the values vary from 5.90 to 7.32. The fault source inputs are shown in
263 Figure 3.

265 2.1.3 Expected seismicity rates

266 Each fault source is characterized by data, such as kinematic, geometry and slip rate
267 information, that we use as inputs for the FiSH code (Pace et al., 2016) to calculate
268 the global budget of the seismic moment rate allowed by the structure. This
269 calculation is based on predefined size-magnitude relationships in terms of the
270 maximum magnitude (M_{max}) and the associated mean recurrence time (T_{mean}). Table
271 1 summarizes the geometric parameters used as FiSH input parameters for each
272 fault source (seismogenic box) shown in Figure 3. To evaluate M_{max} of each source,
273 according to Pace et al., (2016) we first computed and then combined up to five M_{max}
274 values (see the example of the Paganica fault source in Fig. 2b, details in Pace et
275 al., 2016). Specifically, these five M_{max} values are as follows: MMO based on the
276 calculated scalar seismic moment (M_0) and the application of the standard formula
277 $M_w = 2/3 (\log M_0 - 9.1)$ (Hanks and Kanamori, 1979; IASPEI, 2005); two magnitude
278 values using the Wells and Coppersmith (1994) empirical relationships for the
279 maximum subsurface rupture length (MRLD) and maximum rupture area (MRA); a
280 value that corresponds to the maximum observed magnitude (MObs), if available;
281 and a value (MASP, ASP for aspect ratio) computed by reducing the fault length
282 input if the aspect ratio (W/L) is smaller than the value evaluated by the relation
283 between the aspect ratio and rupture length of observed earthquake ruptures, as
284 derived by Peruzza and Pace (2002) (not in the case of Paganica in Fig. 2b).
285 Although incorrect to consider MObs a possible M_{max} value and treat it the same as
286 other estimations, in some cases, it was useful to constrain the seismogenic
287 potentials of individual seismogenic sources. As an example, for the *Irpinia Fault* (id
288 51 in Tables 1 and 2), the characteristics of the 1980 earthquake ($M_w \sim 6.9$) can be
289 used to evaluate M_{max} via comparison with the M_{max} derived from scaling
290 relationships. In such cases, we (i) calculated the maximum expected magnitude

291 (M_{max1}) and the relative uncertainties using only the scaling relationships and (ii)
292 compared the maximum of observed magnitudes of the earthquakes potentially
293 associated with the fault. If M_{Obs} was within the range of $M_{max} \pm 1$ standard
294 deviation, we considered the value and recalculated a new M_{max} (M_{max2}) with a new
295 uncertainty. If M_{Obs} was larger than M_{max1} , we reviewed the fault geometry and/or
296 the earthquake-source association.

297 Because all the empirical relationships, as well as observed historical and recent
298 magnitudes of earthquakes, are affected by uncertainties, the *MomentBalance* (MB)
299 portion of the FiSH code (Pace et al., 2016) was used to account for these
300 uncertainties. MB computes a probability density function for each magnitude
301 derived from empirical relationships or observations and summarizes the results as a
302 maximum magnitude value with a standard deviation. The uncertainties in the
303 empirical scaling relationship are taken from the studies of Wells and Coppersmith
304 (1994), Peruzza and Pace (2002) and Leonard (2010). Currently, the uncertainty in
305 magnitude associated with the seismic moment is fixed and set to 0.3, whereas the
306 catalogue defines the uncertainty in M_{Obs} . Moreover, to combine the evaluated
307 maximum magnitudes, MB creates a probability curve for each magnitude by
308 assuming a normal distribution (Fig. 2). We assumed an untruncated normal
309 distribution of magnitudes at both sides. MB successively sums the probability
310 density curves and fits the summed curve to a normal distribution to obtain the mean
311 of the maximum magnitude M_{max} and its standard deviation.

312 Thus, a unique M_{max} with a standard deviation is computed for each source, and this
313 value represents the maximum rupture that is allowed by the fault geometry and the
314 rheological properties.

315 Finally, to obtain the mean recurrence time of M_{max} (i.e., T_{mean}), we use the criterion
316 of “segment seismic moment conservation” proposed by Field et al. (1999). This
317 criterion divides the seismic moment that corresponds to M_{max} by the moment rate
318 for given a slip rate:

$$319 \quad T_{mean} = \frac{1}{Char_Rate} = \frac{10^{1.5 M_{max} 9.1}}{\mu VLW} \quad (1)$$

320 where T_{mean} is the mean recurrence time in years, Char_Rate is the annual mean
321 rate of occurrence, M_{max} is the computed mean maximum magnitude, μ is the shear
322 modulus, V is the average long-term slip rate, and L and W are ~~geometrical~~
323 ~~parameters of the fault~~ along-strike rupture length and downdip width, respectively.
324 This approach was used for both MFDs in this study, and, in particular, we evaluated
325 M_{max} and T_{mean} based on the fault geometry and the slip rate of each individual
326 source. Additionally, we calculated the total expected seismic moment rate using
327 equation 1. Then, we partitioned the total expected seismic moment rate based on a
328 range given by $M_{\text{max}} \pm 1$ standard deviation following a Gaussian distribution.
329 After the fault source is entered as input, the seismic moment rate is calculated, M_{max}
330 (Fig. 2b) and T_{mean} are defined for each source, we computed the MFDs of expected
331 seismicity. For each fault source, we use two “end-member” MFD models: (i) a
332 *Characteristic Gaussian (CHG)* model, a symmetric Gaussian curve (applied to the
333 incremental MFD values) centred on the M_{max} value of each fault with a range of
334 magnitudes equal to 1-sigma, and (ii) a *Truncated Gutenberg-Richter (TGR, Ordaz,*
335 *1999; Kagan, 2002)* model, with M_{max} as the upper threshold and $M_w = 5.5$ as the
336 minimum threshold for all sources. The b-values are constant and equal to 1.0 for all
337 faults, and they are obtained by the interpolation of earthquake data from the CPTI15
338 catalogue, as single-source events are insufficient for calculating the required
339 statistics. The a-values were computed with the ActivityRate tool of the FiSH code.
340 ActivityRate balances the total expected seismic moment rate with the seismic
341 moment rate that was obtained based on M_{max} and T_{mean} (details in Pace et al.,
342 2016). In Figure 2c, we show an example of the expected seismicity rates in terms of
343 the annual cumulative rates for the Paganica source using the two above-described
344 MFD.
345 Finally, we create a so-called “expert judgement” model, called the *Mixed* model, to
346 determine the MFD for each fault source based on the earthquake-source
347 associations. In this case, we decided that if an earthquake assigned to a fault
348 source (see Table 2 for earthquake-source associations) has a magnitude lower than
349 the magnitude range in the curve of the *CHG* model distribution, the *TGR* model is
350 applied to that fault source. Otherwise, the *CHG* model, which peaks at the
351 calculated M_{max} , is applied. Of course, errors in this approach can originate from the
352 misallocation of historical earthquakes, and we cannot exclude the possibility that
353 potentially active faults responsible for historical earthquakes have not yet been

354 mapped. The MFD model assigned to each fault source in our *Mixed* model is shown
355 in Figure 3.

356

357 **2.2 Distributed Source Inputs**

358 Introducing distributed earthquakes into the PSH model is necessary because
359 researchers have not been able to identify a causative source (i.e., a mapped fault)
360 for important earthquakes in the historical catalogue. This lack of correlation between
361 earthquakes and faults may be related to (i) interseismic strain accumulation in areas
362 between major faults, (ii) earthquakes occurring on unknown or blind faults, (iii)
363 earthquakes occurring on unmapped faults characterized by slip rates lower than the
364 rates of erosional processes, and/or (iv) the general lack of surface ruptures
365 associated with faults generating $M_w < 5.5$ earthquakes.

366 We used the historical catalogue of earthquakes (CPTI15; Rovida et al., 2016; Fig.
367 4) to model the occurrence of moderate-to-large ($M_w \geq 4.5$) earthquakes. The
368 catalogue consists of 4,427 events and covers approximately the last one thousand
369 years from 01/01/1005 to 28/12/2014. Before using the catalogue, we removed all
370 events not considered mainshocks via a declustering filter (Gardner and Knopoff,
371 1977). This process resulted in a **complete catalogue** composed of 1,839
372 independent events. Moreover, to avoid ~~any artificial effects related to~~ double
373 counting due to the use of two seismicity sources, i.e., the fault sources and the
374 distributed seismicity sources, we removed events associated with known active
375 faults from the CPTI15 earthquake catalogue. If the causative fault of an earthquake
376 is known, that earthquake does not need to be included in the seismicity smoothing
377 procedure. The earthquake-source association is based on neotectonics,
378 palaeoseismology and seismotectonics papers (see the supplemental files) and, in a
379 few cases, macroseismic intensity maps. In Table 2, we listed the earthquakes with
380 known causative fault sources. The differences in the smoothed rates given by eq.
381 (2) using the complete and modified catalogues are shown in Figure 5.

382 We applied the standard methodology developed by Frankel (1995) to estimate the
383 density of seismicity in a grid with latitudinal and longitudinal spacing of 0.05° . The
384 smoothed rate of events in each cell i is determined as follows:

385

$$n_i = \frac{\sum_j n_j e^{-\frac{\Delta_{ij}^2}{c^2}}}{\sum_j e^{-\frac{\Delta_{ij}^2}{c^2}}} \quad (2)$$

386 where n_i is the cumulative rate of earthquakes with magnitudes greater than the
387 completeness magnitude M_c in each cell i of the grid and Δ_{ij} is the distance between
388 the centres of grid cells i and j . The parameter c is the correlation distance. The sum
389 is calculated in cells j within a distance of $3c$ of cell i .

390 To compute earthquake rates, we adopted the completeness magnitude thresholds
391 over different periods given by Stucchi et al. (2011) for five large zones (Fig. 4).

392 To optimize the smoothing distance Δ in eq. (2), we divided the earthquake
393 catalogue into four 10-yr disjoint learning and target periods from the 1960s to the
394 1990s. For each pair of learning and target catalogues, we used the probability gain
395 per earthquake to find the optimal smoothing distance (Kagan and Knopoff, 1977;
396 Helmstetter et al., 2007). After assuming a spatially uniform earthquake density
397 model as a reference model, the probability gain per earthquake G of a candidate
398 model relative to a reference model is given by the following equation:

399

$$G = \exp\left(\frac{L-L_0}{N}\right) \quad (3)$$

400 where N is the number of events in the target catalogue and L and L_0 are the joint
401 log-likelihoods of the candidate model and reference model, respectively. Under the
402 assumption of a Poisson earthquake distribution, the joint log-likelihood of a model is
403 given as follows:

404

$$L = \sum_{i_x=1}^{N_x} \sum_{j_y=1}^{N_y} \log p [\lambda(i_x, i_y), \omega] \quad (4)$$

405 where p is the Poisson probability, λ is the spatial density, ω is the number of
406 observed events during the target period, and the parameters i_x and i_y denote each
407 corresponding longitude-latitude cell.

408 Figure 6 shows that for the four different pairs of learning-target catalogues, the
409 optimal smoothing distance c ranges from 30-40 km. Finally, the mean of all the

410 probability gains per earthquake yields a maximum smoothing distance of 30 km
411 (Fig. 6), which is then used in eq. (2).

412 The b-value of the GR distribution is calculated on a regional basis using the
413 maximum-likelihood method of Weichert (1980), which allows multiple periods with
414 varying completeness levels to be combined. Following the approach recently
415 proposed by Kamer and Hiemer (2015), we used a penalized likelihood-based
416 method for the spatial estimation of the GR b-values based on the Voronoi
417 tessellation of space without tectonic dependency. The whole Italian territory has
418 been divided into a grid with a longitude/latitude spacing of 0.05° , and the centres of
419 the grid cells represent the possible centres of Voronoi polygons. We vary the
420 number of Voronoi polygons, N_v , from 3 to 50, generating 1000 tessellations for
421 each N_v . The summed log-likelihood of each obtained tessellation is compared with
422 the log-likelihood given by the simplest model (prior model) obtained using the entire
423 earthquake dataset. We find that 673 random realizations led to better performance
424 than the prior model. Thus, we calculate an ensemble model using these 673
425 solutions, and the mean b-value of each grid node is shown in Figure 4.

426 The maximum magnitude M_{max} assigned to each node of the grid, the nodal planes
427 and the depths have been taken from the SHARE European project (Woessner et
428 al., 2015). The SHARE project evaluated the maximum magnitudes of large areas of
429 Europe based on a joint procedure involving historical observations and tectonic
430 regionalization. We adopted the lowest of the maximum magnitudes proposed by
431 SHARE, but evaluating the impact of different maximum magnitudes is beyond the
432 scope of this work.

433 Finally, the rates of expected seismicity for each node of the grid are assumed to
434 follow the TGR model (Kagan 2002):

$$435 \quad \lambda(M) = \lambda_0 \frac{\exp(-\beta M) - \exp(-\beta M_u)}{\exp(-\beta M_0) - \exp(-\beta M_u)} \quad (5)$$

436 where the magnitude (M) is in the range of M_0 (minimum magnitude) to M_u (upper or
437 maximum magnitude); otherwise $\lambda(M)$ is 0. Additionally, λ_0 is the smoothed rate of
438 earthquakes at $M_w = 4.5$ and $\beta = b \ln(10)$.

439 2.3 Combining Fault and Distributed Sources

440 To combine the two source inputs, we introduced a distance-dependent linear
441 weighting function, such that the contribution from the distributed sources linearly
442 decreases from 1 to 0 with decreasing distance from the fault. The expected
443 seismicity rates of the distributed sources start at $M_w = 4.5$, which is lower than the
444 minimum magnitude of the fault sources, and the weighting function is only
445 applicable in the magnitude range overlapping the MFD of each fault. This weighting
446 function is based on the assumption that faults tend to modify the surrounding
447 deformation field (Fig. 7), and this assumption is explained in detail later in this
448 paper.

449 During fault system evolution, the increase in the size of a fault through linking with
450 other faults results in an increase in displacement that is proportional to the quantity
451 of strain accommodated by the fault (Kostrov, 1974). Under a constant regional
452 strain rate, the activity of **arranged across strike** must eventually decrease (Nicol et
453 al., 1997; Cowie, 1998; Roberts et al., 2004). Using an analogue modelling,
454 Mansfield and Cartwright (2001) showed that faults grow via cycles of overlap, relay
455 formation, breaching and linkage between neighbouring segments across a wide
456 range of scales. During the evolution of a system, the merging of neighbour faults,
457 mostly along the strike, results in the formation of major faults, which are associated
458 with the majority of displacement. These major faults are surrounded by minor faults,
459 which are associated with lower degree of displacement. To highlight the spatial
460 patterns of major and minor faults, Figures 7a and 7b present diagrams from the
461 Mansfield and Cartwright (2001) experiment in two different stages: the approximate
462 midpoint of the sequence and the end of the sequence. Numerical modelling
463 performed by Cowie et al. (1993) yielded similar evolutionary features for major and
464 minor faults. The numerical fault simulation of Cowie et al. (1993) was able to
465 reproduce the development of a normal fault system from the early nucleation stage,
466 including interactions with adjacent faults, to full linkage and the formation of a large
467 through fault. The model also captures the increase in the displacement rate of a
468 large linked fault. In Figures 7c and 7d, we focus on two stages of the simulation
469 (from Cowie et al., 1993): the stage in which the fault segments have formed and
470 some have become linked and the final stage of the simulation.

471 Notably, the spatial distributions of major and minor faults are very similar in the
472 experiments of both Mansfield and Cartwright (2001) and Cowie et al. (1993), as
473 shown in Figures 7a-d. Developments during the early stage of major fault formation
474 appear to control the location and evolution of future faults, with some areas where
475 no major faults develop. The long-term evolution of a fault system is the
476 consequence of the progressive cumulative effects of the slip history, i.e.,
477 earthquake occurrence, of each fault. Large earthquakes are generally thought to
478 produce static and dynamic stress changes in the surrounding areas (King et al.,
479 1994; Stein, 1999; Pace et al., 2014; Verdecchia and Carena, 2016). Static stress
480 changes produce areas of negative stress, also known as shadow zones, and
481 positive stress zones. The spatial distributions of decreases (unloading) and
482 increases (loading) in stress during the long-term slip history of faults likely influence
483 the distance across strike between major faults. Thus, given a known major active
484 fault geometrically capable of hosting a $M_w \geq 5.5$ earthquake, the possibility that a
485 future $M_w \geq 5.5$ earthquake will occur in the vicinity of the fault, but is not caused by
486 that fault, should decrease as the distance from the fault decreases. Conversely,
487 earthquakes with magnitudes lower than 5.5 and those due to slip along minor faults
488 are likely to occur everywhere within a fault system, including in proximity to a major
489 fault.

490 In Figure 7e, we illustrate the results of ~~the~~ analogue and numerical modelling of
491 fault system evolution and indicate the areas around major faults where it is unlikely
492 that other major faults develop. In Figure 7f, we show the next step in moving from
493 geologic and structural considerations. In this step, we combine fault sources and
494 distributed seismicity source inputs, which serve as inputs for the PSH model. Fault
495 sources are used to model major faults and are represented by a master fault (i.e.,
496 one or more major faults) and its projection at the surface. Distributed seismicity is
497 used to model seismicity associated with minor, unknown or unmapped faults.
498 Depending on the positions of distributed seismicity points with respect to the buffer
499 zones around major faults, the rates of expected distributed seismicity remain
500 unmodified or decrease and can even reach zero.

501 Specifically, we introduced a slip rate and a distance-weighted linear function based
502 on the above reasoning. The probability of the occurrence of an earthquake (P_e) with
503 a M_w greater than or equal to the minimum magnitude of the fault is as follows:

504
$$Pe = \begin{cases} 0, & d \leq 1 \text{ km} \\ d/d_{max}, & 1 \text{ km} < d \leq d_{max} \\ 1, & d > d_{max} \end{cases} \quad (6)$$

505 where d is the Joyner-Boore distance from a fault source. The maximum value of d
 506 (d_{max}) is controlled by the slip rate of the fault. For faults with slip rates ≥ 1 mm/yr, we
 507 assume $d_{max} = L/2$ (L is the length along the strike, Fig. 2a); for faults with slip rates
 508 of 0.3 - 1 mm/yr, $d_{max} = L/3$; and for faults with slip rates of ≤ 0.3 mm/yr, $d_{max} = L/4$.
 509 The rationale for varying d_{max} is given by a simple assumption: the higher the slip
 510 rate is, the larger the deformation field and the higher the value of d_{max} . We applied
 511 eq. (6) to the smoothed occurrence rates of the distributed seismogenic sources.
 512 Because we consider two fault source inputs, one using only TGR MFD and the
 513 other only CHR MFD, and because the MFDs of distributed seismicity grid points in
 514 the vicinity of faults are modified with respect to the MFDs of these faults, we obtain
 515 two different inputs of distributed seismicity. These two distributed seismogenic
 516 source inputs differ because the minimum magnitude of the faults is Mw 5.5 in the
 517 TGR model, but this value depends on each fault source dimension in the CHG
 518 model, as shown in Figure 8.

519 Our approach allows incompleteness in the fault database to be bypassed, which is
 520 advantageous because all fault databases should be considered incomplete. In our
 521 approach, the seismicity is modified only in the vicinity of mapped faults. The
 522 remaining areas are fully described by the *distributed input*. With this approach, we
 523 do not define areas with reliable fault information, and the locations of currently
 524 unknown faults can be easily included when they are discovered in the future.

525 3. Results and Discussion

526 To obtain PSH maps, we assign the calculated seismicity rates, based on the
 527 Poisson hypothesis, to their pertinent geometries, i.e., individual 3D seismogenic
 528 sources for the *fault input* and point sources for the *distributed input* (Fig. 8). All the
 529 computations are performed using the OpenQuake Engine (Global Earthquake
 530 Model, 2016) with a grid spacing of 0.05° in both latitude and longitude. We use this
 531 software because it is open source software developed recently by GEM with the
 532 purpose of providing seismic hazard and risk assessments. Moreover, it is widely
 533 recognized within the scientific community for its potential. The ground motion

534 prediction equations (GMPE) of Akkar et al. (2013), Chiou et al. (2008), Faccioli et
535 al., (2010) and Zhao et al., (2006) are used, as suggested by the SHARE European
536 project (Woessner et al., 2015). In addition, we used the GMPE proposed by Bindi et
537 al. (2014) and calibrated using Italian data. We combined all GMPEs into a logic tree
538 with the same weight of 0.2 for each branch. ~~The distance used for each GMPE was~~
539 the Joyner and Boore distance for Akkar et al. (2013), Bindi et al. (2014) and Chiou
540 et al. (2008) and the closest rupture distance for Faccioli et al. (2010) and Zhao et al.
541 (2006).

542 The results of the fault source inputs, distributed source inputs, and aggregated
543 model are expressed in terms of peak ground acceleration (PGA) based on
544 exceedance probabilities of 10% and 2% over 50 years, corresponding to return
545 periods of 475 and 2,475 years, respectively (Fig. 9).

546 To explore the epistemic uncertainty associated with the ~~distribution of activity rates~~
547 ~~over the range of magnitude~~ of fault source inputs, we compared the seismic
548 hazard levels obtained based on the TGR and CHG fault source inputs (left column
549 in Fig. 9) using the TGR and CHG MFDs for all the fault sources (details in section
550 2.1.3). Although both models have the same seismic moment release, the different
551 MFDs generate clear differences. In fact, in the *TGR* model, all faults contribute
552 significantly to the seismic hazard level, whereas in the *CHG* model, only a few faults
553 located in the central Apennines and Calabria contribute to the seismic hazard level.
554 This difference is due to the different shapes of the MFDs in the two models (Fig.
555 2c). As shown in Figure 8, the percentage of earthquakes with magnitudes between
556 5.5 and approximately 6, which are likely the main contributors to these levels of
557 seismic hazard is generally higher in the *TGR* model than in the *CHG* model. At a
558 2% probability of exceedance in 50 years, all fault sources in the *CHG* contribute to
559 the seismic hazard level, but the absolute values are still generally higher in the *TGR*
560 model.

561 The *distributed input* (middle column in Fig. 9) depicts a more uniform shape of the
562 seismic hazard level than that of fault source inputs. A low PGA value of 0.125 g at a
563 10% probability of exceedance over 50 years and a low value of 0.225 g at a 2%
564 probability of exceedance over 50 years encompass a large part of peninsular Italy

565 and Sicily. Two areas with high seismic hazard levels are located in the central
566 Apennines and northeastern Sicily.

567 The overall model, which was ~~created~~ by combining the fault and distributed source
568 inputs, is shown in the right column of Figure 9. Areas with comparatively high
569 seismic hazard levels, i.e., hazard levels greater than 0.225 g and greater than 0.45
570 g at 50-yr exceedance probabilities of 10% and 2%, respectively, are located
571 throughout the Apennines, in Calabria and in Sicily. The fault source inputs
572 contribute most to the total seismic hazard levels in the Apennines, Calabria and
573 eastern Sicily, where the highest PGA values are observed.

574 Figure 10 shows the contributions to the total seismic hazard level by the *fault* and
575 *distributed* source inputs at a specific site (L'Aquila, 42.400-13.400). Notably, in
576 Figure 10, *distributed* sources dominate the seismic hazard contribution at
577 exceedance probabilities greater than ~81% over 50 years, but the contribution of
578 *fault* sources cannot be neglected. Conversely, at exceedance probabilities of less
579 than ~10% in 50 years, the total hazard level is mainly associated with *fault* source
580 inputs.

581 Figure 11 presents seismic hazard maps for PGA at 10% and 2% exceedance
582 probabilities in 50 years for *fault* sources, *distributed* sources and a combination of
583 the two. These data were obtained using the above-described *Mixed* model, in which
584 we selected the most "appropriate" MFD model (TGR or CHG) for each fault (as
585 shown in Figure 3). The results of this model therefore have values between those of
586 the two end-members shown in Figure 9.

587 Figure 12 shows the *CHG*, *TGR* and *Mixed* model hazard curves of three sites
588 (Cesena, L'Aquila and Crotone, Fig. 13c). As previously noted, the results of the
589 *Mixed* model, due to the structure of the model, are between those of the *CHG* and
590 *TGR* models. The relative positions of the hazard curves derived from the two end-
591 member models and the *Mixed* model depend on the number of nearby fault sources
592 that have been modelled using one of the MFD models and on the distance of the
593 site from the faults. For example, in the case of the Crotone site, the majority of the
594 fault sources in the *Mixed* model are modelled using the CHG MFD. Thus, the
595 resulting hazard curve is similar to that of the *CHG* model. For the Cesena site, the

596 three hazard curves overlap. Because the distance between Cesena and the closest
597 fault sources is approximately 60 km, the impact of the fault input is less than the
598 impact of the *distributed* source input. In this case, the choice of a particular MFD
599 model has a limited impact on the modelling of *distributed* sources. Notably, for an
600 annual frequency of exceedance (AFOE) lower than 10^{-4} , the *TGR fault* source input
601 values are generally higher than those of the *CHG* source input, and the three
602 models converge at $AFOE < 10^{-4}$. The resulting seismic hazard estimates depend on
603 the assumed MFD model (*TGR* vs. *CHG*), especially for intermediate-magnitude
604 events (5.5 to ~6.5). Because we assume that the maximum magnitude is imposed
605 by the fault geometry and that the seismic moment release is controlled by the slip
606 rate, the *TGR* model leads to the highest hazard values because this range of
607 magnitude contributes the most to the hazard level.

608 In Figure 13, we investigated the influences of the Mixed *fault* source inputs and the
609 Mixed *distributed* source inputs on the total hazard level of the entire study area, as
610 well as the variability in the hazard results. The maps in Figure 13a show that the
611 contribution of *fault* inputs to the total hazard level generally decreases as the
612 exceedance probability increases from 2% to 81% in 50 years. At a 2% probability of
613 exceedance in 50 years, the total hazard levels in the Apennines and eastern Sicily
614 are mainly related to faults, whereas at an 81% probability of exceedance in 50
615 years, the contributions of *fault* inputs are high in local areas of central Italy and
616 southern Calabria.

617 Moreover, we examined the contributions of *fault* and *distributed* sources along three
618 E-W-oriented profiles in northern, central and southern Italy (Fig. 13b). Note that the
619 contributions are not based on deaggregation but are computed according to the
620 percentage of each source input in the AFOE value of the combined model. In areas
621 with faults, the hazard level estimated by *fault* inputs is generally higher than that
622 estimated by the corresponding *distributed* source inputs. Notable exceptions are
623 present in areas proximal to slow-slipping active faults at an 81% probability of
624 exceedance in 50 years (profile A), such as those at the eastern and western
625 boundaries of the fault area in central Italy (profile B), and in areas where the
626 contribution of the *distributed* source input is equal to that of the *fault* input at a 10%
627 probability of exceedance in 50 years (eastern part of profile C).

628 The features depicted by the three profiles result from a combination of the slip rates
629 and spatial distributions of faults for *fault* source inputs. This pattern should be
630 considered a critical aspect of using fault models for PSH analysis. In fact, the
631 proposed approach requires a high level of expertise in active tectonics and cautious
632 expert judgement at many levels in the procedure. First, the seismic hazard estimate
633 is based on the definition of a segmentation model, which requires a series of rules
634 based on observations and empirical regression between earthquakes and the size
635 of the causative fault. New data might make it necessary to revise the rules or
636 reconsider the role of the segmentation. In some cases, expert judgement could
637 permit discrimination among different fault source models. Alternatively, all models
638 should be considered branches in a logic tree approach.

639 Moreover, we propose a fault seismicity input in which the MFD of each fault source
640 has been chosen based on an analysis of the occurrences of earthquakes that can
641 be tentatively or confidently assigned to a certain fault. To describe the fault activity,
642 we applied a probability density function to the magnitude, as commonly performed
643 in the literature: the TGR model, where the maximum magnitude is the upper
644 threshold and $M_w = 5.5$ is the lower threshold for all faults, and the characteristic
645 maximum magnitude model, which consists of a truncated normal distribution
646 centred on the maximum magnitude. Other MFDs have been proposed to model the
647 earthquake recurrence of a fault. For example, Youngs and Coppersmith (1985)
648 proposed a modification to the truncated exponential model to allow for the
649 increased likelihood of characteristic events. However, we focused only on two
650 models, as we believe that instead of a “blind” or qualitative characterization of the
651 MFD of a fault source, future applications of statistical tests of the compatibility
652 between expected earthquake rates and observed historical seismicity could be used
653 as an objective method of identifying the optimal MFD of expected seismicity.

654 To focus on the general procedure for spatially integrating faults with sources
655 representing distributed (or off-fault) seismicity, we did not investigate the impact of
656 other smoothing procedures on the distributed sources, and we used fixed kernels
657 with a constant bandwidth (as in the works of Kagan and Jackson, 1994; Frankel et
658 al. 1997; Zechar and Jordan, 2010). The testing of adaptive bandwidths (e.g., Stock

659 and Smith, 2002; Helmstetter et al., 2006, 2007; Werner et al., 2011) or weighted
660 combinations of both models has been reserved for future studies.

661

662 Finally, we compared, as shown in Figure 14, the 2013 European Seismic Hazard
663 Model (ESHM13) developed within the SHARE project, the current Italian national
664 seismic hazard map (MPS04) and the results of our model (Mixed model) using the
665 same GMPEs as used in this study. Specifically, for ESHM13, we compared the
666 results to the fault-based hazard map (FSBG model) that accounts for fault sources
667 and background seismicity. The figure shows how the impact of our fault sources is
668 more evident than in FSBG-ESHM13, and the comparison with MPS04 confirms a
669 similar pattern, but with some significant differences at the regional to local scales.

670

671 The strength of our approach lies in the integration of different levels of information
672 regarding the active faults in Italy, but the final result is unavoidably linked to the
673 quality of the relevant data. Our work focused on presenting and applying a new
674 approach for evaluating seismic hazards based on active faults and intentionally
675 avoided the introduction of uncertainties due to the use of different segmentation
676 rules or other slip rate values of faults. Moreover, the impact of ground motion
677 predictive models is important in seismic hazard assessment but beyond the scope
678 of this work. Future steps will be devoted to analysing these uncertainties and
679 evaluating their impacts on seismic hazard estimates.

680

681 **4. Conclusions**



682 We presented our first national-scale PSH model of Italy, which summarizes and
683 integrates the fault-based PSH models developed since the publication of Pace et al.
684 in 2006.

685 The model proposed in this study combines fault source inputs based on over 110
686 faults grouped into 86 fault sources and distributed source inputs. For each fault
687 source, the maximum magnitude and its uncertainty were derived by applying
688 scaling relationships, and the rates of seismic activity were derived by applying slip
689 rates to seismic moment evaluations and balancing these seismic moments using
690 two MFD models.

691 To account for unknown faults, a distributed seismicity input was applied following
692 the well-known Frankel (1995) methodology to calculate seismicity parameters.

693 The fault sources and distributed sources have been integrated via a new approach
694 based on the idea that deformation in the vicinity of an active fault is concentrated
695 along the fault and that the seismic activity in the surrounding region is reduced. In
696 particular, a distance-dependent linear weighting function has been introduced to
697 allow the contribution of distributed sources (in the magnitude range overlapping the
698 MFD of each fault source) to linearly decrease from 1 to 0 with decreasing distance
699 from a fault. The strength of our approach lies in the ability to integrate different
700 levels of available information for active faults that actually exist in Italy (or
701 elsewhere), but the final result is unavoidably linked to the quality of the relevant
702 data.

703 The PSH maps produced using our model show a hazard pattern similar to that of
704 the current maps at the national scale, but some significant differences in hazard
705 level are present at the regional to local scales (Figure 13).

706 Moreover, the impact ~~that~~  using different MFD models to derive seismic activity rates
707 ~~has~~ on the hazard maps was investigated. The PGA values in the hazard maps
708 ~~generated by~~  the *TGR* model are higher than those in the hazard maps ~~generated by~~
709 the *CHG* model. This difference is because the rates of earthquakes with
710 magnitudes from 5.5 to approximately 6 are generally higher in the *TGR* model than
711 in the *CHG* model. Moreover, the relative contributions of fault source inputs and
712 distributed source inputs have been identified in maps and profiles in three sectors of
713 the study area. These profiles show that the hazard level is generally higher where
714 fault inputs are used, and for high probabilities of exceedance, the contribution of
715 *distributed* inputs equals that of *fault* inputs.

716 Finally, the *Mixed* model was created by selecting the most appropriate MFD model
717 for each fault. All data, including the locations and parameters of fault sources, are
718 provided in the supplemental files of this paper.

719 This new PSH model is not intended to replace, integrate or assess the current
720 official national seismic hazard model of Italy. While some aspects remain to be
721 implemented in our approach (e.g., the integration of reverse/thrust faults in the
722 database, sensitivity tests for the distance-dependent linear weighting function
723 parameters, sensitivity tests for potential different segmentation models, and fault
724 source inputs that account for fault interactions), the proposed model represents

725 advancements in terms of input data (quantity and quality) and methodology based
726 on a decade of research in the field of fault-based approaches to regional seismic
727 hazard modelling.

728

729

730

731

732

733

734

735 **References**

736

737

738 Akinci, A., Galadini, F., Pantosti, D., Petersen, M., Malagnini, L., and Perkins, D.:
739 Effect of Time Dependence on Probabilistic Seismic-Hazard Maps and
740 Deaggregation for the Central Apennines, Italy, *B Seismol Soc Am*, 99, 585-
741 610, 2009.

742 Akkar, S., Sandikkaya, M.A. , Bommer, J.J.: Empirical Ground-Motion Models for
743 Point and Extended-Source Crustal Earthquake Scenarios in Europe and the
744 Middle East, *Bulletin of Earthquake Engineering*, ISSN:1570-761X, 2013.

745 Basili, R., Valensise, G., Vannoli, P., Burrato, P., Fracassi, U., Mariano, S., Tiberti,
746 M. M. and Boschi, E.: The Database of Individual Seismogenic Sources
747 (DISS), version 3: Summarizing 20 years of research on Italy's earthquake
748 geology, *Tectonophysics*, 453, 20- 43, 2008.

749 Benedetti, L., Manighetti, I., Gaudemer, Y., Finkel, R., Malavieille, J., Pou, K., Arnold,
750 M., Aumaitre, G., Bourles, D., and Keddadouche, K.: Earthquake synchrony
751 and clustering on Fucino faults (Central Italy) as revealed from in situ Cl-36
752 exposure dating, *J Geophys Res-Sol Ea*, 118, 4948-4974, 2013.

753 Bindi, D., Massa, M., Luzi, L., Ameri, G., Pacor, F., Puglia, R., and Augliera, P.: Pan-
754 European ground-motion prediction equations for the average horizontal
755 component of PGA, PGV, and 5%-damped PSA at spectral periods up to 3.0
756 s using the RESORCE dataset (vol 12, pg 391, 2014), *B Earthq Eng*, 12, 431-
757 448, 2014.

758 Boncio, P., Brozzetti, F. and Lavecchia G.: Architecture and seismotectonics of a
759 regional Low-Angle Normal Fault zone in Central Italy. *Tectonics*, 19 (6),
760 1038-1055, 2000.

761 Boncio, P., Lavecchia, G., and Pace, B.: Defining a model of 3D seismogenic
762 sources for Seismic Hazard Assessment applications: The case of central
763 Apennines (Italy), *J Seismol*, 8, 407-425, 2004.

764 Boncio, P., Pizzi, A., Cavuoto, G., Mancini, M., Piacentini, T., Miccadei, E., Cavinato,
765 G. P., Piscitelli, S., Giocoli, A., Ferretti, G., De Ferrari, R., Gallipoli, M. R.,
766 Mucciarelli, M., Di Fiore, V., Franceschini, A., Pergalani, F., Naso, G., and
767 Macroarea, W. G.: Geological and geophysical characterisation of the
768 Paganica - San Gregorio area after the April 6, 2009 L'Aquila earthquake (M-
769 w 6.3, central Italy): implications for site response, *B Geofis Teor Appl*, 52,
770 491-512, 2011.

771 Bull, J. M., Barnes, P. M., Lamarche, G., Sanderson, D. J., Cowie, P. A., Taylor, S.
772 K., and Dix, J. K.: High-resolution record of displacement accumulation on an
773 active normal fault: implications for models of slip accumulation during
774 repeated earthquakes, *J Struct Geol*, 28, 1146-1166, 2006.

775 Chiou, B. S. J. and Youngs, R. R.: An NGA model for the average horizontal
776 component of peak ground motion and response spectra, *Earthq Spectra*, 24,
777 173-215, 2008.

778 Cornell, C.A.: Engineering seismic risk analysis, *Bull. Seism. Soc. Am.*, 58,1583-
779 1606, 1968.

780 Cowie, P. A.: A healing-reloading feedback control on the growth rate of seismogenic
781 faults, *J Struct Geol*, 20, 1075-1087, 1998.

782 Cowie, P. A., Roberts, G. P., Bull, J. M., and Visini, F.: Relationships between fault
783 geometry, slip rate variability and earthquake recurrence in extensional
784 settings, *Geophys J Int*, 189, 143-160, 2012.

785 Cowie, P. A., Underhill, J. R., Behn, M. D., Lin, J., and Gill, C. E.: Spatio-temporal
786 evolution of strain accumulation derived from multi-scale observations of Late
787 Jurassic rifting in the northern North Sea: A critical test of models for
788 lithospheric extension, *Earth Planet Sc Lett*, 234, 401-419, 2005.

789 Cowie, P. A., Vanneste, C., and Sornette, D.: Statistical Physics Model for the
790 Spatiotemporal Evolution of Faults, *J Geophys Res-Sol Ea*, 98, 21809-21821,
791 1993.

792 D'amato, D., Pace, B., Di Nicola, L., Stuart, F.M., Visini, F., Azzaro, R., Branca, S.,
793 and Barfod, D.N.: Holocene slip rate variability along the Pernicana fault
794 system (Mt. Etna, Italy): Evidence from offset lava flows: *GSA Bulletin*,
795 doi:10.1130/B31510.1, 2016.

796 Faccioli, E., Bianchini, A., and Villani, M.: New ground motion prediction equations
797 for $t > 1$ s and their influence on seismic hazard assessment, In: *Proceedings*
798 *of the University of Tokyo symposium on long-period ground motion and*
799 *urban disaster mitigation*, 2010.

800 Ferranti, L., Palano, M., Cannavo, F., Mazzella, M. E., Oldow, J. S., Gueguen, E.,
801 Mattia, M., and Monaco, C.: Rates of geodetic deformation across active
802 faults in southern Italy, *Tectonophysics*, 621, 101-122, 2014.

803 Field, E. H., Biasi, G. P., Bird, P., Dawson, T. E., Felzer, K. R., Jackson, D. D.,
804 Johnson, K. M., Jordan, T. H., Madden, C., Michael, A. J., Milner, K. R., Page,
805 M. T., Parsons, T., Powers, P. M., Shaw, B. E., Thatcher, W. R., Weldon, R.
806 J., and Zeng, Y. H.: Long-Term Time-Dependent Probabilities for the Third
807 Uniform California Earthquake Rupture Forecast (UCERF3), *B Seismol Soc*
808 *Am*, 105, 511-543, 2015.

809 Field, E. H., Jackson, D. D., and Dolan, J. F.: A mutually consistent seismic-hazard
810 source model for southern California, *B Seismol Soc Am*, 89, 559-578, 1999.

811 Finnegan, N. J., Schumer, R., and Finnegan, S.: A signature of transience in bedrock
812 river incision rates over timescales of $10(4)$ - $10(7)$ years, *Nature*, 505, 391-+,
813 2014.

814 Frankel, A.: Simulating Strong Motions of Large Earthquakes Using Recordings of
815 Small Earthquakes - the Loma-Prieta Mainshock as a Test-Case, *B Seismol*
816 *Soc Am*, 85, 1144-1160, 1995.

817 Frankel, A., Mueller, C., Barnhard, T., Perkins, D., Leyendecker, E. V., Dickman, N.,
818 Hanson, S., and Hopper, M.: Seismic-hazard maps for California, Nevada,
819 and Western Arizona/Utah', *U.S. Geological Survey Open-File Rept.* 97-130,
820 1997.

821 Gallen, S. F., Pazzaglia, F. J., Wegmann, K. W., Pederson, J. L., and Gardner, T.
822 W.: The dynamic reference frame of rivers and apparent transience in incision
823 rates, *Geology*, 43, 623-626, 2015.

824 Garcia-Mayordomo, J., Gaspar-Escribano, J. M., and Benito, B.: Seismic hazard
825 assessment of the Province of Murcia (SE Spain): analysis of source
826 contribution to hazard, *J Seismol*, 11, 453-471, 2007.

827 Gardner, J. K., Knopoff, L.: Is the sequence of earthquakes in Southern California,
828 with aftershocks removed, Poissonian?'. *Bulletin of the Seismological Society*
829 *of America*, 64, 1363-1367, 1974.

830 Gardner, T. W., Jorgensen, D. W., Shuman, C., and Lemieux, C. R.: Geomorphic
831 and Tectonic Process Rates - Effects of Measured Time Interval, *Geology*, 15,
832 259-261, 1987.

833 Gasperini P., Bernardini F., Valensise G. and Boschi E.: Defining Seismogenic
834 Sources from Historical Earthquake Felt Reports, *Bull. Seism. Soc. Am.*, 89,
835 94-110, 1999.

836 GEM: The OpenQuake-engine User Manual. Global Earthquake Model (GEM)
837 Technical Report, doi: 10.13117/GEM.OPENQUAKE.MAN.ENGINE.1.9/01,
838 189 pages, 2016.

839 Gunderson, K. L., Anastasio, D. J., Pazzaglia, F. J., and Picotti, V.: Fault slip rate
840 variability on 10(4)-10(5)yr timescales for the Salsomaggiore blind thrust fault,
841 Northern Apennines, Italy, *Tectonophysics*, 608, 356-365, 2013.

842 Hanks, T. C., and Kanamori, H.: A moment magnitude scale, *Journal of Geophysics*
843 *Research*, 84, 2348–2350, 1979.

844 Helmstetter, A., Kagan, Y. Y., and Jackson, D. D.: Comparison of short-term and
845 time-independent earthquake forecast models for southern California, *B*
846 *Seismol Soc Am*, 96, 90-106, 2006.

847 Helmstetter, A., Kagan, Y. Y., and Jackson, D. D.: High-resolution time-independent
848 grid-based forecast for $M \leq 5$ earthquakes in California, *Seismol Res Lett*,
849 78, 78-86, 2007.

850 International Association of Seismology and Physics of the Earth's Interior (IASPEI):
851 Summary of Magnitude Working Group recommendations on standard
852 procedures for determining earthquake magnitudes from digital data,
853 <http://www.iaspei.org/>

854 commissions/CSOI/summary_of_WG_recommendations_2005.pdf (last
855 accessed December 2015), 2005.

856 Kagan, Y. Y.: Seismic moment distribution revisited: I. Statistical results, *Geophys J*
857 *Int*, 148, 520-541, 2002.

858 Kagan, Y., and Knopoff, L.: Earthquake risk prediction as a stochastic process,
859 *Physics of the Earth and Planetary Interiors*, 14, 97–108, 1977.

860 Kagan, Y. Y. and Jackson, D. D.: Long-Term Probabilistic Forecasting of
861 Earthquakes, *J Geophys Res-Sol Ea*, 99, 13685-13700, 1994.

862 Kamer, Y. and Hiemer, S.: Data-driven spatial b value estimation with applications to
863 California seismicity: To b or not to b, *J Geophys Res-Sol Ea*, 120, 5191-
864 5214, 2015.

865 King, G. C. P., Stein, R. S., and Lin, J.: Static Stress Changes and the Triggering of
866 Earthquakes, *B Seismol Soc Am*, 84, 935-953, 1994.

867 Kostrov, V. V.: Seismic moment and energy of earthquakes, and seismic flow of
868 rock, *Physic of the Solid Earth*, 1, 23-44, 1974.

869 Leonard, M.: Earthquake fault scaling: Self-consistent relating of rupture length,
870 width, average displacement, and moment release. *Bulletin of the*
871 *Seismological Society of America*, 100(5A), 1971- 1988, 2010.

872 Machette, M.N.: Active, capable, and potentially active faults; a paleoseismic
873 perspective, *J. Geodyn.*, 29, 387–392, 2000.

874 Main, I.: Statistical physics, seismogenesis, and seismic hazard, *Rev Geophys*, 34,
875 433-462, 1996.

876 Mansfield, C. and Cartwright, J.: Fault growth by linkage: observations and
877 implications from analogue models, *J Struct Geol*, 23, 745-763, 2001.

878 Meletti, C., Visini, F., D'Amico, V., and Rovida A.: Seismic hazard in central Italy and
879 the 2016 Amatrice earthquake, *Annals of Geophysics*, 59, doi:10.4401/ag-
880 7248, 2016.

881 McClymont, A. F., Villamor, P., and Green, A. G.: Assessing the contribution of off-
882 fault deformation to slip-rate estimates within the Taupo Rift, New Zealand,
883 using 3-D ground-penetrating radar surveying and trenching, *Terra Nova*, 21,
884 446-451, 2009a.

885 McClymont, A. F., Villamor, P., and Green, A. G.: Fault displacement accumulation
886 and slip rate variability within the Taupo Rift (New Zealand) based on trench
887 and 3-D ground-penetrating radar data, *Tectonics*, 28, 2009b.

888 Nicol, A., Walsh, J., Berryman, K., and Villamor, P.: Interdependence of fault
889 displacement rates and paleoearthquakes in an active rift, *Geology*, 34, 865-
890 868, 2006.

891 Nicol, A., Walsh, J., Mouslopoulou, V., and Villamor, P.: Earthquake histories and
892 Holocene acceleration of fault displacement rates, *Geology*, 37, 911-914,
893 2009.

894 Nicol, A., Walsh, J. J., Villamor, P., Seebeck, H., and Berryman, K. R.: Normal fault
895 interactions, paleoearthquakes and growth in an active rift, *J Struct Geol*, 32,
896 1101-1113, 2010.

897 Nicol, A., Walsh, J. J., Watterson, J., and Underhill, J. R.: Displacement rates of
898 normal faults, *Nature*, 390, 157-159, 1997.

899 Ordaz, M. and Reyes, C.: Earthquake hazard in Mexico City: Observations versus
900 computations, *B Seismol Soc Am*, 89, 1379-1383, 1999.

901 Pace, B., Bocchini, G. M., and Boncio, P.: Do static stress changes of a moderate-
902 magnitude earthquake significantly modify the regional seismic hazard? Hints
903 from the L'Aquila 2009 normal-faulting earthquake (Mw 6.3, central Italy),
904 *Terra Nova*, 26, 430-439, 2014.

905 Pace, B., Peruzza, L., Lavecchia, G., and Boncio, P.: Layered seismogenic source
906 model and probabilistic seismic-hazard analyses in central Italy, *B Seismol
907 Soc Am*, 96, 107-132, 2006.

908 Pace, B., Visini, F., and Peruzza, L.: FiSH: MATLAB Tools to Turn Fault Data into
909 Seismic-Hazard Models, *Seismol Res Lett*, 87, 374-386, 2016.

910 Peruzza, L., and Pace B.: Sensitivity analysis for seismic source characteristics to
911 probabilistic seismic hazard assessment in central Apennines (Abruzzo area),
912 *Bollettino di Geofisica Teorica ed Applicata* 43, 79–100, 2002.

913 Peruzza, L., Pace, B., and Visini, F.: Fault-Based Earthquake Rupture Forecast in
914 Central Italy: Remarks after the L'Aquila M-w 6.3 Event, *B Seismol Soc Am*,
915 101, 404-412, 2011.

916 Peruzza, L., Gee, R., Pace, B., Roberts, G., Scotti, O., Visini, F., Benedetti, L., and
917 Pagani, M.: PSHA after a strong earthquake: hints for the recovery, *Annals of
918 Geophysics*, 59, doi:10.4401/ag-7257, 2016

919 Roberts, G. P., Cowie, P., Papanikolaou, I., and Michetti, A. M.: Fault scaling
920 relationships, deformation rates and seismic hazards: an example from the
921 Lazio-Abruzzo Apennines, central Italy, *J Struct Geol*, 26, 377-398, 2004.

922 Roberts, G. P. and Michetti, A. M.: Spatial and temporal variations in growth rates
923 along active normal fault systems: an example from The Lazio-Abruzzo
924 Apennines, central Italy, *J Struct Geol*, 26, 339-376, 2004.

925 Robinson, R., Nicol, A., Walsh, J. J., and Villamor, P.: Features of earthquake
926 occurrence in a complex normal fault network: Results from a synthetic
927 seismicity model of the Taupo Rift, New Zealand, *J Geophys Res-Sol Ea*, 114,
928 2009.

929 Rovida, A., Locati, M., Camassi, R., Lolli, B., and Gasperini P.: CPTI15, the 2015
930 version of the Parametric Catalogue of Italian Earthquakes. Istituto Nazionale
931 di Geofisica e Vulcanologia. doi:<http://doi.org/10.6092/INGV.IT-CPTI15>, 2016.

932 Scotti, O., Clement, C., and Baumont, D.: Seismic hazard for design and verification
933 of nuclear installations in France: regulatory context, debated issues and
934 ongoing developments, *B Geofis Teor Appl*, 55, 135-148, 2014.

935 Stein, R. S., King, G. C. P., and Lin, J.: Stress Triggering of the 1994 M=6.7
936 Northridge, California, Earthquake by Its Predecessors, *Science*, 265, 1432-
937 1435, 1994.

938 Stirling, M., McVerry, G., Gerstenberger, M., Litchfield, N., Van Dissen, R.,
939 Berryman, K., Barnes, P., Wallace, L., Villamor, P., Langridge, R., Lamarche,
940 G., Nodder, S., Reyners, M., Bradley, B., Rhoades, D., Smith, W., Nicol, A.,
941 Pettinga, J., Clark, K., and Jacobs, K.: National Seismic Hazard Model for
942 New Zealand: 2010 Update, *B Seismol Soc Am*, 102, 1514-1542, 2012.

943 Stock, C. and Smith, E. G. C.: Adaptive kernel estimation and continuous probability
944 representation of historical earthquake catalogs, *B Seismol Soc Am*, 92, 904-
945 912, 2002a.

946 Stock, C. and Smith, E. G. C.: Comparison of seismicity models generated by
947 different kernel estimations, *B Seismol Soc Am*, 92, 913-922, 2002b.

948 Stucchi, M., Meletti, C., Montaldo, V., Crowley, H., Calvi, G. M., and Boschi, E.:
949 Seismic Hazard Assessment (2003-2009) for the Italian Building Code, *B*
950 *Seismol Soc Am*, 101, 1885-1911, 2011.

951 Verdecchia, A. and Carena, S.: Coulomb stress evolution in a diffuse plate boundary:
952 1400 years of earthquakes in eastern California and western Nevada, USA,
953 *Tectonics*, 35, 1793-1811, 2016.

954 Visini, F. and Pace, B.: Insights on a Key Parameter of Earthquake Forecasting, the
955 Coefficient of Variation of the Recurrence Time, Using a Simple Earthquake
956 Simulator, *Seismol Res Lett*, 85, 703-713, 2014.

957 Weichert, D. H: Estimation of the earthquake recurrence parameters for unequal
958 observation periods for different magnitudes, *Bulletin of the Seismological*
959 *Society of America*, 70, 1337-1346, 1980.

960 Wells, D. L. and Coppersmith, K. J.: New Empirical Relationships among Magnitude,
961 Rupture Length, Rupture Width, Rupture Area, and Surface Displacement, *B*
962 *Seismol Soc Am*, 84, 974-1002, 1994.

963 Werner, M. J., Helmstetter, A., Jackson, D. D., Kagan, Y. Y., and Wiemer, S.:
964 Adaptively smoothed seismicity earthquake forecasts for Italy, *Ann Geophys-*
965 *Italy*, 53, 107-116, 2010.

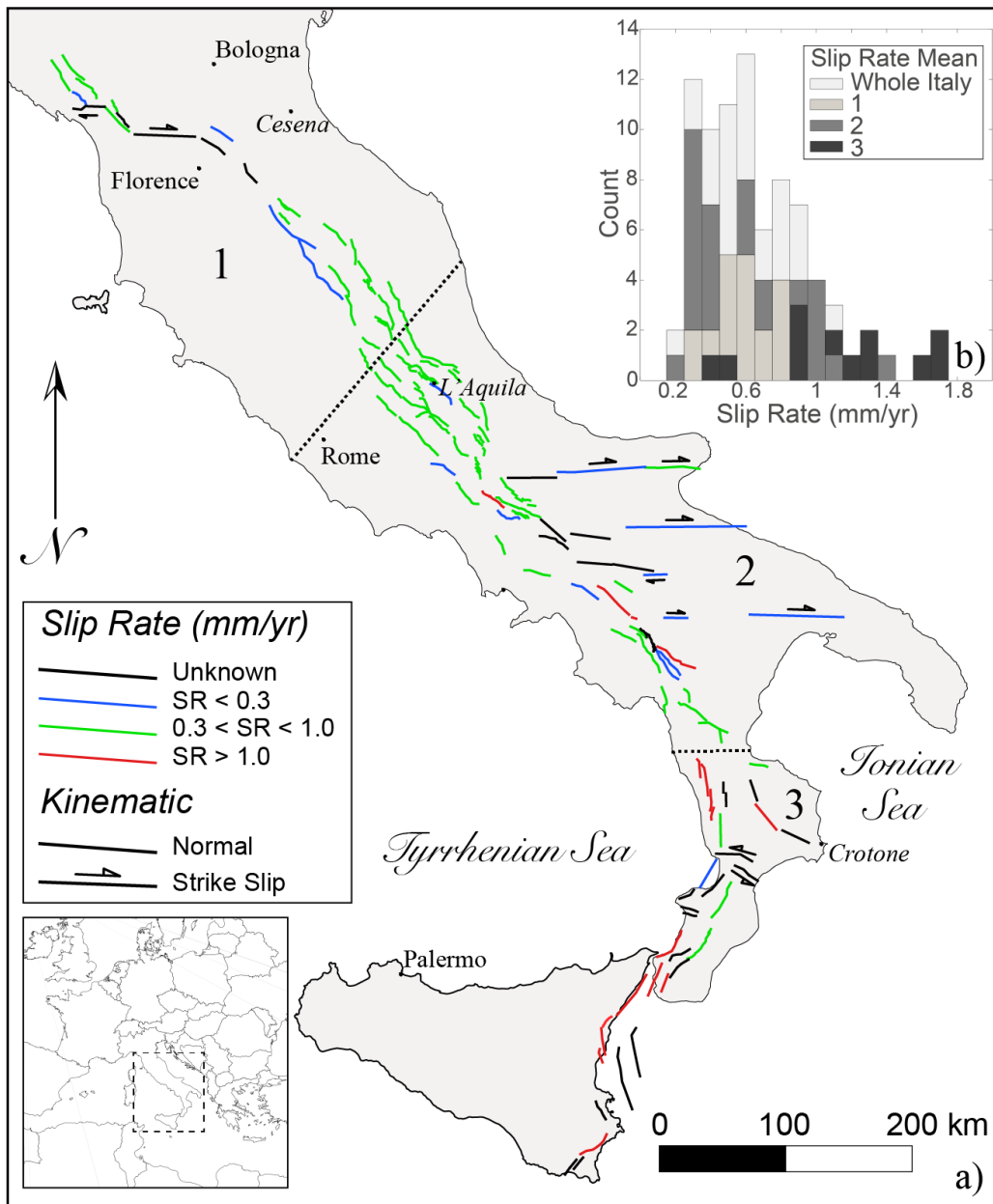
966 Woessner, J., Laurentiu, D., Giardini, D., Crowley, H., Cotton, F., Grunthal, G.,
967 Valensise, G., Arvidsson, R., Basili, R., Demircioglu, M. B., Hiemer, S.,
968 Meletti, C., Musson, R. W., Rovida, A. N., Sesetyan, K., Stucchi, M., and
969 Consortium, S.: The 2013 European Seismic Hazard Model: key components
970 and results, *B Earthq Eng*, 13, 3553-3596, 2015.

971 Youngs, R. R. and Coppersmith, K. J.: Implications of Fault Slip Rates and
972 Earthquake Recurrence Models to Probabilistic Seismic Hazard Estimates, *B*
973 *Seismol Soc Am*, 75, 939-964, 1985.

974 Zechar, J. D. and Jordan, T. H.: Simple smoothed seismicity earthquake forecasts
975 for Italy, *Ann Geophys-Italy*, 53, 99-105, 2010.

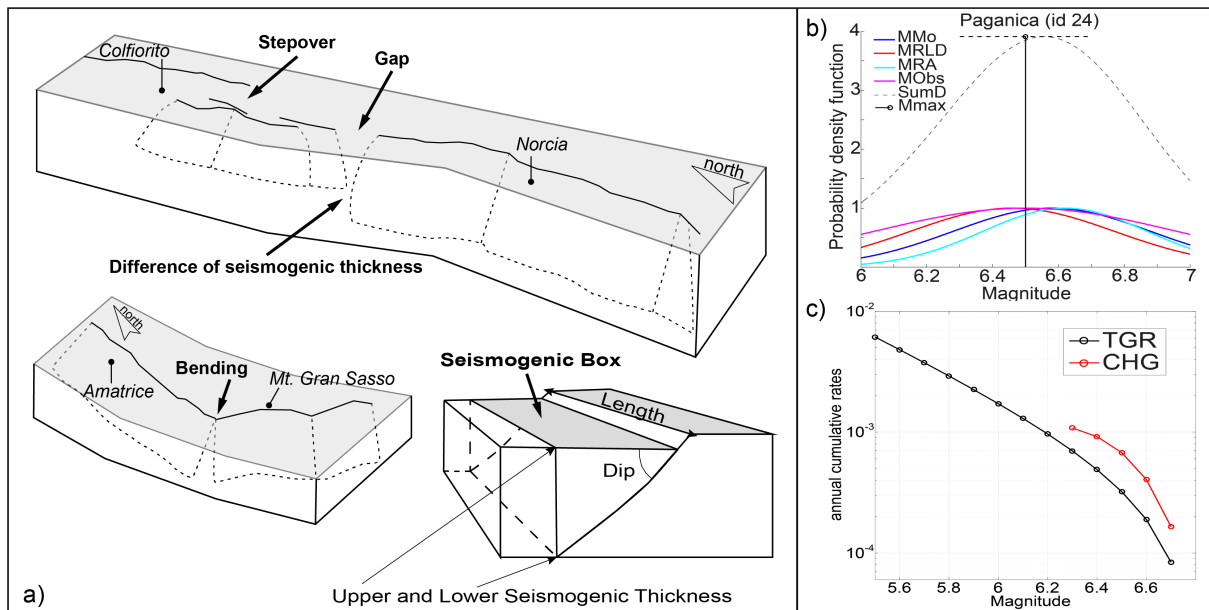
976 Zhao, J. X., Zhang, J., Asano, A., Ohno, Y., Oouchi, T., Takahashi, T., Ogawa, H.,
977 Irikura, K., Thio, H. K., Somerville, P. G., Fukushima, Y., and Fukushima, Y.:
978 Attenuation relations of strong ground motion in Japan using site classification
979 based on predominant period, *B Seismol Soc Am*, 96, 898-913, 2006.

980



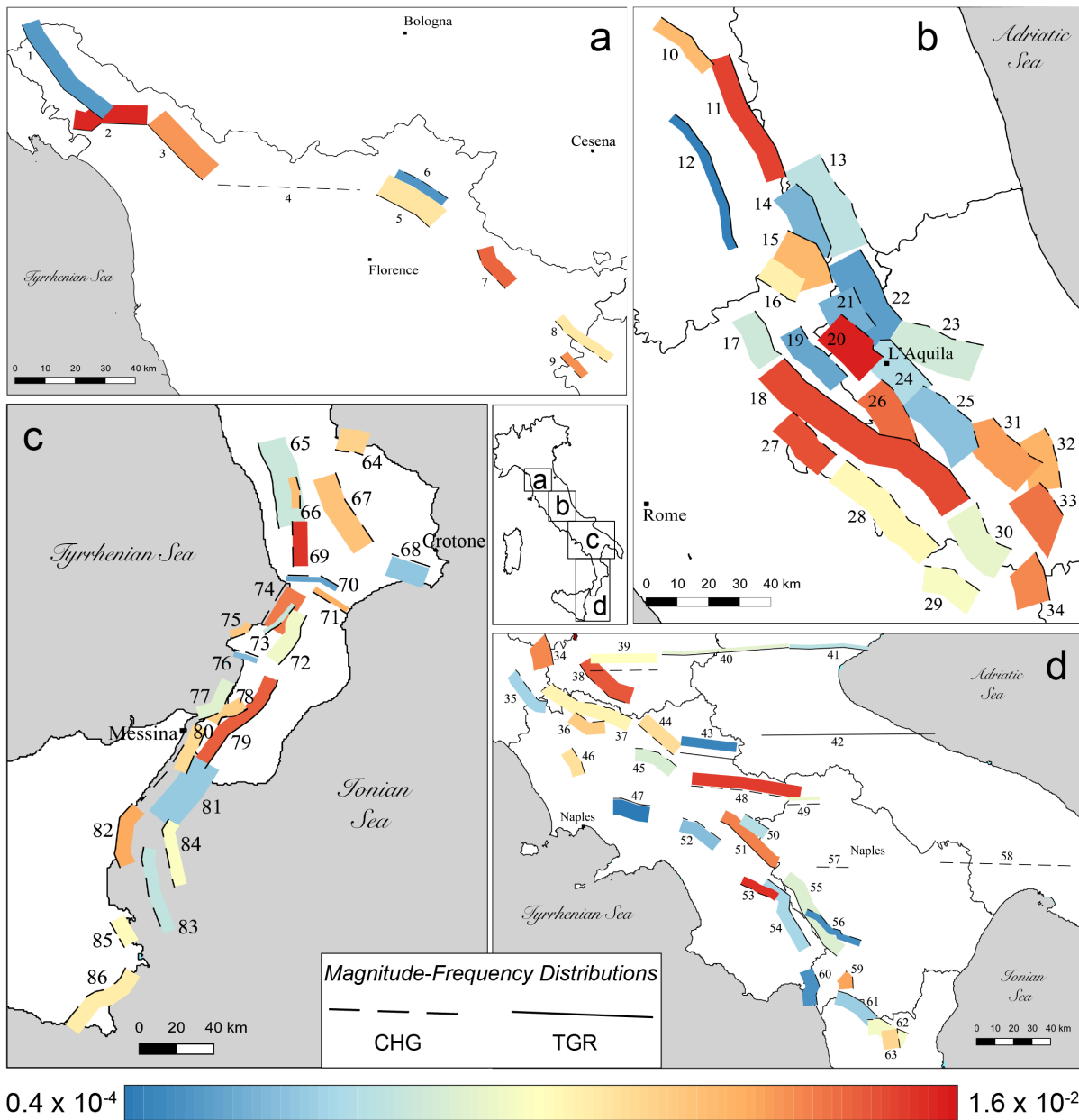
981

982 Fig. 1 a) Map of normal and strike-slip active faults used in this study. The colour
 983 scale indicates the slip rate. b) Histogram of the slip rate distribution in the entire
 984 study area and in three subsectors. The numbers 1, 2 and 3 represent the Northern
 985 Apennines, Central-Southern Apennines and Calabria-Sicilian coast regions,
 986 respectively. The dotted black lines are the boundaries of the regions.



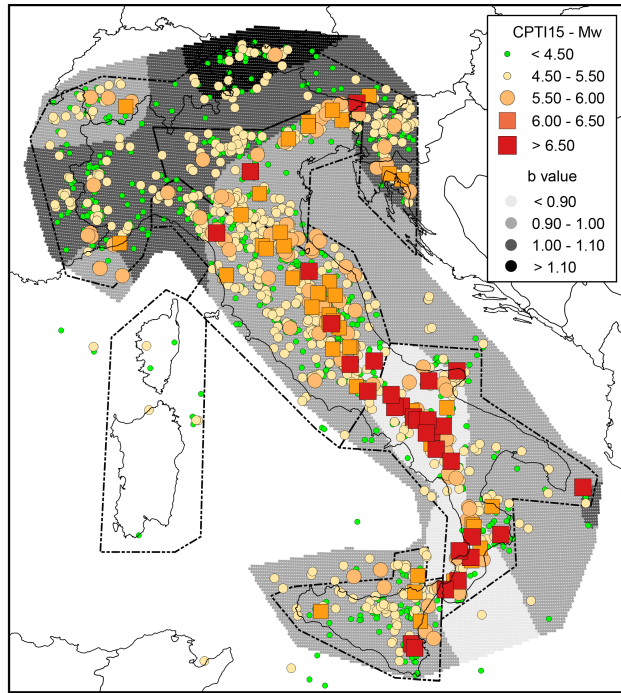
987

988 Fig. 2 a) Conceptual model of active faults and segmentation rules adopted to define
 989 a fault source and its planar projection, forming a seismogenic box [modified from
 990 Boncio et al., 2004]. b) Example of FiSH code output (see Pace et al., 2016 for
 991 details) for the Paganica fault source showing the magnitude estimates from
 992 empirical relationships and observations, both of which are affected by uncertainties.
 993 In this example, four magnitudes are estimated: M_{Mo} (blue line) is from the standard
 994 formula (IASPEI, 2005); M_{RDL} (red line) and M_{RA} (cyan line) correspond to
 995 estimates based on the maximum subsurface fault length and maximum rupture area
 996 from the empirical relationships of Wells and Coppersmith (1994) for length and
 997 area, respectively; and M_{Obs} (magenta line) is the largest observed moment
 998 magnitude. The black dashed line represents the summed probability density curve
 999 (SumD), the vertical black line represents the central value of the Gaussian fit of the
 1000 summed probability density curve (M_{max}), and the horizontal black dashed line
 1001 represents its standard deviation (σ M_{max}). The input values that were used to obtain
 1002 this output are provided in Table 1. c) Comparison of the magnitude–frequency
 1003 distributions of the Paganica source, which were obtained using the CHG model (red
 1004 line) and the TGR model (black line).



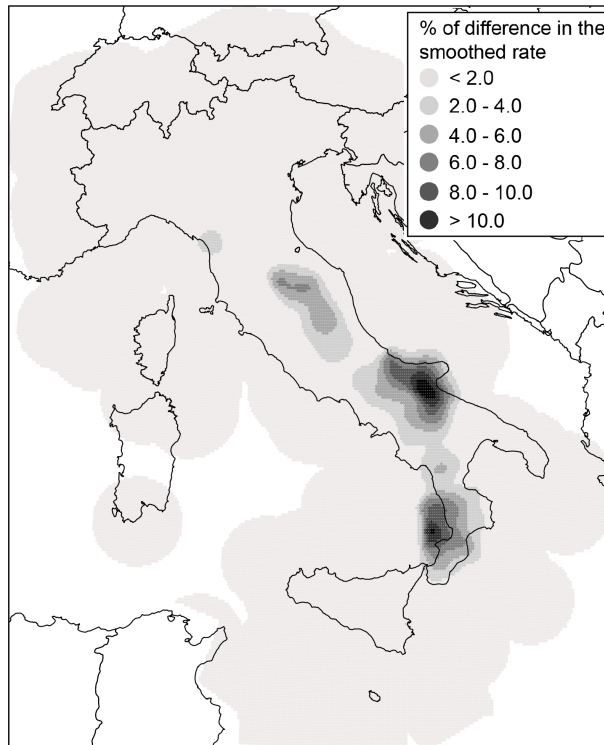
0.4 x 10⁻⁴ 1.6 x 10⁻²
 Activity Rates (#eq $M \geq 5.5$ in a year)

1005
 1006 Fig. 3 Maps showing the fault source inputs as seismicogenic boxes (see Fig. 2a). The
 1007 colour scale indicates the activity rate. Solid and dashed lines (corresponding to the
 1008 uppermost edge of the fault) are used to highlight our choice between the two end-
 1009 members of the MFD model adopted in the so-called *Mixed* model.



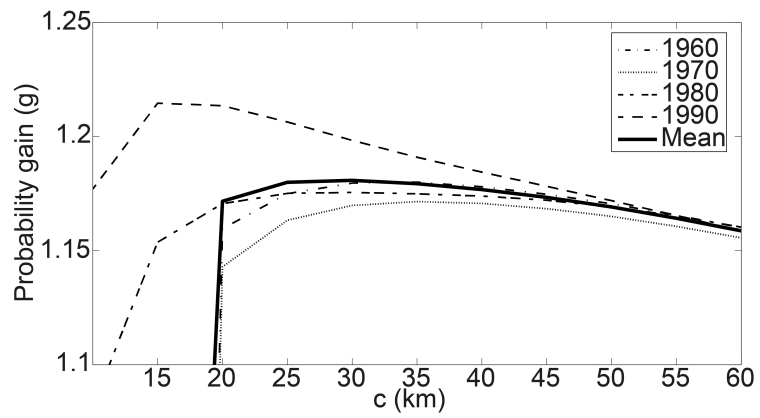
1010

1011 Fig. 4 Historical earthquakes from the most recent version of the historical
 1012 parametric Italian catalogue (CPTI15, Rovida et al., 2016), the spatial variations in b-
 1013 values and the polygons defining the **five macroseismic areas used to assess the**
 1014 **magnitude intervals.**



1015

1016 Fig. 5 Differences in percentages between the two smoothed rates produced by eq.
 1017 (2) using the complete catalogue and the modified catalogue without events
 1018 associated with known active faults (*TGR* model)



1019

1020

1021

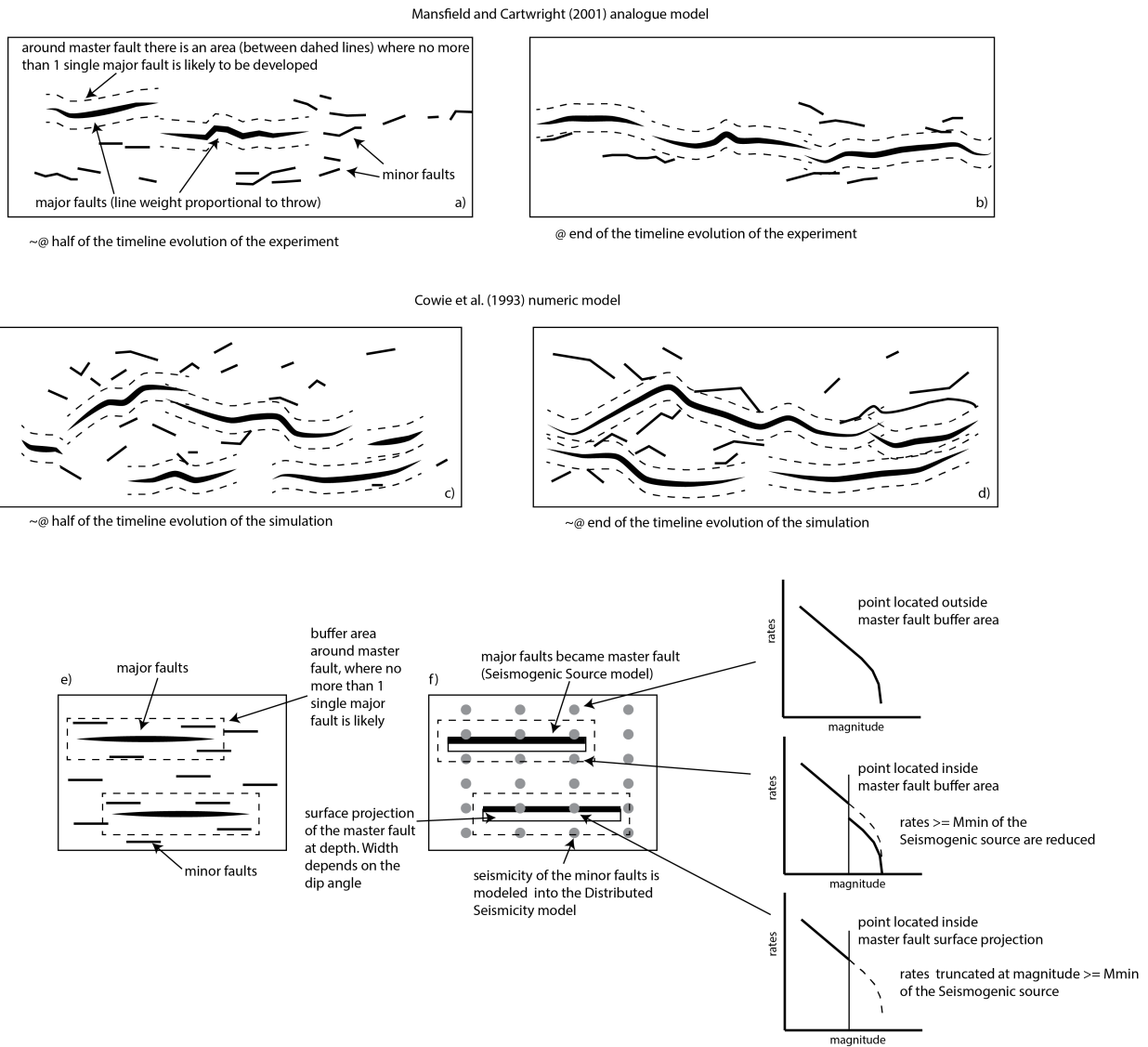
1022

1023

1024

1025

Fig. 6 Probability gain per earthquake (see eq. 3) versus correlation distance c , highlighting the best radius for use in the smoothed seismicity approach (eq. 2)



1026

1027

1028

1029

1030

1031

1032

1033

1034

1035

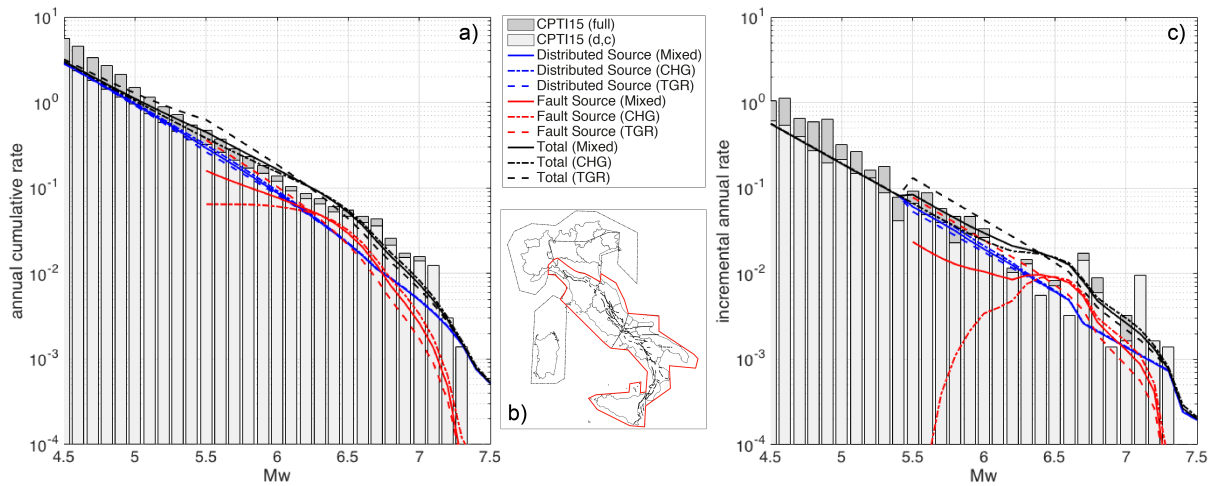
1036

1037

1038

1039

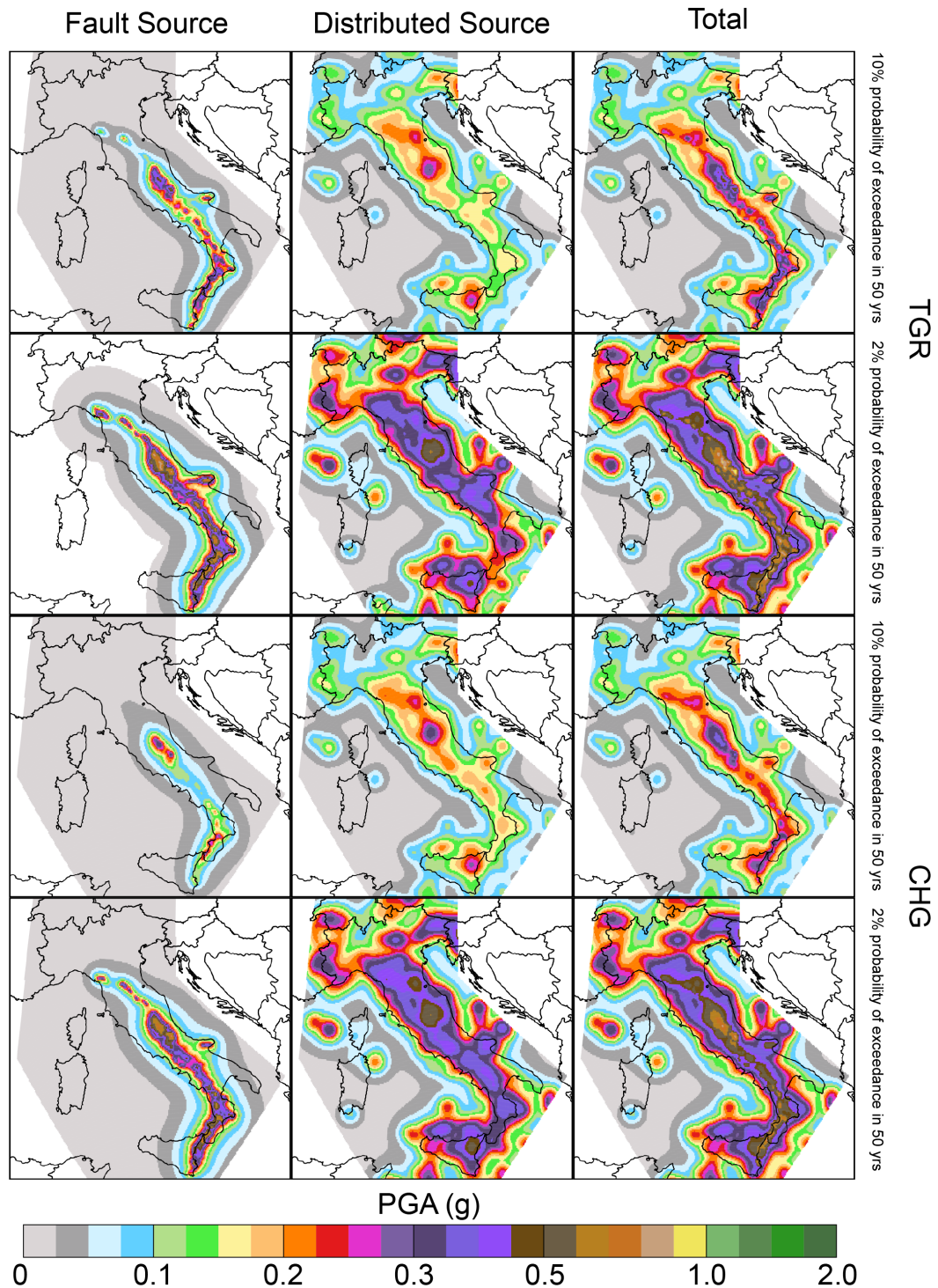
Fig. 7 Fault system evolution and implications in our model. a) and b) Diagrams from the Mansfield and Cartwright (2001) analogue experiment in two different stages: the approximate midpoint of the sequence and the end of the sequence. Areas exist around master faults where no more than a single major fault is likely to develop. c) and d) Diagrams from numerical modelling conducted by Cowie et al. (1993) in two different stages. This experiment shows the similar evolutionary features of major and minor faults. e) and f) Application of the analogue and numeric modelling of fault system evolution to the fault source input proposed in this paper. A buffer area is drawn around each fault source, where it is unlikely for other major faults to develop, and it accounts for the length and slip rate of the fault source. This buffer area is useful for reducing or truncating the rates of expected distributed seismicity based on the position of a distributed seismicity point with respect to the buffer zone (see the text for details).



1040

1041 Fig. 8 a) annual cumulative rate and c) incremental annual rate computed for the red
 1042 bounded area in b). The rates have been computed using: (i) the full CPTI15
 1043 catalogue; (ii) the declustered and complete catalogue (CPTI15 (d, c) in the legend)
 1044 obtained using the completeness magnitude thresholds over different periods of time
 1045 given by Stucchi et al. (2011) for five large zones; (iii) the distributed sources; (iv) the
 1046 fault sources; and (v) summing fault and distributed sources (Total).

1047



1048

1049

1050

1051

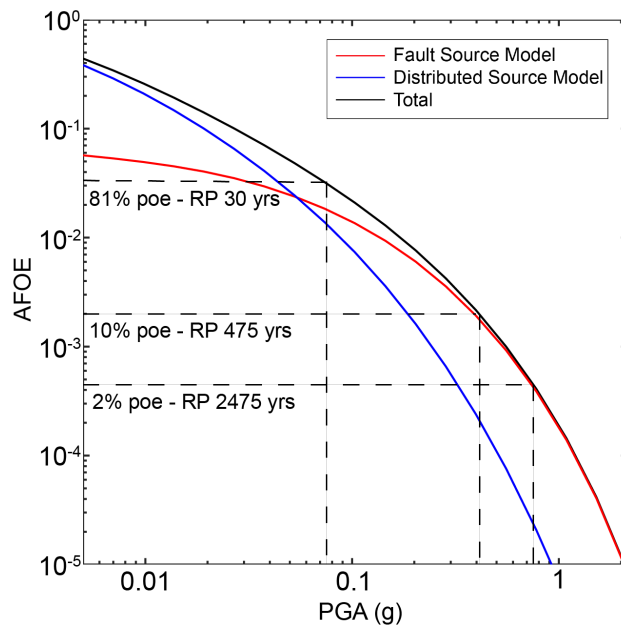
1052

1053

1054

1055

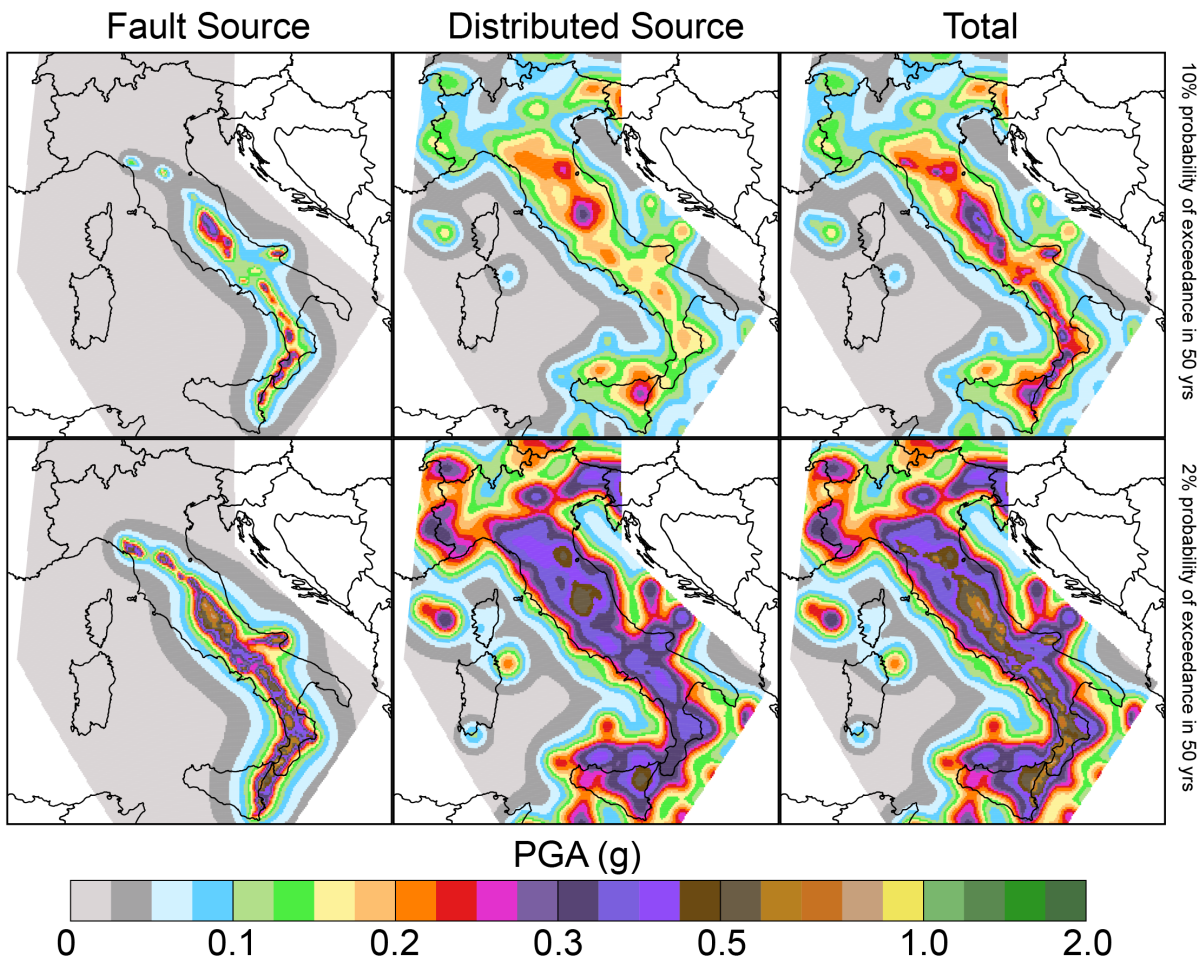
Fig. 9 Seismic hazard maps for the *TGR* and *CHG* models expressed in terms of peak ground acceleration (PGA) and computed for a latitude/longitude grid spacing of 0.05° . The first and second rows show the fault source, distributed source and total maps of the *TGR* model computed for 10% probability of exceedance in 50 years and 2% probability of exceedance in 50 years, corresponding to return periods of 475 and 2475 years, respectively. The third and fourth rows show the same maps for the *CHG* model.



1056

1057 Fig. 10 An example of the contribution to the total seismic hazard level (black line), in
 1058 terms of hazard curves, by the *fault* (red line) and *distributed* (blue line) source inputs
 1059 for one of the 45,602 grid points (L'Aquila, 42.400-13.400). The dashed lines
 1060 represent the 2%, 10% and 81% probabilities of exceedance (poe) in 50 years.

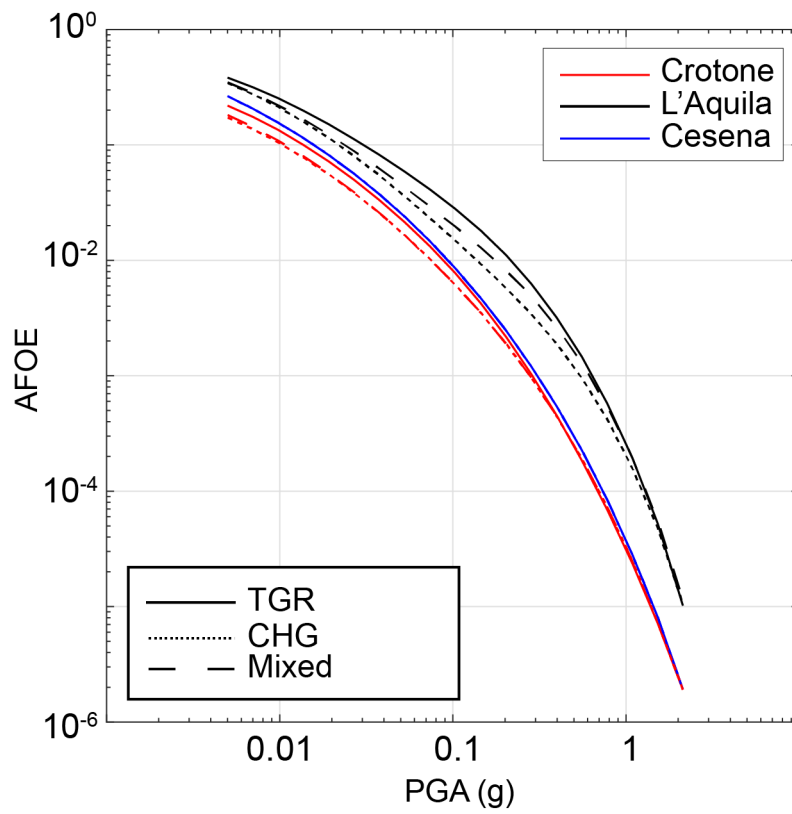
1061



1062

1063

1064 Fig. 11 Seismic hazard maps for the *Mixed* model. The first row shows the fault
 1065 source, distributed source and total maps computed for 10% probability of
 1066 exceedance in 50 years, and the second row shows the same maps but computed
 1067 for 2% probability of exceedance in 50 years, corresponding to return periods of 475
 1068 and 2475 years, respectively. The results are expressed in terms of peak ground
 1069 acceleration (PGA).

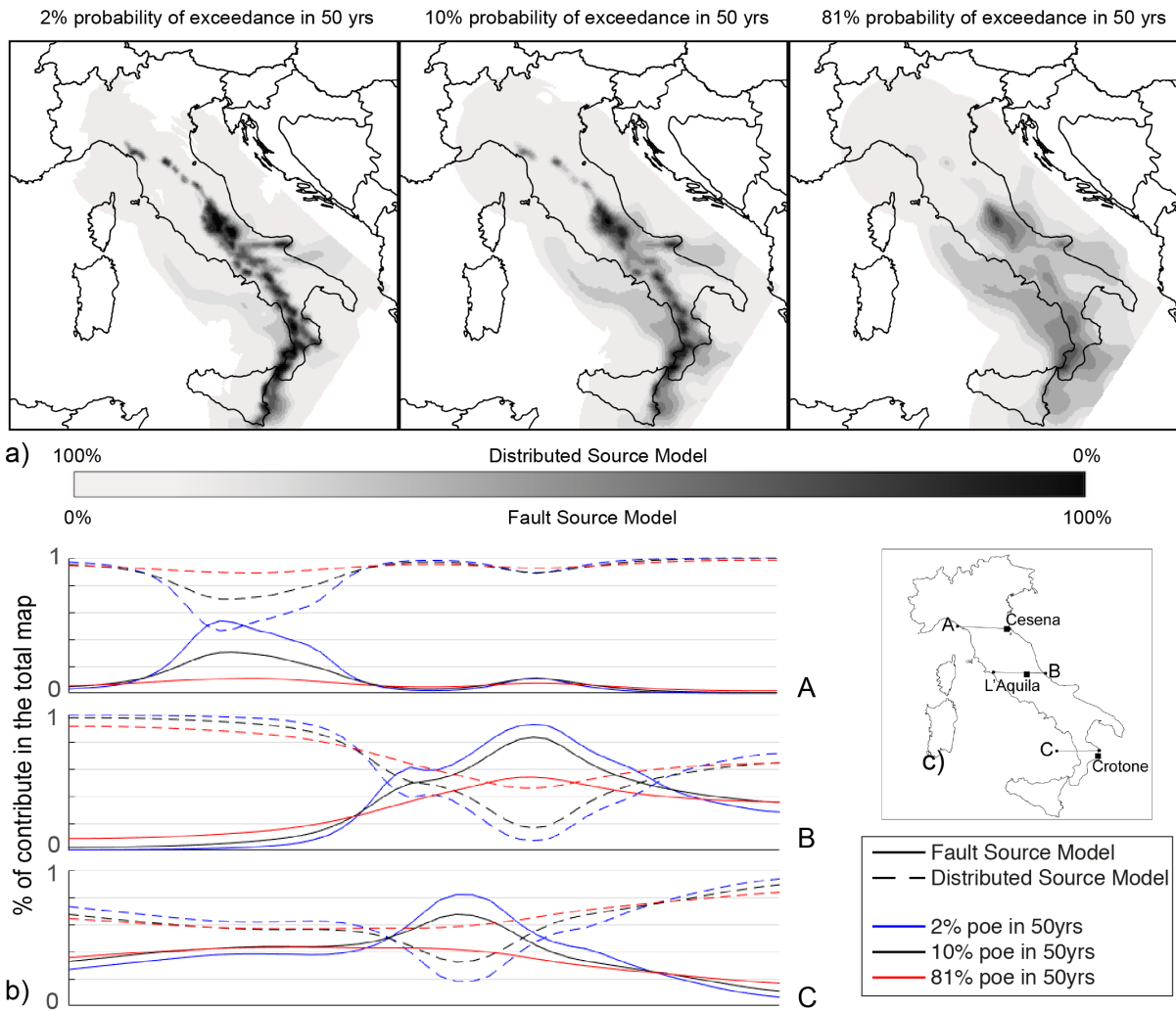


1070

1071 Fig. 12 *CHG* (dotted line), *TGR* (solid line) and *Mixed* model (dashed line) hazard
 1072 curves for three sites: Cesena (red line), L'Aquila (black line) and Crotone (blue line)

1073





1074

1075

1076

1077

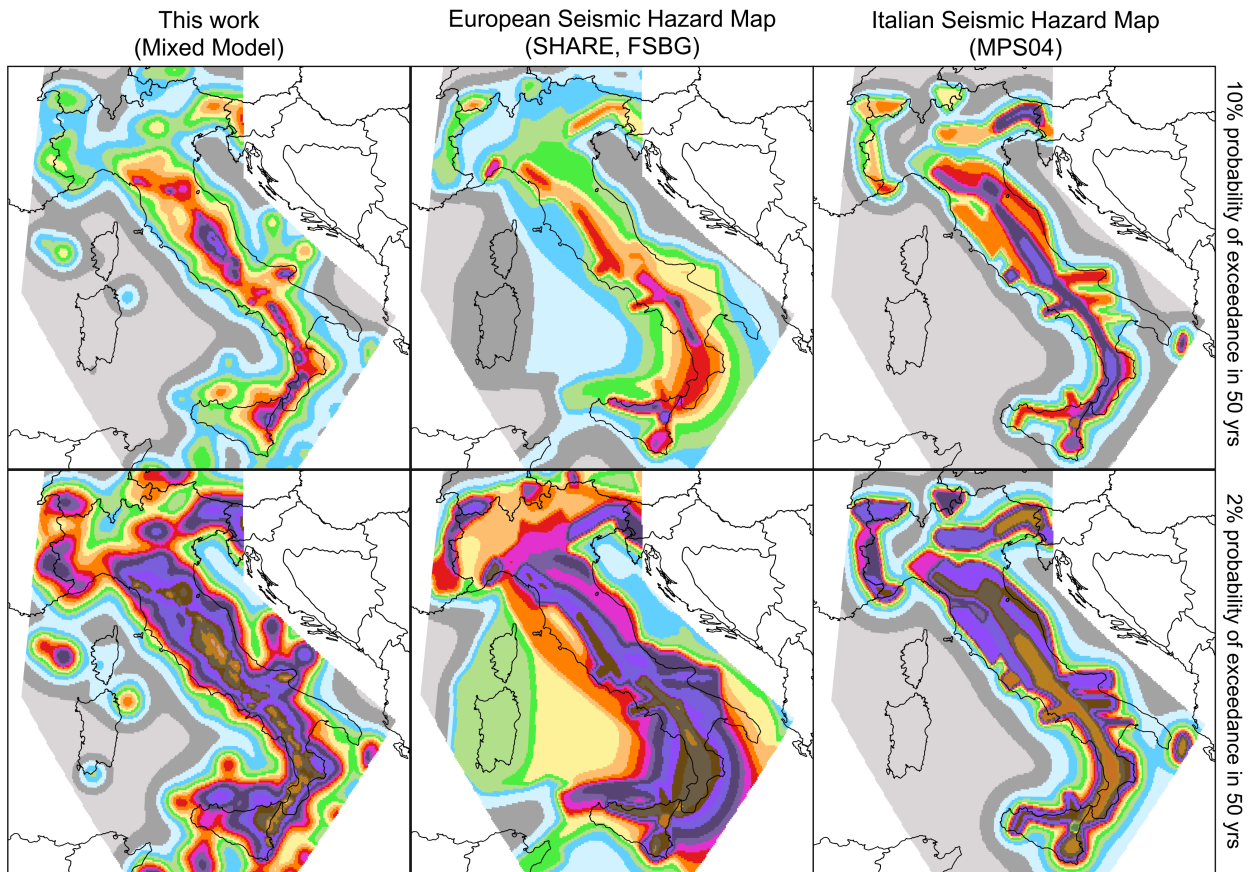
1078

1079

1080

1081

Fig. 13 a) Contribution maps of the Mixed *fault* and *distributed* source inputs to the total hazard level for three probabilities of exceedance: 2%, 10% and 81%, corresponding to return periods of 2475, 475 and 30 years, respectively. b) Contributions of the Mixed *fault* (solid line) and *distributed* (dashed line) source inputs along three profiles (A, B and C in Fig. 13c) for three probabilities of exceedance: 2% (blue line), 10% (black line) and 81% (red line).



1082

1083 Fig. 14 Seismic hazard maps expressed in terms of Peak Ground Acceleration
 1084 (PGA) and computed for a latitude/longitude grid spacing of 0.05° based on site
 1085 conditions. The figure shows a comparison of our model (*Mixed* model, on the left),
 1086 the SHARE model (FSBG logic tree branch, in the middle) and the current Italian
 1087 national seismic hazard map (MPS04, on the right). The same GMPE (Akkar et al.
 1088 2013, Chiou et al., 2008, Faccioli et al., 2010 and Zhao et al., 2006 and Bindi et al.
 1089 2014), were used for all models to obtain and compare the maps.

1090

1091

1092

1093

1094

1095

ID	Fault Sources	L (km)	Dip (°)	Upper (km)	Lower (km)	SR _{min} (mm/yr)	SR _{max} (mm/yr)
1	Lunigiana	43.8	40	0	5	0.28	0.7
2	North Apuane Transfer	25.5	45	0	7	0.33	0.83
3	Garfagnana	26.9	30	0	4.5	0.35	0.57
4	Garfagnana Transfer	47.1	90	2	7	0.33	0.83
5	Mugello	21.0	40	0	7	0.33	0.83
6	Ronta	19.3	65	0	7	0.17	0.5
7	Poppi	17.1	40	0	4.5	0.33	0.83
8	Città di Castello	22.9	40	0	3	0.25	1.2
9	M.S.M. Tiberina	10.5	40	0	2.5	0.25	0.75
10	Gubbio	23.6	50	0	6	0.4	1.2
11	Colfiorito System	45.9	50	0	8	0.25	0.9
12	Umbra Valley	51.1	55	0	4.5	0.4	1.2
13	Vettore-Bove	35.4	50	0	15	0.2	1.05
14	Nottoria-Preci	29.0	50	0	12	0.2	1
15	Cascia-Cittareale	24.3	50	0	13.5	0.2	1
16	Leonessa	14.9	55	0	12	0.1	0.7
17	Rieti	17.6	50	0	10	0.25	0.6
18	Fucino	82.3	50	0	13	0.3	1.6
19	Sella di Corno	23.1	60	0	13	0.35	0.7
20	Pizzoli-Pettino	21.3	50	0	14	0.3	1
21	Monteale	15.1	50	0	14	0.25	0.9
22	Gorzano	28.1	50	0	15	0.2	1
23	Gran Sasso	28.4	50	0	15	0.35	1.2
24	Paganica	23.7	50	0	14	0.4	0.9
25	Middle Aternum Valley	29.1	50	0	14	0.15	0.45
26	Campo Felice-Ovindoli	26.2	50	0	13	0.2	1.6
27	Carsoli	20.5	50	0	11	0.35	0.6
28	Liri	42.5	50	0	11	0.3	1.26
29	Sora	20.4	50	0	11	0.15	0.45
30	Marsicano	20.0	50	0	13	0.25	1.2
31	Sulmona	22.6	50	0	15	0.6	1.35
32	Maiella	21.4	55	0	15	0.7	1.6
33	Aremogna C.Miglia	13.1	50	0	15	0.1	0.6
34	Barrea	17.1	55	0	13	0.2	1
35	Cassino	24.6	60	0	11	0.25	0.5
36	Ailano-Piedimonte	17.6	60	0	12	0.15	0.35
37	Matese	48.3	60	0	13	0.2	1.9
38	Bojano	35.5	55	0	13	0.2	0.9
39	Frosolone	36.1	70	11	25	0.35	0.93
40	Ripabottoni-San Severo	68.3	85	6	25	0.1	0.5
41	Mattinata	42.3	85	0	25	0.7	1
42	Castelluccio dei Sauri	93.2	90	11	22	0.1	0.5
43	Ariano Irpino	30.1	70	11	25	0.35	0.93
44	Tammaro	25.0	60	0	13	0.35	0.93
45	Benevento	25.0	55	0	10	0.35	0.93
46	Volturno	15.7	60	1	13	0.23	0.57
47	Avella	20.5	55	1	13	0.2	0.7
48	Ufita-Bisaccia	59.0	64	1.5	15	0.35	0.93
49	Melfi	17.2	80	12	22	0.1	0.5
50	Irpinia Antithetic	15.0	60	0	11	0.2	0.53

51	Irpinia	39.7	65	0	14	0.3	2.5
52	Volturara	23.7	60	1	13	0.2	0.35
53	Alburni	20.4	60	0	8	0.35	0.7
54	Caggiano-Diano Valley	46.0	60	0	12	0.35	1.15
55	Pergola-Maddalena	50.6	60	0	12	0.20	0.93
56	Agri	34.9	50	5	15	0.8	1.3
57	Potenza	17.8	90	15	21	0.1	0.5
58	Palagianello	73.3	90	13	22	0.1	0.5
59	Monte Alpi	10.9	60	0	13	0.35	0.9
60	Maratea	21.6	60	0	13	0.46	0.7
61	Mercure	25.8	60	0	13	0.2	0.6
62	Pollino	23.8	60	0	15	0.22	0.58
63	Castrovillari	10.3	60	0	15	0.2	1.15
64	Rossano	14.9	60	0	22	0.5	0.6
65	Crati West	49.7	45	0	15	0.84	1.4
66	Crati East	18.4	60	0	8	0.75	1.45
67	Lakes	43.6	60	0	22	0.75	1.45
68	Fuscalto	21.1	60	2	22	0.75	1.45
69	Piano Lago-Decollatura	25.0	60	1	15	0.23	0.57
70	Catanzaro North	29.5	80	3	20	0.75	1.45
71	Catanzaro South	21.3	80	3	20	0.75	1.45
72	Serre	31.6	60	0	15	0.7	1.15
73	Vibo	23.0	80	0	15	0.75	1.45
74	Sant'Eufemia Gulf	24.8	40	1	11	0.11	0.3
75	Capo Vaticano	13.7	60	0	8	0.75	1.45
76	Coccorino	13.3	70	3	11	0.75	1.45
77	Scilla	29.7	60	0	13	0.8	1.5
78	Sant'Eufemia	19.2	60	0	13	0.75	1.45
79	Cittanova-Armo	63.8	60	0	13	0.45	1.45
80	Reggio Calabria	27.2	60	0	13	0.7	2
81	Taormina	38.7	30	3	13	0.9	2.6
82	Acireale	39.4	60	0	15	1.15	2.3
83	Western Ionian	50.1	65	0	15	0.75	1.45
84	Eastern Ionian	39.3	65	0	15	0.75	1.45
85	Climiti	15.7	60	0	15	0.75	1.45
86	Avola	46.9	60	0	16	0.8	1.6

1096

1097 Table 1 Geometric Parameters of the Fault Sources. L, along-strike length; Dip,
1098 inclination angle of the fault plane; Upper and Lower, the thickness bounds of the
1099 local seismogenic layer; SRmin and SRmax, the slip rates assigned to the sources
1100 using the references available (see the supplemental files); and ID, the fault number
1101 identifier.

1102

ID	Fault Sources	Historical Earthquakes				Instrumental Earthquakes		
		yyyy/mm/dd	I_{Max}	I_0	M_w	sD	yyyy/mm/dd	M_w
1	Lunigiana	1481/05/07	VIII	VIII	5.6	0.4		
		1834/02/14	IX	IX	6.0	0.1		
2	North Apuane Transfer	1837/04/11	X	IX	5.9	0.1		
3	Garfagnana	1740/03/06	VIII	VIII	5.6	0.2		
		1920/09/07	X	X	6.5	0.1		
4	Garfagnana Transfer							
5	Mugello	1542/06/13	IX	IX	6.0	0.2		
		1919/06/29	X	X	6.4	0.1		
6	Ronta							
7	Poppi							
8	Città di Castello	1269			5.7			
		1389/10/18	IX	IX	6	0.5		
		1458/04/26	VIII-IX	VIII-IX	5.8	0.5		
		1789/09/30	IX	IX	5.9	0.1		
9	M.S.M. Tiberina	1352/12/25	IX	IX	6.3	0.2		
		1917/04/26	IX-X	IX-X	6.0	0.1		
10	Gubbio						1984/04/29	5.6
11	Colfiorito System	1279/04/30	X	IX	6.2	0.2	1997/09/26	5.7
		1747/04/17	IX	IX	6.1	0.1	1997/09/26	6
		1751/07/27	X	X	6.4	0.1		
12	Umbra Valley	1277		VIII	5.6	0.5		
		1832/01/13	X	X	6.4	0.1		
		1854/02/12	VIII	VIII	5.6	0.3		
13	Vettore-Bove						2016/10/30	6.5
14	Nottoria-Preci	1328/12/01	X	X	6.5	0.3	1979/09/19	5.8
		1703/01/14	XI	XI	6.9	0.1		
		1719/06/27	VIII	VIII	5.6	0.3		
		1730/05/12	IX	IX	6.0	0.1		
		1859/08/22	VIII-IX	VIII-IX	5.7	0.3		
		1879/02/23	VIII	VIII	5.6	0.3		
15	Cascia-Cittareale	1599/11/06	IX	IX	6.1	0.2		
		1916/11/16	VIII	VIII	5.5	0.1		
16	Leonessa							
17	Rieti	1298/12/01	X	IX-X	6.3	0.5		
		1785/10/09	VIII-IX	VIII-IX	5.8	0.2		
18	Fucino	1349/09/09	IX	IX	6.3	0.1		
		1904/02/24	IX	VIII-IX	5.7	0.1		
		1915/01/13	XI	XI	7	0.1		
19	Sella di Corno							
20	Pizzoli-Pettino	1703/02/02	X	X	6.7	0.1		
21	Montereale							
22	Gorzano	1639/10/07	X	IX-X	6.2	0.2		
		1646/04/28	IX	IX	5.9	0.4		
23	Gran Sasso							
24	Paganica	1315/12/03	VIII	VIII	5.6	0.5	2009/06/04	6.3
		1461/11/27	X	X	6.5	0.5		
25	Middle Aternum Valley							
26	Campo Felice-Ovindoli							
27	Carsoli							
28	Liri							
29	Sora	1654/07/24	X	IX-X	6.3	0.2		
30	Marsicano							
31	Sulmona							
32	Maiella							
33	Aremogna C.Miglia							
34	Barrea						1984/05/07	5.9
35	Cassino							
36	Ailano-Piedimonte							
37	Matese	1349/09/09	X-XI	X	6.8	0.2		

38	Bojano	1805/07/26	X	X	6.7	0.1		
39	Frosolone	1456/12/05	XI	XI	7	0.1		
40	Ripabottoni-San Severo	1627/07/30	X	X	6.7	0.1	2002/10/31	5.7
		1647/05/05	VII-VIII	VII-VIII	5.7	0.4		
		1657/01/29	IX-X	VIII-IX	6.0	0.2		
41	Mattinata	1875/12/06	VIII	VIII	5.9	0.1		
		1889/12/08	VII	VII	5.5	0.1		
		1948/08/18	VII-VIII	VII-VIII	5.6	0.1		
42	Castelluccio dei Sauri	1361/07/17	X	IX	6	0.5		
		1560/05/11	VIII	VIII	5.7	0.5		
		1731/03/20	IX	IX	6.3	0.1		
43	Ariano Irpino	1456/12/05			6.9	0.1		
		1962/08/21	IX	IX	6.2	0.1		
44	Tammaro	1688/06/05	XI	XI	7	0.1		
45	Benevento							
46	Volturno							
47	Avella	1499/12/05	VIII	VIII	5.6	0.5		
48	Ufita-Bisaccia	1732/11/29	X-XI	X-XI	6.8	0.1		
		1930/07/23	X	X	6.7	0.1		
49	Melfi	1851/08/14	X	X	6.5	0.1		
50	Irpinia Antithetic							
51	Irpinia	1466/01/15	VIII-IX	VIII-IX	6.0	0.2	1980/11/23	6.8
		1692/03/04	VIII	VIII	5.9	0.4		
		1694/09/08	X	X	6.7	0.1		
		1853/04/09	IX	VIII	5.6	0.2		
52	Volturara							
53	Alburni							
54	Caggiano-Diano Valley	1561/07/31	IX-X	X	6.3	0.1		
55	Pergola-Maddalena	1857/12/16			6.5			
		1857/12/16			6.3			
56	Agri							
57	Potenza	1273/12/18	VIII-IX	VIII-IX	5.8	0.5	1990/05/05	5.8
58	Palagianello							
59	Monte Alpi							
60	Maratea							
61	Mercure	1708/01/26	VIII-IX	VIII	5.6	0.6	1998/09/09	5.5
62	Pollino							
63	Castrovillari							
64	Rossano	1836/04/25	X	IX	6.2	0.2		

65	Crati West	1184/05/24	IX	IX	6.8	0.3
		1870/10/04	X	IX-X	6.2	0.1
		1886/03/06	VII-VIII	VII-VIII	5.6	0.3
66	Crati East	1767/07/14	VIII-IX	VIII-IX	5.9	0.2
		1835/10/12	X	IX	5.9	0.3
67	Lakes	1638/06/08	X	X	6.8	0.1
68	Fuscalto	1832/03/08	X	X	6.6	0.1
69	Piano Lago-Decollatura					
70	Catanzaro North	1638/03/27			6.6	
71	Catanzaro South	1626/04/04	X	IX	6.1	0.4
72	Serre	1659/11/05	X	X	6.6	0.1
		1743/12/07	IX-X	VIII-IX	5.9	0.2
		1783/02/07	X-XI	X-XI	6.7	0.1
		1791/10/13	IX	IX	6.1	0.1
73	Vibo					
74	Sant'Eufemia Gulf	1905/09/08	X-XI	X-XI	7	0.1
75	Capo Vaticano					
76	Coccorino	1928/03/07	VIII	VII-VIII	5.9	0.1
77	Scilla					
78	Sant'Eufemia	1894/11/16	IX	IX	6.1	0.1
79	Cittanova-Armo	1509/02/25	IX	VIII	5.6	0.4
		1783/02/05	XI	XI	7.1	0.1
80	Reggio Calabria					
81	Taormina	1908/12/28	XI	XI	7.1	0.2
82	Acireale	1818/02/20	IX-X	IX-X	6.3	0.1
83	Western Ionian	1693/01/11	XI	XI	7.3	0.1
84	Eastern Ionian					
85	Climiti					
86	Avola					

1103

1104 Table 2 Earthquake-Source Association Adopted for Fault Sources. I_{Max} , maximum
1105 intensity; I_0 , epicentral intensity; M_w , moment magnitude; and sD, standard deviation
1106 of the moment magnitude. For references, see the supplemental files.